Advanced Integrated Optical Beamforming Networks for Broadband Phased Array Antenna Systems

Maurizio Burla

ADVANCED INTEGRATED OPTICAL BEAM FORMING NETWORKS FOR BROADBAND PHASED ARRAY ANTENNA SYSTEMS

by

Maurizio Burla

Samenstelling van de promotiecommissie:

Voorzitter & Secretaris:

Prof. dr. G. van der Steenhoven   University of Twente, The Netherlands

Promotor:

Prof. dr. ir. Wim C. van Etten   University of Twente, The Netherlands

Assistent-promotor:

Dr. ir. Chris G. H. Roeloffzen   University of Twente, The Netherlands

Interne leden:

Prof. dr. ir. Kees Slump   University of Twente, The Netherlands
Prof. dr. Klaus Boller   University of Twente, The Netherlands

Externe leden:

Prof. dr. José Capmany   Universidad Politécnica de Valencia (UPV), Spain
Dr. ir. Bart Verbeek   Chairman IOP Photonic Devices, The Netherlands
Dr. ir. Peter Maat   ASTRON, The Netherlands

ADVANCED INTEGRATED OPTICAL BEAM FORMING NETWORKS
FOR BROADBAND PHASED ARRAY ANTENNA SYSTEMS

PROEFSCHRIFT

ter verkrijging van
de graad van doctor aan de Universiteit Twente,
op gezag van de Rector Magnificus,
prof.dr. H. Brinksma,
volgens besluit van het College voor Promoties
in het openbaar te verdedigen
op woensdag 18 september 2013 om 12.45 uur

door
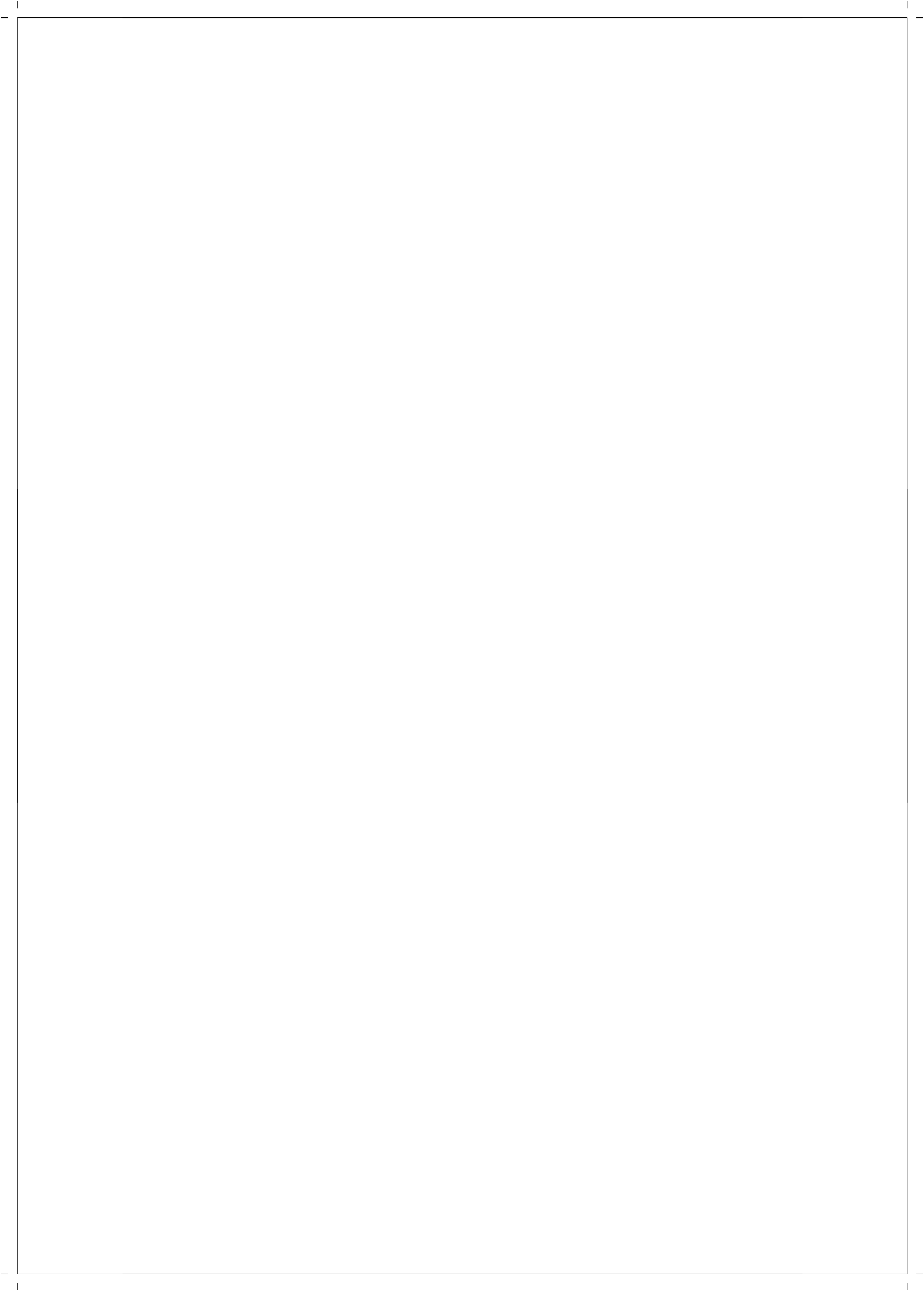
Maurizio Burla

geboren op 13 augustus 1982
te Orvieto, Italië

Dit proefschrift is goedgekeurd door:

De promotor: Prof. dr. ir. W. C. van Etten

De assistent-promotor: Dr. ir. C. G. H. Roeloffzen

To the memory of Frank Kooiman

Summary

Since the first half of the twentieth century, a large interest has been addressed by the scientific and engineering community to the world of phased arrays antennas. Their technology started to be developed during the Second World War for early warning radar techniques to identify threats from the skies. Those capable antennas have been deployed over the years in a number of diversified fields to address different applications needs. First employed almost exclusively in the defense and space domains, nowadays the increased need for broadband connectivity in personal communications is leveraging their diffusion to the field of smart antennas for modern wireless communications.

This thesis deals with a special way to fully exploit and further enhance the high flexibility of those complex yet very powerful type of antennas, mainly in terms of speed, compactness and cost. A number of fields have benefited the extremely low loss and broad bandwidth of optical communication technology. Especially interesting to us are the capabilities and extended possibilities brought to the world of microwave and antenna engineering by the use of optics and, specifically, of integrated photonics. This field is known as integrated microwave photonics. The huge bandwidth and extreme low loss of optical fibers can be harnessed to implement very capable signal processing circuits for high-frequency electrical signals. In particular, very broadband and continuosly tunable time delay units can be realized optically; those are of fundamental interest in a number of signal processing functionalities. Specifically, our interest in this work has been the design, realization, testing and integration in complex systems of novel *beamformers* that employ those delay lines, in conjunction with other components, to control the direction of radiation of a high-performance antenna array. When realized with integrated optical technology, we talk about integrated optical beamformers.

An introduction on the basics of phased arrays and their fundamental theory is given. This will form the basis of the motivation of the following work, and in particular of the use of broadband time delay units to realize antenna "control units" or beamformers. An overview on the works done to date in the field of optically-controlled antennas is presented, together with an introduction on the basic concept of the fascinating new field of integrated microwave photonics. The basic delay units employed in the present work have been the optical ring resonators. First we describe the characteristics of those structural slow-light devices, then we describe the system design and performance analysis of integrated beamformers based on those type of building blocks. After that, we present the actual demonstration of their functionality, their integration in a system demonstrator and the

test. Those steps were performed in collaboration with two important research institutes in the Netherlands, NLR and ASTRON, where two demonstrators have been built for high-data rate airborne satellite communications in the K_u-band and for broadband radio astronomy receivers in the L-band, respectively. A detailed description of the system integration of the on-chip beamformer with a radio astronomy antenna array, of the tuning procedure and the demonstration of its functionality is also given. A demonstration of the squint-free beamsteering capability of the proposed integrated beamformers is provided by analysing the radiation patterns of the array, measured in the 1.0-1.5 GHz band for the integrated system, and in the complete DVB-S band (10.7-12.75 GHz) for the airborne antenna system. This constitutes the first demonstration of this kind for beamformers based on optical ring resonators.

After that, the work has been extended towards a number of directions to further exploit the advantages offered by photonics. We describe a novel time delay technique known as separate carrier tuning (SCT) whose implementation on an integrated platform is demonstrated here for the first time. This technique allows to simplify the integration of a complete time and phase control unit in a single chip. The operating principle and the device schematic are described, followed by the demonstration of broadband and continuously tunable delay and broadband phase shifting of RF signals, simultaneously. The capabilities of the proposed delay line have also been demonstrated in an example system application using a 2-tap complex-coefficients microwave photonic filter (MPF).

On-chip optical beamformers offer a number of very attractive advantages, but are limited by their low degree of parallelism since they generally require a single delay line per antenna element. This becomes problematic for large antenna arrays with a high number of elements. A unique possibility offered by optical modulated systems is to employ wavelength division multiplexing (WDM). In particular, we propose an innovative technique that employs WDM on-chip to dramatically simplify the complexity of an optical integrated beamformer and, in turn, to enable the implementation of control units for large arrays on a single chip. A complete complexity analysis is presented, followed by a novel beamformer design which was realized and demonstrated in its basic functionalities.

Samenvatting

In de eerste helft van de twintigste eeuw heeft de wetenschappelijke en technische gemeenschap grote belangstelling aan de dag gelegd voor het vakgebied van de "phased array"-antennes. Deze technologie werd ontwikkeld gedurende de Tweede Wereldoorlog om door middel van radartechnieken vroegtijdig te kunnen waarschuwen voor dreigingen vanuit de lucht. Deze antennes zijn in de loop der jaren op verschillende gebieden ingezet, om in diverse behoeften te voorzien. Werden zij aanvankelijk uitsluitend gebruikt voor defensie- en ruimtevaartdoeleinden, tegenwoordig heeft de noodzaak voor breedbandige communicatie hun toepassing bevorderd op het gebied van slimme antennes voor moderne, draadloze communicatiesystemen.

Dit proefschrift behandelt een speciale manier om ten volle gebruik te kunnen maken van de grote flexibiliteit van die complexe maar toch zeer krachtige antennes, voornamelijk in termen van snelheid, compactheid en kosten. Een aantal vakgebieden heeft geprofiteerd van het extreem laag verlies en grote bandbreedte van de optische communicatietechnologie. Vooral interessant voor ons zijn de uitgebreide mogelijkheden die dit gebracht heeft voor de wereld van de microgolf- en antennetechniek door het gebruik van de optica en, in het bijzonder, van geïntegreerde fotonica. Dit gebied staat bekend als "geïntegreerde microgolf-fotonica". De enorme bandbreedte en het extreem lage verlies van optische golfgeleiders kunnen worden aangewend om zeer geavanceerde signaalverwerkingscircuits te implementeren voor hoogfrequente, elektrische signalen. In het bijzonder kunnen zeer breedbandige en continu instelbare tijdvertragingen optisch worden gerealiseerd, die van fundamenteel belang zijn om een aantal signaalverwerkingsfuncties te kunnen realiseren. Onze speciale belangstelling gaat uit naar het ontwerp, realisatie, test en integratie van complexe systemen voor nieuwe bundelvormers die zulke vertragingslijnen gebruiken, in combinatie met andere componenten, om de richting van de stralingsbundel van hoogwaardige antenne-arrays te kunnen sturen. In geval van realisatie door middel van geïntegreerd-optische technologie, spreken we over geïntegreerd-optische bundelvormers.

Een inleiding over de basisprincipes van "phased arrays" en hun fundamentele theorie wordt gegeven. Dit zal de basis vormen voor de motivatie voor wat volgt, en in het bijzonder het gebruik van breedbandige vertragingen om stuurcircuits voor antennes ofwel bundelvormers te realiseren. Er wordt een overzicht gepresenteerd van wat er tot nu toe is gedaan op het gebied van optisch-gestuurde antennes, samen met een inleiding op het basisconcept van het fascinerende nieuwe gebied van de geïntegreerde microgolffotonica. De basis voor vertragingselementen in het

onderhavige project bestaat uit optische ring-resonatoren. Eerst beschrijven we de kenmerken van deze zogenaamde "slow light"-componenten, daarna het ontwerp van het systeem en de prestatie-analyse van geïntegreerde bundelvormers die gebaseerd zijn op die bouwstenen. Vervolgens presenteren we de demonstratie van hun functionaliteit, hun integratie in een systeem-demonstratie en de test van het geheel. Die stappen werden uitgevoerd in samenwerking met twee belangrijke onderzoeksinstituten in Nederland, NLR en ASTRON, waar twee demonstraties zijn gebouwd, respectievelijk voor satellietcommunicatie met hoge datasnelheid in de Ku-band, en breedbandige radio-astronomie-ontvangers in de L-band. Daarnaast worden gedetailleerde beschrijvingen gegeven van de systeemintegratie van de bundelvormer, zoals die ontworpen is voor een radio-astronomie-antenne-array, van de inregelprocedures en de demonstratie van de functionaliteit. Een demonstratie van de "squint"-vrije bundel van de voorgestelde geïntegreerde bundelvormers wordt geleverd door het analyseren van de stralingspatronen van het array, gemeten in de 1.0-1.5 GHz-band van het geïntegreerd systeem, en in de volledige DVB-S-band (10.7-12.75 GHz) van het satelliet-antenne-systeem. Dit vormt de eerste demonstratie van dit soort bundelvormers gebaseerd op optische ringresonatoren.

Daarna is het project uitgebreid in een aantal richtingen, om de voordelen die de fotonica biedt verder te benutten. Wij beschrijven een nieuwe techniek die bekend staat als "separate carrier tuning" (SCT), waarvan de toepassing op een geintegreerd platform voor het eerst hier wordt aangetoond. Deze techniek maakt het mogelijk de combinatie van volledige tijd- en faseregeling in een enkele chip te vereenvoudigen. Het schema en werkingsprincipe ervan worden beschreven, gevolgd door de demonstratie van breedbandige, continu afstembare vertraging en gelijktijdige faseverschuiving van breedband RF-signalen. De mogelijkheden van de voorgestelde vertragingslijnen zijn ook aangetoond, met als voorbeeld een 2-taps microgolf fotonisch filter (MPF) met complexe coëfficiënten.

Optische bundelvormers op een chip bieden een aantal aantrekkelijke voordelen, maar zijn beperkt door hun geringe mate van parallellisme, omdat ze in het algemeen één vertragingslijn per antenne-element vereisen. Dit wordt problematisch voor grote antenne-arrays met veel elementen. Een unieke mogelijkheid ontstaat door gemoduleerde, optische systemen te gebruiken die gebaseerd zijn op golflengtemultiplexing. In het bijzonder hebben we een innovatieve techniek voorgesteld die gebruik maakt van golflengtemultiplexing op chip, om een drastische vereenvoudiging van de complexiteit van een geïntegreerd-optische bundelvormer te realiseren, en op zijn beurt, het mogelijk te maken dat regelcircuits voor grote arrays op een enkele chip kunnen worden geïmplementeerd. Een volledige complexiteits-analyse wordt gepresenteerd, gevolgd door een nieuw bundelvormer-ontwerp, dat werd gerealiseerd en gedemonstreerd voor wat betreft zijn basisfunctionaliteiten.

Contents

1

Introduction

In this chapter, an introduction to the research topic is given. The basic concepts of antenna arrays, the fundamentals and the motivation of photonic signal processing of RF signals are briefly described, before introducing the scope of the research project. The chapter closes with a description of the content of each chapter.

1.1   Wireless communications

A series of natural reasons brought men to invent novel methods to communicate when their distance would become very large, so that sounds or visual gestures would no longer be sufficient. With the first answers to this need, the era of telecommunication was born. In fact, in an etymological sense, the word telecommunication means "communicate from a distance" (from Greek *tele*, meaning "far off", "afar", "at or to a distance", and the Latin word *communicare*, meaning "to communicate", or "to make common").

In particular, the discovery of electricity allowed to use completely new methods to transfer data, at a speed very close to the one of light, revolutionizing the way information could be exchanged almost instantaneously all around the globe. At the end of the nineteenth century the "radio era" arrived, with the first discovery of "wire-less" communications by the Italian scientist and Nobel prize winner Guglielmo Marconi. After the first wireless transmission, radio communication evolved very quickly making possible to transmit information at the speed of light between different countries, different continents, and even to and from outer space. All components of the radio devices evolved rapidly, later under the push of improved performance given by the world wars. During the Second World War, a component of tremendous importance of modern systems was invented, the magnetron, which practically allowed to extend the usable spectral region employed for communications and radar towards much higher frequencies than before: the microwave spectrum [1]. This allowed to produce also smaller and more compact wired-to-wireless transducers, or antennas. The increase in frequency and the corresponding miniaturization of the devices have induced a large diffusion of radio systems, and wireless transmission of information is nowadays widely employed in the daily life of everyone. In addition to that, in recent years, the amount of data per unit time (or data rate) that wireless devices must be able to handle has dramatically increased, mainly due to the progress in integrated electronics and the corresponding fast-increasing data content of multimedia services, for example in internet, home entertainment or mobile telephony. The need for faster wireless connectivity, in turn, pushes the technological development by calling for faster and smaller digital signal processors, but also for radio systems with analog front-ends capable to handle those high-speed and rapidly-varying analog signals, such as broadband and reconfigurable transmitters, receivers and antennas. Broadband reconfigurable antennas, that is, antennas whose radiation properties can be modified electronically, will be the main interest of our work.

An antenna is a device that converts electromagnetic energy from a guide (guided energy, e.g. in a cable or a waveguide) into free-space (radiated energy) and vice versa. The size, shape and material of the antenna influence largely the direction, the frequency band of possible operation and how efficiently this conversion can be performed [2–4]. It is generally desirable to transmit radio waves with the maximum possible energetic efficiency to the receiver, and this is strongly linked to the capability of the antenna to concentrate power in a specified direction. This aspect, in turn, is connected to the physical dimensions of the antenna, its shape

and the arrangement of the radiating elements.

1.2 Antenna arrays

A new idea on a particular type of antenna was introduced in order to increase the efficiency of communications by another Nobel laureate, the German inventor Karl Ferdinand Braun, who for the first time demonstrated enhanced transmission of radio waves in specific directions. Using multiple antennas arranged in an *array* configuration allows to increase the transmission efficiency, thus allowing a higher signal to noise and interference ratio (SNIR) and, in turn, a higher data rate. Also, using arrays in receiving systems can improve the collection efficiency in presence of very weak sources, for example in the case of very large distance man-made radio sources, as in overseas communications, or weak reflected signals by objects illuminated by a radar, or even electromagnetic sources originating from outer space, as in the case of radio astronomy. It is with this type of applications that antenna arrays started to be employed and developed.

A simple example can be used to explain how an array of elementary antenna elements can be employed to control the direction of transmission or reception of radio waves.
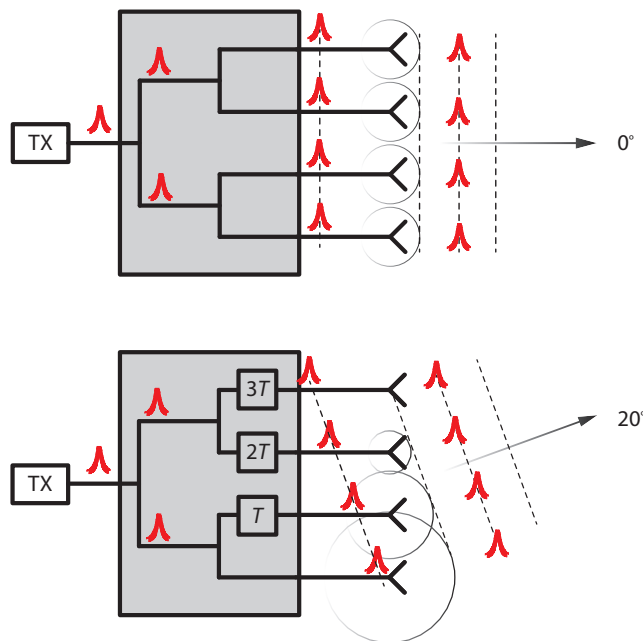
Figure 1.1: Operating principle of a phased array antenna

Let us consider an array of four elementary antenna elements placed vertically

and equally spaced, as in Fig. 1.1(a). A transmitter TX generates a pulse which we want to transmit in horizontal direction. It is possible to create a simple network which divides the pulse and connects the transmitter to the antennas. If the line characteristics and their lengths are all the same, the pulse will be divided in four parts which will arrive at the same time at the antenna elements, and thus will be transmitted in the horizontal direction.

Now, let us suppose that we want to transmit the pulse to a different direction, for example 20 degrees upwards, but without physically moving the antennas. That can be done by using the same splitting network, but where we have introduced certain *time delays* in the feed network, linearly increasing from top to bottom, multiples of a basic time delay T, see Fig. 1.1(b). The larger the value of T, the higher the beam tilt compared to the horizontal direction. This principle can be applied in exactly the same way in the receiving direction, by simply inverting the sense of propagation of the pulse through free space and through the antenna feeding system.

The amount of delay relates to the tilt angle ϑ_0 according to the relation

$$T = \frac{L}{c_0} = \frac{d\sin(\vartheta_0)}{c_0} \tag{1.1}$$

as shown in Fig. 1.2, where d is the inter-element distance and c_0 is the speed of light in free-space.
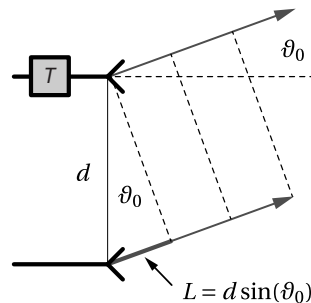
Figure 1.2: Relation between tilt angle and delay between two adjacents elements

1.2.1   Beam forming networks

The performance of the phased array depends strongly upon the characteristics of the network that connects the individual elements with the transmitter or receiver; that is known as beam-forming network (BFN) or, simply, beamformer. As seen in the simple example shown before, the task of this network is mainly to provide the correct delays in such a way that the transmitted (or received) signal would be sent in the desired direction.

In Fig. 1.1 we have chosen on purpose to show the propagation of a pulse, as this is the common scenario in modern communication systems, where broadband signals are often codified in the form of temporal sequences of very short, thus broadband, pulses. In order to preserve the characteristic of the information signal, it is important that the antenna system is capable of handling those pulses without disrupting their shape, in terms of temporal and spectral profiles. This requires, in turn, a broadband performance for all the components involved: for example, the antenna and the amplifiers must be capable of transmitting all the frequency components with the same gain and, most importantly, the delay lines shall be able to provide the same delay to all the components that constitute the pulse, that is, should introduce negligible dispersion.

If this is not the case, an undesired phenomenon known as *beam squint* occurs, consisting of the fact that the pointing direction is not constant but changes with frequency, as will be accurately analyzed in Chapter 2. In case of transmission of broadband pulses, this is particularly disruptive as it creates a sort of spatial filtering effect, where different frequency components of the pulse would be transmitted in different angular directions, and receivers located at different angular positions would receive only a limited spectral portion of the initially transmitted pulse.

For narrowband applications, on the contrary, very often phase shifters are used instead of delay lines, as they are generally simpler to implement. A large amount of literature is available describing the implementation of microwave phase shifters for antenna control [5, 6].

However, for modern applications where large instantaneous bandwidths are required, broadband delay lines must be used, often referred to as true-time-delay (TTD) lines. Their fundamental characteristic consists of the fact that they provide a constant amount of delay over the whole frequency band of interest [2]. In order to allow beamsteering the delay lines they must be tunable, and shall provide relatively large delay, especially in the case of large antenna arrays, and shall be able to operate at high frequencies.

It is generally difficult to realize electronic beamformers with broad instantaneous bandwidth, continuous amplitude and delay tunability and, at the same time, capable of feeding large arrays. To date, purely electronic solutions for TTD cannot meet the requirements [2].

True time delay lines employing traditional microwave components may imply bulky, complex and heavy beamformers, see as example the metallic waveguide BFN used for multibeam multi-feed satellite communications [4]. Monolithic integration has improved the compactness of variable time delays sensibly, via the use of reconfigurable microwave monolithic integrated circuits (MMIC); nonetheless, those solution do not easily offer broadband and continuous tunability, or are usually limited to mid- to low-power applications and frequencies below few tens of GHz [7]. For high-power applications in the mm-wave range, bulky and energy-hungry vacuum tube solutions are still the only possibility in practical applications [2]. Recent advances in microelectronics and analog circuit design and technology have shown an unprecedented performance for phased array systems operating well into the mm-wave range (30-40 GHz) [8] with ultra-wideband (UWB)

performance (3-15 GHz), equivalent to a percentage instantaneous bandwidths as large as 200 % [8], and able to generate up to several tens of independent beams. Those solutions are very compact (from few to few tens of square millimeters of dye area), and very attractive for a number of systems in the imaging, radar and high-data rate communication applications, offering high sensitivity in passive imaging systems (radiometers), and high resolutions in active imaging systems [8]. However, even those state-of-the-art systems cannot offer continuous tunability (or are completely not tunable, and thus defined *staring arrays*) and broadband delays beyond approximately one hundred picoseconds. The need to achieve large aperture antenna arrays with tunable beam direction and large instantaneous bandwidths is present and asks for different types of solutions. Quoting a world-renowned expert in the field, M.J. Mailloux [2],

> *Conventional phased arrays operate over bandwidths that are inversely proportional to the array size. The use of true time delays instead of phase shifts would eliminate the bandwidth restriction due to beam squint, but unfortunately the only viable time-delay technology at the time of this writing consists of switched sections of transmission lines. For example, a large array of 50 wavelengths on a side and scanning to 60° would need a total time delay from zero to 50 sin(60°), or 43 λ. To obtain precision equivalent to an N-bit phase shifter, about N + 6 bits is necessary. If these units are made with discrete time-delay bits, as is the common practice for phase shifters, the units become too bulky and heavy, and so lossy as to be impractical for most applications, except perhaps for stationary ground-based arrays at relatively low frequencies.*

Over the years alternative technologies have been proposed to overcome those limitations. With introduction of fast analog-to-digital converters (ADC), it is possible to employ digital processors instead of physical delay lines. This brought the advantage of complete and fast reconfigurability, an unprecedented flexibility in the excitation coefficients, which are generated by a digital processor and not by physical delay lines, that reflects into an unprecedented beam shape control. Nonetheless, real-time adaptive digital processors with wide bandwidth for third-generation mobile networks may become extremely complex, and consume much electrical power, large part of which is dissipated as heat in the digital processing unit, to become critical for spaceborne applications [9]. In fact, due to the high performance required, a high degree of parallelism is introduced which makes digital real-time beamformers very bulky and costly. Also, those processors cannot generally handle data beyond a few gigahertz of bandwidth due to the speed limitations of analog-to-digital converters. If those limitations can be acceptable for ground based applications, the weight, bulk and energy requirements of digital beamforming limit their application to mobile or satellite platforms [10] and experts have been starting to look at different directions [11].

1.3 Microwave Photonics

Since the eighties, engineers started to investigate the possibility to use optics generate delays for microwave antenna beamforming [12, 13], giving birth to a novel field known as *microwave photonics.*

The interest in using photonic techniques for feeding large antennas arises from the main feature of photonics, that is, the ultra-low attenuation of optical fibers combined with their ultra-wideband performance. This comes in addition to their very low cost, bulk and weight and "natural" EMI immunity when compared to microwave transmission lines.

The basic schematic of an optical beamformer is very similar to the one of a traditional BFN, where the electrical processor is replaced by an optical processor, and where electrical-to-optical (E/O) and optical-to-electrical (O/E) converters are employed, as shown in Fig. 1.3.
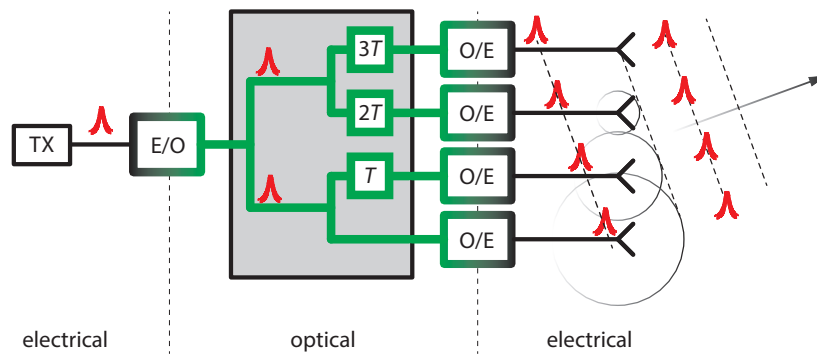
Figure 1.3: Operating principle of a phased array antenna based on an optical beamformer

A number of optical beam forming (OBF) architectures have been proposed over the years to address several desired characteristics, as:

- ultra-wide instantaneous band (tens of GHz)

- high operating RF frequency (microwave and millimeter-wave bands)

- true-time-delay performance

- EMI-free operation

- agile and fast reconfigurability for beam control

- multibeam capability

In particular, integrated on-chip solutions started to be proposed as well in order to address the following features:

- low size, weight, volume (low bulk) compared to traditional microwave solutions

- low power consumption (200 mW per thermal tuning unit, reduced by a factor 80k when employing electro-optical tuning[1])

- low cost (for high yield photonic integration)

Initially, the development was carried on within – and limited to – the military research framework, for very high performance systems (e.g. wideband radar applications, antenna remoting and control using optical fibers in very large radar antennas) [13], in fact, in a context where cost would not be a limiting factor. Later on, the diffusion and cost reduction of photonic components due, in turn, to the large diffusion of optical communication networks, slowly allows the OBF techniques to spread towards a number of other fields such as spaceborne applications and radio astronomy. All that, together with the current trend towards a higher and higher data rate requested by personal wireless applications, is opening the path towards the potential diffusion of complex and high-performance OBF systems also in the field of personal communications [14].

1.3.1   Integrated microwave photonics

Photonics solutions proposed over the years have shown the desired high performance in terms of speed, bandwidth and reconfigurability. However, they are often regarded with certain skepticism from the antenna and microwave engineering communities due to the generally high bulk, low system performance, high power consumption and costs [5]. This is due to the fact that they were generally based on bulk optics and discrete standard optoelectronic devices.

The current challenge is providing the high performance typical of photonic solutions, while retaining the advantages offered by microelectronics (very low space occupation, consumption, and unit cost). In this context several authors [12,15–17] see in integrated microwave photonics (IMWP) an answer to this need, as an enabling technology for the exploitation of the advantages of microwave photonics and its large-scale deployment in commercial applications. In fact, to the well known advantages of photonics, integrated solutions add also compactness and light weight, thus extending the application possibilities of optically-fed smart antennas to domains where size and weight are critical (e.g. aerospace) and reduces the cost thanks to the high yield and reproducibility of the CMOS compatible fabrication equipment.

The current trend is to harness the enormous progress in integrated optics to provide flexible, reconfigurable and general-purpose microwave photonic processors [2, 3], that can assist or even replace current analog microwave filters and front-ends, enabling better performance or completely novel functionalities.

---

[1]For electro-optical tuning we intend that filter characteristics (e.g. group delay) can be induced by refractive index change produced by means of electro-optic effect, as opposed to thermo-optical tuning where changes are produced by means of thermo-optic effect.

1.4 Research objective

The goal of the research presented in this thesis was to investigate the design, system integration and test of novel architectures for optical beam forming networks for antenna arrays, that are completely programmable, providing wideband and continously tunable delays, and integrated on single photonic chips that can be realized in a standard CMOS foundry. The actual research activities have been carried out in the framework of a large Dutch national project, with the aim of realizing two demonstrators as described below (Sec. 1.5).

Our work fits in a context where satellite communications (SATCOM) systems have been aiming towards higher and higher operating frequencies in order to provide wider bandwidths for the ever-increasing need of data rate. Most of the currently deployed systems operate at Ku-band and are moving towards even higher frequencies (e.g. Ka-band). Phased array antennas are very useful in SATCOM applications, thanks to the capability to produce highly-directive beams which can be shaped and scanned electronically [2, 4]. This field is a particularly interesting application for optical beamforming since, besides operating at high frequencies for the reasons seen above, it requires large arrays to achieve sufficient G/T to compensate for the low power signals, and requires seamless beamsteering due to the continuously varying relative position between mobile receivers and the satellite. In addition to that multibeaming and fast beam switching are desired characteristics that have been effectively demonstrated using photonic solutions (see Chapter 3).

Another important application is modern radio-astronomy, where the current trend in building new instrument (e.g. SKA, [18]) is strongly directed towards the widespread use of phased arrays, both in the form of aperture arrays (Fig. 1.4) or as phased array feeds (PAF) in conjunction with large reflectors. A dedicated workshop on the use of phased arrays for radio astronomy has been established in recent years for sharing knowledge among the experts in the field [19]. In this field, due to the extremely low power received in the science cases of interest, the collection efficiency (and in turn the area) of the antennas and their robustness to interference should be very high [19]. For this reason, photonic solutions are regarded with high interest, and optical systems are commonly deployed for signal clock and local oscillator distribution [20], for antenna remoting through analog optical links [21, 22] and more recently also for beamforming.

In particular, our aim has been to demonstrate the use of integrated photonics as an enabling technology to provide unprecendented performance to the targeted antenna system. The integrated microwave photonics approach enables an ambitious set of joint specifications, as detailed in the next section, that cannot be achieved by different technological approach.

1.5 The MEMPHIS project

This ambitious scope described above required the development of a novel approach, that is, the integration of electronics and photonics in integrated systems.
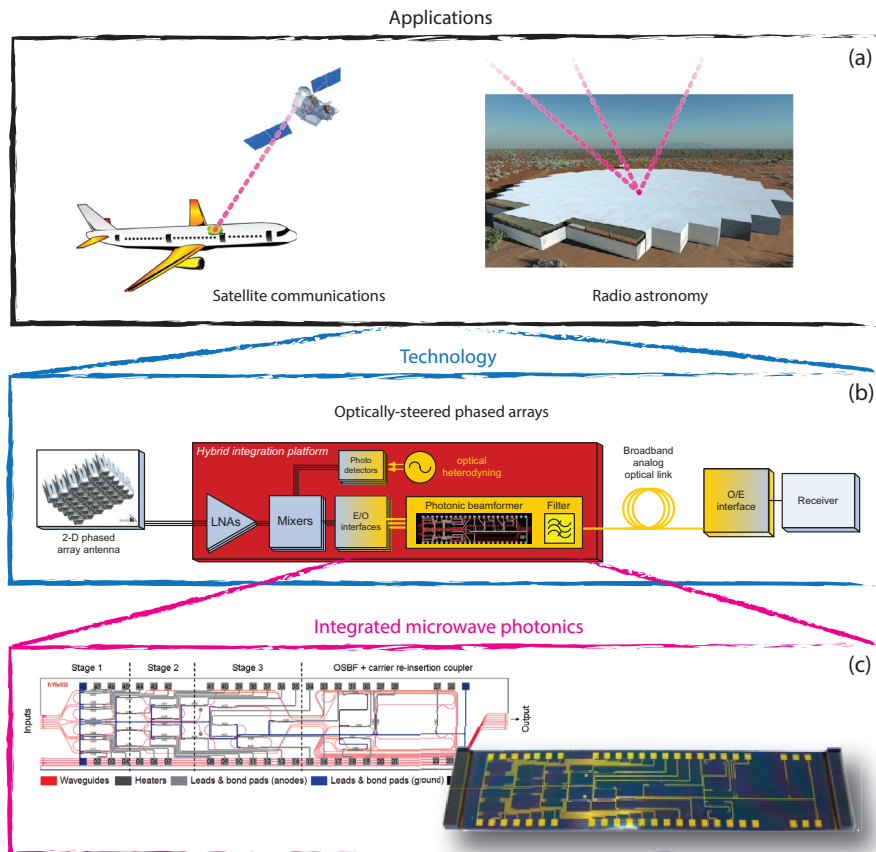
Figure 1.4: Applications of the microwave photonics technology developed in the thesis (a) (picture from http://www.skatelescope.org/). Schematic of an optically-controlled antenna array, including optical local oscillator generation and antenna remoting via analog photonic link (b). Schematic and image of an integrated optical beamforming network chip (c).

This has been the main focus of the MEMPHIS project –in the framework of which this thesis has been carried out – supported by the Smart Mix Programme of the Netherlands Ministry of Economic Affairs and the Netherlands Ministry of Education, Culture and Science.

The work aimed at the realization of two demonstrators, whose aim is to prove the broadband characteristic of photonic integrated beamformers for application to radio astronomy and satellite communications, respectively. Both demonstrators employ an on-chip beamformer capable of providing broadband delays for the two target applications. Below we will show a functional schematic and an impression of the desired system integration scheme.

The technology required for those applications originates from a close collaboration of the Microwave Photonics team at the University of Twente with several academic and industrial partners from the Netherlands (LioniX BV, NLR, TNO, Astron, Cyner, TU/e and TU-Delft).

1.5.1 Demonstrator 1

The main focus of this demonstrator is the development of an aperture antenna for radio astronomy, using a photonic technology in order to implement a beamformer capable of operation over a large instantaneous bandwidth ($\approx$8 GHz), and/or multiple simultaneous beam capability. The distinctive feature of the beamformer employed in this demonstrator is the use of multiple optical carriers at different frequencies, in order to demonstrate a novel hardware-compressive architecture based on the reuse of the same delay units. The corresponding concept is described in detail in Chapter 7.

System architecture

The optical beamforming system consists of two main parts: an indium phosphide (InP) transmitter chip (MWL-TX), realized at TU/e (Eindhoven University of Technology), including four multi-wavelength lasers with 4 high-speed modulators, and a multiplexer based on an arrayed-waveguide grating. The four wavelengths are modulated by four electrical signals originating from different antenna elements. The modulators are fed by suitable modulator drivers. The modulated signals are multiplexed on the InP chip, and then fed to the optical beamformer, which is realized on a separate silicon nitride/silicon oxide (Si_3N_4/SiO_2) chip employing TriPleX™technology [23, 24]. This chip is designed at UT-TE (University of Twente) and realized by LioniX B.V. The two chips are designed in order to allow their connection by butt-coupling. The multiplexed signals enter the optical beam forming network (OBFN) chip and then are demultiplexed and delayed in a wavelength-selective manner and recombined in a binary-tree pattern. The delayed and combined signals are then routed to a photodetector.

System specifications

Table 1.1 summarizes the system specifications for Demonstrator 1.

Table 1.1: Key parameters of the OBFN system for radio astronomy applications (Demonstrator 1)

Parameters	Value	Unit
Antenna configuration	Planar, separable illum.	
Frequency range	2 – 10	GHz
Frequency range (minimum)	3 – 5	GHz
Instantaneous bandwidth	8	GHz
Instantaneous bandwidth (minimum)	2	GHz
Nr. elements in one tile	64 (8×8)	–
Inter-element spacing (x direction)	37.5	mm
Inter-element spacing (y direction)	37.5	mm
Antenna element gain	0	dBi
Antenna element gain flatness in band	5	dB
Antenna element cross pol. level	< 6	dB
Impedance (differential)	100	Ω
Gain antenna tile (8×8)	> 15 – 17	dBi
Beamwidth antenna tile (8×8)	≈10	degrees
Beamwidth total array	≈2	degrees
Antenna polarization	dual linear (switched)	–
RF front-end gain	70	dB
Cross-polarization isolation (XPI)	<-15	dB
Scan angle (elevation)	±30	degrees
Scan angle (azimuth)	±30	degrees

System integration

Fig. 1.5 shows an impression of the envisioned electronic-photonic system integration of the optical beamformer with the other subsystems. A silicon common base will be used to mount both the MWL-TX and the OBFN. The optical chips are mounted directly on a metal base used both as a mechanical support for the complete integrated system, and as a temperature-stabilized heat sink. The optical connections are realized by means of butt-coupling between the MWL-TX and the OBFN, and by means of fiber pigtailing between the chip and the output fiber to the photodetector. A printed-circuit-board (PCB) is employed to host the electrical drivers for the lasers and modulators array on the MWL-TX chip, and for the electrical connections for OBFN tuning. The connections between PCB and optical chips are realized via wire bonding.
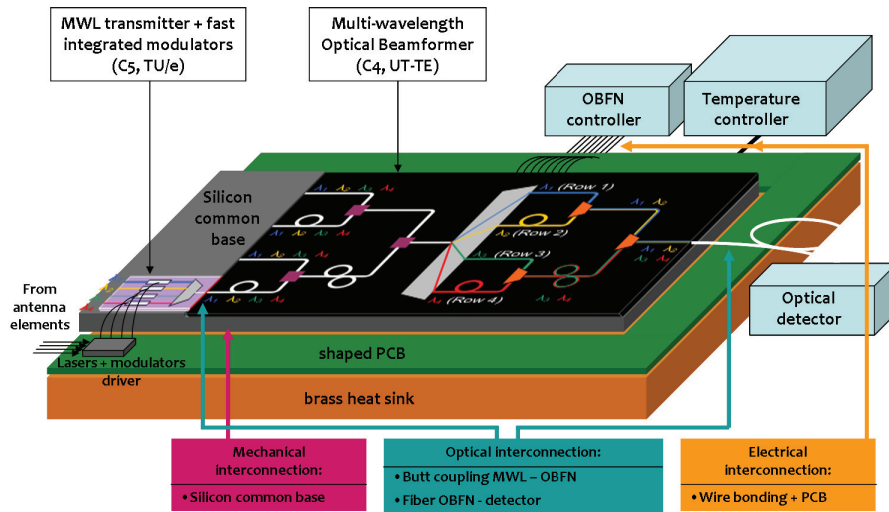
Figure 1.5: Schematic of Demonstrator 1 (broadband phased array for radio astronomy)

1.5.2   Demonstrator 2

The main focus of this demonstrator is the development of a special satellite antenna, which uses a "photonics core" that will provide a breakthrough in broadband connectivity, allowing live TV and fast internet connection on board of commercial airplanes. This system shall be able to track satellites without any mechanical movement, keeping a low profile, thus a much lower air drag and fuel consumption, thus providing higher performance and a "greener" solution compared to other systems for airborne satellite communications.

System architecture

The system architecture of Demonstrator 2 is similar to the one of Demonstrator 1, with the main difference that this time the laser is off-chip, and three different chips are interconnected. First, an integrated 1×16 splitter is realized with a binary tree architecture in TriPleX™technology designed and realized by LioniX B.V. The waveguide spacing at the output facets match the one of a modulator array realized by Oclaro and featuring 16 Mach-Zehnder modulators in indium phosphide. The modulators outputs are connected to the optical beamformer designed in UT-TE and realized by LioniX B.V., featuring 16 inputs, 40 optical ring resonators, an optical sideband filter integrated on the same chip. All the components are fully-tunable employing thermo-optical mechanism. The output is routed to a detector that could be directly integrated on the same system.

System specifications

Demonstrator 2 will be based on the requirements for an aircraft antenna for satellite communication. The configuration will be a receive-only antenna operating in Ku-band. For demonstration purposes, the antenna to be realized will correspond to a subsection of the actual airborne antenna required for satellite signal reception, therefore showing a lower gain and a larger beamwidth. The demonstrator will show some of the required capabilities of an airborne SATCOM antenna as summarized in Table 4.1 indicating the system parameters.

System integration

Fig. 1.6 shows an impression of the system integration of the optical beamformer with the other subsystems. Similarly to what envisioned for Demonstrator 1, also in this case the different chips are mounted on a silicon common based mechanically supported by a brass heat sink. A shaped PCB is used here to host the modulator drivers and the electrical connections, brought on the photonic chips via wire bonding. The optical connections are realized via butt coupling between splitter, modulator array, OBFN and detector, while the laser input is connected to the integrated splitter via a fiber pigtail.

Table 1.2: Key parameters of the OBFN system for DVB-S applications (Demonstrator 2)

Parameters	Value	Unit
Antenna configuration	Planar, separable illum.	
Frequency range	10.7 - 12.75	GHz
Bandwidth	2.05	GHz
Nr. elements in one tile	64 (8×8)	–
Inter-element spacing (x direction)	11.8	mm
Inter-element spacing (y direction)	11.8	mm
Gain antenna tile (8×8)	> 22	dBi
Gain total array (25 tiles)	≈37	dBi
Beamwidth antenna tile (8×8)	≈10	degrees
Beamwidth total array	≈2	degrees
Antenna polarization	dual linear (switched)	–
RF front-end gain	70	dB
Cross-polarization isolation (XPI)	<-15	dB
Minimum CNR (25+ tiles, 33 MHz BW)	8	dB
Scan angle (elevation)	±45	degrees
Scan angle (azimuth)	±45	degrees
LO emission	according to EN 320 186	
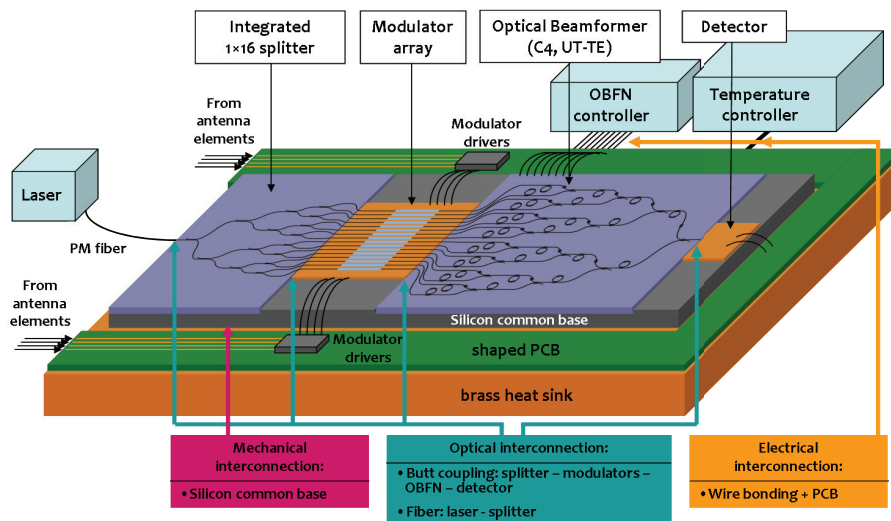
Figure 1.6: Schematic of Demonstrator 2 (broadband satellite communications)

1.6   Thesis outline

After this introduction, the thesis starts with a review of the basic concept on antenna arrays given in Chapter 2. The concept of microwave photonics as an extension to microwave signal processing capabilities offered by the photonic approach is then described in Chapter 3. A complete system analysis of the photonic beamformer system is described in Chapter 4, followed by the design of a photonic integrated beamformer for a specific case study. Chapter 5 reports on the characterization, system integration and test of the optical beamforming network (OBFN). Chapter 6 describes the novel on-chip demonstration of a phase and delay tuning technique known as separate carrier tuning, which enables a significant simplification of the network structure. Chapter 7 describes the application of a wavelength-division multiplexing approach and its benefits in the implementation of a novel type of photonic beamformer. The thesis ends with conclusions and recommendations in Chapter 8.

2

Antennas, Phased Arrays and Beam Forming Theory

In this chapter, the theory of antenna arrays will be described. Starting from the fundamental characteristics of antennas, the concept of array of antennas will be introduced and its advantages evaluated. The concept of array factor will be introduced and its expression will be given for a number of common array architectures. The relation between array factor and antenna feeding network will be explained. The principle of pattern multiplication will be introduced. The condition for absence of grating lobes will be derived analytically and discussed. The bandwidth of an array and the problem of frequency squint will be analyzed in detail. The chapter concludes with a discussion of the requirements for wideband beamsteering, showing the limitations of the narrowband phase-shifter approach and introducing the photonic true-time-delay solution for broadband antenna array beamforming.

2.1   Antennas

An antenna can be defined as *the structure associated with the region of transition between a guided wave and a free-space wave, or vice versa* ([3]), or *a transducer that converts a guided wave propagating on a transmission line into an electromagnetic wave propagating in an unbounded medium* (as in [25]). In analogy with microwave engineering, an antenna can be seen as an "impedance transformer", between the characteristic impedance of a transmission line, and the intrinsic impedance of free space, 377 Ω. Again, citing the elegant definition of Kraus ([3]), "the antenna, like the eye, is a transformation device converting electromagnetic photons into circuit currents; but, unlike the eye, the antenna can also convert energy from a circuit into photons radiated into space." In brief, *the antenna converts photons to currents and vice versa.*

Antennas are realized in different shapes, materials, and sizes: the antenna size becomes particularly meaningful when compared to the operating wavelength, as will be further detailed in the following. Those characteristics are decided in the design phase, based on the requirements and constraints given by the desired application. Their choice will determine, in turn, the radiation characteristics and the electrical characteristics of the antenna.

2.2   Antenna parameters

As from the definitions given above, the antenna can be characterized differently when looked at from the transmission line or from the space surrounding it. From the transmission line perspective, the antenna behaves like a 2-terminal component (or a 1-port microwave circuit) which can be associated to a complex *impedance*, with a resistive and a reactive component which are *scalar* quantities. From the free-space perspective, instead, the antenna can be usefully characterized by *vector* field components functionals called *radiation patterns* (*field patterns* or *power patterns*). The term *radiation* refers to the *energy* conveyed by the electric and magnetic *fields* constituting an electromagnetic wave propagating in free-space. The definitions of those quantities will be employed in this thesis and are given below.

2.2.1   Radiation pattern

Let us consider a 3-dimensional spherical coordinate system (r, ϑ, φ) as described in Appendix A). The **radiation pattern** is a function of the spatial coordinates (ϑ, φ) describing the intensity and polarization of the fields generated by the antenna (*field pattern*), or how the power is radiated by the antenna in a specified direction (*power pattern*).

2.2.2 Field pattern

Let us still consider the same spherical coordinate system (r, ϑ, φ). The field pattern is a 2-variable function $f(\vartheta, \varphi)$ whose value is proportional to the field intensity (E or H) at a certain distance r from the antenna in the direction (ϑ, φ).

The actual *value* of this function, that is, the actual intensity of the field, depends upon the distance r. Still, at distances which are large compared to the antenna size and the wavelength (see later in this chapter the definition of field regions, Sec. 2.2.3), the *shape* of the field pattern is independent of distance. For this reason, it is interesting to define a function whose value is independent of distance. This is the *normalized field pattern*, which is defined as

$$f(\vartheta, \varphi)_{\mathrm{n}} \triangleq \frac{f(\vartheta, \varphi)}{f(\vartheta, \varphi)_{\max}} \quad \text{[dimensionless]} \tag{2.1}$$

and where $f(\vartheta, \varphi)_{\max}$ is the maximum field pattern. The normalized field pattern is a dimensionless function with maximum value of unity.

In defining the field patterns, so far we have only discussed about field intensity. In practice, let us consider for example the electric field E. To completely specify the radiation pattern with respect to field intensity and polarization requires six patterns, which are:

1. The r component of the electric field, $E_r(r, \vartheta, \varphi)$, measured in $[\mathrm{V\,m^{-1}}]$

2. The ϑ component of the electric field, $E_\vartheta(r, \vartheta, \varphi)$, measured in $[\mathrm{V\,m^{-1}}]$

3. The φ component of the electric field, $E_\varphi(r, \vartheta, \varphi)$, measured in $[\mathrm{V\,m^{-1}}]$

4. The phases of these fields components, $\delta_r(r, \vartheta, \varphi)$, $\delta_\vartheta(r, \vartheta, \varphi)$ and $\delta_\varphi(r, \vartheta, \varphi)$, measured in [deg] or [rad].

Those can be grouped in a *vector field pattern*

$$\mathbf{E}(r, \vartheta, \varphi) = \mathbf{a}_r E_r(r, \vartheta, \varphi) e^{j\delta_r(r, \vartheta, \varphi)} + \mathbf{a}_\vartheta E_\vartheta(r, \vartheta, \varphi) e^{j\delta_\vartheta(r, \vartheta, \varphi)} + \mathbf{a}_\varphi E_\varphi(r, \vartheta, \varphi) e^{j\delta_\varphi(r, \vartheta, \varphi)}.$$
$$\tag{2.2}$$

where $\mathbf{a}_r$, $\mathbf{a}_\vartheta$ and $\mathbf{a}_\varphi$ are the unit vectors in direction r, ϑ and φ, respectively.

For many applications, having information about polarization and field intensities in all directions is not necessary, and it is sufficient to have information about the spatial distribution of radiated power. Instead of considering the intensities of the field components, the antenna patterns can also be expressed in terms of radiated power. Thus we talk about *power patterns*. Before doing that, we classify the field regions, based on the characteristics of the dominating field components, and we introduce the Poynting vector, which will be used in the definition of the power patters.

2.2.3 Field Regions

It is common to subdivide the space surrounding an antenna into three regions, based on the characteristics of the dominating field in each.

a) *reactive near-field region*: space in the immediate surroundings of the antenna, where the reactive field component dominates.

b) *radiative near-field region* (or *Fresnel region*): space comprised between the reactive near-field and the far-field, where the radiative fields are already dominant, but the field patterns still depend on the distance from the antenna.

c) *far-field region* (or *Fraunhofer region*): distances at which the functions describing the field patterns are *independent* of the distance from the antenna.

In [26] a thorough discussion of field regions is given. Despite the boundaries among those regions are not abrupt and are not uniquely defined[1], for the scope of our work, it is important to note that at distances which are sufficiently large compared to the dimensions of the antenna and to the wavelength, the shape of the field patterns as well as of the normalized power pattern are independent of distance. The region of space where this is true is known as *far-field* of the antenna, or Fraunhofer region. In this thesis, as in most applications, we are interested in the patterns obtained in this far-field condition.

2.2.4   Poynting vector

Let us consider the flow of power carried by an electromagnetic wave [25]. Let **E** be the electric field (in V/m) and **H** the magnetic field (in A/m) of the wave. The Poynting vector S is defined as

$$\mathbf{S} = \mathbf{E} \times \mathbf{H} \quad [\mathrm{W\,m^{-2}}] \tag{2.3}$$

The direction of **S** is the direction of propagation of the wave. The Poynting vector represents the power per unit area carried by the wave. In fact, if we consider an aperture of area A, with an outward surface unit vector $\mathbf{a}_r$, the total power that flows through the aperture is

$$P_{\mathrm{rad}} = \int_A \mathbf{S} \cdot \mathbf{a}_r \, \mathrm{d}A \quad [\mathrm{W}] \tag{2.4}$$

S is a function of time. It is of practical interest to calculate its time-average value. Assuming sinusoidal fields and using Euler's formula we can write the average power density of the wave [25] which is

$$\mathbf{S}_{\mathrm{av}} = \frac{1}{2} \mathrm{Re}\left[\mathbf{E} \times \mathbf{H}^*\right] \quad [\mathrm{W\,m^{-2}}] \tag{2.5}$$

In the far-field of the antenna, the electromagnetic field generated by the antenna can be locally approximated as a plane wave, propagating outwards in direction $\mathbf{a}_r$,

---

[1]Commonly the Fresnel region is considered to start at a distance $R_1 = 0.62\sqrt{D^3\lambda}$ and the Fraunhofer region at a distance $R_2 = 2D^2/\lambda$, where λ is the wavelength and D is the maximum dimension of the antenna [26]. D is also assumed to be large compared to the wavelength, $D > \lambda$. Note that those values are not valid for all types of antennas, refer to [26] for a complete discussion.

with ϑ and φ components $E_\vartheta(r,\vartheta,\varphi)$ and $E_\varphi(r,\vartheta,\varphi)$ respectively. In this assumption, the average power density becomes [25]

$$\mathbf{S}_{\text{av}}(\vartheta,\varphi) = \mathbf{a}_r \frac{|E_\vartheta(r,\vartheta,\varphi)|^2 + |E_\varphi(r,\vartheta,\varphi)|^2}{Z_0} \quad [\text{W m}^{-2}] \tag{2.6}$$

where Z_0 is the intrinsic impedance of free-space.

2.2.5 Normalized power pattern

Normalizing the magnitude of the average power density vector $S_{\text{av}} = |\mathbf{S}_{\text{av}}|$ with respect to its maximum, gives the *normalized power pattern*

$$P_{\text{n}}(\vartheta,\varphi) = \frac{S(\vartheta,\varphi)}{S(\vartheta,\varphi)_{\text{max}}} \quad [\text{dimensionless}] \tag{2.7}$$

The power pattern is a useful quantity to formally describe how the antenna radiates power in space. As it is, this quantity depends on the distance from the antenna. As for the field patterns, it is again desirable to give a definition that is independent of distance. For this reason we can use, in the definition, the power radiated per *unit of solid angle* instead of per *unit area*.

The power radiated per unit of solid angle can be derived from the flux of the Poynting vector. Let us consider the direction $\mathbf{a_r}$, in Cartesian coordinates

$$\mathbf{a_r} = \mathbf{a}_x \sin\vartheta\cos\varphi + \mathbf{a}_y \sin\vartheta\sin\varphi + \mathbf{a}_z \cos\vartheta \tag{2.8}$$

where $\mathbf{a}_x$, $\mathbf{a}_y$ and $\mathbf{a}_z$ are the unit vectors of the x, y and z axes, respectively.

The *radiated power per unit area* in direction $\mathbf{a_r}$ is derived by the expression of the flux of the Poynting vector (2.4), as follows

$$\frac{dP_{\text{rad}}}{dA}(\mathbf{a_r}) = \frac{1}{2}\text{Re}\left[\mathbf{E} \times \mathbf{H}^* \cdot \mathbf{a_r}\right] \tag{2.9}$$

and by considering

$$\frac{dA}{d\Omega} = \frac{r^2\sin\vartheta d\vartheta d\varphi}{\sin\vartheta d\vartheta d\varphi} = r^2 \tag{2.10}$$

we obtain the *radiated power per unit solid angle* in direction (ϑ,φ)

$$\frac{dP_{\text{rad}}}{d\Omega}(\vartheta,\varphi) = \frac{1}{2}r^2\text{Re}\left[\mathbf{E} \times \mathbf{H}^* \cdot \mathbf{a_r}\right]. \tag{2.11}$$

Since E and H have a $1/r$ dependence on distance, the radiated power per unit solid angle is independent of distance.

Similarly to the procedure that led to Eq. (2.7), we can also obtain the normalized power pattern by considering the *power radiated per unit of solid angle $U(\vartheta,\varphi)$* (in W ster^{-1}) in direction (ϑ,φ), known as *radiation intensity*. This quantity, in the far-field condition, is independent of the distance from the antenna. By normalizing to its maximum value we obtain a definition of the normalized power pattern equivalent to Eq. (2.7):

$$P_n(\vartheta,\varphi) = \frac{U(\vartheta,\varphi)}{U_{\max}} = \frac{\frac{dP_{\mathrm{rad}}}{d\Omega}(\vartheta,\varphi)}{\max_\Omega \frac{dP_{\mathrm{rad}}}{d\Omega}} \quad \text{[dimensionless]} \tag{2.12}$$

2.2.6   Lobes

The patterns usually consist of a *main lobe* of radiation, and *minor lobes* (or *side-lobes*), as visible in Fig. 2.1. The shape, levels and direction of those lobes can vary largely and depends on the type of antenna that is considered.

The described field or power patterns are commonly represented either in 3-dimensional spherical coordinates (r,ϑ,φ) as in Fig. 2.1(a), or by plane cuts through the main lobe axis, Fig. 2.1(b). To show the minor lobes in more details, the same patterns are commonly represented in cartesian coordinates instead of spherical coordinates, and with their value in decibel scale, through the simple transformation

$$P_n(\vartheta,\varphi)_{\mathrm{dB}} = 10\log_{10}[P_n(\vartheta,\varphi)] \quad \text{[dimensionless]}. \tag{2.13}$$

2.2.7   Directivity, efficiency and gain

It is often useful, for practical applications of antennas, to compare the performance of the antenna under study to the one of a reference antenna. This reference antenna is the so-called *isotropic radiator*, that is, an ideal antenna capable of radiating the same amount of power density in all directions. It follows that the power density from the isotropic radiatior is constant over a sphere centered at the antenna. Although this type of antenna is impossible to realize, and of little practical interest, it constitutes a useful reference to compare the radiation characteristics of real antennas with each other. With respect to the isotropic radiator, we can define directivity and gain of an antenna as follows.

The **directivity** D of an antenna is defined as the ratio between the power density radiated in direction (ϑ,φ) and the power density radiated by the isotropic radiator, radiating the same amount of total power P_{rad}.

$$D(\vartheta,\varphi) = \frac{\frac{dP_{\mathrm{rad}}}{d\Omega}(\vartheta,\varphi)}{\frac{P_{\mathrm{rad}}}{4\pi}} \quad \text{[dimensionless]}. \tag{2.14}$$

Note that, by definition, the power radiated by the isotropic radiator is the same in all directions, that is, the total radiated power P_{rad} is uniformly spread over the full solid angle 4π.

It is possible to use the directivity to compare antennas with each other. For practical applications, however, it is difficult to measure the total *radiated* power, P_{rad}, while it is much easier to measure the *input* power to the antenna, P_{in}. In fact, in a real antenna the radiated power is less than the input power, due to losses. Those are accounted for by introducing the **radiation efficiency** η:
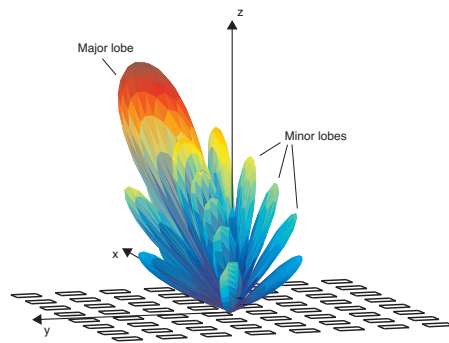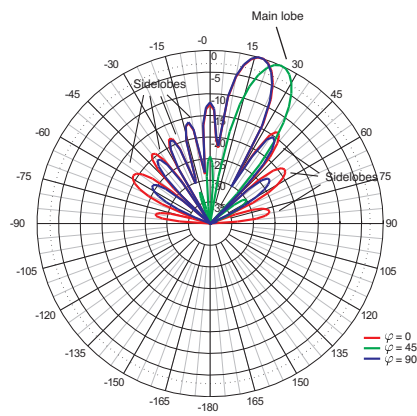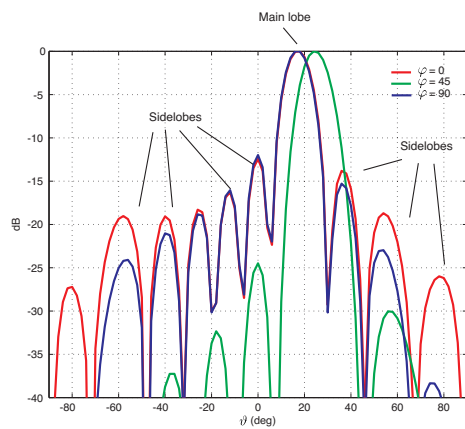
Figure 2.1: Radiation lobes of an antenna radiation pattern. 3D-view (a), polar plots (b) and rectangular plots (c).

$$\eta = \frac{P_{\text{rad}}}{P_{\text{in}}} \leq 1 \tag{2.15}$$

When we replace the reference radiated power of Eq. (2.14) with the input power, using the expression (2.15), we obtain the definition of antenna **gain** G:

$$G(\vartheta, \varphi) = \frac{\frac{dP_{\text{rad}}}{d\Omega}(\vartheta, \varphi)}{\frac{P_{\text{in}}}{4\pi}} \quad \text{[dimensionless].} \tag{2.16}$$

From Eqs. (2.14), (2.15), (2.16) follows the relation between directivity and gain:

$$G(\vartheta, \varphi) = \eta \cdot D(\vartheta, \varphi) \tag{2.17}$$

Gain is commonly expressed on a logarithmic scale, and in this case it is indicated in dBi (where the "i" indicates that we consider the isotropic radiator as a reference, unity-gain antenna):

$$G(\vartheta, \varphi)_{\text{dBi}} = 10\log_{10}[G(\vartheta, \varphi)] \quad \text{[dBi]} \tag{2.18}$$

2.2.8   Effective isotropic radiated power ($EIRP$)

For a point-to-point wireless communication system, it is generally very important that the employed antennas have a high gain, in order to minimize the power needed for transmission. In fact, it is undesired to transmit in directions where there are no receivers. An antenna with high gain can be seen as capable of "concentrating" the power to the desired direction – and reducing the power density in unwanted directions – in a more effective way when compared to an antenna having a lower gain in the same direction. This concept is represented by the effective isotropic radiated power and is clarified by an example.

The **effective isotropic radiated power** ($EIRP$) is defined as

$$EIRP = P_{\text{in}} \cdot G_{\text{max}} \quad \text{[W]} \tag{2.19}$$

where G_{max} is the maximum gain, achieved in direction ($\vartheta_{\text{max}}, \varphi_{\text{max}}$). The $EIRP$ represents the power that would be needed in transmission, when using an isotropic radiator instead of the considered antenna, in order to have the same power radiated by the considered antenna in the direction of maximum gain.

Example 2.1
Let us consider (Case 1) a transmitting antenna with a maximum gain $G_1 = 3$ dBi and an input power $P_1 = 5$ W (7 dBW). Assume the antenna is oriented in such a way that the direction of maximum gain is aligned to the desired pointing direction. The $EIRP$ will be $EIRP_1 = P_1 \cdot G_1 = 7\,\text{dBW} + 3\,\text{dBi} = 10$ dBW. Using this type of antenna (with a $G_{\text{max}} = 3\,\text{dBi}$) allows to reduce the required transmitted power to 5 W (7 dBW), instead of the 10 W (10 dBW) that would be needed using the isotropic radiator ($G_{\text{max,iso}} = 0\,\text{dBi} = 1$).

Let us suppose now (Case 2) to replace the antenna with an even more directive one, having a maximum gain $G_2 = 10$ dBi. In order to have the same *EIRP* it is now sufficient to feed an input power of only 1 W (0 dBW). In fact, in both cases the *effective* radiated power in the desired direction is $EIRP_1 = EIRP_2 = 10$ dBW.

Table 2.1: Comparison of antennas with different gain and same *EIRP*

Isotropic	Antenna 1	Antenna 2
$G_{iso} = 0$ dBi	$G_1 = 3$ dBi	$G_2 = 10$ dBi
$P_{iso} = 10$ dBW (10 W)	$P_1 = 7$ dBW (5 W)	$P_2 = 0$ dBW (1 W)
$EIRP_{iso} = 10$ dBW	$EIRP_1 = 10$ dBW	$EIRP_2 = 10$ dBW

The two antennas in this example have the same effective radiated power in the direction of interest (that is, where the gain is maximum) but in Case 2 this was achieved by using only *one fifth* of the power that had to be used in Case 1, and *one tenth* of the power that would have been needed using an isotropic radiator, simply thanks to the higher antenna gain. □

2.2.9 Radiation resistance

Let us consider a circuit representation of a wireless communication system, as in Fig. 2.2. Fig. 2.2(a) represents the transmission system as composed by a transmitter, a transmission line and a transmitting antenna. The antenna can be represented as a *load*, generally complex, connected to the output of the transmission line. The impedance of this load can be separated in a resistive and a reactive component, respectively indicated as R_A and X_A, as

$$Z_A = \underbrace{R_{\text{rad}} + R_{\text{loss}}}_{R_A} + j X_A. \tag{2.20}$$

We can define **radiation resistance** as the resistance that would dissipate the same amount of power which is *radiated* by the antenna, when the current in the resistance is the same current at the input terminals of the antenna. Note that a part of the input power to the antenna is not radiated but dissipated as ohmic losses on the antenna structure. For this reason, the real part of the antenna input impedance has been written as the sum of two terms, the radiation resistance R_{rad}, and the term R_{loss}, also known as *nonradiative* or *loss resistance*, accounting for the ohmic losses.

2.2.10 Effective area

Let us now consider Fig. 2.2(b). This represents a receiving antenna connected to a receiver. The receiving antenna is situated in the field radiated by the transmitting antenna on the left of the figure. We assume the distance is such that the receiving
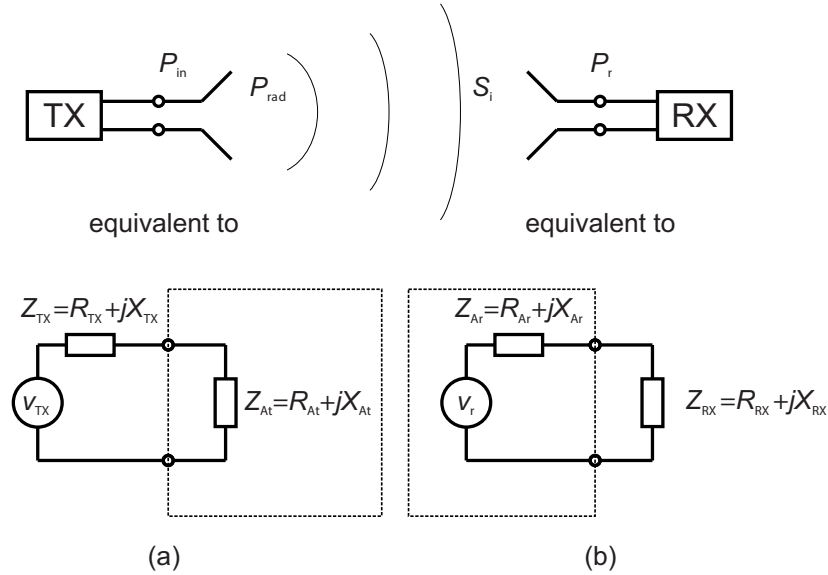
Figure 2.2: Equivalent circuit of a wireless communication link

antenna is in the far-field region of the transmitting antenna. The power density per unit area is considered to be constant over the area of the receiving antenna, and is indicated by the Poynting vector S_i, as described in Section 2.2.4. Here, the subscript "i" is used to indicate the incident Poynting vector on the receiving antenna. This antenna collects a part of the power of the passing electromagnetic wave and delivers it to the input of the receiver. As such, it converts the wave into a current in the load and can be represented as the Thévenin equivalent circuit as in the lower part of Fig. 2.2(b). The voltage V_r is induced by the passing wave and produces a current I_{RX} through the equivalent input impedance of the receiver Z_{RX} equal to

$$I_{RX} = \frac{V_r}{Z_{RX} + Z_{Ar}} \quad [A] \tag{2.21}$$

where V_r and I_{RX} are effective (rms) values.

In general the terminating impedance Z_{RX} is complex, as well as the antenna impedance Z_{Ar} as shown in the Eq. (2.20). Thus we can write

$$Z_{RX} = R_{RX} + jX_{RX} \tag{2.22}$$

$$Z_{Ar} = R_{Ar} + jX_{Ar} = R_{rad} + R_{loss} + jX_{Ar}. \tag{2.23}$$

If we assume the power delivered by the antenna to the receiver is P, we can write

$$P = I_{RX}^2 R_{RX} \tag{2.24}$$

from which follows that the current magnitude is

$$I_{RX} = \frac{V_r}{\sqrt{(R_{rad} + R_{loss} + R_{RX})^2 + (X_{Ar} + X_{RX})^2}} \tag{2.25}$$

and inserting this expression into Eq. (2.24)

$$P = \frac{V_r^2 R_{RX}}{(R_{rad} + R_{loss} + R_{RX})^2 + (X_{Ar} + X_{RX})^2} \tag{2.26}$$

Based on our assumption, the surface power density S_i is constant over the area A of the receiving antenna, and Eq. (2.20) reduces to the simple product

$$P_{rad} = \int_A \mathbf{S}_i \cdot \mathbf{a}_r \, dA = A \cdot S_i = P \quad [\text{W}] \tag{2.27}$$

and substituting in Eq. (2.26) yields

$$A = \frac{V_r^2 R_{RX}}{S_i \left[(R_{rad} + R_{loss} + R_{RX})^2 + (X_{Ar} + X_{RX})^2 \right]} \tag{2.28}$$

If we assume that the antenna impedance is matched to the input impedance of the receiver (maximum power transfer), we can write

$$X_{RX} = -X_{Ar} \tag{2.29}$$

$$R_{RX} = R_{Ar} \quad = R_{rad} + R_{loss} \tag{2.30}$$

and Eq. (2.28) becomes the **effective area**

$$A_e = \frac{V_r^2}{4 S_i (R_{rad} + R_{loss})} \tag{2.31}$$

The term $V_r^2/4(R_{rad} + R_{loss})$ represents the power P_r made available by the antenna to the receiver[2], that is, the power delivered to the receiver when it is impedance matched to the antenna. For this reason, we can also define the **effective area** of an antenna as *the ratio between the power made available at its output terminals (P_r), and the surface power density (S_i) incoming on the antenna*:

$$A_e = \frac{P_r}{S_i} \quad [\text{m}^2] \tag{2.33}$$

---

[2]In the electrical network in Fig. 2.2(b), in maximum power transfer conditions as in Eq. (2.30), the power delivered to the load is:

$$P_{RX} = R_{RX} I_{RX}^2 = R_{RX} \left(\frac{V_r}{R_{Ar} + R_{RX}} \right)^2 = R_{Ar} \left(\frac{V_r}{2 R_{Ar}} \right)^2 = \frac{V_r^2}{4 R_{Ar}} = \frac{V_r^2}{4(R_{rad} + R_{loss})} \tag{2.32}$$

In these terms, the effective area does not represent a physical area, but instead the effectiveness of the antenna to collect power from the incoming wave and make this power available to the receiver. From Eq. (2.31), the maximum effective area will be obtained when the loss resistance of the antenna R_{loss} is zero.

The effective area is useful to calculate the power made available at the input terminals of the receiver, when knowing the surface power density of the incoming wave. In fact, from Eq. (2.33) we can immediately calculate the power made available at the input terminals of the receiver:

$$P_{\mathrm{r}} = A_{\mathrm{e}} \cdot S_{\mathrm{i}} \quad [\text{W}] \tag{2.34}$$

As for the effective area, we remember from the previous subsection that the antenna gain was also providing a relation between the power at the antenna terminals and the power radiated by the antenna, for the case of a transmitting antenna. Due to the reciprocity principle, it is possible to establish a univocal relation between the antenna gain and the effective area of an antenna [3] as follows:

$$G = 4\pi \cdot \frac{A_{\mathrm{e}}}{\lambda_0^2} \Leftrightarrow A_{\mathrm{e}} = G \cdot \frac{\lambda_0^2}{4\pi} \tag{2.35}$$

2.3   Radiowave propagation: Friis transmission formula

In many practical applications, antennas are used in a wireless communication system to transmit information from a transmitter to a receiver. In this application scenario, for the design of the wireless link, it is important to determine a relationship between the power delivered to the transmitting antenna, P_{in}, and the power ultimately delivered to the receiver, P_{r}.

We assume the separation r between the antennas is large enough to consider a far-field regime, as described in Section 2.2. The transmitting and the receiving antennas have effective areas A_{et} and A_{er}, and radiation efficiencies η_1 and η_2, respectively. We also assume that the antennas are impedance matched respectively to the transmitter and to the receiver, meaning that no power is reflected back neither from the input of the transmitting antenna nor from the input of the receiver. Let us consider the antennas as oriented in such a way that the directions of their maximum gain point at each other, as motivated in the Example 2.1.

If the transmitting antenna were isotropic and lossless, we would have that the surface power density at the receiving antenna would be:

$$S_{\mathrm{iso}} = \frac{P_{\mathrm{t}}}{4\pi r^2} \quad [\text{W/m}^2] \tag{2.36}$$

that is, uniformly distributed over a sphere of radius r. In the real case, the power density at the receiver is obtained using the definition of antenna gain as

$$S_{\mathrm{r}} = G_{\mathrm{t}} S_{\mathrm{iso}} = \frac{P_{\mathrm{t}} G_{\mathrm{t}}}{4\pi r^2} \quad [\text{W/m}^2] \tag{2.37}$$

From the definition of effective area (2.33), the received power can be calculated as

$$P_\mathrm{r} = S_\mathrm{r} A_\mathrm{er} = \frac{P_\mathrm{t} G_\mathrm{t} A_\mathrm{er}}{4\pi r^2} \quad [\mathrm{W}] \tag{2.38}$$

and, using the relation between gain and effective area (2.35), can be rewritten as

$$P_\mathrm{r} = P_\mathrm{t} G_\mathrm{t} G_\mathrm{r} \left(\frac{\lambda}{4\pi r}\right)^2 \quad [\mathrm{W}] \tag{2.39}$$

This equation is known as **Friis transmission formula** after Harald T. Friis who first published it in 1946 [27]. The ratio $P_\mathrm{r}/P_\mathrm{in}$ is known as power transfer ratio and it is useful in link budget calculations.

In a more general case, it is possible to take into account the effects of misalignment of the antenna pointing and polarization, impedance mismatch, and absorption of the medium by including additional factors. Equation (2.39) becomes

$$\frac{P_\mathrm{r}}{P_\mathrm{in}} = G_\mathrm{t}(\vartheta_\mathrm{t}, \varphi_\mathrm{t}) G_\mathrm{r}(\vartheta_\mathrm{r}, \varphi_\mathrm{r}) \left(\frac{\lambda}{4\pi r}\right)^2 (1 - |\Gamma_\mathrm{t}|^2)(1 - |\Gamma_\mathrm{r}|^2) |\boldsymbol{a}_\mathrm{t} \cdot \boldsymbol{a}_\mathrm{r}^*|^2 e^{\alpha r} \tag{2.40}$$

where the introduction of the argument in the gain terms $G_\mathrm{t}(\vartheta_\mathrm{t}, \varphi_\mathrm{t})$, $G_\mathrm{r}(\vartheta_\mathrm{r}, \varphi_\mathrm{r})$ allows to account for misalignment of the antenna pointing, Γ_t and Γ_r represent the reflection coefficients at the transmitter and receiver interfaces resulting for impedance mismatch, $|\boldsymbol{a}_\mathrm{t} \cdot \boldsymbol{a}_\mathrm{r}^*|^2$ is an attenuation term representing the effect of misalignment between the vectors $\boldsymbol{a}_\mathrm{t}$ and $\boldsymbol{a}_\mathrm{r}$, respectively indicating the polarization of the transmitting and receiving antenna, and α is the absorption coefficient of the medium.

2.4 Antenna arrays

From the discussion in the previous section, it is apparent that in point-to-point communications it is desirable that the employed antennas have a high gain. A way to increase the gain of an antenna is to arrange *multiple* basic antenna elements into an *array*. An **antenna array** is a set of elementary antenna elements with a specific spatial arrangement and orientation[3], fed by a network called *beamformer*. This network is used to provide *excitations* to the single elements which can be decomposed as an amplitude term $|C_i|$ and a phase term α_i. Those excitations, in conjunction with the arrangement of the elements, will determine the radiation characteristic of the array according to a specific mathematical relation that we are going to analyze in the following of this section.

Let us consider the general array depicted in Fig. 2.3. This array consist of N antennas, with the same orientation with respect to the cartesian coordinates x, y, z. The versors of the x, y, z axes are respectively indicated as $\mathbf{a}_x, \mathbf{a}_y, \mathbf{a}_z$. The i-th antenna is excited with a complex excitations $C_i = |C_i| e^{j\alpha_i}$. The position of the i-th antenna is indicated by the vector $\mathbf{r}_i = (r_i, \vartheta_i, \varphi_i)$ with respect to the origin of the

---

[3]Here and in the following of this chapter, *same orientation* indicates that the radiation patterns of the individual elements of the array are all the same with respect to the reference system x, y, z.

coordinate system in use. A reference antenna located at the origin $O_{x,y,z}$ and excited by the excitation $C_0 e^{-j\alpha_0} = 1e^{-j0}$ would produce, in the point p, indicated by the vector $\mathbf{r} = (r, \vartheta, \varphi)$, a radiated field

$$\mathbf{E}_0(\mathbf{r}) = \mathbf{E}_0(r, \vartheta, \varphi) = \mathbf{f}(\vartheta, \varphi) \frac{e^{-jk_0 r}}{4\pi r} \tag{2.41}$$

where $\mathbf{f}(\vartheta, \varphi)$ is the vector electric field, as in Eq. (2.2), radiated by the elementary antenna of the array, $k_0 = 2\pi / \lambda_0$ is the propagation constant, λ_0 is the wavelength in the medium (in this case, free-space), $r = |\mathbf{r}|$ is the distance from the origin, while ϑ and φ respectively indicate elevation and azimuth angles in the spherical reference coordinate system (Appendix A).
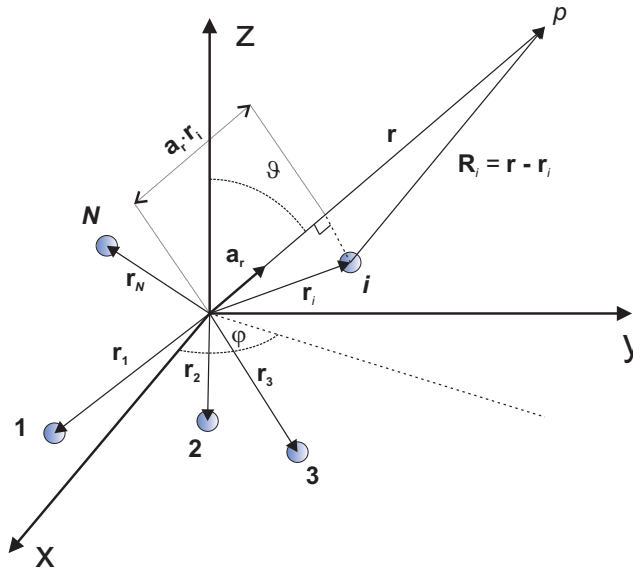
Figure 2.3: Schematic representation of an antenna array composed by N identical elements

Our scope is to calculate the total field generated by the array in the point indicated by $\mathbf{r}$. For the superposition principle, which applies thanks to the linearity of Maxwell's equations, the total field can be obtained by the sum of the single electric fields contributions $\mathbf{E}_i$ by the single antenna elements. When $\mathbf{R}_i = \mathbf{r} - \mathbf{r}_i$ represents the position of the observation point with respect to the i-th antenna element, the i-th electric field contribution by the i-th antenna element will be

$$\mathbf{E}_i(\mathbf{r}) = |C_i| e^{j\alpha_i} \mathbf{f}_i(\vartheta, \varphi) \frac{e^{-jk_0 |\mathbf{r} - \mathbf{r}_i|}}{4\pi |\mathbf{r} - \mathbf{r}_i|} \tag{2.42}$$

and the total radiated field will be

$$\mathbf{E}(\mathbf{r}) = \sum_{i=1}^{N} \mathbf{E}_i(\mathbf{r}) = \sum_{i=1}^{N} |C_i| e^{j\alpha_i} \mathbf{f}_i(\vartheta, \varphi) \frac{e^{-jk_0|\mathbf{r}-\mathbf{r}_i|}}{4\pi|\mathbf{r}-\mathbf{r}_i|} \tag{2.43}$$

where $|\mathbf{r} - \mathbf{r}_i|$ is the distance between the i-th element and the observation point. This expression can be simplified in a useful way under certain assumptions.
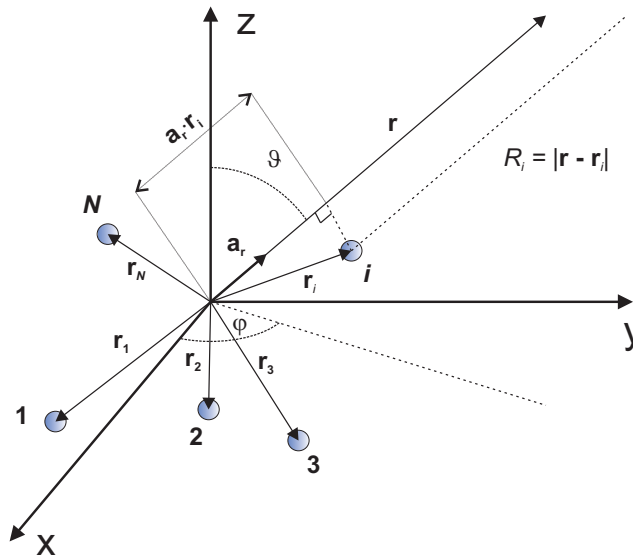
Figure 2.4: Schematic representation of an antenna array composed by N identical elements

Firstly, if we consider the antenna elements to be *identical* and with equal orientation, they will all have the same field pattern, thus we can replace $\mathbf{f}_i(\vartheta, \varphi)$ with $\mathbf{f}(\vartheta, \varphi)$ in Eq. (2.43). Secondly, let us consider the position $\mathbf{r}$ to be in the *far-field region* of radiation, as described in Section 2.2.3. If we also assume that the distances of the elements from the origin are such that $|\mathbf{r}| \gg r_i, \forall i$, we can consider the "rays" R_i connecting the single antennas to the point indicated by $\mathbf{r}$ to be essentially parallel, as in Fig. 2.4. With this assumption, the distance from the i-th element to the far-field point $\mathbf{r}$ can be approximated as

$$|\mathbf{r} - \mathbf{r}_i| \approx r - \mathbf{a_r} \cdot \mathbf{r}_i \tag{2.44}$$

This allows two useful approximations in the expressions (2.42) and (2.43):

- *Amplitude approximation:* in the amplitude term $1/|\mathbf{r} - \mathbf{r}_i|$, we can replace $|\mathbf{r} - \mathbf{r}_i| \approx r$;

- *Phase approximation*[4]*:* in the phase term, we can replace $-jk_0|\mathbf{r} - \mathbf{r}_i|$ with $-jk_0(r - \boldsymbol{a_\mathbf{r}} \cdot \mathbf{r}_i)$.

The total radiation field of the array (2.43) can be rewritten

$$\mathbf{E}(\mathbf{r}) = \sum_{i=1}^{N} |C_i| e^{j\alpha_i} \mathbf{f}(\vartheta, \varphi) \frac{e^{-jk_0 r + jk_0 \mathbf{a_r} \cdot \mathbf{r}_i}}{4\pi r}$$

$$= \mathbf{f}(\vartheta, \varphi) \frac{e^{-jk_0 r}}{4\pi r} \sum_{i=1}^{N} |C_i| e^{j\alpha_i + jk_0 \mathbf{a_r} \cdot \mathbf{r}_i} \qquad (2.45)$$

By definition, radiation pattern, directivity and gain are proportional to the power radiated per unit of solid angle $\mathrm{d}P_{\mathrm{rad}}/\mathrm{d}\Omega$ which, in turn, is proportional to $16\pi^2 r^2 |\mathbf{E}|^2$ [4]. Thus for an array we can write that the directivity is

$$D(\vartheta, \phi) \propto 16\pi^2 r^2 |\mathbf{E}|^2$$

$$= |\mathbf{f}(\vartheta, \varphi)|^2 \left| \sum_{i=1}^{N} |C_i| \, e^{j\alpha_i + jk_0 \mathbf{a_r} \cdot \mathbf{r}_i} \right|^2$$

$$= |\mathbf{f}(\vartheta, \varphi)|^2 |F(\vartheta, \varphi)|^2 \qquad (2.46)$$

Notably, the directivity is proportional to the product of the field pattern $\mathbf{f}(\vartheta, \varphi)$ of the reference antenna, and the **array factor** which we defined as

$$F(\vartheta, \varphi) = \sum_{i=1}^{N} C_i \, e^{jk_0 \mathbf{a_r} \cdot \mathbf{r}_i} \qquad (2.47)$$

where $C_i = |C_i| e^{j\alpha_i}$ is the complex excitation of the i-th element. This is an important result known as *principle of pattern multiplication.* This principle is important because it represents the fact that *it is possible to modify the radiation characteristics of an array of equal antenna elements, simply by changing the space distribution of the antennas or their electrical excitation*, without modifying their individual radiation characteristics. In fact, $|C_i|$ and α_i represent the amplitude and the phase excitations of the i-th element of the N-elements array, respectively. $\mathbf{a_r}$ is the unit vector pointing towards the position of the observer and $\mathbf{r}_i$ is the position of the i-th antenna element with respect to the origin of the reference coordinate system, as in Fig. 2.4. The array factor thus describes the effect of the *spatial arrangement* (given by the geometrical layout of the array, $\mathbf{a_r} \cdot \mathbf{r}_i$) and the effect of the *complex excitation* ($|C_i|$, α_i) of each individual antenna element forming the array.

In many practical cases, the array factor F is the one that ultimately determines the radiation characteristics of the array. In fact, many arrays employ basic antenna

---

[4]The "stronger" $|\mathbf{r} - \mathbf{r}_i| \approx r$ approximation cannot be used for the phase term, since the phase differences due to different path lengths from the various antennas could still be substantial, if (as commonly happens) λ_0 is comparable with $\mathbf{a_r} \cdot \mathbf{r}_i$. In fact, those phase differences are the ones which determine the interference effects that – in turn – enable the formation of a directive beam of radiation, which is the ultimate goal of the antenna array itself.

elements which generally have low directivity, e.g. dipoles, horns, or patches. Thus, since the radiation pattern is the product of the radiation pattern of the element (quasi-omnidirectional) and the array factor (highly directive), the shape of the radiation pattern of the complete array is dictated mainly by the shape of the array factor (highly directive). For this reason, in the following our attention will be focused on the array factor, irrespective of the specific pattern of the basic antenna element.

As an important consequence, phased array antenna technology allows fast and accurate beam pattern shaping and reconfigurability, by means of reconfiguring the array factor F. By itself, this conclusion motivates the diffusion of phased arrays in many fields of applications. The reconfigurability of the array factor is achieved through the use of a so-called beamforming network, or beamformer. A beamformer can be generally defined as a network capable of generating the desired amplitude and phase excitations at each specific antenna element of the array. Since the complex excitations are defined by the input-output responses of the beamforming network, the ability to reconfigure those responses allows, in turn, to accordingly modify the radiation pattern as desired. The relation between the radiation pattern and the excitation of the single antenna elements is described by the array factor Eq. (2.47).

In the following we will see how the general expression of the array factor (2.47) can be specified for two noteworthy cases of antenna elements arrangements, namely, linear arrays and planar arrays.

2.4.1 Linear arrays

Let us consider $N+1$ elements along the x axis, equally spaced at a distance d from each other, as in Fig. 2.5. The elements are numbered as $n = 0,1,...,N$. The n-th element is excited by a complex coefficient $|C_n|e^{j\alpha_n}$. The position vector of the n-th antenna becomes

$$\mathbf{r}_n = nd\mathbf{a}_x. \tag{2.48}$$

so that, in turn, the scalar product in the exponential of Eq. (2.47) becomes

$$\mathbf{a_r} \cdot \mathbf{r}_n = nd\cos\psi = nd\sin\vartheta\cos\varphi \tag{2.49}$$

where ψ indicates the angle formed between the x axis and the direction of the observer, $\mathbf{r}$. The array factor of a linear array can be written as

$$F(\psi) = F(\vartheta,\varphi) = \sum_{n=0}^{N} C_n e^{j\alpha_n + jnk_0 d\cos\psi} = \sum_{n=0}^{N} C_n e^{j\alpha_n + jnk_0 d\sin\vartheta\cos\varphi} \tag{2.50}$$

As expected from the symmetry of the array geometry, the function $F(\psi)$ shows cylindrical symmetry with respect to the array axis x. In fact, its dependance on the position of the observer depends only on the angle ψ formed between the x-axis and the vector $\mathbf{r}$ indicating the position of the observer. This angle is known as *scanning angle*.
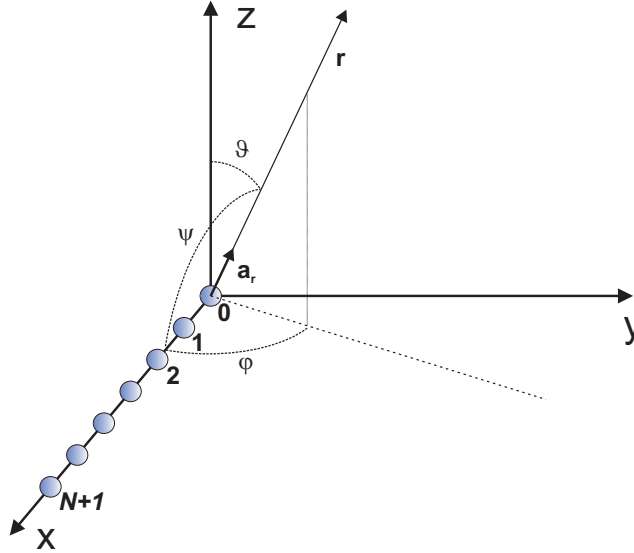
Figure 2.5: Schematic representation of a linear antenna array composed by $N + 1$ identical, equally spaced elements with the same orientation

In the introduction to this section, it was stated that a possible reason of using an array is to increase the directivity of an antenna system. Now, based on the analysis given so far, we can also show that it is possible to control the shape of the directivity function, and in particular the angular position at which the maximum directivity occurs, by simply controlling the phases of the excitation of the antennas of the array.

Let each antenna be fed with the same constant amplitude $|C_n| = C, \forall n$. Suppose that it is desired to have the maximum of radiation in the arbitrary direction ψ_0, corresponding to the angle (ϑ_m, φ_m) (where the subscript 'm' stays for maximum). To make sure the radiated field reaches its maximum in this specific direction, we simply impose that the array factor (2.50) reaches its maximum for the same scanning angle. The array factor (2.50) will be maximum when

$$F(\psi_0) = \sum_{n=0}^{N} C = \max_{\psi} F(\psi) \tag{2.51}$$

This condition is obtained when the phase of excitation of the n-th antenna is imposed to be

$$\alpha_n = -nk_0 d \cos \psi_0 \tag{2.52}$$

and the array factor (2.50) becomes

$$F(\psi) = \sum_{n=0}^{N} C e^{jnk_0 d(\cos\psi - \cos\psi_0)} \tag{2.53}$$

We can observe two main cases:

- *Broadside array:* the maximum of radiation is achieved for $\psi_0 = \pi/2$ (direction orthogonal to the array axis). The excitation phases are $\alpha_n = 0, \forall n$.

- *End-fire array:* the maximum of radiation is achieved for $\psi_0 = 0$ (direction of the array axis). The excitation phases are $\alpha_n = -nk_0 d$, equal to the phase shift experienced by a plane wave propagating in direction $-\mathbf{a}_x$.

In our assumption of uniform excitation $C = 1$, the array factor reduces to a geometrical series[5]:

$$
\begin{aligned}
F(\psi) &= \sum_{n=0}^{N} e^{jnk_0 d(\cos\psi - \cos\psi_0)} \\
&= \frac{1 - e^{j(N+1)k_0 d(\cos\psi - \cos\psi_0)}}{1 - e^{jnk_0 d(\cos\psi - \cos\psi_0)}} \\
&= e^{j\frac{N}{2}k_0 d(\cos\psi - \cos\psi_0)} \frac{\sin\left[\frac{N+1}{2}k_0 d(\cos\psi - \cos\psi_0)\right]}{\sin\left[\frac{k_0 d}{2}(\cos\psi - \cos\psi_0)\right]}
\end{aligned}
\tag{2.54}
$$

By applying the substitution

$$u = k_0 d \cos\psi \tag{2.55}$$
$$u_0 = k_0 d \cos\psi_0 \tag{2.56}$$

the magnitude of the array factor (2.54) becomes

$$|F(u)| = \frac{\sin\left[\dfrac{N+1}{2}(u + u_0)\right]}{\sin\left[\dfrac{u + u_0}{2}\right]} \tag{2.57}$$

This is the periodic function which has been plotted in Fig. 2.6. It shows a maximum at $u = -u_0$, and the corresponding lobe is called *main lobe*. The height of the main lobe is $F(-u_0) = N + 1$, that is, the sum *in phase* of the fields radiated by the single elements. The main lobe repeats periodically at $u = -u_0 + 2m\pi$, $m \in \mathbb{Z}$, interleaved with $N-1$ *secondary lobes* occurring at $u = -u_0 + \frac{2m+1}{N+1}\pi$, $m \in \mathbb{Z}$. The highest secondary lobe occurs at a distance $\Delta u = \pm\frac{3\pi}{N+1}$ from the main lobe, and its height is approximately $2/(3\pi)$ times that of the main lobe (that is, -13.5 dB).

It is important to note that only a subset of this function maps to a physically valid array factor. In fact, from Eq. (2.55) follows that u corresponds to a physically valid scanning angle ψ only in the range

---

[5]for a geometrical series $\sum_{n=0}^{N} w^n = \frac{1-w^{N+1}}{1-w}$
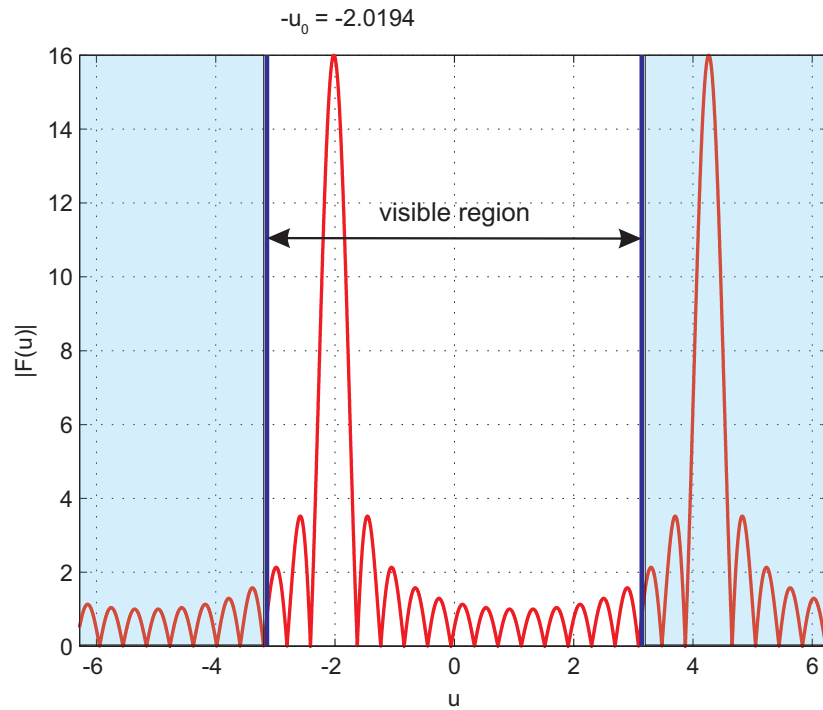
Figure 2.6: Array factor as a function of u. $N = 15$ (16 elements), $-u_0 = -2.0194$
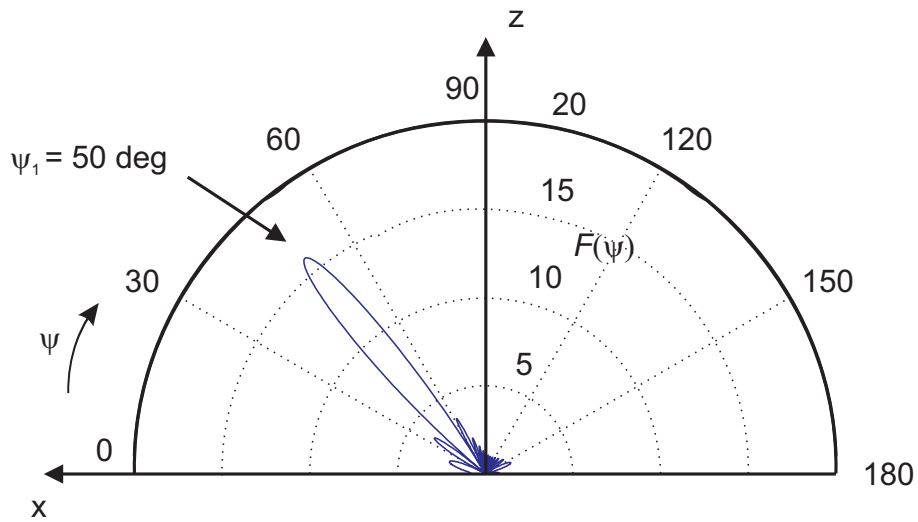
Figure 2.7: Array factor as a function of ψ. $N = 15$ (16 elements), $\psi_0 = 50$ deg

$$-k_0 d \leq u \leq k_0 d \qquad (2.58)$$

being $\cos\psi$ limited between -1 and 1 when $\psi \in \mathbb{R}$. This range of values for u is called *visible region*, because it corresponds to the range where the scanning angle ψ is a real number between 0 and $180°$. The visible region is centered around $u = 0$ (corresponding to $\psi = \pi/2$, that is, the broadside direction) and spans between

$$-2\pi d/\lambda_0 \leq u \leq 2\pi d/\lambda_0 \qquad (2.59)$$

The array factor corresponding to the visible region shown in Fig. 2.6, is displayed in Fig. 2.7. It can be seen that the visible region maps to the range $\psi \in [0, 180°]$, with a single main lobe in $\psi_0 = 50°$ (corresponding to $u = -u_0 = -2.0194$) and $N - 1 = 14$ minor lobes (sidelobes).

From Eq. (2.59) it is immediately clear that the choice of d (spacing between adjacent antenna elements) with respect to λ_0 (operating wavelength) will determine the dimension of the visible region and, in turn, the portion of function $|F(u)|$ Fig. 2.6 which is going to map to the "physical" array factor, and ultimately determine the shape of the array factor of the array.

2.4.2 Grating lobes

In most applications, it is desirable to have a *single* main lobe of radiation from an antenna array. From the previous analysis, we saw that this happens when only the main lobe, positioned at $u = -u_0$, corresponding to the desired scanning angle $\psi = \psi_0$, falls in the visible region of the array. Following up the analysis, we can now derive a very important condition on the choice of d/λ_0 to achieve this result and avoid the presence of grating lobes. We call *grating lobes* the main lobes, different from the one in $u = -u_0$, that fall in the visible region. This happens when the ratio d/λ_0 is not sufficiently small, such that $F(\psi)$ reaches its maximum also for additional ψ angles between 0 and $180°$ in addition to the scanning angle ψ_0.

The array factor reaches its maximum

$$\max_{\psi} F(\psi) = \max_{\psi} \sum_{n=0}^{N} C_n e^{jnk_0 d(\cos\psi - \cos\psi_0)} = \sum_{n=0}^{N} C \qquad (2.60)$$

when

$$k_0 d(\cos\psi - \cos\psi_0) = 2m\pi, \quad m \in \mathbb{Z} \qquad (2.61)$$

Let us now calculate the angles ψ for which this condition is satisfied. From Eq. (2.61) follows

$$\cos\psi = \cos\psi_0 \pm m\frac{\lambda_0}{d}, \quad m \in \mathbb{Z} \qquad (2.62)$$

The solutions are:

- for $m = 0$, the maximum is in direction $\psi = \psi_0$

- for $m = \pm 1$, Eq. (2.62) may or may not have a real solution. If it has a real solution, then there is a grating lobe entering the visible region in

$$\psi = \arccos\left[\cos\psi_0 \pm \frac{\lambda_0}{d}\right] \tag{2.63}$$

It follows that the condition to avoid grating lobes is that Eq. (2.62) must not have any real solution for $m = 1$. This is true when, for $m = 1$ the second term of the equality is larger than one, that is

$$\left|\cos\psi_0 \pm \frac{\lambda_0}{d}\right| > 1 \tag{2.64}$$

From this discussion, we can obtain the condition for the ratio d/λ_0 for the absence of grating lobes

$$\begin{cases} \dfrac{\lambda_0}{d} > 1 - \cos\psi_0, & \text{for } \cos\psi_0 < 0 \tag{2.65} \\[2mm] \dfrac{\lambda_0}{d} > 1 + \cos\psi_0, & \text{for } \cos\psi_0 > 0 \tag{2.66} \end{cases}$$

which gives

$$\frac{d}{\lambda_0} < \frac{1}{1 + |\cos\psi_0|} \tag{2.67}$$

This is the condition of absence of grating lobes. For a broadside array $\psi_0 = \pi/2$, thus it is sufficient that the inter-element spacing $d < \lambda_0$. Nonetheless, this is a limit case where the grating lobe is about to appear. In fact, as soon as ψ_0 reduces, the main lobe in u_0 moves away from $u = 0$ and a grating lobe enters the visible region. See Example 2.2. To avoid this, d must be reduced. For the more general case of a non-broadside, arbitrary pointing direction ψ_0, the condition of absence of grating lobes given by Eq. (2.67) reduces to

$$d < \frac{\lambda_0}{2} \tag{2.68}$$

The derivation performed so far demonstrates that, for a linear array of equally-spaced elements, it is sufficient to keep the *element spacing below half a wavelength* to avoid the appearance of grating lobes, for *any desired scanning angle*.

Example 2.2
Let us consider a 16-elements linear array ($N=15$) operating at frequency $f_0 =1$ GHz (wavelength $\lambda_0 \approx 30$ cm). The elements are placed on the x axis as in Fig. 2.5. Let the distance between adjacent elements be $d=15$ cm. In this condition, according to Eq. 2.59, the visible region is

$$-2\pi d/\lambda_0 \leq u \leq 2\pi d/\lambda_0 \tag{2.69}$$

or, using Eq. (2.68)

$$-\pi \le u \le \pi \tag{2.70}$$

which is the case represented in Fig. 2.6.

Let us now design the excitation in order to have the maximum of the array factor in direction $\psi_0 = 50$ deg. Let us assume uniform amplitude excitations $C_n = C = 1$. The required excitation phases will be according to Eq. (2.52)

$$\begin{aligned}
\alpha_n &= -nk_0 d \cos\psi_0 \\
&= -n\frac{2\pi}{30} \cdot 15 \cdot \cos(50), \quad n = 0, ..., 15 \\
&= -n\pi \cdot 0.643, \qquad\qquad n = 0, ..., 15
\end{aligned} \tag{2.71}$$

The array factor can be calculated with Eq. (2.57), where $N = 15$ and u_0 is

$$\begin{aligned}
u_0 &= k_0 d \cos\psi_0 \\
&= \frac{2\pi}{\lambda_0} \cdot d \cos\psi_0 \\
&= \pi \cdot \cos(50) = 2.0194
\end{aligned} \tag{2.72}$$

The magnitude of the array factor $|F(u)|$ is also plotted in Fig. 2.6, where the maximum is at $-u_0 = -2.0194$ as just calculated. In this example, for any scanning angle, there will never be grating lobes since the condition (2.68) is satisfied.

Let us now imagine to further separate the elements of the linear array to an inter-element distance of $d_2 = 30$ cm, while keeping the same operating frequency. This distance equals the wavelength ($d_2 = \lambda_0$), thus the condition for absence of grating lobes (2.68) is no longer satisfied. In fact, by considering the same excitation calculated before from Eq. (2.71), the visible region will now be

$$-2\pi d/\lambda_0 \le u \le 2\pi d/\lambda_0 \tag{2.73}$$

and using Eq. (2.68)

$$-2\pi \le u \le 2\pi \tag{2.74}$$

which is represented in Fig. 2.8.

From the figure, it can be seen that there are two values of u for which the magnitude of the array factor $|F(u)|$ is maximum. In fact, for $\lambda_0/d = 1$, Eq. (2.62) has real solutions *both* for $m = 0$ and for $m = -1$. According to Eq. (2.63), they are

$$\psi_0 = \arccos\left[\cos\psi_0\right] \qquad\qquad = 50 \text{ deg} \tag{2.75}$$

$$\begin{aligned}
\psi_1 &= \arccos\left[\cos\psi_0 - \frac{\lambda_0}{d}\right] \\
&= \arccos\left[\cos(50\text{ deg}) - 1\right] \approx 110.93 \text{ deg}
\end{aligned} \tag{2.76}$$

This result is represented in Fig. 2.9.
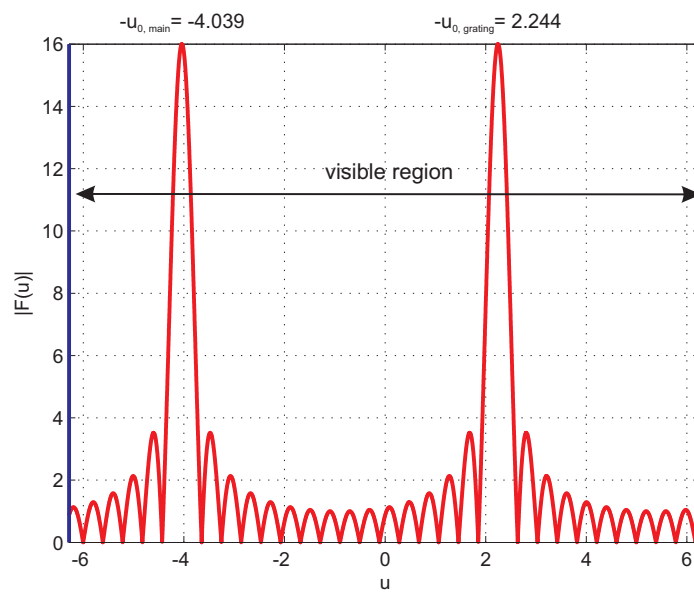
Figure 2.8: Array factor as a function of u in presence of a grating lobe. $N = 15$ (16 elements), $d = \lambda_0$. The main lobe is at $-u_{0,\text{main}} \approx -4.039$ and the first grating lobe appears at $-u_{0,\text{grating}} \approx 2.244$.
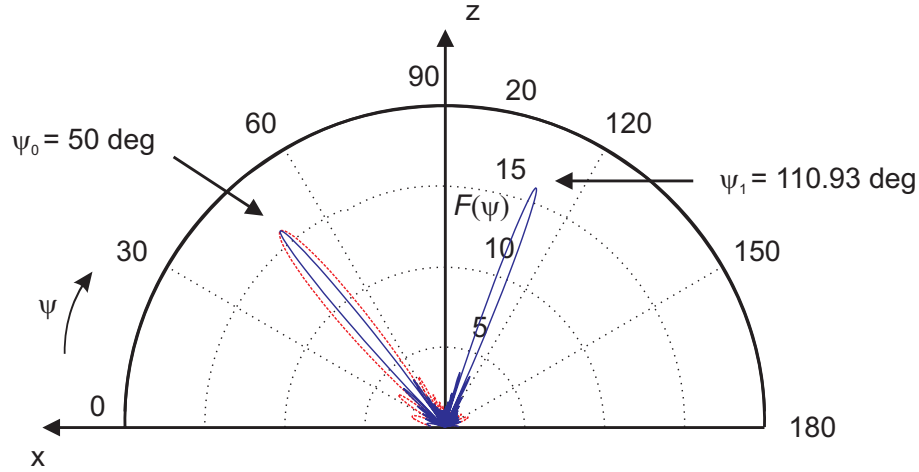
Figure 2.9: Array factor as a function of ψ in presence of a grating lobe. $N = 15$ (16 elements), $d = \lambda_0$. The main lobe is at $\psi_0 = 50$ deg and the first grating lobe appears at $\psi_1 \approx 110.93$ deg. For comparison, the red dotted line shows the array factor obtained with $d = \lambda_0/2$ as in Fig. 2.7.

2.4.3 Planar arrays

After the analysis of linear arrays, we consider another common architecture: the planar array. In this case, the elements are arranged on a 2-dimensional grid on a planar surface. We again consider a cartesian coordinate reference system, where the versors of the x, y, z axes are respectively indicated as $\mathbf{a}_x, \mathbf{a}_y, \mathbf{a}_z$. For simplicity, let us consider the common case of an $(N+1) \times (M+1)$ rectangular array as in Fig. 2.10. Let us assume the elements are placed in the xy plane, with an inter-element spacing of d_x along the x direction and d_y along the y direction. We use two indexes, m and n, to specify the position of the single elements of the array. In particular, the vector specifying the position of the (m, n)-th element is

$$\mathbf{r}_{mn} = \mathbf{a}_x m d_x + \mathbf{a}_y n d_y \tag{2.77}$$

with $n = 0, ..., N$, $m = 0, ..., M$. Accordingly, the complex excitation coefficient of the (m, n)-th element is

$$C_{mn} = |C_{mn}| e^{j\alpha_{mn}} \tag{2.78}$$

The general expression of the array factor (2.47) can be written as two nested sum operators:

$$F(\vartheta, \varphi) = \sum_{m=0}^{M} \sum_{n=0}^{N} C_{mn} \, e^{j k_0 \mathbf{a_r} \cdot \mathbf{r}_{mn}} \tag{2.79}$$
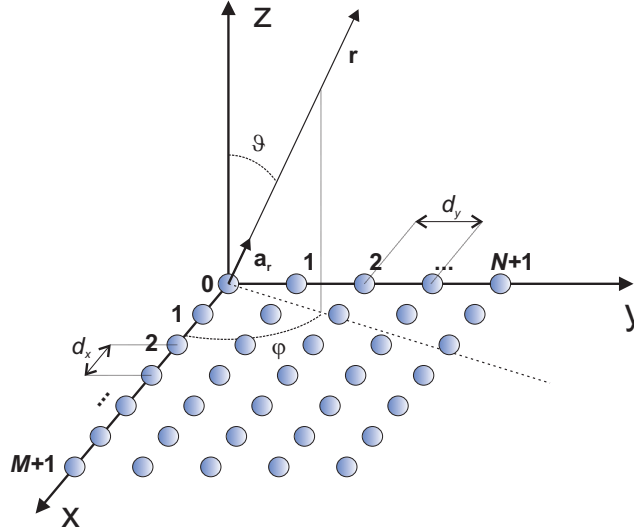
Figure 2.10: Schematic representation of a planar antenna array composed by $(N+1) \times (M+1)$ identical elements with the same orientation

Example 2.3

At this point it is very interesting to notice the relation between the excitation pattern C_{mn} of the antenna array and the far field pattern indicated by F. Analyzing the expression given by Eq. (2.79) it can be noticed that the far field from an array is the 2-dimensional discrete time Fourier transform (DTFT) of the field distribution of the array. In fact, according to the definition of DTFT [28]

$$F(u,v) = \sum_{m=-\infty}^{\infty} \sum_{n=-\infty}^{\infty} f[m,n]e^{-j2\pi(um+vn)} \tag{2.80}$$

Eq. (2.80) is equivalent to Eq. (2.79) provided that we replace

$$f[m,n] = C_{mn} \tag{2.81}$$

$$u = -\frac{k_0}{2\pi}d_x\cos(\psi) = -\frac{k_0}{2\pi}d_x\sin(\vartheta)\cos(\varphi) \tag{2.82}$$

$$v = -\frac{k_0}{2\pi}d_y\cos(\gamma) = -\frac{k_0}{2\pi}d_y\sin(\vartheta)\sin(\varphi) \tag{2.83}$$

where ψ is the angle formed between $\mathbf{a}_r$ and $\mathbf{a}_x$ and γ is the angle formed between $\mathbf{a}_r$ and $\mathbf{a}_y$ (see Appendix A). This result is very important because it leads to the observation that Fourier optics is a valid model to explain the far-field radiation from arrays.

Let us consider a planar aperture S_a on a perfect conductor. Let us consider a cartesian coordinate system as in Fig. 2.11. When we desire to determine the far-
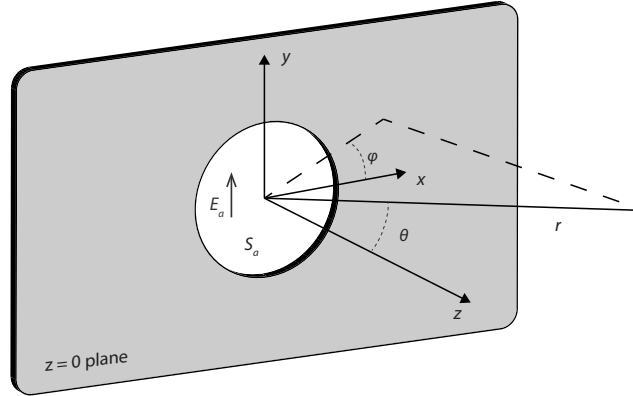
Figure 2.11: An aperture S_a on the $z = 0$ plane, with a tangential field $\mathbf{E}_a$

field radiation from a planar aperture, the Fourier transform method [4] is widely used. This method is also the basis of Fourier optics. In that situation, the far-field in cartesian coordinates can be expressed as [4]

$$\mathbf{E}(x, y, z) = \frac{1}{4\pi^2} \iint\limits_{+\infty}^{+\infty} \mathbf{f}(k_x, k_y) e^{j\mathbf{k}\cdot\mathbf{r}} \, dk_x \, dk_y \tag{2.84}$$

where $\mathbf{k}\cdot\mathbf{r} = k_x x + k_y y + k_z z$. This equation is very important and constitutes the basic equation of Fourier optics, indicating that *an arbitrary electric field* $\mathbf{E}(x, y, z)$ *can be represented, for $z > 0$, as a spectrum of plane waves*, since $\mathbf{f}(k_x, k_y) e^{j\mathbf{k}\cdot\mathbf{r}}$ is a plane wave with vector amplitude $\mathbf{f}$ which propagates in direction $\mathbf{k}\cdot\mathbf{r}$.

When $z = 0$, the field solution of Eq. (2.84) must represent the known field on the radiating aperture $\mathbf{E}_a$. In particular, the x and y components of the field are equal to the assumed known aperture tangential fields:

$$\mathbf{E}_{\tan}(x, y, 0) = \mathbf{E}_a(x, y) = \frac{1}{4\pi^2} \iint\limits_{+\infty}^{+\infty} \mathbf{f}_t(k_x, k_y) e^{-jk_x x - jk_y y} \, dk_x \, dk_y \tag{2.85}$$

which, inverted, gives

$$\mathbf{f}_t(k_x, k_y) = \iint\limits_{S_a} \mathbf{E}_a(x, y) e^{jk_x x + jk_y y} \, dx \, dy \tag{2.86}$$

This equation indicates that the radiated field $\mathbf{f}$ is the 2-dimensional Fourier transform of the field on the aperture, where the spatial frequency domain (k_x, k_y) is seen as the dual description of the spatial (x, y) domain.

This result assimilates the previous finding to the Fourier optics [29]. The fundamental of Fourier optics consists in the study of classical optics using Fourier transforms.

The planar array problem can be seen as the same problem as the example of the planar aperture discussed here, where the function describing the excitation fields on the aperture $\mathbf{E}_a$, instead of being a continuous field distribution on the spatial coordinates x and y as in Fig. 2.11, is instead a *discrete* field distribution which is non-zero only in correspondence of the elements of the array. For this reason, it is also possible to define a discrete Fourier transform as in Eq. (2.79) instead of a continuous Fourier transform used in Fourier optics.

Similarly, the planar array problem can be also seen as an application of the Huygens-Fresnel principle. In fact, while in Fourier optics the wave is regarded as a superposition of plane waves which are not related to any identifiable sources but as the natural modes of the propagation medium itself, according to the Huygens-Fresnel principle the wave is regarded as a superposition of expanding spherical waves which radiate outward from actual sources via a Green's function relationship. For the array problem, the physical sources are the antenna elements forming the array.

Finally, the problem can also be seen as an application of the Fraunhofer diffraction theory. In optics, the Fraunhofer diffraction equation is used to model the diffraction of waves when the diffraction pattern is viewed at a long distance from the diffracting object. The equation is

$$U(x, y, z) \propto \iint_{\text{Aperture}} A(x', y') e^{-i \frac{2\pi}{\lambda} (lx' + my')} dx' \, dy'$$

$$\propto \iint_{\text{Aperture}} A(x', y') e^{-ik(lx' + my')} dx' \, dy' \tag{2.87}$$

which in fact appears in to be in the same form as Eq. (2.86). ◪

The versor indicating the position of the observer can be written in cartesian coordinates as (Fig. 2.11)

$$\mathbf{a_r} = \mathbf{a}_x \sin\vartheta \cos\varphi + \mathbf{a}_y \sin\vartheta \sin\varphi + \mathbf{a}_z \cos\vartheta \tag{2.88}$$

For a rectangular planar array, the array factor (2.47) becomes

$$F(\vartheta, \varphi) = \sum_{m=0}^{M} \sum_{n=0}^{N} |C_{mn}| e^{j\alpha_{mn} + j k_0 (m d_x \sin\vartheta \cos\varphi + n d_y \sin\vartheta \sin\varphi)} \tag{2.89}$$

Similarly to the case of a linear array, this equation allows to determine the phases of the excitations of the single elements that are required to generate a beam pattern with a maximum in direction (ϑ_0, φ_0). Those have to be chosen such that Eq. (2.89) is maximum, that is

$$\alpha_{mn} = -k_0 (m d_x \sin\vartheta_0 \cos\varphi_0 + n d_y \sin\vartheta_0 \sin\varphi_0) \tag{2.90}$$

This means that when the elements of the array can be excited independently of one another, it is possible to direct the beam position in any desired direction (ϑ_0, φ_0). This also means it is possible to *scan* the beam on two planes (the xz and the yz plane).

Separable illumination

In many cases, though, scanning in a single plane is sufficient, and a 2-dimensional array can be seen, in a recursive way, as a *linear array* whose elements are, in turn, *linear arrays*. The latter are called *subarrays*. Let us consider an example.

Example 2.4

Let us suppose it is desired to scan only in the xz plane. The planar array can then be considered as a linear array in direction x, whose elements are $M+1$ linear subarrays placed along the y direction. In other words, we have to group the elements along the y direction, as in Fig. 2.12. Doing that, we can reduce the feeding problem of a planar array into two feeding problems of linear arrays. In practice, the feeding problem will be divided into two parts. First, how to feed the elements of a single subarray; then, will be decided how to feed the subarrays.
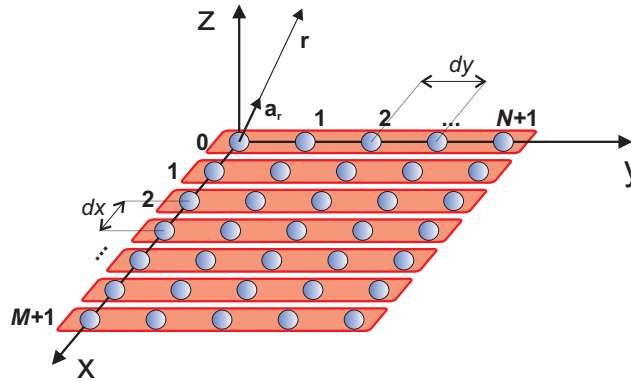
Figure 2.12: Schematic representation of a linear antenna array composed of $N+1 \times M+1$ identical elements with the same orientation. The elements can be grouped in $M+1$ linear subarrays in the y direction. Those subarrays, in turn, can be seen as a $N+1$ linear array in x direction. This allows to separate the feeding problem of a 2-dimensional array into the feeding problem of two linear arrays. When this is possible we talk about *separable illumination*.

To make sure the beam direction is in the desired plane, we need to feed each subarray in such a way that it has its maximum of radiation orthogonal to its axis (which is parallel to y). That is to say, each subarray shall operate as a broadside linear array (see Subsection 2.4.1). To do so, we feed the n-th element of each subarray with the same identical excitations with zero phase

$$A_n = |A_n|e^{j0} = |A_n|, \text{ with } n = 0, ..., N, \forall m. \tag{2.91}$$

This can be immediately motivated by substituting $\psi_0 = \pi/2$ in Eq. (2.52). Then, since each of the $N+1$ elements of a single subarray has the same phase, that sub-

array will have a maximum of radiation in a direction orthogonal to its axis, that is, it will be radiating broadside as desired.

We pass to the second part of the feed problem. Now that we know that each subarray will radiate broadside (on the plane $\phi = 0$), we need to give a phase relation among the subarrays that creates a beam in the specific direction $(\vartheta_0, 0)$. For this scope, we feed the single subarrays with the following complex coefficients

$$B_m = |B_m| e^{j\alpha_m}, \; \alpha_m = -m k_0 d_x \cos \vartheta_0, \text{ with } m = 0, ..., M \tag{2.92}$$

as we would do for any linear array, according to Eq. (2.52), where we have substituted ψ_0 with $\pi/2 - \vartheta_0$ (see Fig. 2.10). In this way we make sure that the linear $M + 1$-elements array in direction x will have a main lobe pointing at ϑ_0. Now, we can join the two solutions and determine the coefficients C_{mn}. They can be obtained by cascading (multiplying) the two solutions A_n and B_m and will be

$$C_{mn} = A_n B_m = |A_n| e^{j0} |B_m| e^{-j m k_0 d_x \sin \vartheta_0} \tag{2.93}$$

with $m = 0, ..., M$ and $n = 0, ..., N$.

In general, for a planar array, we talk about *separable illumination* in all the cases in which it is possible to write the excitations as the product

$$C_{mn} = A_n B_m = |A_n| e^{j\alpha_n} |B_m| e^{j\beta_n} \tag{2.94}$$

from which follows that the array factor can be written as

$$F(\vartheta, \varphi) = \sum_{m=0}^{M} |A_m| e^{j\alpha_m + j k_0 (m d_x \sin \vartheta \cos \varphi)} \cdot \sum_{n=0}^{N} |B_n| e^{j\alpha_n + j k_0 (n d_y \sin \vartheta \sin \varphi)} \tag{2.95}$$

$$= F_x(\vartheta, \varphi) \cdot F_y(\vartheta, \varphi) \tag{2.96}$$

that is, as *the product of two array factors, one of the single subarray, and the other of the linear array whose elements are the subarrays.* Note that the phases of all the elements at the m-th position are the same. This result is very important because it allows to simplify the implementation of the physical network that has to be built to feed the array.

2.4.4   Phase shifters vs true-time-delays: array bandwidth

From the previous sections on linear and planar arrays, we saw that feeding each element of the array with the proper phase excitation, it is possible to achieve the desired direction (ϑ_0, φ_0) for the main lobe of radiation of the array. Given the desired pointing direction, the phase excitations to be provided to each element can be calculated using Eq. (2.52) and Eq. (2.90) for a linear and a rectangular array, respectively.

In practical applications, the *phase excitation distribution* corresponds to the *relative phase shift* of the signals fed to the single antenna elements of the array. In

practice, those desired phase shifts are obtained using a group of tunable 2-ports microwave networks called *phase shifters*. Those are connected between the signal port, that is, the output of the transmitter or the input of the receiver, and each antenna element, as represented in Fig. 2.13. Those devices are capable of generating a variable phase shift of the output signal with respect to the input signal. The network formed by the phase shifters and the amplitude control devices is called *feed network*, *beamforming network*, or *beamformer*.
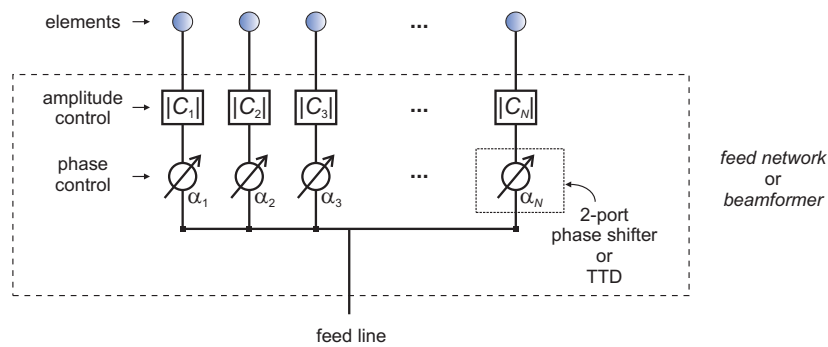
Figure 2.13: Schematic representation of an antenna array feed network

Two types of phase shifters are generally employed:

- *Constant-phase phase shifter* (or *true-phase*): generates a phase shift which is *constant with respect to frequency*. The phase shift is between 0 and 360°.

- *Constant-delay phase shifter* (or *true-time-delay*, TTD): generates a phase shift which is *linear with respect to frequency*. The phase shift at the central operating frequency can be $\gg 360°$.

The consequences of employing either type of device are well visible when analyzing the array performance with respect to frequency, that is, the behaviour of the array when the operating frequency changes with respect to the nominal central frequency for which the array has been designed. This behaviour will determine whether or not the array is capable of processing *wideband* signals. In particular, we are interested in the effects that frequency variations have on the radiation pattern of the array. The *wideband performance* of an array is very important in modern communication systems, due to the need of wider and wider operating bandwidths, required to accommodate the increasing demand of data rate. This fundamental concept can be studied analytically by analyzing how the mathematical formulas for the array factor depend on frequency.

In the study performed so far, we have considered a propagation constant k_0, corresponding to a specific wavelength λ_0 and frequency $f_0 = c_0/\lambda_0$, with c_0 speed of light in the medium, according to the following relation:

$$k_0 = \frac{2\pi}{\lambda_0} = \frac{2\pi f_0}{c_0} \tag{2.97}$$

Let us consider a linear array with $N+1$ elements, equally spaced by d and with a uniform amplitude excitation. The array factor for this type of array was derived in Subsection 2.4.1, Eq. (2.50), and using Eq. (2.97) can be rewritten with an explicit dependence on frequency as

$$F(\psi, f) = \sum_{n=0}^{N} C_n e^{j\alpha_n} e^{jn\frac{2\pi f}{c_0} d \cos\psi} \tag{2.98}$$

To make sure the main beam forms an angle ψ_0 with the axis of the array, the phase progression shall be given by Eq. (2.52). The equation is repeated here for convenience:

$$\alpha_n = -nk_0 d \cos\psi_0 \tag{2.99}$$

The latter equation can also be made explicitly dependent on frequency. This will be done in the following, showing that the expression (2.99) which represents the required phase excitations will take a different form in the case of using phase shifters compared to the case of using true time delays.

Phase shifter

When employing phase shifters, the phase excitation according to Eq. (2.99) of the n-th element of the array becomes

$$\alpha_n = -n\frac{2\pi f_0}{c_0} d \cos\psi_0 \tag{2.100}$$

This equation represents a phase shift which is *constant* with frequency, since α_n does not depend on f. Substituting this equation in the Eq. (2.98) we obtain

$$F(\psi, f) = \sum_{n=0}^{N} C_n e^{jn\frac{2\pi f}{c_0} d \left(\cos\psi - \frac{f_0}{f}\cos\psi_0\right)} \tag{2.101}$$

The pointing angle will be the one that makes the exponent become zero, that is

$$\cos\psi = \frac{f_0}{f}\cos\psi_0 \tag{2.102}$$

$$\psi = \arccos\left[\frac{f_0}{f}\cos\psi_0\right] \tag{2.103}$$

which shows that *the scanning angle changes with frequency*. For $f = f_0$ the maximum points in the desired direction ψ_0, but varying f the beam undergoes a deviation. This deviation is known as *frequency squint*. This phenomenon is shown for an example in Fig. 2.14.

This result has a very important practical implication, that is, a wideband signal cannot generally be processed using a phased array antenna employing phase
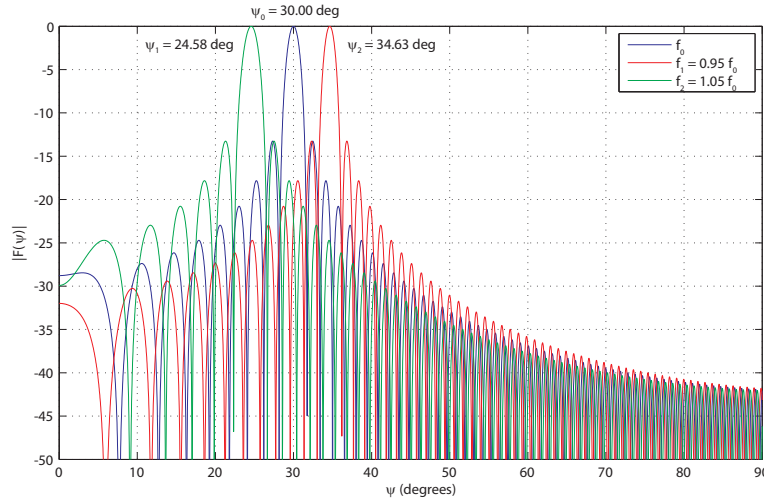
Figure 2.14: Frequency squint effect in a 64-elements linear array. The nominal
pointing direction is $\psi_0 = 30$ degrees. A percentage variation of $\pm 5\%$
creates a visible change in pointing direction.

shifters only. In fact, when operating in transmission, the different frequency components of the signal will be radiated in different directions. In reception, instead, only the portion of the spectrum of the signal originating from direction ψ_0 will be received, correspoding to a *passband filtering* around the central frequency of the array. This problem originates from the use of phase shifters which give a constant phase shift with frequency, which can only be optimal for a single frequency f_0.

Delay line

Let us now analyze what happens when a delay line is used to generate the required phase shift α_n at frequency f_0. The phase shift given by a delay line of length L is (see [25], Sec. 2-4, page 70)

$$\alpha = -\beta L \tag{2.104}$$

where $\beta = 2\pi/\lambda = 2\pi f/v_p$ is the propagation constant of a lossless transmission line used as delay line, λ being the wavelength and v_p the phase velocity in the delay line. We need to decide the length L_n of the n-th delay line such that the pointing direction is ψ_0 as desired. We impose

$$\underbrace{\alpha_n = -nk_0 d\cos\psi_0}_{\text{desired phase excitations}} = -\beta L_n = -\frac{2\pi f}{v_p}L_n \tag{2.105}$$

where $v_p = 1/\sqrt{\mu_0 \epsilon_0 \epsilon_r}$ is the phase velocity in the transmission line (note that the phase velocity depends on the permittivity ϵ_r of the material constituting the line where the guided waves propagate[6]). Thus the line should have a length that satisfies the following equation:

$$-\frac{2\pi f}{v_p} L_n = -n k_0 d \cos \psi_0 = -n \frac{2\pi f}{c_0} d \cos \psi_0 \qquad (2.106)$$

which, substituting $c_0 = 1/\sqrt{\mu_0 \epsilon_0}$, gives that the length should be

$$L_n = n \frac{v_p(f_0)}{c_0} d \cos \psi_0 = \frac{n d \cos \psi_0}{\sqrt{\epsilon_r(f_0)}} \qquad (2.107)$$

where f_0 indicates the central operating frequency. For a non dispersive transmission line, ϵ_r is constant with frequency. This means that v_p is also constant with frequency, and as a consequence all the frequency components of a signal propagate at the same phase velocity. In turn, this means that $\beta = 2\pi f / v_p$ and thus the phase shift βL_n are *linear* with frequency.

In conclusion, from Eqs. (2.105) and (2.107), the phase excitation given by the n-th delay line L_n is

$$
\begin{aligned}
\alpha_n &= -\frac{2\pi f}{v_p} \frac{n d \cos \psi_0}{\sqrt{\epsilon_r(f_0)}} \\
&= -\frac{2\pi f}{\frac{1}{\sqrt{\mu_0 \epsilon_0 \epsilon_r(f)}}} \frac{n d \cos \psi_0}{\sqrt{\epsilon_r(f_0)}} \\
&= -n \frac{2\pi f}{c_0} d \cos \psi_0 \frac{\sqrt{\epsilon_r(f)}}{\sqrt{\epsilon_r(f_0)}} \qquad (2.108)
\end{aligned}
$$

which, as far as the transmission line can be considered *non dispersive* ($\epsilon_r(f) = \epsilon_r(f_0) = \text{const}(f)$), can be rewritten as

$$\alpha_n = -n \frac{2\pi f}{c_0} d \cos \psi_0 \qquad (2.109)$$

Note that this equation is equal to Eq. (2.100) apart from the fact that f appears in place of f_0. For this reason, it represents a phase shift which is *linear* with frequency, and not constant as for Eq. (2.100). This time, by substituting the phase shift term given by Eq. (2.108) in Eq. (2.98) we obtain

---

[6]In case of optical delay lines, instead of the permittivity, it is more common to consider the *refractive index* of the material. This quantity is commonly indicated as n (not to be confused with the array element index n) and is related to the dielectric constant by the following expression

$$n = \sqrt{\epsilon_r \mu_r}$$

where ϵ_r and μ_r respectively indicate the relative permittivity and the relative permeability of the material. For most of the materials employed in the realization of optical transmission lines, μ_r is very close to 1 at optical frequencies. Thus $n \approx \sqrt{\epsilon_r}$.

$$F(\psi, f) = \sum_{n=0}^{N} C_n e^{jn\frac{2\pi f}{c_0} d(\cos\psi - \cos\psi_0)} \tag{2.110}$$

As in the case of phase shifters, the pointing angle is the one that maximizes F. In this case, however, F is always maximum at $\psi = \psi_0$ independently of f. This shows that, differently from the case of using phase shifters, using delay lines the scanning angle *does not change* with frequency.

Dispersive effects

The previous conclusion is valid as long as the assumption of non dispersive delay line, that is, $\sqrt{\epsilon_r(f)} = \mathrm{const}(f)$, holds. When this is not the case, Eq. (2.108) can no longer be simplified as Eq. (2.109), and the array factor becomes

$$F(\psi, f) = \sum_{n=0}^{N} C_n e^{jn\frac{2\pi f}{c_0} d\left(\cos\psi - \frac{\sqrt{\epsilon_r(f)}}{\sqrt{\epsilon_r(f_0)}}\cos\psi_0\right)} \tag{2.111}$$

that has a maximum in the pointing direction

$$\cos\psi = \frac{\sqrt{\epsilon_r(f)}}{\sqrt{\epsilon_r(f_0)}} \cos\psi_0 \tag{2.112}$$

or

$$\psi = \arccos\left[\frac{\sqrt{\epsilon_r(f)}}{\sqrt{\epsilon_r(f_0)}} \cos\psi_0\right] \tag{2.113}$$

which is no longer independent of frequency.

2.4.5 Conclusions

As a conclusion of this subsection, it was shown that the solution of the frequency squint problem requires a device capable of generating a linear phase shift with frequency, or equivalently, a constant delay with frequency. This can be generated by an ideal delay line, or any device offering a linear phase-vs-frequency characteristic. A physical delay line approximates this characteristic sufficiently well over a frequency range that can be sufficient for the desired bandwidth of operation.

It is important to notice that in many applications, only a limited percentage bandwidth[7] is sufficient for the goal. In this case, a solution using a tunable network of phase shifters might be sufficient and it is generally simpler to implement,

---

[7]The *percentage bandwidth* of a passband signal, frequency-limited between f_1 and f_2, can be defined as the absolute bandwidth (which we define as $f_2 - f_1$) divided by the central frequency:

$$B_\% = \frac{f_2 - f_1}{(f_2 + f_1)/2} \tag{2.114}$$

Let us consider, for example, a passband signal with a bandwidth of 1 GHz. If the significative spectral components lie between 1 GHz and 2 GHz, the percentage bandwidth will be $(2-1)/1.5 \approx 66.66\%$. If the same signal is upconverted to the 9-10 GHz bandwidth, the absolute bandwidth will still be 1 GHz, but the percentage bandwith will reduce to $(10-9)/9.5 \approx 10.53\%$.

allowing ease of reconfigurability of the beam pattern of the array. Different architectures of phase shifters have been proposed and largely deployed in operating system. Examples of phase shifter architectures are given for example in [30].

In other cases, however, when the application requires a larger percentage bandwidth, the beam squint that would be produced by using a phase shifter based beamformer does no longer give an acceptable behaviour. In those cases, a true-time-delay approach is required. Different types of transmission lines can be used to create the desired delays, depending on the system requirements in terms of e.g. amount of delay, absolute frequency and operating bandwidth, compactness, weight, bulk and possibility of tuning. Tunable delay lines are in general not easy to achieve as opposed to the tunable phase shifters architectures described before. For this reason, most applications use switched delay lines with digital control that allows to change the length of a delay path in discrete steps, by using multiple delay line subsections with different lengths, dynamically inserting (or removing) them from the signal path using electronic switching circuits. Those switches can be commonly based on varactors or MEMS (micro electro mechanical systems). Provided that the component used for switching is not limiting the operating bandwidth, a delay line with multiple bits can achieve a relatively large delay, with relatively small discrete delay "steps", over the percentage bandwidth for which the transmission line can be considered non-dispersive, that is, having a constant relative permittivity ϵ_r (see Subsubsection 2.4.4). An example of this solution is shown in Fig. 2.15 that shows the schematic representation of a 6-bits switched TTD, with a minimum step of $\lambda_0/4$.
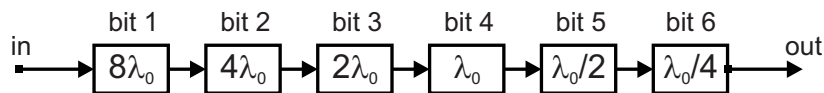
Figure 2.15: Schematic of a 6-bits switched TTD, with a minimum step of $\lambda_0/4$

Recent application scenarios might require bandwidths that can reach the order of several tens of GHz. While recent developments in the construction of ultra-wideband radiating elements with unprecedented bandwiths allow to keep up with the needs, this trend poses a serious challenge towards the design of the beamforming networks, since the percentage bandwith required are often beyond the bandwidth of operation of the transmission lines themselves. In addition to that, together with larger bandwidths, the current trend towards spaceborne application of phased arrays and the simultaneous trend towards micro- and nano- satellites poses a serious limit to the weight and bulk of the phased array systems. For those reasons, researchers started to look at the possibility to use *photonics* solutions and technology to provide a viable alternative to the construction of antenna feed networks, encouraged by the extremely large bandwidth and extremely low loss, reduced weight and bulk, mechanical flexibility and interference immunity of optical fibers when compared to microwave transmission lines. The approach

to realize microwave signal processing based on the use of photonic components poses a full new series of perspectives, possibilities as well as challenges, which will be introduced, analyzed and discussed in the following chapter about *microwave photonics.*

3

Microwave Photonics and Optical Beamforming

This chapter introduces the specific context of the present work, that is, the field of microwave photonics (MWP). We will describe the advantages of using photonics technology and techniques in order to generate, transport and process high-frequency (microwave or RF) electrical signals. The promising advantages of this approach will be introduced, the current challenges for the diffusion of this field will be explained, and the possible solutions proposed by the scientific community to face those challenges will be presented. Among them, special emphasis will be given to modern techniques for optimization of the MWP link and to the unprecedented advantages of using a photonic integrated approach in microwave photonic signal processing, using photonic integrated circuits (PICs) to replace discrete optical components which are bulky, more expensive and less reliable. Special attention will be given to the photonic techniques for microwave signal processing, *that are, microwave photonic filtering and optical beamforming. A review of photonic beamforming techniques will be given.*

3.1   Introduction

Microwave photonics is the field that studies the interaction between microwaves and optical waves. Specifically, it deals with the use of photonic technology for generation, transport, control and processing of microwave signals. Bringing together the advantages of RF engineering and optoelectronics, it aims at exploiting "the best of both worlds" [31], [15] to provide added value in terms of new functionalities, features and improved performance, compared to traditional only-electronic or only-optical solutions.

Microwave photonics has attracted the interest of both the research community and of the commercial sector, and promises to have a bright future. Initially, the research activities in this field were driven by the need of systems with unprecedented performance for defense applications, where the cost constraints were secondary to achieving high performance. Recently, the application field has extended towards civil applications in the fields of e.g. communications (including cellular, wireless and satellite communications), radars, sensors and instrumentations, e.g. for medical imaging; in these fields there has been and there is an increasing demand for speed, bandwidth and dynamic range, together with reduced dimensions, weight and power consumption [17]. In addition to that, reconfigurability, tunability and strong immunity to electromagnetic interference (EMI) are also desirable in these applications.

Digital signal processing (DSP), with its great flexibility and reconfigurability, is one of the techniques that enabled a strong evolution of the instruments used in the above mentioned applications. Nonetheless, DSPs are normally bound to operating frequencies below several gigahertz, primarily due to the limits in the analog-to-digital conversion process [6]. The push towards higher operating frequencies is possible in some cases, but bears drawbacks in terms of complexity of architecture, power consumption, weight and cost. An example is given by advanced digital signal processors for antenna array beamforming on board on communication satellites. Those state-of-the-art computers are capable of generating tens or hundreds of antenna beams simultaneously and with complete reconfigurability, but indeed have a very high power consumption, are bulky and can weight up to multiple hundreds of kilograms, which are very critical, scarce and thus expensive resources within a spaceborne platform [32].

Those limitations in speed, weight and costs of the DSPs rise the need to delegate the high-frequency processing functions to equally-flexible front end analog solutions. An attractive answer to this need can be obtained by exploiting the aforementioned added value obtained by bringing together the inherent broadband, lightweight and high-flexibility characteristics of photonic solutions with the well-established and unprecedeted flexibility of digital electronics processors. In fact, the unique capabilities offered by photonics for processing ultra-wide bandwidth, high-frequency microwave signals make it a promising alternative for wideband microwave signal processing. But how does a *microwave photonic signal processor* look like? An analog MWP processor can be built by implementing a so-called *microwave photonic system* (MWP system), as will be described in the following of this

chapter.

3.2 Microwave photonics fundamentals

3.2.1 MWP links and MWP systems

In the previous section we have discussed the importance of developing high performance analog signal processors, and how this can be done by employing microwave photonic technology to build an *MWP system*. Before describing how an MWP system works, it is necessary to describe the basic operating principle and the performance parameters of the so-called *MWP link*.

An MWP link is the "workhorse" or the "heart" of any MWP system [17]. The most simple schematic of an MWP link (also known as analog optical link, AOL, or analog photonic link, APL) is represented in Fig. 3.1(a). It consists of:

- a modulation device, for electrical-to-optical (E/O) conversion

- an optical fiber (the transmission medium)

- a photodetector (PD), for optical-to-electrical (O/E) conversion

a) MWP *link*

RF input → **E/O** modulator → → **O/E** photodetector → RF output

b) MWP *system*

RF input → **E/O** modulator → **Functionality** - delay - phase shift - filtering - ... → **O/E** photodetector → RF output

electrical domain   *optical domain*   *electrical domain*
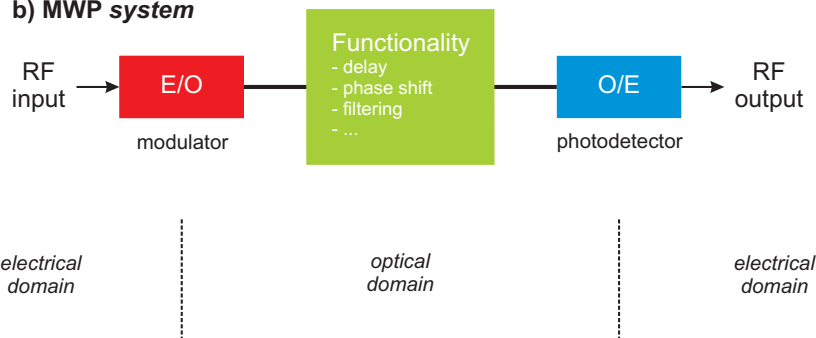
Figure 3.1: High-level schematic of an MWP link (a) and an MWP system (b)

The most diffused upconversion scheme is intensity modulation with direct detection (IM/DD) technique, and more recently phase modulation schemes are also

spreading for high-performance applications, as will be described in the following. Two broad categories of MWP links can be classified based on the modulation device: (*i*) *direct modulation*, where a laser carrier is directly modulated with the RF information signal and operates both as light source as well as modulator; (*ii*) *external modulation*, where a continuous wave (CW) laser is used as light source only, and an external electro-optic modulator operates as modulation device.

In the direct modulation scheme, the information electrical signal is simply superimposed to the DC current used to bias the laser around the desired operating point. The signal current is linearly translated into corresponding variations in the optical power. Those variations are then recovered at the photodetector, where optical power to electrical current conversion occurs [22]. Despite its great simplicity, this scheme suffers heavily from a phenomenon known as chirp, a fluctuation of the instantaneous optical frequency which creates severe line broadening, which can easily be an order of magnitude wider than the RF information signal bandwidth, rendering the system impractical in many microwave photonics applications. The second type of APL offers an higher degree of freedom, thanks to the possibility to separately optimize laser and modulator, and better frequency stability, but also higher costs and complexity since two separate devices are used for light generation and modulation. The choice between the two approaches is usually dictated by the specific application requirements.

From the description given so far, the MWP link looks like a system used for RF signal transport. How is the signal processing functionality added to such a link? An MWP system is based on *adding functionalities* between the two conversions, that is, including a sort of "processing engine" in the optical section of the link, or equivalently, in the optical domain. In fact, as shown in Fig. 3.1(b), in the following of this thesis we will refer to electrical domain as the parts of the signal flow that precedes the modulation device, and the ones that follow the photodetector; instead we will refer to optical domain to indicate the section where the information signal is carried by an optical signal, between the modulation and the detection devices.

The specific advantages offered by processing in the optical domain, as mentioned in Section 3.1, are the following:

1. large bandwidth (tens to hundreds of GHz)

2. constant attenuation over the entire microwave frequency range

3. small size (chips of dimensions of a few cm^2)

4. lightweight (few kg compared to tens to hundreds of kg of a digital beamformer)

5. low-cost and low-loss medium (e.g. optical fiber compared to coaxial cables)

6. low power consumption (in the order of watts; the use of liquid crystals tuning compared to thermal tuning allows an even further reduction to the microwatt power range)

7. immunity to electromagnetic interference (EMI)

8. potential of large tunability (over tens or hundreds of GHz bandwidth, while keeping passbands as narrow as few MHz)

MWP systems promise to add all those advantages to multiple application fields, such as generation, distribution, control and processing of microwave signals. A detailed overview of applications of MWP systems will be given in Section 3.3. However, it is also important to notice that the promised advantages listed above are conditioned to the way the MWP link is realized. In fact, in order to obtain full functionality for the MWP system, it is necessary that the MWP link around which the MWP processor is realized needs to have sufficient performance, in terms of a number of figures of merit that will be detailed in the following.

3.2.2 MWP links: figures of merit

When implementing a MWP link scheme as in Fig. 3.1, it is important to make considerations on how the conversions and the optical signal transport are realized and analyze the impact of this to the MWP performance. In particular, E/O and O/E conversions add loss, noise and distortions to the RF signal to be processed. It is particularly important, in any MWP link or system, to minimize the losses. In fact, as it will be shown in the following, the relation between the RF loss and the optical loss L is, generally[1], *quadratic.*

In order to characterize and be able to compare different MWP links in a rigorous manner, a number of *figures of merit* have been defined and are widely used in literature. Those are:

- link gain (g_{link})

- noise figure (NF)

- input and output intercept points (IIP_n and OIP_n)

- spurious free dynamic range (SFDR)

The figures of merit above indicate, respectively, the effects of losses, noise and nonlinearities of the link. The SFDR represents, in a single figure, the joint effects of noise and nonlinearities. Those are important parameters in any MWP system that will be used in this thesis. Below the definitions and the mathematical expressions of each of those are described in more detail.

---

[1]For example, assuming an intensity-modulated signal with double sideband and full carrier (DSB-FC), the RF loss will be less than quadratic if the applied optical loss is not constant over the whole optical spectrum. This is the case that will apply when, in the following, we will employ true time delay line introducing delay (and, correspondingly, higher attenuation) only over one sideband of a DSB-FC signal. An accurate mathematical modeling of this phenomenon is reported in [33].

3.2.3   Link gain

The *link gain* indicates how the RF power is transferred through the MWP link (or system). Let us consider the general expression of the transfer function of the link (or system)

$$H(\omega) = |H(\omega)| \exp\left(j\phi(\omega)\right) \propto \frac{E_{\text{out}}}{E_{\text{in}}} \tag{3.1}$$

where E_{out} and E_{in} are the output and the input electrical fields, respectively, $|H(\omega)|$ is the magnitude of the transfer function, while $\phi(\omega)$ is the phase of the transfer function. The link gain is the square of the magnitude transfer function $|H(\omega)|^2$

$$g(\omega) = |H(\omega)|^2. \tag{3.2}$$

and indicates the power transfer from the RF input to the RF output as in Fig. 3.1 as a function of frequency[2]. More specifically, the link gain is defined as the ratio between the RF power[3] *delivered* to the load, P_{L}, and the *available* power at the source[4] [34], Fig. 3.2(a):

$$g = \frac{P_{\text{L}}}{P_{\text{S}}} \tag{3.4}$$

Starting from this point, we will assume a link based on external modulation. Our aim is to express the gain in terms of the physical parameters of the MWP link. First of all, let us model the MWP link as a 2-port microwave network, as in Fig. 3.2(b).

In Fig. 3.2 three parts can be identified: the equivalent circuit of the source, the 2-port network equivalent to the MWP link, and the load resistance. We modeled the source as its Thévenin equivalent [35], that is, as a voltage source V_{S} in series to a source resistance R_{S} that represents the resistance seen at the output terminals of the source, and we modeled the load as a resistance[5] R_{L}. Z_{in} and Z_{out} represent, respectively, the input impedance of the MWP link or system (input impedance of the modulation device) and the output impedance of the MWP link or system (output impedance of the photodetector).

---

[2]For ease of notation, in the following we will omit the explicit link gain dependence upon ω.

[3]Since the link gain is defined as the ratio between the input and output RF powers only, we will only consider the AC (i.e. the time varying) terms of the input and output electrical voltages and currents when calculating those powers.

[4]The power delivered to the load is $P_{\text{L}} = I_{\text{L}}^2 R_{\text{L}}$. The available power at the source is defined as the power that is delivered to a complex load *matched* to the source, that is, of impedance equal to the complex conjugate of the input impedance of the source. For a real load impedance R_{L}, the matching condition reduces to $R_{\text{L}} = R_{\text{S}}$, and the available power is

$$P_{\text{S}} = I_{\text{L}}^2 R_{\text{L}} = \left(\frac{V_{\text{S}}}{2}\right)^2 R_{\text{S}} = \frac{1}{4} V_{\text{S}}^2 R_{\text{S}} \tag{3.3}$$

[5]*Real* source and load impedances have been assumed in this discussion as this corresponds to the usual configuration encountered during our experiments as well as in most application scenarios, where generators and test equipment generally exhibit a purely real 50 Ω impedance over the frequency range of interest.
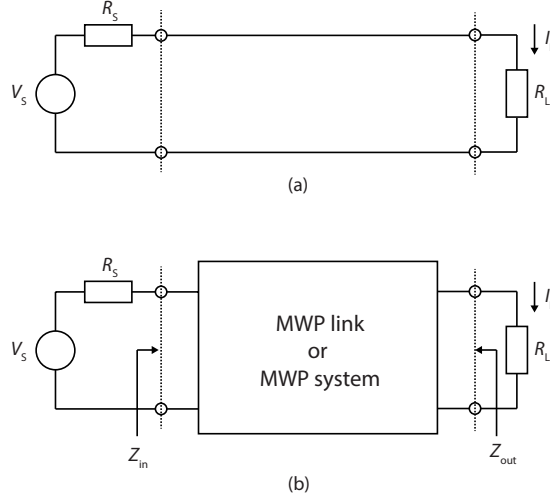
Figure 3.2: MWP link modeled as a microwave network

We start by expressing the available source power. By definition [36] the available source power is the power delivered to the load in condition of maximum power transfer, that is, when the source is terminated on a resistance which is equal to the internal resistance of the source, R_S. Thus, the available source power will be

$$P_S = \frac{\left\langle V_S^2(t) \right\rangle}{4 R_S} \tag{3.5}$$

where V_S is the Thévenin equivalent source voltage[6]. The symbol $\langle \cdot \rangle$ represents the time average of the time varying signal. The power delivered to the load will be

$$P_L = \left\langle I_L^2(t) \right\rangle R_L \tag{3.6}$$

where I_L is the current[7] delivered to the load resistance R_L (Norton equivalent source current). Thus, the general expression of the link gain becomes

$$g = \frac{P_L}{P_S} = \frac{\left\langle I_L^2(t) \right\rangle R_L}{\left\langle V_S^2(t) \right\rangle / 4 R_S} \tag{3.7}$$

We need to find the expression of the load current I_L as a function of the MWP link parameters. In doing that, we will start from the load (right in Fig. 3.2) and proceed towards the source (left). At this point, to be able to proceed, we must make an assumption on the impedance matching scheme employed in connecting

---

[6]When using a scheme based on a directly modulated laser, we would have used the Norton equivalent source current [34].

[7]We use current in expressing the power delivered to the load, because the photodetector is generally modeled as a current source.

the three sections mentioned above, Fig. 3.3(a). In this specific case we choose the so-called "lossy impedance matching" condition [37], that is, we assume the following:

- the input impedance of the modulation device and the output impedance of the photodetector are purely real, that is, $Z_{in} = R_{in}$ and $Z_{out} = R_{out}$ (Fig. 3.3(b))

- the condition of maximum power transfer [34] is satisfied by adding suitable input and output matching networks (IMN and OMN, respectively) at the MWP link input and output (Fig. 3.3(c)). In practice, we add matching resistors in such a way that $R_{in} = R_S$ and $R_{out} = R_L$ (Fig. 3.4).
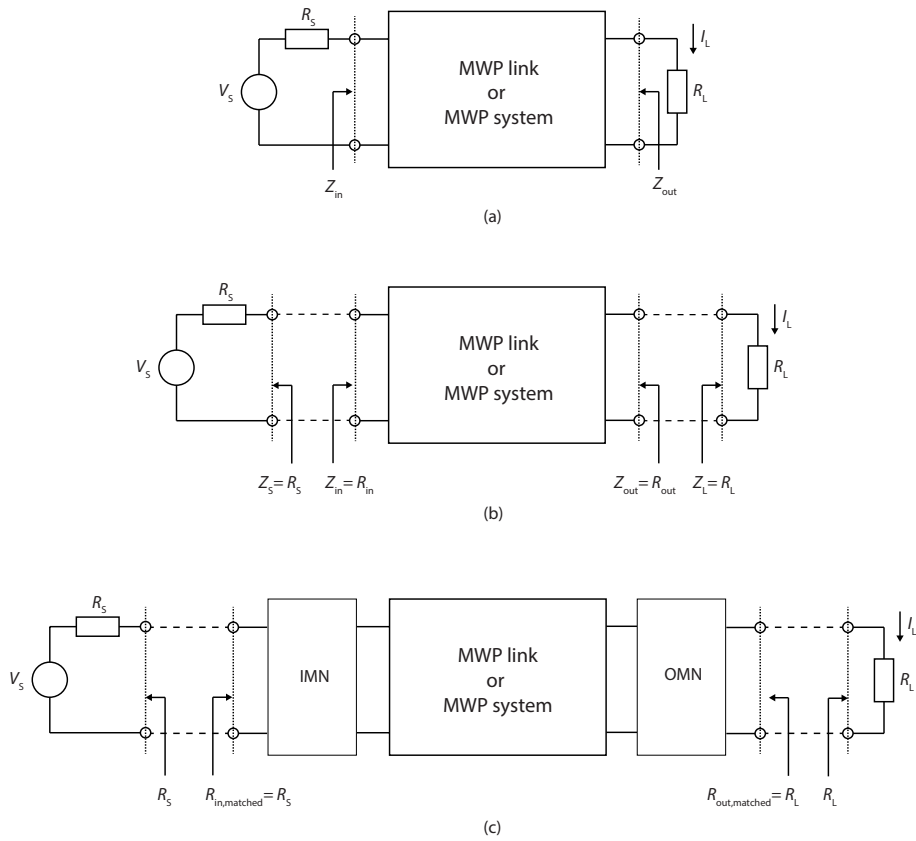
Figure 3.3: Lossy impedance matching condition in an MWP link modeled as a microwave network

The current delivered to the load I_L is closely related to the received optical power at the photodetector, P_{det}. The received optical power is converted to the detected photocurrent I_{det} (Fig. 3.4(c)), according to the relation
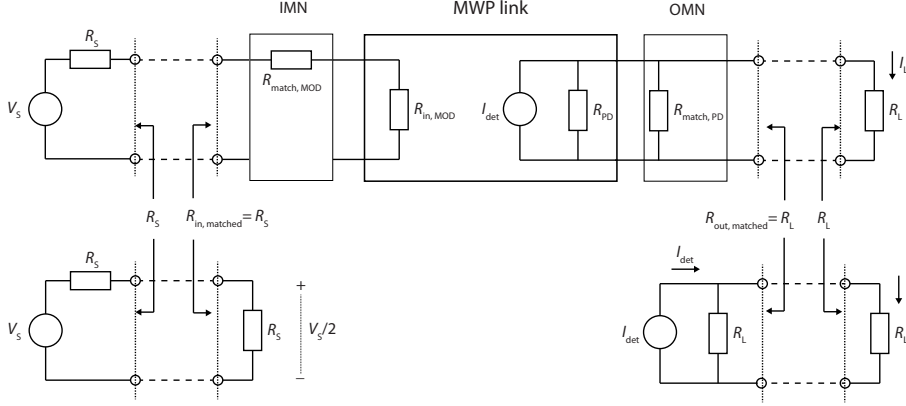
Figure 3.4: Lossy impedance matching condition in an MWP link modeled as a microwave network

$$I_{\text{det}}(t) = r_{\text{PD}} P_{\text{det}}(t) \tag{3.8}$$

where r_{PD} is the photodetector responsivity in A/W. The received optical power at the detector can be split into the constant average optical power P_{av} and the modulated optical power P_{mod} as

$$P_{\text{det}}(t) = P_{\text{av}} + P_{\text{mod}}(t). \tag{3.9}$$

Similarly, the photocurrent can be divided into a constant average photocurrent I_{av} and a modulated photocurrent I_{mod} as

$$I_{\text{det}}(t) = I_{\text{av}} + I_{\text{mod}}(t). \tag{3.10}$$

As shown in Fig. 3.4, in order to match for maximum power transfer, a matching resistor $R_{\text{match,PD}}$ is inserted at the output of the PD in order to make the equivalent Norton circuit of the PD to have an internal resistance equal to the load resistance R_{L}. As discussed previously, only the AC part of the photocurrent $I_{\text{mod}}(t)$ will contribute to the link gain. In this condition, the AC current delivered to the load is half of the modulated photocurrent:

$$I_{\text{L}}(t) = \frac{1}{2} r_{\text{PD}} P_{\text{mod}}(t) \tag{3.11}$$

where P_{mod} is the modulated optical power.

Now, using the definition in Eq. (3.7) and the expression of the load current from Eq. (3.11) above, we can calculate the link gain of the MWP link. The modulated optical power depends on the type of modulation scheme that is used. As anticipated before, it can already be shown that the relation between the optical power and the RF power is quadratic. In fact, starting from Eq. (3.11):

$$P_L(t) = I_L^2 R_L = \left(\frac{1}{2} r_{PD} P_{mod}(t)\right)^2 R_L = \frac{1}{4} r_{PD}^2 R_L P_{mod}^2(t). \tag{3.12}$$

In particular, direct modulation or external modulation will have different expressions, as shown in the following.

Direct modulation

In a directly modulated MWP link a laser is used as both the optical carrier source and the modulation device. An intensity-modulated (IM) optical signal is obtained by modulating the injection current of the laser diode (LD) around a suitably chosen bias point. The modulated optical power impinging on the photodetector (PD) will be converted back to electrical domain according to Eq. (3.11). The electrical to optical and the optical-to-electrical conversions are schematically represented in Fig. 3.5
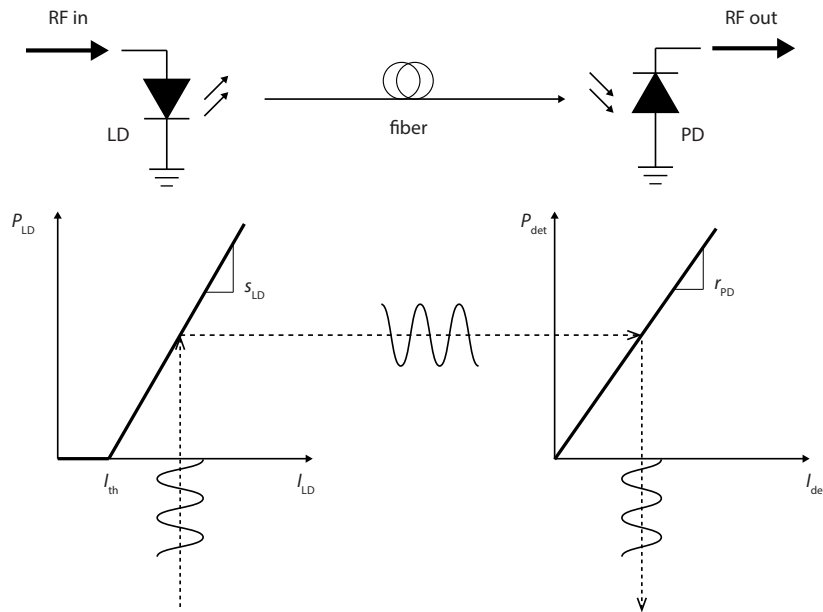
Figure 3.5: Schematic representation of a directly modulated link (DML). LD: laser diode; PD: photodetector; s_{LD}: laser slope efficiency (W/A); r_{PD}: photodetector responsivity (A/W).

It can be shown [22] that, for a direct modulation link, the link gain will assume the expression

$$g_{DML} = \frac{1}{4}\left(\frac{r_{PD} s_{LD}}{L}\right)^2 \tag{3.13}$$

where s_{LD} is the laser slope efficiency expressed in W/A and $L \geq 1$ is the optical loss of the APL.

Eq. 3.13 shows that the link gain of a DML link depends only on two device parameters (laser slope efficiency, s_{LD}, and photodetector responsivity, r_{PD}) and on only one system parameter (the optical loss in the APL, L). Two very important conclusions can be drawn from this results. First, minimizing the value of the optical loss is of primary importance, since the gain is proportional to $(1/L^2)$, meaning for each 1 dB optical loss will correspond to 2 dB RF loss. Second, the link gain does not depend on the LD average optical power. As a direct consequence, for a DML, once the APL components have been selected, the only design parameter that can be used to alter the link gain is the optical loss L in the link.

External modulation

In an MWP link based on external modulation, the laser is operated in continuous wave (CW) mode while an external device is employed to provide light modulation, as in Fig. 3.6(a). For external modulation, the link gain is a function of more system parameters, thus offering a larger degree of freedom to the designer in order to optimize the link performance when compared to the direct modulation case. The expression of the modulated optical power and of the link gain have been derived in [22] for the common case of Mach-Zehnder modulator (MZM) and is reported here for completeness. In fact, IM/DD links based on external modulation are at the basis of the optical beamforming signal processing approach employed in this thesis.

As seen from Eq. (3.11), we need the expression of the modulated optical power in order to obtain the current delivered to the load; in turn, the latter can be inserted in the definition Eq. (3.7) to obtain the expression of the link gain.

The detected optical power of an MWP link using a MZM can be written as

$$P_{\mathrm{det,MZM}}(t) = \frac{P_{\mathrm{i}}}{2L} \left(1 - \cos\left[\pi \left(\frac{V_{\mathrm{B}}}{V_{\pi,\mathrm{DC}}} + \frac{V_{\mathrm{RF}}(t)}{V_{\pi,\mathrm{RF}}} \right) \right] \right) \tag{3.14}$$

where P_{i} is the input optical power to the modulator, L is the optical loss, V_{B} is the modulator bias voltage, V_{RF} is the modulating RF signal and $V_{\pi,\mathrm{DC}}$ and $V_{\pi,\mathrm{RF}}$ are the DC and the RF half-wave voltages, respectively. Note that L in the above equation comprises two terms, the modulator insertion loss, L_{mod} and an excess loss, L_{ex}, such that $L = L_{\mathrm{mod}} L_{\mathrm{ex}}$. An example of this excess loss is the connector losses in the APL.

In small signal approximation regime $V_{\mathrm{RF}} \ll V_{\pi,\mathrm{RF}}$, the argument of the cosine can be expanded in a Taylor series as the sum of a DC term, $P_{\mathrm{av,MZM}}$, plus a term which have a linear, quadratic and cubic dependence on the modulating signal $V_{\mathrm{RF}}(t)$; respectively, $P_{\mathrm{mod,MZM}}$, $P_{\mathrm{NL2,MZM}}$ and $P_{\mathrm{NL3,MZM}}$. The DC term will contribute to the noise, while the quadratic and cubic terms contribute to the nonlinear distortion.
The DC term has the following expression

$$P_{\mathrm{av,MZM}} = \frac{P_{\mathrm{i}}}{2L} \left(1 - \cos\phi_{\mathrm{B}} \right) \tag{3.15}$$

where ϕ_B is the bias angle, defined as

$$\phi_B \triangleq \frac{\pi V_B}{V_{\pi,DC}}. \tag{3.16}$$

In Fig. 3.6(b) the DC term $P_{av,MZM}$ normalized to the input power P_i is represented. This is known as the transfer function of an MZM, and allows to graphically determine the bias point, thus the operating region, of the MZM.

(a)

(b)
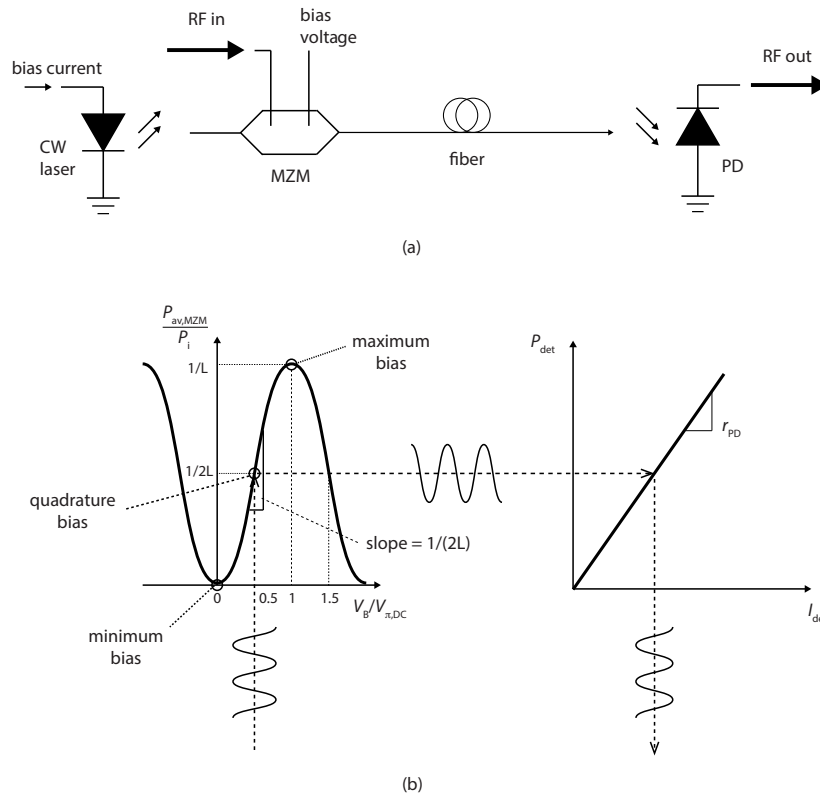
Figure 3.6: Schematic of an externally modulated MWP link (a); transfer function of Mach-Zehnder modulator (in quadrature bias) and photodetector (b)

For the link gain calculation we only consider the contribution of the linear component, whose expression is

$$P_{mod,MZM}(t) = \frac{P_i}{2L_{mod}} \frac{\pi V_{RF}(t)}{V_{\pi,RF}} \sin \phi_B \tag{3.17}$$

where L_{mod} is the insertion loss of the modulator. The term $P_{mod,MZM}(t)$ represents the linear relation between the input RF signal (modulating input voltage) V_{RF} and the optical power variation $P_{mod,MZM}$.

Again, according to the initial hypothesis of operation at maximum power transfer (or lossy impedance matching) condition, the V_{RF} in Eq. (3.17) is

$$V_{\text{RF}}(t) = \frac{1}{2} V_{\text{S}}(t).$$ (3.18)

Now, inserting Eq. (3.18) in Eq. (3.17), the latter in Eq. (3.11) and, in turn, the result in the general gain expression Eq. (3.7), we obtain the expression of the link gain in a MZM external modulated MWP link:

$$g_{\text{MZM}} = \left(\frac{\pi r_{\text{PD}} R_{\text{L}} P_0 \sin\phi_{\text{b}}}{4 L V_{\pi,\text{RF}}} \right)^2.$$ (3.19)

Based on this expression, a number of important considerations can be done. First, it is worth noting that the link gain scales quadratically with the input optical power P_0. This is a very important result since, differently from the directly modulated links, the link gain can be increased by modifying this system parameter and in particular can be increased by simply using higher optical power. This technique has been employed to effectively demonstrate MWP links with a positive link gain instead of loss [38].

Second, it is possible to increase the link gain by choosing a modulator with a lower half-wave voltage. This can be regarded as the sensitivity of the modulator and is a device parameter, that is, its optimization is addressed at component design level and cannot be influenced further by the link system designer after the specific MZM component has been chosen. Typical values for this parameter in commercial MZMs is around 3.5 to 4.5 V. In [39], a $V_{\pi,\text{RF}}$ as low as 1.08 V has been demonstrated at 6 GHz.

Third, the link gain can be influenced by the system designer by setting a different bias point of the modulator. In fact, choosing $V_{\text{B}} = \frac{1}{2}V_{\pi,\text{DC}}$ makes $\phi_{\text{b}} = \pi/2$, which maximizes the sine term at the numerator of Eq. (3.19). This condition is known as quadrature biasing and, in addition to maximizing the gain with respect to V_{B}, it also compresses all even-order distortion terms; for this reason this is the most common way of operation in an MWP link based on MZM.

Fourth, similarly to the directly-modulated link, a possible way to increase the link gain is to minimize the losses of the link. Compared to a directly-modulated link, external modulation requires an additional component to be added between the light source and the detector, thus adding extra losses due to the insertion loss of the MZM. This is due to (*i*) connector losses, (*ii*) fiber to chip coupling losses, and (*iii*) quadrature biasing which adds 3 dB of insertion loss in addition to previous loss terms. In average, those three terms of loss add up to a 5 to 7 dB optical loss. Since 1 dB optical loss corresponds to 2 dB RF loss, the insertion losses of the link can seriously deteriorate the MWP link gain, giving between 10 to 14 dB of RF losses. However, using external modulation allows to independently maximize the optical power of the laser.

3.2.4   Noise

The second figure of merit of an MWP link or system is the *noise figure*, which measures the noise in the MWP system. In fact, the E/O and the O/E conversions also add noise to the system. The three main sources are thermal noise, shot noise and relative intensity noise (RIN). When optical amplifiers are employed in the optical signal chain, also the amplified spontaneous emission (ASE) noise will be added and, in fact, will usually dominate over the other noise sources. This is often the case in experiments that aim to demonstrate MWP systems at proof-of-principle level; those setups often employ multiple discrete optical components, which add losses that need to be compensated in order to have sufficient link gain for the demonstration. Erbium-doped fiber amplifier (EDFA) is an example of amplifier commonly used for the purpose.

Total noise power

Similarly to the discussion done for the photocurrent, where the PD is represented by an equivalent controlled current source $I_{\text{det}}(t)$, each noise source can be represented as an individual current source, as shown in Fig. 3.7.
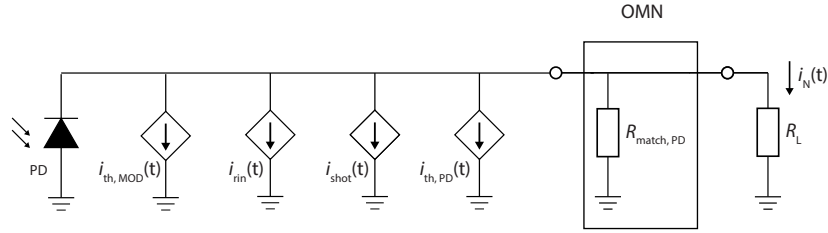
Figure 3.7: Circuit representation of noise sources as current sources. OMN: output matching network

If we define $i_{\text{th,MOD}}$ as the equivalent current source corresponding to the thermal noise generated at the modulator, i_{shot} the shot noise current, i_{rin} the RIN noise current and $i_{\text{th,PD}}$ the thermal noise current produced at the detector, and since we have assumed lossy impedance matching ($R_{\text{match,PD}} = R_{\text{L}}$), the total noise current flowing through the load can be written as

$$i_{\text{N}}(t) = \frac{1}{2} \left(i_{\text{th,MOD}}(t) + i_{\text{shot}}(t) + i_{\text{rin}}(t) + i_{\text{th,PD}}(t) \right) \tag{3.20}$$

and the total noise power is the electrical power dissipation created by this current on the load resistance R_{L}:

$$p_{\text{th}} = \left\langle i_{\text{N}}^2(t) \right\rangle R_{\text{L}}. \tag{3.21}$$

It can be shown [22] that the variance of the individual current terms are

$$\left\langle i_{\text{th}}^2(t) \right\rangle = \frac{4kTB}{R} \tag{3.22}$$

$$\left\langle i_{\text{shot}}^2(t) \right\rangle = 2qI_{\text{av}}B \tag{3.23}$$

$$\left\langle i_{\text{rin}}^2(t) \right\rangle = \text{rin}I_{\text{av}}^2 B \tag{3.24}$$

The term "rin" indicates the laser relative intensity noise, defined as the power spectral density of the relative power fluctuation of the laser $\Delta p / P_{\text{av}}$ [40]. Note that the variance of the thermal noise current $\left\langle i_{\text{th}}^2(t) \right\rangle$ generated at the modulator and the one generated at the photodetector have the same expression, where we assumed that the internal resistance of the modulator and the photodetector are both equal to R. The difference is that the current at the modulator is generated at the input of the link, thus experiences the MWP link gain g before being evaluated at the link output, while the noise current at the detector is generated directly at the link output. Since the link gain is generally negative (in dB scale), the thermal noise at the PD generally gives a much higher contribution to the total noise. The total noise power dissipated on the load resistance R_{L} can then be written as

$$p_{\text{N}} = \left(1 + g\right)p_{\text{th}} + \frac{1}{4}p_{\text{shot}} + \frac{1}{4}p_{\text{rin}} \tag{3.25}$$

where p_{th}, p_{shot} and p_{rin} respectively represent the thermal noise power[8], the shot noise power and the relative intensity noise power, whose expressions are:

$$p_{\text{th}} = \left\langle i_{\text{th}}^2(t) \right\rangle R_{\text{L}} \qquad = kTB \tag{3.26}$$

$$p_{\text{shot}} = 2q\, I_{\text{av}}\, B\, R_{\text{L}} \qquad = 2q\, r_{\text{PD}} P_{\text{av}}\, B\, R_{\text{L}} \tag{3.27}$$

$$p_{\text{rin}} = 10^{\frac{\text{RIN}}{10}}\, I_{\text{av}}{}^2 B R_{\text{L}} = 10^{\frac{\text{RIN}}{10}}\, r_{\text{PD}}^2 P_{\text{av}}{}^2\, B\, R_{\text{L}}. \tag{3.28}$$

where I_{av} is the average noise current term, which is obtained when the average optical power reaches the PD. For an externally-modulated MWP link, the average optical power is expressed by Eq. (3.15). Using the definition of photocurrent r_{PD} given by Eq. (3.8), the average photocurrent is given by

$$I_{\text{av,MZM}} = \frac{r_{\text{PD}}P_{\text{i}}}{2L_{\text{MZ}}}\left(1 - \cos\phi_{\text{B}}\right). \tag{3.29}$$

In Eq. (3.25) note that the term $(1 + g)p_{\text{th}}$ includes both the contribution of the thermal noise from the modulation device[9] $(gkTB)$ and the one of the the PD matching resistor (kTB). Once the expression of the noise power at the output of the link is known, it is possible to calculate the noise figure, as shown in the following.

---

[8]Note that the thermal noise at the output has two terms, one part originating from the modulator, $g\,p_{\text{th}}$, and a part originating from the photodetector, p_{th}.

[9]The gain term g appears since the thermal noise power originated from the modulator (kTB) is generated at the input of the MWP link, but is evaluated at the output after it has experienced the MWP system gain.

Noise figure

Similarly to what is commonly done in the field of microwave engineering, useful figures of merit representing the noise performance of an MWP link are the noise factor (F) or the noise figure (NF). The *noise factor* of any 2-port microwave network is defined as the ratio between the total available output noise power spectral density and the portion of that noise that is produced by the actual noise source connected to the input of the device, at the standard temperature of 290 K [37]. In these terms, the noise factor is an rigorous way to indicate which fraction of the output noise has been originated by the actual 2-port network.

The *noise figure* is simply defined as the noise factor expressed in decibel scale, that is, NF $= 10 \log_{10}(F)$. In the specific case in which the *input* noise is simply considered to be the thermal noise power from a matched resistor, that is, $n_{in} = kTB$, the noise figure can be more simply defined as the degradation of the signal-to-noise ratio through the system:

$$\text{NF} = 10 \log_{10} \left(\frac{s_{in}/n_{in}}{s_{out}/n_{out}} \right). \tag{3.30}$$

The relation between the signal powers is given by the definition of link gain, thus we can write $s_{out} = g \, s_{in}$. Finally, the output noise power is the total link noise reported before in Eq. (3.25), thus $n_{out} = p_N$. The expression of the noise figure becomes

$$\text{NF} = 10 \log_{10} \left(\frac{p_N}{gkTB} \right). \tag{3.31}$$

Now that we know the expression of the noise figure, we can think about ways to minimize it.

Note that the noise figure is independent of the noise equivalent bandwidth B of the receiver; in fact, p_N at the numerator, given by Eq. (3.25), depends linearly on B, exactly like the thermal noise in the denominator.

The total noise power appears at the numerator in the noise figure Eq. (3.31) and, from Eq. (3.25), we see that the average noise current I_{av} given by Eq. (3.29) appears in both the shot noise and the RIN terms. Similarly, we see that the link gain g appears at the denominator. Thus, increasing the link gain and/or reducing the noise current will then directly reduce the noise figure. The link gain can be increased by choosing an MZM with a low $V_{\pi,\text{RF}}$, as visible in Eq. (3.19).

In addition, for the sake of minimizing the NF, it is also interesting to observe the different dependence of the link gain g in Eq. (3.19) and of the average photocurrent I_{av} in Eq. (3.10) on the MZM bias point. In fact, we can observe that g decreases with ϕ_B as $\sin^2 \phi_B$, while I_{av} decreases as $1 - \cos \phi_B$. It follows that low biasing the MZM away from quadrature ($\phi_B = \pi/2$) and towards the minimum transmission point ($\phi_B = 0$) will reduce the noise figure, because the RIN and shot noise power terms p_{rin} and p_{shot} (which depend linearly and quadratically upon I_{av}), will reduce faster than the link gain when reducing the MZM bias.

In conclusion, the noise figure of a MWP link is considered to be one of the key elements to evaluate the actual usefulness of the link. In recent years, several

research groups managed to realize MWP links with sub-10 dB noise figure, employing a low $V_{\pi,\text{RF}}$ modulator with low biasing, together with a high-power laser source and a custom-made photodetector with a very high power handling capability [41, 42]. A recent review of MWP links achieving $g > 0$ and NF < 20 dB are reported in [43].

3.2.5 Nonlinear distortions

The transfer functions of the directly modulated laser or of the external electro-optical modulator (EOM) used in the previous MWP link examples show a non-linear characteristic. For this reason, the E/O conversion will introduce non-linear distortions to the output RF signal. In addition to that, the photodetector also shows non linearities, although they are usually much smaller than those introduced by the modulation devices [37] and can thus be neglected. An effective way to evaluate those non-linearity effects are the so-called single-tone and the two-tone tests. In particular, the two-tone test is the most common way to characterize non-linearity of any microwave network, not only of MWP systems.

Two-tone test

Let us consider two perfectly sinusoidal tones at closely spaced frequencies f_1 and f_2, which are inserted at the input of the link. Due to the mentioned non-linearities of the modulation device, the input-output characteristic can be expanded as a Taylor series around the operating (bias) point. This infinite series can be truncated (i.e. approximated) by a polynomial with a finite number of terms. The first term shows a linear dependence from the input, the second a quadratic one, and so on, until the k-th term having a k-th power relation to the input. In this condition, the two perfectly sinusoidal tones at the input of the non-linear transfer function, will generate terms at k times their frequency, called *harmonic distortions*, plus additional frequency components called *intermodulation distortions* (IMDs). The k-th component generates harmonics and intermodulation products of the corresponding order. The second-order intermodulation (IMD2) products are due to the quadratic non-linearity in the link, and produce two additional frequency components at $(f_1 \pm f_2)$. The third-order intermodulation (IMD3) products are due to the cubic non-linearity of the link, and produce four additional frequency components at $(2f_1 \pm f_2)$ and $(2f_2 \pm f_1)$.

Those frequency components are graphically represented in Fig. 3.8. Based on this spectrum it is possible to note some important facts. The frequency components that fall closest to the fundamental frequencies f_1 and f_2 are the third-order intermodulation products (IMD3) at $2f_1 - f_2$ and $2f_2 - f_1$. In general, it is practically very difficult, if not impossible, to filter out those terms. In fact, as soon as the fundamental frequency components start to broaden, the IMD3 terms – in turn – broaden with at double the speed, thus tend to overlap with the fundamental tones and can no longer be filtered out. For this reason, the IMD3 represents the main limitation in terms of non linearity for an MWP link. Differently, the harmonic distortion terms (HD2 and HD3) at $2f_1$, $2f_2$, $3f_1$ and $3f_2$, the second order intermod-
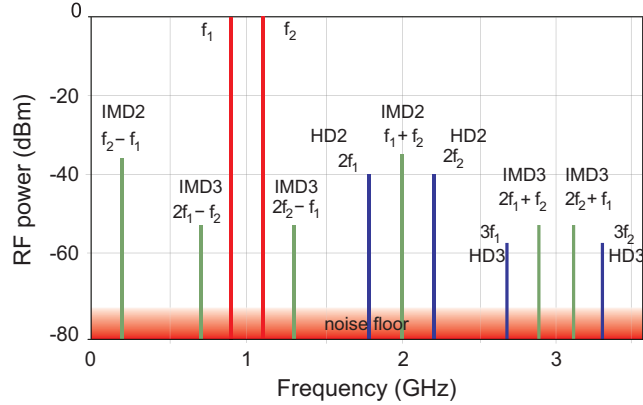
Figure 3.8: A typical 2-tone test RF output spectrum

ulation distortion terms (IMD2) at $f_1 + f_2$ and $f_2 - f_1$ as well as the the third-order intermodulation products (IMD3) at $2f_1 + f_2$ and $2f_2 + f_1$ are relatively distant from the fundamental components, and can usually be filtered out.

Suboctave and multioctave bandwidths

So far, in our analysis of nonlinear distortions, we have considered the situation for narrowband, pure sinusoidal input signals. It it worth noting that, as soon as the bandwidth increases, the situation changes. As soon as the frequency lines f_1 and f_2 start to broaden, the IMD and the HD spectral components in Fig. 3.8 will also broaden in frequency. At a certain point, the IMD3 terms at $2f_1 - f_2$ and $2f_2 - f_1$ will overlap with the fundamentals around f_1 and f_2. If we keep increasing the signal bandwidth, also the HD2 as well as the IMD2 will start to overlap with the fundamental, creating distortion that also cannot be filtered out. Precisely, the IMD2 terms will start interfering with the fundamental as soon as the information signal bandwidth reaches one octave, meaning that the highest frequency component f_{high} is more than twice of the lowest frequency component f_{low}. Summarizing, we can conclude:

- for a narrowband signal (sub-octave bandwidth, $f_{\text{high}} < 2f_{\text{low}}$) the non-linear distortion is dominated by the IMD3 terms;

- for a wideband signal (multi-octave bandwidth, $f_{\text{high}} \geq 2f_{\text{low}}$) the non-linear distortion is dominated by the IMD2 terms.

From the previous discussion about non linearities, we have seen that, independently of the signal bandwidth, there is always a number of nonlinear distortion components that can potentially interfere with the information signal. For a high-performance MWP link (or the MWP system built on its basis) it is thus important to investigate the possibilities of reducing the amount of distortion. For

example, as will be shown in the following, not all the spurious frequency components in Fig. 3.8 increase at the same speed when increasing the signal power. This can be used at the advantage of a virtually distortion-free link provided that the signal power keeps below a certain maximum limit.

Intercept points

To effectively analyze how the power of each component of the output spectrum varies with respect to the input signal power, let us represent three curves, representing the output signal power, the IMD2 power and the IMD3 power versus the fundamental signal power at the input. Those three curves are displayed in Fig. 3.9 in dBm power scales, that are, logarithmic scales. The output signal power is a line with slope equal to 1 and an offset equal to the link gain, g. Each IMD2 term will also be a linear function, but with a slope of 2 due to the quadratic relation with the input signal power. Correspondingly, each IMD3 term will have a slope of 3 due to the cubic relation with the input signal power.

If we represent on the same graph the noise power defined on a 1 Hz bandwidth, there are two points in which the IMD2 and the IMD3 lines intercept the noise power level. For input powers below those points (at the left of those points in the graph) the IMD2 and IMD3 products will be below the noise level, thus would not visible in the output spectrum shown in Fig. 3.8. On the opposite side, for input powers that are sufficiently high, the three lines (extrapolated fundamental output power, IMD2 power and IMD3 power) intercept in two points, called *intercept points*. For the intercept point between the fundamental and the IMD2, the input and output powers corresponding to this point are called, respectively, 2$^{\text{nd}}$ order input intercept point (IIP2) and output intercept point (OIP2); similarly, for the IMD3, they are called 3$^{\text{rd}}$ order input (IIP3) and output (OIP3) intercept points. The relation between those points is given through the link gain as

$$\text{OIPn (dBm)} = \text{IIPn (dBm)} + \text{G (dB)} \tag{3.32}$$

3.2.6 Spurious-free dynamic range

Based on the discussion on noise and non-linear distortions, and conveniently making use of Fig. 3.9, it is possible to define a figure of merit that accounts for the effects of both noise and distortions, that is, the spurious free dynamic range (SFDR) of order n. The SFDR_n can be defined both in terms of input and output powers of the MWP link, respectively, as

- the ratio between the input power for which the intermodulation distortion power of order n (IMDn) is equal to the noise power (measured over 1 Hz bandwidth), and the input power for which the output signal power equals the noise power.

- the maximum SNR at the MWP link output that can be achieved, while keeping the IMDn power below the noise power.
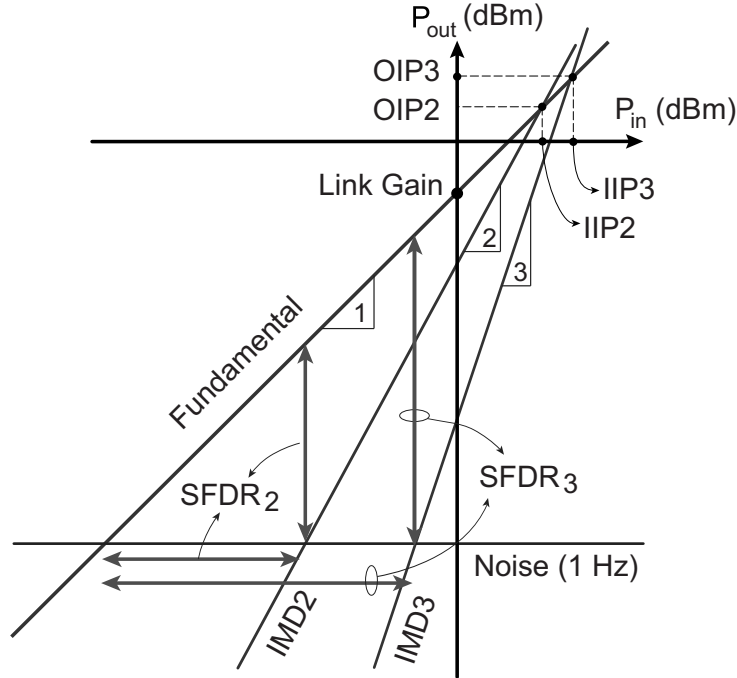
Figure 3.9: SFDR definition

The SFDR_n can be expressed in relation to the other figures of merit of MWP links, using graphical considerations [22] as shown in the following.

Let us consider Fig. 3.10. The two diagonal lines indicate the power of the fundamental (with slope 1:1) and the power of the IMDn (with slope n:1) at the output. In the gray right triangle in figure, the vertical leg represents OIP$n - P_{\text{N}}$. Being the slope of the IMDn line equal to n, the horizontal (shorter) leg of the right triangle will be equal to $\frac{1}{n}$ (OIP$n - P_{\text{N}}$). It follows that

$$\text{SFDR}_n = (\text{OIP}n - P_{\text{N}}) - \frac{1}{n}\,(\text{OIP}n - P_{\text{N}}) \tag{3.33}$$

$$= \frac{n-1}{n}\,(\text{OIP}n - P_{\text{N}}) \tag{3.34}$$

and since the noise power (in dB scale) can be rewritten as [22]

$$P_{\text{N}} = G + \text{NF} - 174 \tag{3.35}$$

it follows
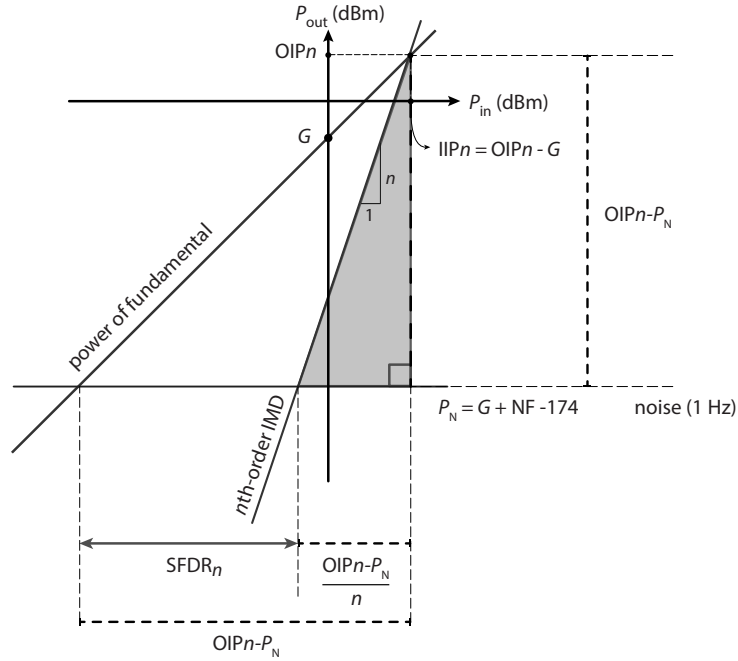
Figure 3.10: Relation between SFDR and figures of merit: graphical representation

$$\text{SFDR}_n = \frac{n-1}{n}(\text{OIP}n - \text{NF} - G + 174) \quad \left[\text{dB} \cdot \text{Hz}^{\left(\frac{n-1}{n}\right)}\right] \tag{3.36}$$

$$= \frac{n-1}{n}(\text{IIP}n - \text{NF} + 174) \quad \left[\text{dB} \cdot \text{Hz}^{\left(\frac{n-1}{n}\right)}\right] \tag{3.37}$$

where Eq. (3.32) has also been used.

The SFDR$_n$ is generally expressed in dB, and the bandwidth over which the noise is measured must be specified. More often however, for the sake of uniformity and ease of comparison, the SFDR$_n$ is expressed in dB $\cdot$ Hz$^{(\frac{n-1}{n})}$. This means that the specified value indicates the SFDR$_n$ over the bandwidth of 1 Hz, and if we want to calculate it over the band B, we must scale it down according to the relation [22]

$$\text{SFDR}_{n,B} = \text{SFDR}_{n,1\text{ Hz}} - \left(\frac{n-1}{n}\right)10\log_{10}(B). \tag{3.38}$$

The optimization of the SFDR of an MWP link over a large bandwidth has been the main objective of research in the field. A number of possible solutions have been proposed in literature and will be described in the following.

3.3   Applications of microwave photonics

3.3.1   Microwave signal distribution

As discussed in the previous chapter, the basis of any MWP system is an MWP link. APLs are not only at the basis of the operation of any MWP system, but have also been the first applications of the MWP technique, with the specific scope of replacing coaxial cables in microwave signal transport. In fact, propagation losses in coaxial cables scale up very fast with signal frequency: even the highest quality cables have losses that, already at 6 GHz, can be as high as 190 dB/km [44]. Instead, optical fibers offer extremely low propagation losses, around 0.2 dB/km, in addition to low size, low weight, improved mechanical flexibility, EMI immunity and flat attenuation of the whole spectrum of interest. Those advantages have been the driving force for a number of microwave photonics applications, first of all signal distribution. Example of applications are:

- Radio-over-fiber for wireless systems. The MWP link is used to connect the complex signal processing section of the network to multiple antennas, moving the complex signal processing capabilities from the numerous base stations towards only one or few centralized nodes. This allows a strong reduction of overall complexity and cost, and operating frequencies that extend well into the millimiter-wave range [45].

- Antenna remoting for military and aerospace applications. Size and weight are very important factors for airborne and spaceborne applications. Optical fibers are nowadays commonly used on those platforms to replace the heavier and stiffer coaxial cables, not only for their huge bandwidth (which allows wavelength division multiplexing (WDM) and thus a further reduction of the number of physical connections needed), but also their mechanical properties. The smaller size and higher flexibility of fibers compared to electrical cables facilitates installation and deployment and sometimes fiber represents the only viable solution when in-flight deployment of mechanical structures is required [46]. In some applications where the antennas may operate in electromagnetically hostile environments, the use of fiber optics allows to electrically separate the antennas from the sensitive active electronics [47]. In addition to that, optical fibers are generally much cheaper than coaxial cables, and low-dynamic range lasers and PD can cost as little as a few dollars.

- Radio astronomy. Modern radio telescopes are realized employing multiple antennas distributed over very large areas in order to increase their resolution and sensitivities [18, 48, 49]. This requires to connect multiple individual antennas that can be spatially very far from each other, and in hostile environments. APLs can be used for LO signal distribution to the elements of the array and to transfer the received signals from the individual antennas to the central processing core [21].

- Minor applications include e.g. EMC sensors and MRI signal distribution, exploiting the EMI immunity properties of APLs.

3.3.2 Microwave signal generation

If signal distribution has been for years the main driver for microwave photonics, the latest developments in the field have been strongly driven by the generation of high purity microwave signals and by broadband waveforms with high-complexity time profiles or frequency envelopes [50]. The really strong added value provided by microwave photonics lays in the large frequency tunability and in the possibility to generate extremely high frequencies, up to the THz range, using simpler techniques compared to the traditional electronic ones. Besides the generation, a whole set of problems rises when there is need of distributing those generated signals. The fact of having a photonic generation of high-frequency signals brings the advantage that those signals are already in the optical domain and can be more easily transported using fibers with no need of further E/O conversion as it would happen if the waveforms were generated with purely-RF techniques [31].

3.3.3 Microwave signal processing

As already discussed in the introduction, microwave photonics signal processing techniques are a very promising way of implementing wideband and highly-flexible analog front-end solutions to implement highly-complex function in conjunction with RF or digital electronics. In particular, MWP techniques have enabled filtering, tunable true-time delays, and wideband phase shifters for microwave signals. The peculiar advantages of MWP techniques are first of all the operational bandwidths, and the potential for fast and agile reconfigurability [16]. In this thesis we demonstrate how, combining those three functionalities, it is possible to implement highly complex functions such as microwave photonic filtering and optical beamforming for phased array antennas.

In addition to that, those functionalities can often be implemented even on a single photonic integrated circuit (PIC). As will be discussed in more detail in the following, merging the field of integrated optics with microwave photonics can bring advantages in terms of stability, bulk and performance and, in some cases, even enable functionalities that are not possible otherwise. Prominent experts in the field have envisioned the possibility to realize multiple signal processing functionalities using a general purpose integrated photonic processor [16]. As a matter of fact, as will be more extensively discussed in the following, in recent years more and more functionalities are being implemented in an integrated optical manner [17].

3.4 Optical beam forming techniques

The application of MWP technology and techniques to the control of phased array antennas is the main topic of this thesis. In the present section, optical technology for phased arrays will be described in its main advantages and principles, including an overview of the main optical beam forming schemes reported in literature over the years. The most debated issues related to the use of photonic technology for

antenna control will be described as well, followed by a description of the current ideas for possible solutions and performance improvement.

As introduced in Chapter 2, modern communication systems require high performance, innovative and flexible antennas. The required features regard the beam characteristics, in particular advanced beam control features (e.g. capability of electronic scanning with no moving parts, with fast and accurate beam scanning resolution; squint-free beamsteering; ultra-wide bandwidth; multiple independently steerable beams), physical characteristics (e.g. in terms of bulk, size, weight; conformable shape), high reliability in terms of temperature fluctuation and mechanical stress (that might occur in harsh environment applications such as airborne or spaceborne platforms) and a relatively low cost. All this is required in order to allow the diffusion of advanced antenna technology towards a number of applications ranging from few-count, high-end ones such as radars, remote sensing platforms, satellite or airborne communication systems, through radio astronomy, air traffic control, and down to everyday applications as automotive and cellular and/or personal wireless communications [51].

3.4.1   Phased array technology

In Chapter 2 we have shown how a very attractive way to satisfy the set of requirements described above is to use phased array antennas. The array is a discrete set of elementary antennas (antenna elements, AE) connected by a so-called beamforming network. As such, an array offers an inherently high degree of reliability, due to the redundance given by the presence of multiple independent elements: if the array system is well designed, the failure of one or a few element does not affect too much the overall performance, phenomenon known as graceful degradation. The main advantage of the discrete construction is the possibility to independently control the electromagnetic excitation of the basic AEs which, in turn, gives a complete control over the radiation characteristics, as it has been mathematically shown in Chapter 2. We have concluded the chapter stating that the performance of the array is directly related to the performance of the feeding or beamforming network (BFN) used to provide the desired complex (amplitude and delay) excitation to the individual antenna elements.

Generally speaking, a tradeoff exists between the performance of a BFN and its complexity, intended as size and weight (bulk), reliability, reconfigurability and cost. In particular, for squint-free beamsteering operation, it has been demonstrated (Chapter 2) that is utterly necessary to realize true time delay (TTD) control of the AE phase excitations whenever wide bandwidth performance is of interest.

In Chapter 1 we have seen how it is difficult for purely electronic solutions to realize beamformers simultaneously capable of continuous amplitude and delay tunability, with broad instantaneous bandwidth and capable to generate large tunable delays, thus to feed large arrays. We have also seen how a number of alternative solutions started to be proposed, such as MEMS, digital beamforming and optical beamforming.

3.5 A historical overview

In [51], Curcio *et al.* gave a thorough review of multiple optical beamforming solutions up to 2006, completed by a careful analysis of the main issues, limits but also the unique advantages of optically-steered arrays. Here, we summarize his conclusions and update the discussion with an overview of the current trends and the solutions proposed by the experts in the field.

3.5.1 OBF principles

In the previous chapter we have seen how, in phased array technology, a suitable control over the amplitude and phase of the antenna excitation coefficients allows a complete reconfigurability of the antenna radiation characteristics. Separate amplitude and phase control are generally needed for the purpose. It was also analyzed, in Sec. 2.4.4, how the type of phase control is a primary factor in determining the wideband performance of the array. Consequently, two main techniques in optical beamforming are analyzed: *phase control* architectures and *time control* architectures.

3.5.2 OBF schemes

Independently of the phase or time control architecture, two main schemes for optical beamforming processors can be found in literature. Those have been accurately classified in [51] in *direct detection* and *heterodyne detection* schemes. Let us clarify the difference between those schemes by considering their schematics in Fig. 3.11.

Both schemes include a number of MWP links, their difference being the signal carried by link:

- in a *direct detection scheme*, the MWP links carry the information signals to be transmitted or received by the elements of the array. Each link contains the proper time delay or phase shift units that implement the proper phase weighting directly on the information signal.

- in a *heterodyne detection scheme*, the MWP links do not carry the information signal, but a reference RF signal. This reference signal, after experiencing phase shift in the optical domain, is downconverted to the electrical domain and mixed with the RF signal originated from, or to be transmitted by each individual antenna element. It can be shown that the phase shift experienced by the RF reference signal translates to a corresponding phase shift on the RF signal received from, or to be transmitted by the antenna element.

In the following sections, we will briefly analyze the most relevant OBF techniques reported to date, classifying them in two large groups of phase control and time control techniques.
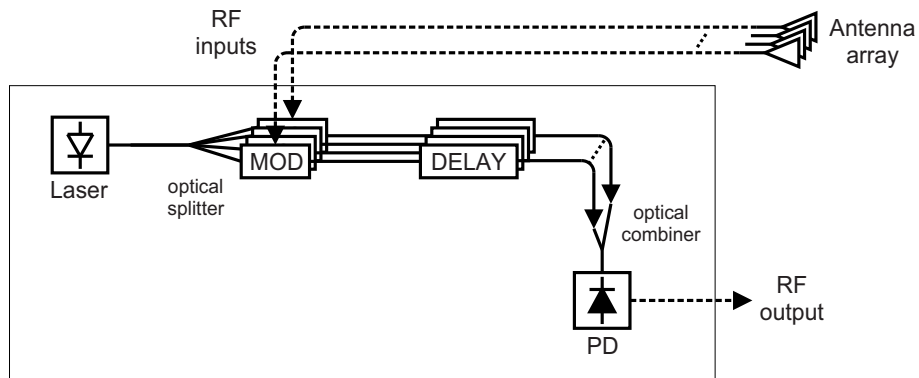
(a) direct detection scheme
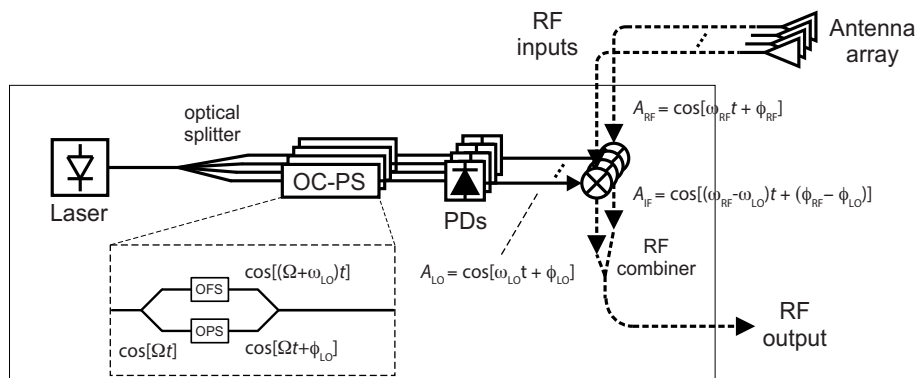
(b) heterodyne detection scheme

Figure 3.11: OBF schemes: direct detection (a) and heterodyne detection (b). OC-PS: optically-controlled phase shifter. (Inset: OFS: optical frequency shifter; OPS: optical phase shifter).

3.6 Phase control OBF techniques

Phase control OBF techniques are characterized by the use of photonic technology for the implementation of microwave phase shifters (PS) for the scope of beam steering. As widely discussed previously, the use of this technique will result in antenna systems with instantaneous bandwidth limited by frequency squint. Nonetheless, this technique has been regarded as a very interesting solution for reconfigurable arrays whose operation can be reconfigured to operate on a very wide frequency range [52]. The most common schemes are based on a *coherent* (or heterodyne) detection architecture, as shown in Fig. 3.11(b), while less common are the schemes based on *non-coherent* detection architectures.

3.6.1 Coherent approaches

The heterodyne detection architecture uses an optical interferometer with a phase control unit on one arm, as in the inset of Fig. 3.11(b). The two arms generally carry signals with different optical frequency, e.g. Ω and $(\Omega + \omega_{LO})$. The resulting beat signal is detected using one (or an array of) photodetector and will have an RF phase that depends on the optical phase shift provided by the phase shifter in the optical interferometer. By varying the optical phase shift ϕ_{LO}, it is possible to control the phase of the resulting beat signal at the PD output, which in turn can be used to provide the desired phase excitation to a specific antenna element.

A main distinction can be made between systems based on bulk optical devices and systems based on integrated optical devices. In bulk optics, the phase control unit is generally referred to as optical control processor (OCP). Generally in bulk optics the waveforms are combined over a plane known as sampling plane, where the interference pattern is formed which presents different phase shifts at different points on the plane (Fig. 3.12). By spatial sampling of this field (e.g. by means of an array of fibers) it is possible to obtain multiple optical signals, with different optical phases, which in turn can be used to feed multiple antenna elements using the parallel scheme shown in Fig. 3.11(b). Generally, the OCP inserted in the interferometer can provide control of the multiple optical phases simultaneously.

The OCP can be realized in several different ways, but the most common approaches [53] use two main categories of devices, namely acousto-optic or liquid crystal spatial light modulators (SLM). A very clear review of the solutions of this type proposed up to 1997 has been presented by Riza [53].

Another category of bulk optics devices employs Fourier-transform optical beamforming (FT-OBF), where the Fourier transform property of lenses is employed [29]. This approach is based on the fact that the far field antenna pattern is related to the spatial Fourier transform of the antenna aperture illumination [4]. A replica of the beam shape to be realized is implemented on a mask and then imaged via the lens on the sampling plane, in order to generate the desired phase excitation. Again, a review of the most significant of those works have been presented by Riza [53]. More recent examples of application of this technique to the control of multibeam planar arrays for telecommunication satellites has been reported in [54]. The pro-
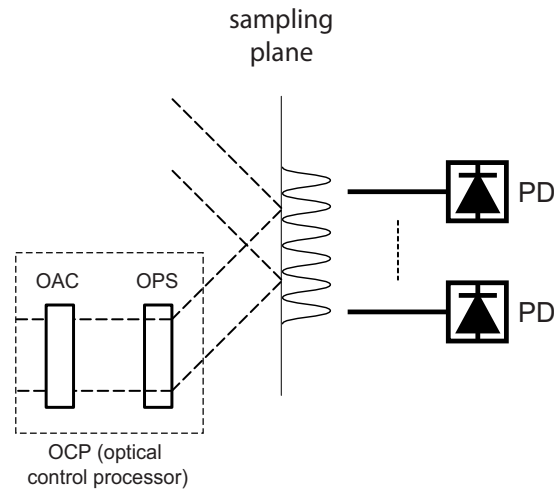
Figure 3.12: Bulk optical heterodyning system. OAC: optical amplitude control;
            OPS: optical phase shifter.

posed FT-OBF uses an amplitude-only spatial light modulator (A-SLM) to spatially
modulate the optical beam with the same profile as a desired antenna radiation
pattern. Multiple simultaneous beam capability has also been implemented by
employing multiple wavelengths [55]. Beam width control capability was demon-
strated more recently, allowing a variable footprint of the antenna on the Earth sur-
face [56].

As clearly emphasized in [51], bulk optics solutions are generally more attrac-
tive than integrated optical ones for large 2D antenna arrays, since they feature a
hardware-compressive architecture, thanks to the fact that a single OCP can pro-
vide parallel control to a large number of elements simultaneously, because it can
process multiple optical paths simultaneously based on space division multiplex-
ing. As a drawback, the use of bulk optics require high mechanical tolerances and is
more sensitive to vibrations and thermal fluctuations which easily affect the accu-
racy of the optical phases. Integrated optics systems, on the contrary, offer a much
higher phase stability and more accurate control over the optical phases, employ-
ing integrated waveguide interferometers where the phase shifters are realized us-
ing thermo-optical, piezoelectric or electro-optical effect. Their drawback is that
they generally require a separate waveguide per antenna element, thus becoming
much more hardware intensive than the free-space optics solutions. Nonetheless,
the current technological progress in micro and nanofabrication allows an increas-
ingly high level of integration and thus the possibility to integrate a larger and larger
number of waveguides realized with high accuracy. In Chapter 7, we will introduce
a novel technique that promises to overcome this limitation, by employing wave-
length division multiplexing in order to reduce the hardware complexity of inte-

grated beamformers.

An important issue described by Curcio [51] is also the way the two optical wavelengths needed at the interferometer input are generated. In fact, in order to have a working systems, the two optical signals have to keep a specific amplitude and phase relation in order to generate the desired amplitude and phase on the interference plane. In particular, the two waves should present phase coherence in order to generate a well-controlled phase for the beat signal and, in turn, for the optically-generated RF signals. In order to have phase coherence, the most common techniques use either a single laser source with sufficient coherence length in conjunction with a frequency shifter on one of the interferometer arms, as shown in Fig. 3.11(b), or a dual laser source where the phase coherence between the lasers is kept by injection locking techniques [57].

Integrated optics for phase shifters-based OBF

As already emphasized in the previous sections, of particular interest to our research is the use of integrated optics for microwave signal processing. Photonic integrated circuits (PIC) have been used starting from the mid-nineties to implement optically controlled microwave phase shifters for single antenna elements or complete beamformers [51]. The basic operating principle of coherent beamformers in Fig. 3.11(b) is here implemented on an integrated waveguide form, distinguishing between schemes employing two lasers or, alternatively, a single laser plus a frequency shifter. Already in 1985, Soref [58] suggested a lithium niobate electro-optic chip implementing both the function of phase shifter and frequency shifter. The proposed frequency shift technique is based on the single-side band quadrature method commonly adopted in electrical communications. This proposed scheme promised to be realizable in a very compact device but is as well very sensitive to amplitude and phase variations of the microwave and optical signals employed. For this reason, several improvements to increase the stability and robustness of this scheme have been proposed over the years [59, 60], as well as multiple-output optically-controlled phase shifters in order to feed complete arrays with a single optical chip, employing a single optical frequency shifter, thus avoiding to replicate the hardware for all the antenna elements of the array [61]. Horikawa *et al.* showed a similar scheme to control 8-elements arrays up to 18 GHz [62]. Additional works have been proposed using polymers with electro-optical properties: in some cases, the control of large arrays could be achieved with a single electrical control signal by properly adjusting the length of the electrodes used to provide the desired phase shift to the different antenna elements [60, 63].

Additional solutions have been proposed by Stulemeijer [64] who presented a photonic chip capable of beamsteering a 16 element array with a complete 360 degree phase shift and 20 dB amplitude suppression, based on electro absorption modulators. Kuhlow and Grosskopf proposed an integrated beamformer using thermo optic effect on silicon, operating at 60 GHz with continuous phase and amplitude control [65]. Riza proposed a lithium niobate beamformer feeding up to a hundred elements based on a surface acoustic wave transducer [66].

3.6.2 Non-coherent approaches

In his review, Curcio [51] classifies three categories of non-coherent approaches, namely fiber optic beamforming, in-phase/quadrature (IQ) modulators and optical injection locking.

Fiber optics have been used since the very beginning of optically fed phased arrays history, to distribute optical signals to and from active front-ends based on microwave monolithic integrated circuits (MMIC) [67]. Besides the signal distribution, this allowed also the implementation of phase and true time delay control, employing either direct or heterodyne detection. To our knowledge, the first IM/DD scheme of this type was proposed by Benjamin and Seeds in the early nineties with the name of fiber optic prism [68]. A heterodyne version of the fiber optic prism has been proposed by Volker [69], allowing to reach even higher frequencies, and further extended by Belisle to feed a two-dimensional array [70].

Coward *et al.* [71] proposed an optical integrated IQ phase shifter capable of realizing a reference local oscillator (LO) signal for the scheme in Fig. 3.11(b) which can be controlled in *both* amplitude and phase. The operating principle is based on two lasers cascaded to two MZMs fed by the same reference signal 90-degree out of phase. The two optical signals are then fed to a photodetector (PD). By independently varying the bias of the modulators and the intensity of the lasers, it is possible to generate a reference signal continuosly varying over the 4 quadrants of the IQ plane. This scheme was further improved in terms of operating bandwidth by several authors [72, 73]. Riza proposed a beamformer based on the same principle, but using spatial light modulators (SLM), realized with bidimensional nematic liquid crystals, as variable attenuators [74]. In this way he added the flexibility of this solution to the hardware compressive characteristic of the free space architectures, making it suitable for large phased array antennas.

Finally, several authors proposed the use of optical injection locking as a way to accurately control the phase and frequency of microwave oscillators, to be used to provide the desired LO signals in the antenna phase control scheme [75–77].

3.7 Time delay control OBF techniques

In Chapter 2 the motivations for using true-time-delay control of phased arrays have been thoroughly discussed. Correspondingly, optical TTD techniques received large attention in literature. A brief historical review is presented here based on the review from Curcio [51].

A signal propagating in a waveguide experiences a group delay τ_g that depends on the path length l and on the group velocity in the waveguide, v_g

$$\tau_g = \frac{l}{v_g} \tag{3.39}$$

In particular, the group delay variation $\Delta\tau$ follows the equation

$$\Delta \tau_{\mathrm{g}} = \frac{\partial \tau_{\mathrm{g}}}{\partial l} \Delta l + \frac{\partial \tau_{\mathrm{g}}}{\partial v_{\mathrm{g}}} \Delta v_{\mathrm{g}} = \frac{1}{v_{\mathrm{g}}} \Delta l + \frac{l}{v_{\mathrm{g}}^2} \Delta v_{\mathrm{g}} \tag{3.40}$$

As a consequence, the group delay can be adjusted by either varying the path length or acting on the propagation group velocity. This result allows to classify the time delay beamforming techniques in two large categories, namely *variable length delay lines* (VLDL) and *variable propagation velocity lines* (VPVL) [51]. Different solutions generally offer different performance parameters, in particular in terms of: (*i*) complexity, which depends on the architecture of the delay line and on the number of antenna elements that can be fed with the same control unit; (*ii*) continuous or discrete delay control capability, and the directly related quantization errors; (*iii*) insertion loss, which directly affects the dynamic range of the system; finally, (*iv*) bandwidth.

3.7.1 Variable length delay lines

Historically, the first variable optical time delays were of the VLDL type, in particular they were switched delay lines (SDL), by far the most common type of VLDL to date. In the latter approach the length of the optical waveguide is changed in discrete steps by selectively interconnecting a cascade of optical waveguides of different length, by means of suitable optical switches. Many solutions of this type have been proposed in the following years, employing different types of optical switching technology (either bulk optics or integrated optics) and delay lines (free space, fibers or integrated waveguides). Switched delay lines differ in terms of architecture, that is, the configuration of the delay line components, which directly affects the performance in terms of complexity, continuous tunability and loss, and in terms of technology employed for switches and delay lines.

The main architectures proposed in literature can be classified [78] in three types, that are: parallel optical delay lines (PADEL), square root optical delay lines (SRODEL) and binary fiber optical delay lines (BIFODEL). Their schematics are represented in Fig. 3.13. Most of those architectures are based on a direct detection scheme, as in Fig. 3.11(a), where the information signals originated from the individual antenna elements are being propagated through the delay lines, despite in some cases [79] a heterodyne detection scheme has been employed. They present a different level of complexity: for a number B of bits, the PADEL requires 2^B delay lines per each AE, the SRODEL solution requires $2^{B/2+1}$ delay lines per AE, while the BIFODEL is the most component-efficient, requiring only B delays per AE.

The structures described above have been realized in both bulk optics and integrated optics format. The bulk optics solutions allow to feed large bidimensional arrays using a limited number of switches thanks to the high degree of parallelism offered by the spatial light modulators employed, since a single SLM can control many parallel light beams feeding the same number of AEs. Their drawback lays mainly in the fact that when the delays are realized in free space the structure becomes large and bulky, requiring large free space paths, and offers a limited stability and robustness against thermal and mechanical stresses, due to the high degree of
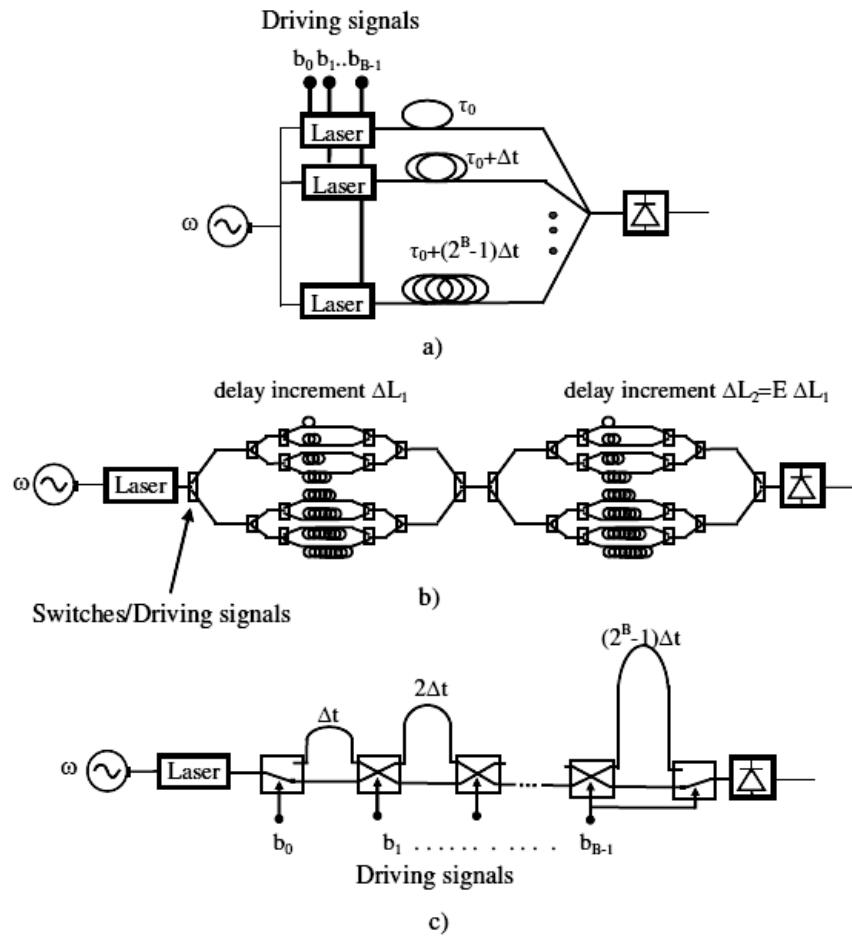
Figure 3.13: SDL architectures: (a) PADEL; (b) SRODEL; (c) BIFODEL (picture from [51], with permission. Courtesy of the author).

accuracy required at all times for the free space optical paths. Integrated optical structures, instead, can offer more compact delay lines for the same amount of delay, thanks to the higher refractive index of the integrated waveguides compared to free space. The switches can also be more compact and stable, but the waveguide and switch losses have to be taken in careful account in order to keep a sufficiently low insertion loss for the system. In both cases, often fiber optics have been used as a solution for reducing both the bulk (compared to the free space optics case) as well as the losses (which are lower than in integrated optical waveguides) and to correspondingly increase the amount of achievable delay.

Bulk optics

For the bulk optics approach, the main difference between the proposed architectures resides in the different types of switching devices have been employed. Dolfi *et al.* [80, 81] proposed nematic liquid crystal (NLC) SLMs used in conjunction with polarization beam splitters (PBS) and a corner prism reflector to implement a basic delay unit based on polarization switching. He configured multiple of those in a BIFODEL architecture and obtained a beamformer capable of feeding up to ten thousand independently programmable delay channels.

The proposed structure was improved in the following years by Dolfi himself and by other researchers. Riza [82] proposed a similar scheme, operating in both transmit and receive modes, based on direct detection instead of heterodyning in order to relax the specifications over the time coherence of the laser and reduce the phase errors due to thermal variations and mechanical vibrations. In addition, he improved the scanning speed by using two independent systems operating in time division. With those architectures, for large delays, long free space paths are required. Other improvements came on the side of compactness by employing holography [83] or propagating the light beams through a glass instead of in air, with reduced dimensions and improved robustness [84], or employing winded fiber optics delays. Those structures allowed to answer the need for large tunable broadband delays for large antenna arrays.

In 1996 Dolfi *et al.* provided a demonstration of his proposed BIFODEL, over the range 2.7-3.1 GHz and with a maximum delay of 1.8 ns tunable with 5 bit accuracy. They demonstrated squint-free 20 degrees beamsteering with an insertion loss per delay stage as low as 1.5 dB.

More improvements by Riza *et al.* brought to a system with 35 μs beam switching time and a SNR over 96 dB [85] based on ferroelectric liquid crystals (FLC).

For applications at higher frequencies, the delay resolution becomes more and more important. Improvements in this sense have been achieved by employing a technique called index switching. With this technique, a 2-states delay line can be achieved by employing a polarization rotator based on liquid crystal and a birifringent crystal. By selecting the desired polarization, the rotator allows the propagating wave to experience either of the two refractive indexes of the material, allowing a well-controlled delay difference. More units of this type can be arranged in a BIFODEL architecture [86] to form a complete beamformer.

Acousto optic devices have also been employed for VLDLs, where for example AOMs were used as optical delay lines switches. In fact, by driving the AOM with acoustic waves of different frequencies, it is possible to modify the optical deflection angle of the light inciding onto it, and thus select the delay line of desired length within an array [87]. The achieved isolation between delays can be as high as 30 dB with a loss below 10 dB.

A conceptually very simple technique has been proposed by Herczfeld *et al.* in 1987 [88], that consists in stretching an optical fiber wrapped around a piezoelectric material: a continuous variation of the applied field will correspond to a continuous fiber stretch and thus a seamless delay variation. Generally high voltages are required in order to achieve sufficient time delays.

Integrated optics

For the integrated optics approach, researchers have proposed different switching technology and have employed either on-chip delays or fiber-based delays.

In 1984 Soref proposed a SRODEL system with delay lines based on fiber optics and on-chip switches [89]. In 1989, Goutzoulis realized a BIFODEL with gallium arsenide switches, with a remarkable maximum delay value around 5 μs, operating in the 0.5-1 GHz range [90]. The work developed at Hughes Research Labs in 1991 [13] is particularly meaningful in the field of optically controlled arrays as it represents the very first demonstration of the wide instantaneous bandwidth and squint-free operation of a phased array antenna steered by optical means. They presented and demonstrated a PADEL structure, operating at both L-band and X-band, showing a beam steering of 28 degrees with 4 degrees resolution, without beam squint. In 1992 Ackerman and co-workers realized a 6 bit time-steered radar in the 3-6 GHz band, with a max delay around 30 ns and a well-controlled insertion loss [91]. In the same year, Goutzoulis *et al.* proposed a TTD based on both electronic and optical time delays, arranged as a 6-bit BIFODEL. Shortly after, they also demonstrated its operation using a 16 element array radiating in L-band which was scanned ± 45 degrees without observable squint [92].

Several authors proposed solutions where the delay lines themselves have also been integrated on-chip. Photonic integrated beamformers have been proposed in almost all the available integration platforms, such as polymer technology [93–95], silica [96–99], lithium niobate (LiNbO$_3$) [62], gallium arsenide (GaAs) and indium phosphide (InP) [100, 101].

In 1992 Sullivan *et al.* realized a GaAs device with switches and waveguide integrated on the same chip, featuring a maximum delay of 0.5 ns and 2 bits resolution, with an insertion loss of 3 dB per stage [102]. Silica waveguides have been used by Ng *et al.* to show a 4-bit PADEL delay with a maximum delay of approximately 4 ns. In 1991 Yap *et al.* [103] filed a patent where they propose integrated waveguide segments, arranged in a spiral-like layout, and interconnected with multiple photodetectors, electronic switches and directly modulated lasers in order to have a series-like active tunable integrated delay line. In 1995 Paquet *et al.* proposed the use of thermo-optical switches to implement a delay line based on BIFODEL struc-

ture and silica waveguides for delay [104]. Wang *et al.* proposed in 1996 the use of polymer nonlinear material to implement both switches and delay lines [105].

An innovative approach was proposed by Chen [106], who employed a delay line where light is coupled into a substrate and it propagates through multiple internal reflections. Holographic grating couplers are arranged in an array layout and used to tap off the light after a desired number of bounces, thus varying the amount of delay. This structure is an intrinsically compact, thanks to the "bounce-like" propagation of light but, for the same reason, it also suffers high attenuation for large delays that needs to be compensated for use in beamforming. This structure has been employed to realize a 6 bit TTD used to feed an 8 element array at K-band, with a maximum delay of approximately 450 ps.

"MEMS-like" switching techniques have also been employed: Riza employed micro-actuator switches for fiber delay lines based on piezoelectric effect [107], and Magel *et al.* proposed a switch with metallic membranes that are electrostatically attracted in and out of contact with the optical waveguides, changing the refractive index and correspondingly the amount of total delay [108].

In 2003, Shi *et al.* proposed what is possibly the first integrated TTD line with continuous tunability [109]. Based on the same principle as the demonstration from Chen, it employs dispersive holographic couplers to provide continuous tunable delay.

More recently (2006), F. Soares *et al.* proposed a 4-AEs, 3-bit true-time-delay beamformer fully-integrated on a single indium phosphide (InP) chip [110]. Each TTD uses a 3-bit BIFODEL architecture. The signals to be transmitted by the four antenna elements are carried by four separate wavelengths, and multiplexed and demultiplexed using an array waveguide grating (AWG). This solution guarantees a very fast beam switching (below 40 ns for a complete scan through all the 8 beams), but only a limited number of delay lines can be implemented on a single chip, limiting both the number of antenna elements and the number of bits. The high fiber-to-chip losses have been mitigated using specifically-designed spot-size converters.

3.7.2   Variable propagation velocity lines

In the previous section we have seen that it is not easy to create compact and stable tunable delay lines. Most of the times, the complexity comes from the need to be able to connect and switch among a large number of lines of different lengths. It would be indeed very attractive if it were possible to reconfigure the delay without need of many different delay lines. In fact, Eq. (3.40) tells us that, in order to realize tunable delay lines, instead of changing the delay line length, it is also possible to change the speed of the information signal (group velocity) in a waveguide with the same physical length. For this scope, a number of solutions have been proposed over the years, in which it has been possible to change delay without changing the propagation path through the delay line, but by means of relating the amount of delay to the optical wavelength employed as carrier of the RF signal. Thanks to the absence of switches, connections and large number of delay lines, this approach

offers a number of advantages especially in terms of compactness, ease of construction and reliability.

The main techniques to achieve "wavelength-tunable" delays proposed to date are based on dispersive delay lines, fiber Bragg gratings, structures including arrayed waveguide gratings, or a combination of those. Strictly speaking, only the dispersive delay line is a variable propagation velocity line (that is, a delay line in which the group delay is not constant with the optical frequency); nonetheless, historically, all the techniques above have been referred to as VPVLs due to the fact that they share with the same wavelength tuning mechanism.

High dispersion fibers

As the refractive index of a transmissive optical medium generally depends on frequency, different spectral components travel at different speeds $v = c_0/(n\lambda)$: this phenomenon is known as group velocity dispersion (GVD) or chromatic dispersion. As a consequence, the group delay also depends on frequency.

In 1992 Soref and Esman proposed to use the chromatic dispersion effect in high dispersion fibers (HDFs) in order to create tunable optical delay lines in association with a tunable laser [111, 112]. By changing the wavelength, the time delay of the fiber can be changed continuously. The maximum achievable delay can be varied by variable dispersion and length, while the delay resolution depends on the limiting factor between laser linewidth and wavelength stability. The insertion loss depends on fiber coupling and attenuation and can be kept lower than in architectures involving integrated optics.

The most straightforward architecture for a beamformer employing fiber dispersion for a N-elements array consists of N tunable lasers, each connected to an intensity modulator, a high dispersion fiber and a detectors [111] as shown in Fig. 3.14. By independently tuning the wavelength of each laser, it is possible to independently change the delay associated to each element of the array. Despite its high flexibility, this architecture requires a large amount of hardware and complex control for arrays with many elements.

A less hardware-intensive architecture, known as fiber optic prism (FOP), was presented by Esman in 1993 [113]. It uses a single tunable laser and modulator, with N optical channels consisting of HDFs sections of different lengths connected to normal dispersion fibers (Fig. 3.15). The lengths engineered in such a way to achieve the desired delay progression along the elements of the array, with equalized delays (thus broadside pointing direction) at the central wavelength. He demonstrated a squint-free broadband beamsteering of a 2-elements array over two octaves in the 2-8 GHz band. The total angular scan of approximately 15 degrees was demonstrated with a beam steering per unit wavelength tuned of ≈ 0.28 deg/nm.

This solution was extended for either transmit or receive modes (Fig. 3.16) [114, 115], or both [116, 117]. As a complete demonstration, Frankel and Esman showed an 8-elements transmit array in the 2-18 GHz band and a full scanning capability of ±53 degrees, and a 2-element receiver in the 6-16 GHz band with ±35 degrees, showing amplitude unbalances among the channels around 3 dB and 15 degrees
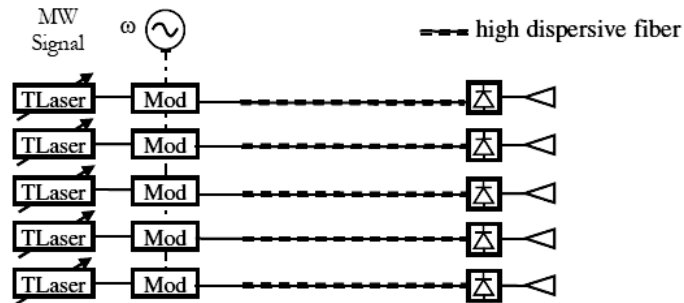
Figure 3.14: High dispersion fiber (HDF) delay lines beamformer (picture from [51], with permission. Courtesy of the author)
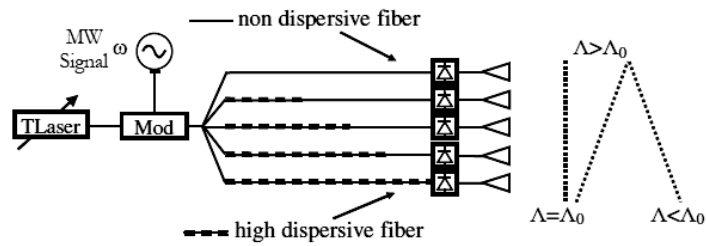

Figure 3.15: High dispersion fiber (HDF) delay lines beamformer: transmit scheme (picture from [51], with permission. Courtesy of the author)
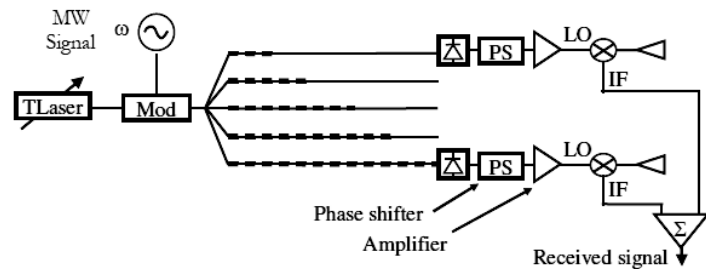

Figure 3.16: High dispersion fiber (HDF) delay lines beamformer: receive scheme (picture from [51], with permission. Courtesy of the author)

mainly due to impedance mismatches in the microwave section.

The main drawbacks of the HDF solution are mainly their bulk, as large arrays require long fibers to provide large delay tuning ranges, thermal instability, since the group delay varies sensibly with temperature, creating delay variations and ultimately beam pointing errors, and losses for large delays at high RF frequencies. Nonetheless, thanks to their operating principle, FOP architectures offer a straightforward expansion towards multibeam capability. In fact, by wavelength multiplexing different RF signals on the fiber optics network it is possible to create multiple independent beams simultaneously without duplicating the FOP hardware, provided that the wavelength spacing is kept sufficiently high to avoid aliasing among the different RF signals: this, in turn, imposes a lower limit on the angular spacing between two simultaneous beams in the spatial domain.

Multiple examples of extension of the FOP architecture to the bidimensional arrays have also been demonstrated. A cascaded, hardware-compressing architecture has been proposed by Frankel *et al.* [118] in order to feed a 4×4 array with separable illumination (see Chapter 2) and demonstrated squint-free, independent elevation and azimuth steering of ±30 degrees over the 6-18 GHz range, limited only by the bandwidth of they employed microwave components.

The Naval Research Laboratories (NRL) also showed the first mm-wave optically controlled antenna, working in K_a-band and with a squintless beamsteering of ±60 degrees, employing piezoelectric fiber stretchers to reach the sub-picosecond delay resolution required for the high RF frequency [119].

Compared to the scheme initially proposed by Soref, the FOP-based architectures allow the use of a single laser and modulator, providing a remarkable reduction of complexity. A further step in this direction has been realized with the introduction of the so-called programmable dispersion matrix (PDM) by Tong *et al.* in 1996 [120]. Instead of using one fiber per delay element, this approach uses a common delay line of BIFODEL type, fed by a multiple wavelength laser and a single modulator (Fig. 3.17). N wavelengths are employed in a N-elements array. All the wavelengths propagate through the common delay line and are then separated at the output using a N-channels wavelength demultiplexer. Each output feeds a single photodetector (PD) and antenna element. For the receiving scheme, PDs and MZM are simply swapped. Besides using a common delay lines shared by all the channels, the main advantage of this structure is that there is no longer need for tunable sources, instead a fixed multiwavelength laser can be used. As a drawback, continuous TTD control is no longer possible due to the BIFODEL structure. Similarly to the FOP, 2D PDMs have also been proposed [121].

Fiber Bragg gratings

In the previously described HDF approach, very long fibers are needed to provide large delays, posing problems of thermal stability of the OBFN performance. An important improvement in this direction came from the use of fiber Bragg gratings (FBG) as time delay units, first proposed by Ball et all. in 1994 [122] and demonstrated for the first time in 1997 at the Naval Research Laboratory [123, 124]. An FBG
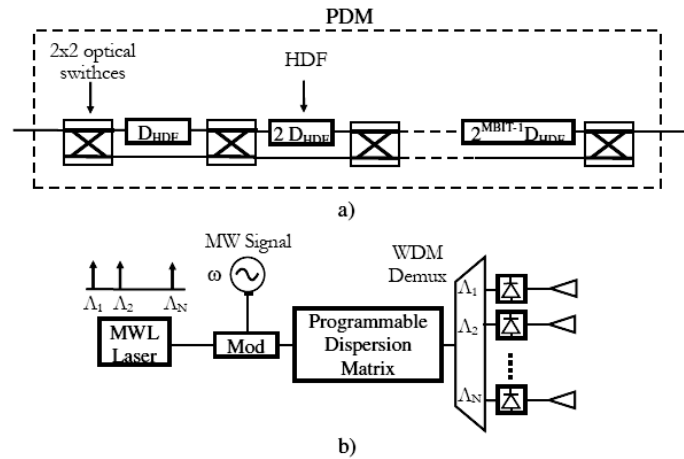
Figure 3.17: Programmable dispersion matrix (PDM): (a) architecture; (b) beam-forming scheme (picture from [51], with permission. Courtesy of the author)

is a distributed Bragg reflector realized in a segment of optical fiber which reflects specific wavelengths of light [125]. By placing several FBGs with maximum reflectivity at different wavelength along the fiber, it is possible to achieve reflection at different points on the fiber by changing the wavelength. Including this device in a scheme employing a circulator, a variable delay line is obtained (Fig. 3.18). In this sense, the delay tuning mechanism in a FBG-based optical delay is similar to the one used in HDFs.
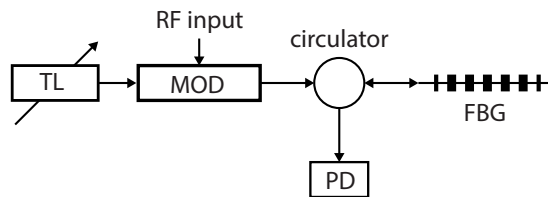
Figure 3.18: Fiber Bragg grating (FBG) variable delay line

Being the delay based on reflection, it allows to divide by half the length requirement for the delay system, with a sensible advantage in terms of bulk, stability and loss. On the other hand, in order to have a transmissive delay line, the use of a circulator, a Y-junction or a 3 dB coupler is required, adding complexity and extra loss due to the insertion of an additional component (of at least 6 dB per round-trip).

The minimum achievable delay depends on the spacing of the gratings along

the fiber. Due to the physical dimensions of the FBG, this creates a lower limit for the delay resolution of approximately 10 ps, thus limiting the usable RF frequency to 3-4 GHz [126].

Similarly to the fiber optic prism, Soref proposed the so-called fiber grating prism, where each element of the array is connected to a fiber with gratings operating at the same set of wavelengths, but placed at increasing distances from each other when moving from element to element, as shown in Fig. 3.19. In this way, employing a single tunable laser and an optical splitter, it was possible to address a specific set of FBGs and create a specific beam pointing direction.
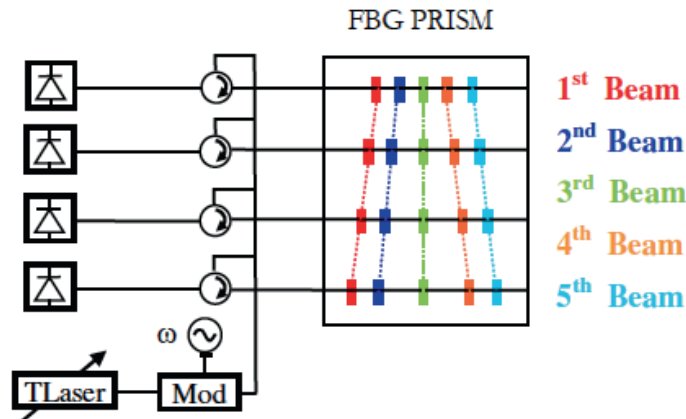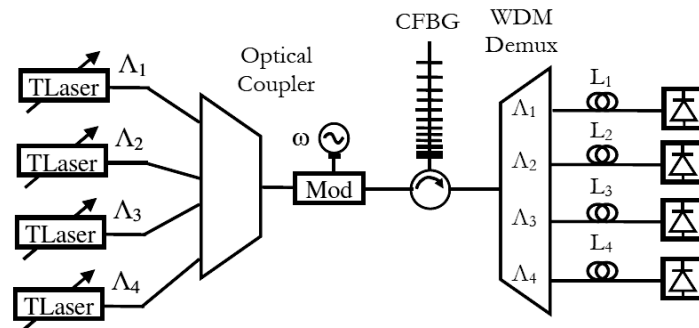

Figure 3.19: Fiber Bragg grating prism (picture from [51], with permission. Courtesy of the author)

As soon as chirped fiber Bragg gratings (CFBG) became available, the limitation in the achievable time resolution could be solved. In fact, in a chirped grating, the period of the grating varies with the position along the grating itself, allowing to implement a broadband reflector, where different wavelengths are reflected at different points within the grating. From our point of view, that is, when a CFBG is used as a delay line, a wavelength-selective reflectivity within the length of the grating is possible, enabling a very fine tuning of the effective reflection point and, in turn, a very fine delay tuning accuracy.

Corral *et al.* [127] proposed a scheme with a single broadband CFBG, fed by an array of independently tunable lasers, a wavelength combiner and a demultiplexer, as in Fig. 3.20, similar to the scheme of the programmable dispersion matrix shown before.

A similar architecture using multiple CFBG (Fig. 3.21) allows to reduce the number of laser sources and of the wavelength demultiplexer, in a very similar way to the FBG prism in Fig. 3.19. In addition to that, having separate CFBGs adds more

Figure 3.20: Chirped fiber Bragg grating (CFBG) beamformer architecture (picture from [51], with permission. Courtesy of the author)

flexibility in the phase distribution, while adding more lasers is now a straightforward way to achieve multibeam capability [128] .

Solutions to increase the delay tuning accuracy were proposed that use for example mechanical strain [129] or strain and temperature obtaining a resolution in the picosecond range [130].
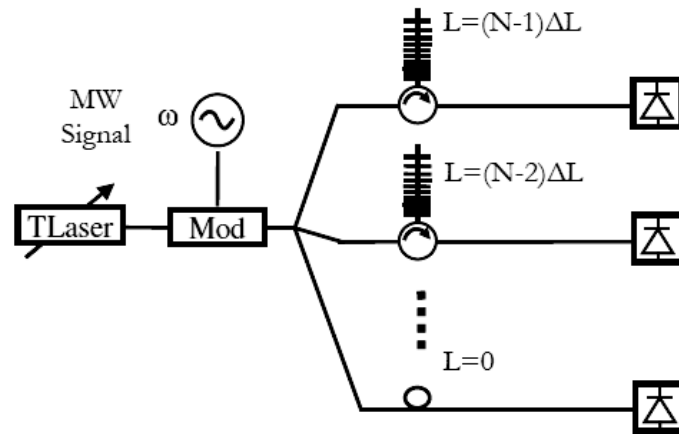
Arrayed waveguide gratings

An interesting approach employed for wavelength-selective routing of signals through delay lines of different length is based on the use of arrayed waveguide gratings (AWG, or *phasar*). First proposed by Smit [131], this multiport device allows to selectively route the power from the input to a specific output, based on its frequency. By connecting lines of different lengths to the ports, as represented in Fig. 3.22, is again possible to select the desired delay line by varying the carrier wavelength.

The first example of employing an AWG for beamforming dates back to 1996 when Jalali's group [132] demonstrated a wavelength selective time delay based on a recirculating AWG. They implemented an 8-bits TTD employing silica waveguide delay lines in C-band (1550 nm) and with 0.8 nm channel spacing. The main issue in this scheme is the temperature fluctuation of the spectral response of the phasar, with a drift of approximately 1 GHz per degree centigrade, which can be easily compensated using active temperature stabilization whenever the application requires operation in highly varying environmental conditions.

A similar example of a fully-integrated beamformer was proposed by Soares [110] who implemented the structure in InP technology. Four separate wavelengths are generated by four different lasers, are multiplexed and then inserted on the chip where an AWG is used to demultiplex and route them to four different delay lines. One has a fixed length and is used as reference, while the other three are switched with a BIFODEL architecture with 3-bits each. The delayed signals are then recom-

Figure 3.21: Chirped fiber Bragg grating beamformer architecture using multiple CFBGs and a single tunable laser source (picture from [51], with permission. Courtesy of the author)
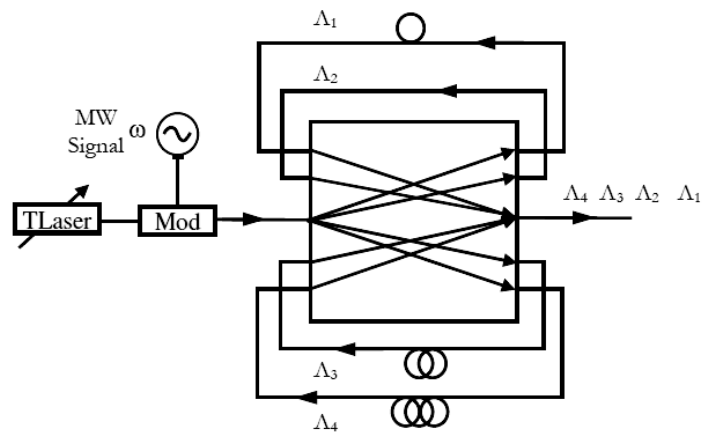
Figure 3.22: Variable delay line based on an arrayed waveguide grating (AWG) (picture from [51], with permission. Courtesy of the author)

bined using the same AWG and routed to the output, where they can be demultiplexed and used to feed an array of PDs connected to the individual antennas. The limitation in the InP wafer dimension does not allow to realize beamformers with a larger number of bits and to feed arrays with more than 4 elements. To overcome this problem, Soares also proposed a version where only the AWG is implemented on chip, and the delays are obtained via optical fibers. Unfortunately, the mode profile in the InP waveguide is much smaller than the one in the fiber, and this creates high fiber-to-chip coupling losses. For this reason, the latter architecture relies heavily on the use of specifically designed spot-size converters in order to keep the losses within an acceptable limit.

Bi-dimensional beamformers were also presented, where separate cascaded stages are used for azimuth and elevation control [133]. Differently from the 2D architecture described for HDFs, here no RF downconversion is performed between the two stages, instead a wavelength conversion is operated by means of a semiconductor optical amplifier (SOA).

Vidal *et al.* proposed a very interesting solution where they combined AWGs with HDFs in order to realize multi-beam architecture, exploiting the frequency periodicity of the AWG [134, 135].

3.8 Recent developments

More recently, a number of novel technologies became available and allowed demonstrations of novel type of optical beamforming schemes.

Yi *et al.* recently proposed the use of the use of liquid crystal on silicon to implement a continuosly tunable beamformer, based either on constant phase shift in frequency [52] or true time delay [136]. The authors employed a commercial Wave Shaper from Finisar Inc.

Very recently, Sancho *et al.* demostrated the use of a single, very compact and low-loss photonic crystal to implement multiple variable true time delays for microwave photonic filtering applications [137]. The operation is based on the slow-light properties of photonic crystals, in which the group delay can be increased to very high values depending on the wavelength. Photonic crystals have attracted much attention in the past, but lost attention due to the extreme difficulty in their realization. The authors demonstrated a a 1.5 mm long device capable to generate delays as high as 70 ps while keeping the losses below 10 dB, over the complete 0-50 GHz band. The demonstration was conducted by configuring the photonic crystal to implement a multitap microwave photonic filter, with a very similar configuration to the one shown in Fig. 3.21, where multiple laser sources can be independently tuned to achieve different time delays from a single device.

3.8.1 Conclusions and target for the thesis

From the historical overview given above, it is important to draw some useful conclusions that can help us to proceed towards the design of innovative beamformers with improved performance.

A very important observation is the following. Let us remember that the main reason for introducing optical solutions has been mainly the need to provide *large delays* in conjunction with *broad bandwidths* and *limited bulk*, with flexible, seamless and fast delay control. In some of the previously analyzed solutions, however, it appears that the optical solutions can also become very bulky and heavy when increasing the delay, in fact vanishing the advantage initially expected from the introduction of the photonics solutions.

In particular, bulk optics and fiber based solutions can become very large and heavy when large delays are needed, while integrated solutions generally cannot provide very high delay amounts. As a consequence, we have seen how researchers have introduced solutions based on two "combat lines":

1. use as small and simple TTDs as possible (for the same amount of delay);

2. use as few TTDs as possible (for the same number of antenna elements).

The first point has been addressed by (i) proposing delay lines architectures that reuse the same delay sections (e.g. BIFODEL) to provide multiple delay values, and (ii) solutions increasing the refractive index instead of the physical length of the structures (e.g. materials with high refractive index) and dispersion (e.g. HDFs). More recently, a novel approach has been the one to increase the delay by using structural resonances enhancing the delay (e.g. ORRs).

The second point was addressed mainly by employing space multiplexing, as in bulk optics, where a single delay unit can handle up to thousands of parallel light beams that carry the delay information for the same number of antenna elements, or wavelength division multiplexing, as in PDM or CFBG.

In this thesis, we aim at addressing all points, by

1. delay reuse structure (binary tree)

2. structural delay enhancement via creation of resonance (ORRs) and also

3. multi-wavelength (MWL) architecture for WDM (Chapter 7)

3.9   Limitations, current trends and solutions

As in many other technological fields, also in the field of antenna beamforming the main issue is the balance between system performance on one side, and the complexity and cost of the proposed solution on the other. The main characteristic defining the performance are related to a number of important parameters, such as angular resolution, maximum scan angle, beam shaping capability, number of (re-configurable) simultaneous beams, possibility of simultaneous operation in transmission and reception and, finally, speed of reconfigurability. In addition to that, following the discussion on the performance analysis of analog optical links given in the previous sections, it is clear how important at system level are parameters like insertion loss, dynamic range and signal to noise ratio.

The characteristics mentioned above are typically used to evaluate *any* beamforming system. Considering those performance parameters, optical beamforming attracted attention starting from the eighties, mainly because it promised major advantages in terms of extremely wide bandwidth (several hundreds GHz) in optical fibers, low weight, low cost and immunity to electromagnetic interference (offered by optical fibers when compared to coaxial cables or other microwave transmission lines), in conjunction with the possibility to provide large amounts of delay (and thus the capability to feed very large arrays) and to provide easy clock and local oscillator signal distribution, thanks to the extremely low fiber loss compared to other types of transmission lines. The promise of those breakthrough capabilities has been the engine which pushed the development of not only optical beamforming research, but which had the merit to generate interest in the whole field of microwave photonics, which nowadays spans over a much larger range of novel applications, compared to the mere replacement of functions traditionally performed using RF technology [12, 16].

Nonetheless, as Herczfeld *et al.* noted in recent years [138], in the past four decades a considerable amount of important research results has been generated, but no major application emerged. An accurate analysis of the situations brought the major experts in the fields to draw the conclusion that the main problems in MWP are the following:

- *Limited gain / dynamic range performance.* OBFs often present high conversion loss and low dynamic range (especially in receive mode), thus their performance in those terms is often lower compared to the RF systems they aim to replace. This is mainly due to the low link gain and the inherent nonlinearity of the intensity modulated-direct detection (IM/DD) MPL commonly employed.

- *High cost and low reliability.* Most OBF systems are are often based on complex assemblies composed by long fiber optics and/or bulk optical devices, which in the chosen configurations can be very sensitive to thermal and mechanical stress. In addition, those systems are generally assembled manually, based on expensive off-the-shelf optical and RF components, thus bringing low yield and very high cost.

- *Advances in digital and RF electronics.* The possibility to implement extremely flexible, real time digital beamforming processors created a very attractive alternative to analog RF beamformers in many fields of applications (e.g. radioastronomy), reducing the interest in optical solutions. Analog RF technology is also showing a fast pace of evolution towards higher frequency and broader instantaneous bandwidths.

- *Natural resistance of microwave engineers to the optical approach.* Considering the previous weaknesses of photonic solutions, microwave engineers gradually abandoned the idea that optical approach could be a solution, despite the need is still present.

In fact, to date, there is a number of application fields where no microwave or digital beamforming solution is yet capable of providing the desired beamforming performance. This is particularly true for very large arrays where broadband and continuous delay tunability is required, or for the envisioned array systems operating at frequencies up and well into the THz frequency range. In those fields, to date the optical solution appears to be the only candidate [2]. In those cases, the advantages of photonic solutions overcome the mentioned drawbacks in a number of applications. One example is given by airborne and spaceborne systems, where there is need to realize multiple beams with fast beam switching capability, with strict constraints of weight and bulk. Optical technology can also provide a solution for large phased array antennas operating over a large bandwidth, for which to date no electronic solution can provide the desired performance, as well as for arrays operating at extremely high frequency, making unpractical to realize purely electronic delay lines due to the high losses.

Since the need for the advantages offered by optical solution is still present, the researchers in the field are looking into ways to solve the main limitations of high cost, low reliability and poor performance by two main combined lines of action:

- *Introduction of novel MWP link schemes* that can provide the required SFDR characteristics to match the purely electronic solutions: the inherent non-linearity of the IM/DD analog links can be overcome by employing phase modulated (PM) optical links: modulation is direct and linear, and the main challenge moves to the detector/demodulator realization. A number of very attractive solutions, both coherent and non-coherent for phase demodulation have been proposed in recent years [16, 17, 139]. Very recently, an optical beamformer based on phase modulated links has been proposed [140, 141].

- Implementation of beamforming (and, more in general, multiple microwave photonics functionalities) in an *integrated optical form*. The progress in integrated optics allows to realize many of the same functionalities traditionally performed with fibers or bulk optics on a single chip, often realized with a CMOS compatible process. Similarly to the integrated microelectronic revolution, photonic integration brings a number of fundamental breakthrough advantages, mainly a substantial reduction of size, weight and unit cost, higher yield and a revolutionary improvement in the performance thanks to the high accuracy that modern fabrication techniques allow.

3.9.1   Integrated Microwave Photonics (IMWP)

In Section 3.3 we have briefly described the fields of application of microwave photonics, emphasizing the specific advantages that the MWP technique can add with respect to purely RF solutions. A number of laboratory demonstrations have demonstrated the capabilities of those solutions; nonetheless, in real life applications, not many MWP systems have been deployed nor have reached a widespread diffusion.

A number of factors have been identified as the reason of this delay in a large-base diffusion of MWP solutions. The first factor is closely linked to the fact that the MWP systems are based on MWP links which do not yet offer sufficient performance in terms of *dynamic range*. For example, in optical beamforming, in Section 3.4 we have shown MWP processors with impressive performance in terms of true-time-delay bandwidth and gain flatness that in some cases are demonstrated over bandwidths in excess of tens of GHz, but their dynamic range is not sufficient to actually replace deployed traditional microwave solutions. This has recently been identified [12] to be the limiting factor of optical beamforming and the reason of the decrease of interest in the last years over this specific topic. Same considerations can be applied to several recent demonstration of MWP pulse shaping techniques.

Other factors which are at least as important, are *reliability* and *cost*. Most of the demonstrated MWP systems are composed by *discrete* (mostly off-the-shelf) photonic and RF-photonic components, such as laser sources, modulators, fiber pigtails, polarization controllers, prisms, photodetectors, and more. This poses several issues that are not easy to solve. For example, the size of the complete system can easily become very large, despite most of it will be composed by the packages and by the fiber pigtails used for interconnection of the separate photonic components. Fiber connections are delicate, sensitive to temperature variations and mechanical stress, and all this affects the system sturdiness and reliability. In addition to that, the materials and the work necessary for packaging add substantial cost to the complete system. For components that need to be temperature stabilized, the presence of multiple components with individual packages will in most cases require multiple independent temperature control systems, adding extra bulk and cost. Those factors have sensibly slowed down the deployment of microwave photonic solutions for the replacement of pure-RF solutions.

When the aforementioned problems (power consumption, cost and reliability) could be removed, it would be possible to fully exploit the promised ultra-broadband and reconfigurability performance of MWP systems, giving them the capabilities to replace not only coaxial cables for signal transport, but also a number of pure-microwave analog processing devices.

The major experts in the field [15, 16] believe that an answer to this problem could come from RF photonic *integration*. Similarly to what happened to electronics with large scale integration using CMOS technology, or analog microwave monolithic integrated circuits (MMIC) for high-frequency applications, photonic integration allows a number of benefits in terms of footprint reduction, reduced inter-element coupling losses, packaging costs and reduced power dissipation while bringing the potential of increasing system performance. In fact, the reduced components size and the absence of optical fibers increases the optical phase stability and reduces temperature sensitivity compared to the use of discrete components connected by fiber pigtails. A number of systems, for example the ones that require low propagation delays, as optical phase locked loops, or the ones that need the integration of a large number of multiple basic building blocks (BBB), such as optical beamformers for large antenna arrays, might not even be realizable without an

integrated approach. In these terms, photonic integration becomes not only a way to bring performance a step forward, but instead a real *enabling technology* for a number of signal processing functions.

As clearly described in [17], the recent trend of large-scale photonic integrated circuit (PIC) technology driven by high-capacity "digital" optical communications has definitely influenced the progress of integrated microwave photonics, providing a ground of different technologies that have been investigated for the scope of providing the best possible integration platform. Indeed, as such, this trend has followed the requirements and needs of the driving application, that is, providing PICs with very high speed, high component counts and as the possibility to integrate as many diverse functionalities as possible on a single chip [142]. In fact, in digital optical communications the integration capability has benefited a higher priority with respect to the optimal performance for each individual functionality (e.g. modulation, propagation loss, optical amplification, etc.). Microwave photonics application, instead, have to deal with very stringent performance requirements deriving from their scope of handling "analog" optical signals. For this reason, in most cases, in order to have performant and effective MWP systems, the priority in the choice of the integration approach should be the highest possible performance for the individual functions. In addition to this consideration, the MWP techniques address a much lower volume market when compared to optical digital communications. As a consequence, the authors of [17] are convinced that those differences will induce the PIC producers to take a different, novel approach to the realization of MWP PICs, that takes into considerations the specific needs of the MWP applications.

Two excellent reviews of the history, status and progress of the application of integrated technology to microwave photonics, including the most representative examples in all its fields of application, have been given by Marpaung *et al.* in [17] and by Capmany *et al.* in [16].

4

System Analysis and Design

The present chapter describes the system analysis and design of the optical integrated beamfomers that have been realized and demonstrated in this work. The description starts from the basic building blocks – delays and combiners – and continues towards the integration of those to form a complex processing network. The network, in turn, is inserted into the antenna processing system and the performance of the system is then analyzed analytically. The system analysis allows the performance evaluation, in terms of signal to noise ratio, at the output of the OBFN system, providing an efficient design method for the microwave photonic processor.

4.1   Basic Building Blocks of the OBFN

Chapter 2 introduced the basic functions to be performed by a beamforming network, namely, amplitude control, delay control and signal splitting/combining. Those functions are all elegantly summarized in the equation of the array factor, Eq. (2.47).

In the approach employed in this research work, those basic beamforming functions are realized using a physical network, the beamforming network, which employs optical technology. In the previous chapter an overview of possible optical beamforming solutions was given, comparing their performance criteria in terms of bandwidth, flexibility of operation and tunability, bulk and cost. Among the various possibilities of implementation, we have highlighted the advantages of an integrated photonic approach in terms of compactness, lightweight, cost, programmability, EMI immunity, robustness. In this section, the architecture of an integrated optical beamformer based on optical ring resonators (ORRs) will be described.

The discussion reported in the following three sections has been clearly presented by Meijerink *et al.* in [33], where a description of the basic building blocks, the network architecture and a system analysis is given. Here we report a summary of those results which has been extended in order to fit the scope of this thesis.

4.1.1   Delay elements

Let us consider a receiving phased array antenna (PAA). Each antenna element (AE) can be seen as capable of generating an RF signal which has to be processed by the beamformer of the array, according to the mathematical description of array theory given in Chapter 2. The basic operation performed by the array beamformer is to modify amplitude and phase relation among the individual AE signals, as desired to form the desired beam pattern, and to combine them into a single RF signal, as visible in the schematic of Fig. 2.13.

In subsection 2.4.4 of Chapter 2 the requirements for a wideband beamformer has been given, in terms of a *linear phase response* being required in each delay path.

Delay based on transmission lines

The desired wideband linear characteristic for a delay unit, expressed in Eq. (2.109), can be obtained by using a physical delay line. The specific length corresponds to a specific slope for the phase response, thus to a specific amount of group delay on the AE signal being processed.

As discussed in Subsection 2.4.4, a physical delay line gives the desired linear phase characteristic as long as dispersive effects are negligible. To overcome this limitation, *optical* delay lines have been proposed as a promising solution, offering an extremely large bandwidth when compared to any type of RF delay line, and extremely low losses, being the latter also a very important requirement for an antenna feeding network, as will be discussed and demonstrated in the *System analysis* section of this chapter.

Nonetheless, a physical delay line is usually a bulky solution and, most importantly, it does not easily allow continuous tunability, since it is generally not possible or difficult to tune continuosly, reversibly and rapidly the length of a transmission line. The characteristic of seamless tunability is needed in order to be able to generate an arbitrary beam pointing direction, which is of primary importance in many applications, namely, radio astronomy, mobile personal communications, or satellite reception.

Delays based on optical filters

Apart from using delay lines of different physical lengths, an attractive possibility to modify the time delay of an RF signal is to employ *optical filters* in which the *group delay response* can be modified as desired. In fact, when an optical carrier is modulated by an RF signal, propagates through an optical waveguide and is converted back to electrical domain by a photodetector, the effective time delay experienced by the RF signal is given by the *group delay* of the optical waveguide. Now, the group delay can be modified either by modifying the *length* of the optical waveguide, or by including a filter with *tunable group delay response*.

Optical ring resonators (ORRs)

As described in [143], an extremely compact and very effective way of implementing continuous tunability for the group delay of an optical waveguide is to exploit the properties of optical filters based on ring resonators [99, 144, 145]. By placing a ring waveguide structure in proximity of the waveguide, and by varying its coupling factor to the waveguide, it is possible to implement a tunable optical filter called *optical ring resonator* (ORR). Such a filter has a time-discrete impulse response and, equivalently, a frequency-periodic transfer function. This type of structure can be easily modelled as a digital filter, as explained in more detail in [146] where an analitical expression for the filter transfer function has been calculated. The period of the transfer function is called free spectral range (FSR) and equals the inverse of the round trip time of the ring, τ_r or RTT[1].

---

[1]The circumference of the ring determines its round-trip time (RTT):

$$RTT = \frac{L \cdot N_g}{c} = \frac{L}{v_g} \quad \text{[s]} \tag{4.1}$$

Where RTT is the round trip time, L is the circumference of the ORR, N_g is the group index and v_g is the group velocity in the optical waveguide. The FSR of the ring resonator is the inverse of the RTT:

$$FSR = \frac{1}{RTT} \quad \text{[Hz]} \tag{4.2}$$

For reduced OBFN chip dimensions, it is desired to reduce the circumference L to the minimum. The minimum dimension of the ring is given by the minimum waveguide bending radius that can be reliably realized with the technological process which gives an acceptable loss, and the minimum length of a tunable Mach-Zehnder interferometer. In fact, the realized ORRs have a race-track shape, where the bends radius is determined by the minimum waveguide bending radius, and the length of the MZI is determined by the length of the directional couplers and of the tuning element (heater) [147].

In the ideal case of a lossless waveguide, the ORR operates as an all-pass filter, with a unitary magnitude transfer function, and with a phase response showing 2π phase transitions centered at the frequencies for which the resonance condition is satisfied, that is, when the ring length corresponds to an integer number of wavelengths.

The phase response of the ORR can be derived as shown in [143] and is expressed as

$$\Phi(\Omega) = \arctan\left[\frac{\frac{r}{1-\kappa}\sin(\Omega+\phi)}{1-\frac{r}{1-\kappa}\cos(\Omega+\phi)}\right] - \arctan\left[\frac{r\sqrt{1-\kappa}\sin(\Omega+\phi)}{1-r\sqrt{1-\kappa}\cos(\Omega+\phi)}\right] \quad (4.3)$$

where Ω is the optical frequency, r is the amplitude transmission factor of the ring cavity ($r = e^{-\alpha L}$), ϕ is the phase shift in the ring waveguide, and κ is the power coupling coefficient, or coupling factor, between the input-output waveguide and the ring waveguide. The propagation loss of the waveguide expressed in dB/cm can be expressed as [143]

$$P_{\mathrm{l}} = 20\log(e^{\alpha}) = 20\alpha\log(e) \approx 8.686\alpha \quad \text{[dB/cm]} \quad (4.4)$$

Those parameters control the phase response of the ORR filter. The value of the power coupling coefficient κ determines the quality factor of the resonator, while the phase shift ϕ controls the actual resonance frequency at which the resonance occurs. The phase response is plotted in Fig. 4.1 for different values of ϕ (Fig. 4.1, top left) and κ (Fig. 4.1, top right).

The group delay response of the filter can be calculated by differentiation of the phase response with respect to frequency. In fact, the relation between phase and group delay is

$$\tau(\Omega) = \frac{\partial\Phi(\Omega)}{\partial\Omega} \quad (4.5)$$

The resulting expression for the group delay is [143]

$$\tau(\Omega) = \frac{r\sqrt{1-\kappa}\cos(\Omega+\phi) - r^2\sqrt{1-\kappa}}{1 - 2r\sqrt{1-\kappa}\cos(\Omega+\phi) + r^2\sqrt{1-\kappa}} + \frac{r^2 - r\sqrt{1-\kappa}\cos(\Omega+\phi)}{1 - \kappa - 2r\sqrt{1-\kappa}\cos(\Omega+\phi) + r^2} \quad (4.6)$$

This delay response can be plotted with respect to frequency over one FSR. Again it is possible to notice the effect of the parameters κ and ϕ on the delay characteristics. The delay response is plotted in Fig. 4.1 for different values of ϕ (Fig. 4.1, bottom left) and κ (Fig. 4.1, bottom right). The peak value of the delay is approximately inversely proportional to the width of the curve, since the area underneath the delay curve in one period is always equal to one [33]. This imposes a trade-off between the highest delay value and the bandwidth over which the delay can be provided.

For our purpose of implementing a compact and continuously tunable delay line, it should be noticed that the ORR offers a linear phase slope or, equivalently,
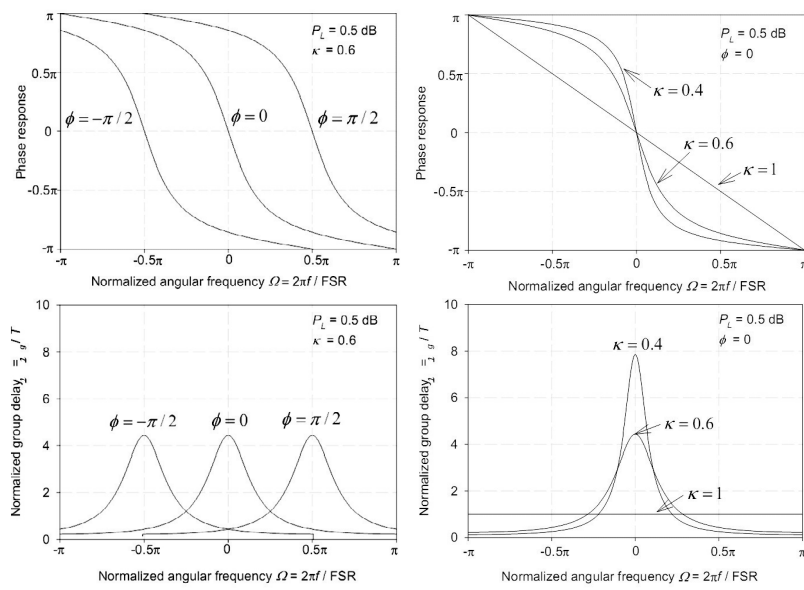
Figure 4.1: Phase response (top) and delay response (bottom) of a single ring resonator for different values of the phase shift in the ring ϕ (left) and of the coupling coefficient κ (right) (picture edited from [143], with permission).

a flat delay response, in a limited neighbourhood of the resonance frequency, as respectively shown in the top right and bottom right graphs of Fig. 4.1. In fact, we can define an interval of frequencies $[f_{\text{res}} - f_\epsilon, f_{\text{res}} + f_\epsilon]$ in which the phase response approximates the desired linear phase characteristic sufficiently well, meaning that the actual phase response of the ORR differs from the desired linear phase characteristic less than a maximum phase error ϕ_ϵ that can be chosen as little as desired.

Delay bandwidth

In the antenna applications, the deviation ϕ_ϵ between the desired phase and the actual phase should be as little as possible, ideally zero, to avoid degradation of the produced array factor [4]. For this purpose, a maximum value for the phase error can be determined from the system specifications. In practice, from Fig. 4.1 it can be seen that the bandwidth $[f_{\text{res}} - f_\epsilon, f_{\text{res}} + f_\epsilon]$ in which the delay is sufficiently flat (or the phase response is sufficiently linear) reduces by increasing the amount of delay (or increasing the phase slope).

   This condition, together with the consideration described so far, leads to the important conclusion

 • *For a fixed value of maximum phase error, the frequency interval over which the phase error is below the allowed maximum decreases when increasing the amount of required delay, and vice versa.*

   This statement expresses the inherent *trade-off* between *bandwidth* and *group delay* given when using a single ORR as a group delay element. According to the discussion done so far, this value will determine a maximum frequency interval, or frequency band, over which the delay element can be effectively used.

Multi-ring resonator delay units

The limitation imposed by the bandwidth-delay trade-off given by a single ORR filter can be removed by *cascading* multiple ORRs units. Because of their full tunability, it is possible to cascade more ORR units and tune them in order to approximate the desired phase response over a wider bandwidth (see dotted line in Fig. 4.2), with no inherent percentage bandwidth limitation.

   The total response of a cascade of linear time-invariant (LTI) filters can be obtained as the product of the individual responses. As a consequence, the total phase response of the cascade is the sum of the phase responses of the individual ORR filters, and so is for the group delay response. Thanks to the full tunability of the individual delay responses, in terms of both resonance frequency and quality factor (Fig. 4.1), it is possible compose the responses and consequently to shape the total group delay response in such a way to give a flat delay response over a larger bandwidth than when using a single ring resonator. Equivalently, this corresponds to a phase response that can be kept approximately linear, with a phase error (below the maximum imposed by the specifications) over a larger frequency band than when using a single ORR. This is shown for the example of three ORRs in Fig. 4.2.
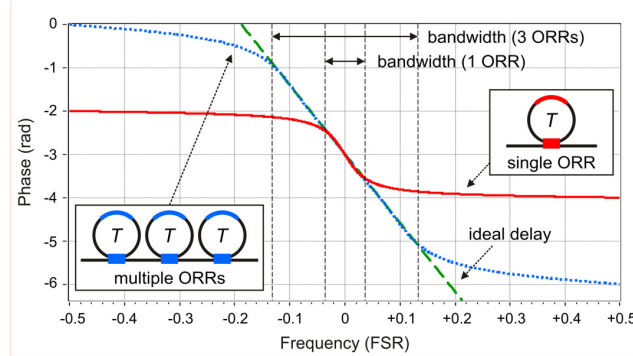
Figure 4.2: Phase response of a single ring resonator (red solid line) and of the cascade of 3 ring resonators (blue dotted line) compared with the phase response of an ideal delay line (green dashed line)

Similarly to the discussion given for a single ORR, in case of a delay element composed by multiple ORRs it can be observed that

- *In an optical delay line composed by a cascade of multiple ORRs, a trade-off exists among maximum delay, delay bandwidth, phase error (or delay ripple) and number of ORRs.*

In practice, given the required group delay τ_g, the ripple ϕ_ϵ can be made arbitrarily small by either bringing the resonance frequencies of the different ORRs closer to each other (thus reducing the delay bandwidth, *BW*) or by increasing the number of rings N of the cascade (thus increasing the complexity of the delay element).

In the common case of a practical antenna array application, the operating bandwidth is generally specified; the maximum tolerated phase error can be derived from the specifications in terms of beam pointing accuracy; the maximum delay for each delay section is determined in conjunction with the maximum steering angle and by the array architecture. In this case, the complexity of the delay elements increases when reducing the tolerable phase error, and with increasing values of the required maximum delay and the required optical bandwidth. The final complexity of the delay units and, in turn, of the complete beamformer, will depend upon those factors as well as the spectral efficiency of the chosen optical modulation format, as will be described in more detail in the following discussion.

4.1.2 Optical combiners

The summation in Eq. (2.47) indicates that the signals received by the individual elements must be combined not only with specific delays, but also with proper amplitude weighting terms in order to form the beam pattern according to the desired
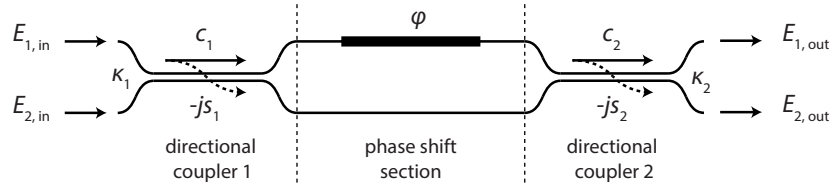
Figure 4.3: Schematic layout of a Mach-Zehnder interferometer used as combiner

array design criteria [148]. This can be achieved by properly tuning the coupling ratio among the signals originating from the individual antenna elements.

For this purpose, it is desirable to have a combining unit that can be tunable through a wide range of values (coupling factor ideally ranging from 0 to 1). In this way, it is possible to combine two channels and provide them with the desired amplitude coefficient using a single device. A possible solution can be implemented in integrated optics by employing the Mach-Zehnder interferometer (MZI) structure, which consists of two cascaded 3 dB couplers connected by two optical waveguide branches, with a tunable optical phase shifter in one arm [143, 147]. A schematic view is shown in Fig. 4.3.

4.2   Network Architecture

Thanks to the integration possibilities offered by integrated optical technology [24], the individual delay elements and the optical combiners described in Subsections 4.1.1 and 4.1.2 can be properly arranged in a single optical chip, in order to create different programmable delay paths between each input (corresponding to an individual antenna element) and the output, with tunable delay and amplitude levels.

An example of a binary-tree OBFN is shown in Fig. 4.4 for a 16×1 OBFN, consisting of four sections, 16 inputs ports and 1 output port. In this design we employ a binary-tree topology, which allows to realize increasing tuning delay ranges as required in a linear phased array. The path connecting Input 1 to the output is considered the reference path, the one with minimum delay. A binary-tree structure allows to generate the desired delay and amplitude profile distribution [148], (see Chapter 2), and at the same time to minimize the complexity of the network, as shown for example in [33]. Different architectures can also be of interest in other cases, as highlighted for example in [143] and in Chapter 7.

The final architecture of the beamformer will be designed based on several aspects. First of all, the number of input-output channels will depend on the number of antenna elements of the array, in conjunction for example with the fact that there might or might not be a pre-combining of the multiple AEs in the electrical domain before optical processing. The type of array (linear, planar, or conformal), the operating RF frequency, the antenna element spacing and the maximum required beam steering angle will determine the amount of delay needed in each
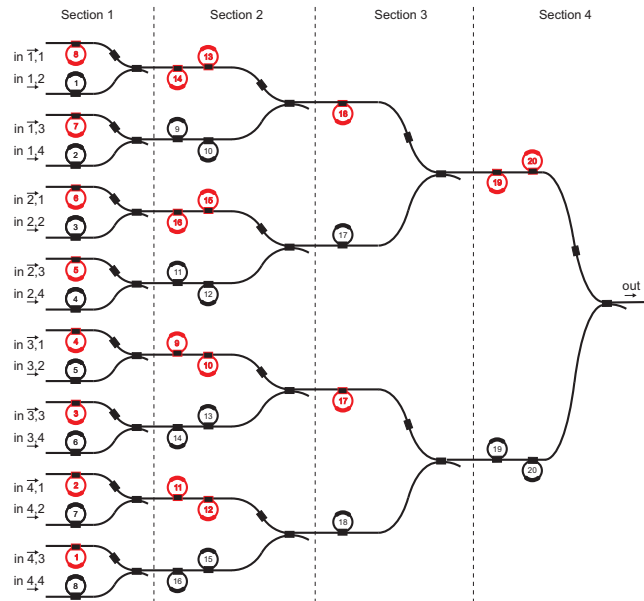
Figure 4.4: Schematic layout of a binary-tree 16×1 OBFN

path, and thus, according to the discussion given in an earlier stage, the complexity of each delay unit. Another important aspect to determine the complexity of the delay units is the required optical bandwidth, that depends on the operating RF bandwidth, and the optical modulation technique that will be employed when converting the RF signal to a modulated optical signal, a necessary step in order to perform the RF signal processing in the optical domain (see Chapter 3).

Given this large number of factors influencing the design of a beamformer, different aspects will be discussed in separate sections. First, the possible modulation techniques will be overviewed and the chosen one will be described in more detail. Then, a system analysis will be given in the general case. Finally, a case study will be considered and the design of the corresponding beamformer will be described in detail. *One of the scopes of this chapter is to provide a design tool for OBFNs based on ORR delay units. The case study can be seen as an example of design that can be used as a guide to multiple other specific cases.*

4.3 System Analysis

In the practical applications, the optical beam forming network constitutes the *processing core* of an optically beamformed antenna array system. This system is composed by multiple parts and components. The choice of (*i*) the signal processing technique employed, (*ii*) the system architecture, and (*iii*) the components and

their parameters will determine the final performance of the phased array system. Those three items will be discussed in the following subsections.

The optical beam forming network is incorporated in what will be referred to as *optical beam forming system*. A schematic of the OBFN system is shown in Fig. 4.5.
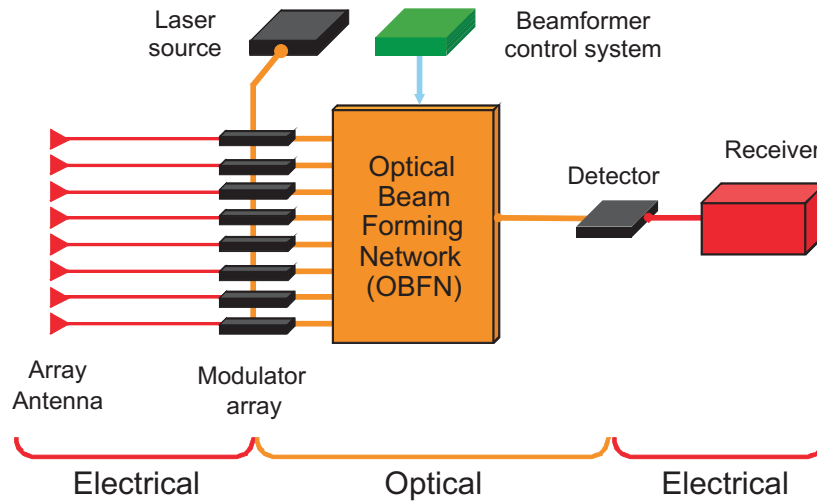
Figure 4.5: System setup of the optical beam forming system for phased array antennas

4.3.1   Photonic Signal Processing Techniques

As discussed in Chapter 3, in a microwave photonic signal processing system the RF signal to be processed has to be converted to the optical domain, and converted back to the electrical domain, respectively prior and after optical processing. The way in which the E/O conversion is performed will influence the choice of the technique to be employed in the inverse O/E conversion. A complete discussion on the design of optical modulation and detection scheme for the integrated optical beamformer has been presented in [33] and is summarized here.

The aim that is kept into consideration when choosing the modulation and detection techniques for optical beamforming is threefold. First, the trade-off between bandwidth, amount of delay, delay ripple and complexity of the delay element described before requires to keep the optical delay bandwidth as small as possible in order to simplify the structure of the individual delay elements and, ultimately of the OBFN chip itself. In addition to that, the modulation and detection schemes should be as simple and low-cost as possible to implement, especially in the case of complex beamformers feeding an array with a large number of antenna elements. Finally, according to the discussion given in Chapter 3, any microwave photonic processing system is required to have a minimum impact on

the spurious-free dynamic range of the total system, that should be kept as large as possible. This translates into the requirement to keep loss, noise and non-linear distortion of the processor as low as possible.

Narrowband optical sources

A first design step in order to keep a low bandwidth need for the delay element, is to choose light sources that are narrowband when compared to the bandwidth of the modulating information signals. In this way, the bandwidth of the modulated optical signals to be processed will be determined by the optical modulation, and not by the bandwidth of the optical source signal.

Direct modulation vs external modulation

After choosing the type of optical source, we need to choose the most suitable type of optical modulation, again taking into consideration the aforementioned criteria of bandwidth, simplicity, and impact on the dynamic range. The simplest approach to perform E/O conversion would be to use a directly modulated laser for each antenna element. Unfortunately, direct modulation of a laser causes frequency chirping and consequent spectral broadening [40], the dynamic range would be limited by the high noise and distortion levels at high frequencies [38], [39], and finally the use of separate lasers (one per AE) would create optical beat interference noise.

The alternative solution is to perform E/O conversion by external modulation of a *common* continuous-wave (CW) laser source and using coherent optical combining on-chip. This allows to employ a coherent optical approach which solves the problems described before, related to the use of multiple laser sources. To be able to implement this solution, the coherence length of the laser shall be much larger than the maximum delay path length difference among the delay channels: in this way it is possible to maintain optical coherence between the different delay paths and, provided the possibility to adjust the relative optical phases between the paths, it is possible to maintain a condition of coherent combining.

Optical modulation format: intensity modulation (IM)

Once it is made clear that the best choice is to use a common, narrow-linewidth laser, we can proceed discussing the most suitable type of optical modulation. Thanks to its simplicity, the most immediate choice would be *intensity modulation (IM) and direct detection (DD)* by means of a photodiode. IM can be implemented by means of a Mach-Zehnder modulator (MZM) or an electro-absorption modulator (EAM). Let us analyze how this choice impacts on the design of the optical delay units.

Let us consider an information signal originating from each antenna element as a bandpass signal, with a frequency bandwidth between f_{min} and f_{max}, and a central RF frequency f_{RF}.

The optical intensity is proportional to the square of the optical field ($I \propto |E|^2$), thus optical intensity modulation would generate an optical field which is propor-

tional to the square-root of the modulating signal, and not to the modulating signal itself. Thus the generated optical spectrum at the modulator output would consist of the optical carrier plus a theoretically infinite number of sidebands. In practice, only a finite number of sidebands will be significant, and this number will increase with the modulation depth. To minimize the complexity and the linear distortions, the modulation index can be chosen in such a way that only the sidebands of first order are significant. In this way the delay elements in the OBFN can be designed so as to provide a flat group delay response only over the bandwidth covering the optical carrier, indicated as f_o, and the first order sidebands. As a result of this discussion, the minimum optical bandwidth required to perform optical beamforming in case of IM/DD is equal to twice the maximum frequency of the modulating RF signal, that is, $2(f_{RF} + f_{max})$.

In fact, the delay unit should provide a flat delay response, or a linear phase response, over the whole optical frequency range spanning between the lowest frequency component of the first lower sideband, up to the highest frequency of the first upper sideband, that is, $[f_0 - f_{RF} - f_{max}, f_0 + f_{RF} + f_{max}]$, that corresponds to a bandwidth of $2(f_{RF} + f_{max})$.

Note the limitation that this approach poses on the maximum value of the absolute RF operating frequency. In fact the required delay bandwidth does not only depend on the bandwidth of the actual information signal ($f_{max} - f_{min}$) but also on the RF carrier frequency itself (f_{RF}), undesirably limiting the use of this approach to relatively low RF carrier frequency applications. In fact, especially in case of high-frequency PAAs with large diameters, the use of delay elements able to provide the desired delay over the complete bandwidth would lead to an excessively complex OBFN in terms of practical realization, due to the trade-off discussed previously in this section.

From the trade-off discussion provided when describing the operating principle of a ORR-based optical delay line, it started to become clear that the delay bandwidth is a "precious" resource, in the sense that it is obtained at the expense of other desirable characteristics, as maximum delay, delay flatness, and complexity.

From the previous discussion over intensity modulation, however, it is immediately clear that the IM/DD approach is not "delay bandwidth efficient", in the sense that a large amount of the delay bandwidth is not used to delay an actual information signal, but instead it provides a linear phase slope also over a large frequency range, $f_o - (f_{RF} - f_{min})$ to $f_o + (f_{RF} - f_{min})$, which does not carry any information. In addition to that, only one of the two sidebands would be sufficient to recover the whole information signal after optical processing. The optical carrier is only employed for O/E conversion. Thus a better choice would be to employ an optical modulation format that is more delay bandwidth efficient.

Optical single-sideband suppressed-carrier modulation (OSSB-SC)

A much more attractive possibility would be to employ an optical single-sideband suppressed-carrier (OSSB-SC) modulation format. The RF signals originating from the different AEs could be optically modulated by removing one of the sidebands

and the optical carrier.In this way the optical bandwidth to be delayed would only correspond to one RF sideband, and the required optical delay band for all the delay units would be $[f_0 + f_{min}, f_0 + f_{max}]$, which corresponds to a bandwidth of $(f_{max} - f_{min})$, lower than in the IM case, and has the additional important advantage of being now *independent* from the RF carrier frequency f_{RF}.

After delay, those modulated signals can be optically combined *coherently* into a single waveguide of the OBFN. The phases of each sideband can be adjusted relative to each other using optical programmable phase shifters. At this point, the optical carrier can be re-inserted in the combined signal, to form an optical single-sideband full-carrier (OSSB-FC) signal, that can be converted back to the electrical domain using a photodetector (PD). When the O/E conversion is realized with a PD consisting on a balanced photodiode pair, the even-order distortions can be suppressed and the effect of relative intensity noise (RIN) can be considerably reduced (see [22, 149]) when compared to the use of an unbalanced photodetector.

Different techniques can be used to implement OSSB-SC modulation. Those can be classified in three groups. Filter-based techniques first implement IM and then use one or more bandpass filters to remove the carrier and the undesired sidebands. Optical heterodyning techniques use two optical carriers, one of them is intensity modulated using the baseband information data and then mixed to the other unmodulated optical carrier for frequency translation. This approach is convenient in the cases in which baseband information data are available, for example in beamformers that feed a transmit phased array antenna. Finally, techniques based on the phase-shift method are based on the use of two quadrature carriers and a Hilbert transformer. Optical implementation allow multi-octave operation but usually require a complex setup, e.g. using a dual-parallel MZM [150].

For this particular application, the most attractive solution consists of the filter-based technique. In fact, this requires only one laser for all the AEs, one intensity modulator per AE and also one OSBF per AE, placed directly after each intensity modulator. With this approach, every AE would require its own OSBF. However, thanks to the linearity of both the OSBF and the OBFN, their order can be reversed, in such a way that only one common OSBF can be placed at the OBFN output, after the combining point, to remove the undesired sideband of all AE signals. The resulting system architecture is shown in Fig. 4.6. The preferred intensity modulator in this application is the Mach-Zehnder (MZM), being more linear than EAMs and being able to inherently suppress the optical carrier with proper biasing, thus making less stringent the requirements on the OSBF selectivity.

There are multiple possible choices in the OSBF implementation. A relatively simple solution consists of an MZI with an ORR in one of its arms [24, 151]. This architecture provides broad and flattened passbands and stopbands, and since such an OSBF consists of the same building blocks as the OBFN, that are, ORRs and directional couplers, both the OBFN and the OSBF can be integrated on the same chip.

Synchronization of the optical phase

The proposed OBFN system uses a single laser. As discussed previously, this allows to implement a optical *coherent* beamformer. This requires the possibility to set and to maintain an optical coherence condition in each combining point, in such a way that the optical signals in each delay path are synchronized at wavelength level.

In practice, maintaining optical synchronization is not a trivial problem, especially in the case in which optical fibers are present between the splitting and the combining points. In the experimental setup that will be described in the next chapter, the splitting and modulation were done by means of commercial, fiber-based components, that were connected to each other and to the integrated chip by means of optical fibers. This makes the optical phase of the signals very sensitive to temperature changes and to mechanical stress and vibrations. Different solutions to stabilize the OBFN response have been proposed [33]; finally, a temperature stabilization approach has been employed in the tests [33, 152].

In the ongoing implementation of the beamformer, however, the complete optical circuit, that is, all parts between the laser and the photodetectors, including the modulators, is expected to be integrated on a single chip. This would make the optical phase in the system much less sensitive to mechanical vibrations and stress, since no fiber optics will be used between the splitting and combining points, and the fact of having all the optical components integrated on a single chip will make the temperature much easier to control. In [33], an analysis of the effects of temperature fluctuations was performed, showing the feasibility of the proposed temperature control scheme.

4.3.2   System Architecture

After the analysis and selection of the desired modulation format, it will now be described the system architecture (Fig. 4.6) based on which the system analysis will be performed. In this discussion, it is assumed that the modulation format has been chosen according to the discussion reported in Sec. 4.3.1, that is, an optical single-sideband suppressed carrier (OSSB-SC) modulation.

Let us suppose the phased array is composed of N antenna elements. The optical power from a continuous wave (CW) laser (Fig. 4.6a) is split into N paths (b), where N is the number of OBFN inputs. In each path, the light enters the optical input of a modulator. The RF signal originating from each antenna element (c) enters the RF port of the corresponding modulator. The modulator is set in such a way to provide an optical output signal with the desired modulation format. In particular, in case of Mach-Zehnder modulators (MZM), the bias point will be chosen to give the minimum optical transmission, thus maximizing the suppression of the optical carrier. This will yield an optical double-sideband suppressed carrier (ODSB-SC) modulation at the output of each MZM (d).

The modulated signals are then inserted into the corresponding OBFN channel to be delayed and combined as desired (e), according to Eq. (2.47). As described in the previous section, the ORRs used as delay filters provide the desired delay (or,
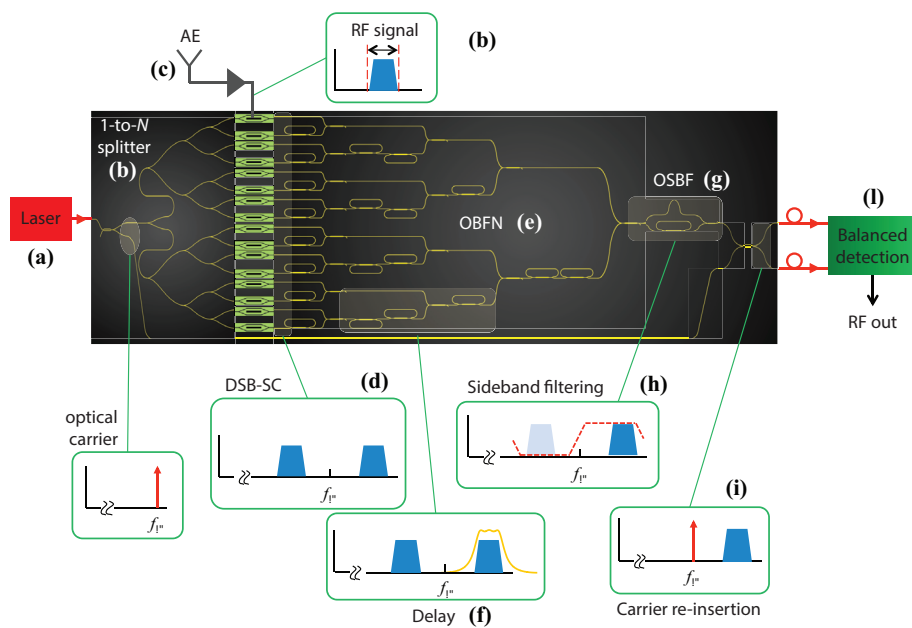
Figure 4.6: System setup of the optical beam forming system for phased array antennas (picture edited from [153], with permission)

equivalently, the desired phase slope) only across a limited bandwidth. The ORRs of the OBFN are tuned in such a way to provide delay only over one specific sideband (the upper sideband or the lower sideband) of the ODSB-SC modulated signal obtained by each of the MZMs (f). After the signals are combined by the binary-tree network, the combined signal enters an optical sideband filter (OSBF, g). This filter has been realized in the same chip as the optical beamformer [147], and has the function to suppress the lower sidebands for all the signals, and to further suppress the optical carrier (h).

The resulting signal at the output of the OSBF filter is the combination of the signals received by the individual antenna elements with proper delays and amplitude weighting, modulated on the optical carrier with OSSB-SC modulation. This optical signal can be transferred to the electrical domain using an electro-optical converter. As discussed in the previous section, the simplest solution is the use of direct detection. For this, the optical carrier needs to be reinserted[2] and this can be done by tapping off a part of the laser power, routing it to the carrier re-insertion coupler which is also integrated on-chip, cascaded to the OSBF (i). The carrier re-insertion coupler has a double output that can be routed to a balanced photodetector for direct detection (l).

4.3.3 System Parameters and Performance Analysis

The system analysis of the optical beamformer system has been derived and presented by Meijerink *et al.* in [33]. For convenience here we repeat the mathematical results as a starting point for an extended discussion on the implications that those results have on the choice of the parameters in a practical beamformer design application.

System Modelling

The system analysis [33] models the beamformer system as a 2-port RF network, characterized by three fundamental parameters, namely *gain*, *noise figure* and *non-linear distortions*. First, the system has been modelled in order to obtain the relation between the input voltage (to the modulators) and the output current (from the photodiode). The result has then been employed to derive the expressions of gain, noise figure and non linearities. Finally, those relations have been used to determine an expression for the carrier-to-noise ratio at the beamformer output.

The beamformer system can be modelled as a N-inputs, 1-output RF network. According to the system description given before, each input corresponds to an antenna element (AE) with an antenna gain G_{AE}, cascaded to a low-noise amplifier (LNA) with gain G_{LNA} and effective noise temperature at the input T_{LNA}. This $N \times 1$ network can be reduced to a 1×1 network having the same input and output powers P_{in} and P_{out}, respectively, but composed by an "equivalent", single antenna

---

[2]The amount of optical power of the carrier that is being re-inserted can be adjusted by a proper choice of the coupling factor of the directional couplers used in the splitting of the carrier and the one used for the carrier re-insertion. The carrier phase can also be adjusted to match the one of the information signal by a tunable phase shifter.

with gain G_a and an "equivalent" 2-port RF network with gain G_{rec}. The "equivalent" system has a power gain $G_{sys} = G_a G_{rec}$ and an effective noise temperature (again, at the input of the "equivalent" 2-port network) $T_{sys} = T_a + T_{rec}$. T_a includes the effects of the sky noise (cosmic microwave background radiation, atmospheric noise, earth noise, interfering extraterrestrial sources) and T_{rec} models the equivalent noise temperature of the LNAs and of the OBFN, reported to the input.

Relation between input voltages and output current

The first step towards the derivation of the system parameters as a function of the parameters of its constituting components (laser, OBFN, modulators, detector), is to obtain the relation between the input and the output signals in the optical beamformer. The relation has been derived in [33] as

$$I_{out}(t) = -\frac{\pi R_{pd} P_o}{2 V_\pi L_{lc} L_{cd}} \sqrt{\frac{\kappa(1-\kappa)}{N L_{mp} L_{up}}} \sum_n a_n V_n(t - \tau_n) + I_{sn,out}(t). \quad (4.7)$$

where

- R_{pd} is the responsivity of the photodetector [A/W]

- P_o is the optical power provided by the laser [W]

- V_π is the RF half-wave voltage of the MZM

- L_{lc} is the coupling loss between the laser and the circuit

- L_{cd} is the coupling loss between the circuit and the photodetector

- κ is coupling coefficient of the directional coupler used to prelevate a part of the laser power for carrier reinsertion before direct detection

- N is the number of OBFN inputs

- L_{mp} is the optical loss given by the chip in the modulated signal path

- L_{up} is the optical loss given by the chip in the unmodulated signal path (for carrier re-insertion)

- a_n is the n-th amplitude tapering coefficient

- V_n is the input voltage at the n-th modulator

- τ_n is the delay provided by the N-th channel of the beamformer

- $I_{sn,out}$ is the shot noise current

Gain of the OBFN system

In the equivalent 1×1 model of the system, we defined

$$G_{\text{sys}} = G_{\text{a}} G_{\text{rec}} \qquad (4.8)$$

It is possible to derive the expressions of those gain terms by using Eq. (4.7) to relate the inputs and output of the system in terms of power. If we assume that the input voltages $V_n(t)$ are combined coherently, it can be shown [33] that the *coherent gain* or *signal gain* is given by

$$G_{\text{sys}} = \frac{G_{\text{AE}} G_{\text{LNA}} R_{\text{m}} R_{\text{L}} (\pi R_{\text{pd}} P_{\text{o}})^2 \kappa (1-\kappa) \eta_{\text{t}}}{4 (V_\pi L_{\text{lc}} L_{\text{cd}})^2 L_{\text{mp}} L_{\text{up}}}, \qquad (4.9)$$

where

- η_{t} is the so-called *taper efficiency*, defined as $\frac{1}{N} \left(\sum_n a_n \right)^2$, which equals 1 for uniform tapering

- R_{m} is the input impedance of the MZM

- R_{L} is the load impedance on which the photocurrent given by Eq. (4.7) is dissipated.

Instead, the *incoherent gain* or *noise gain* is given by

$$G_{\text{rec}} = G_{\text{LNA}} G_{\text{OBF}}, \qquad (4.10)$$

with

$$G_{\text{OBF}} = \frac{R_{\text{m}} R_{\text{L}} (\pi R_{\text{pd}} P_{\text{o}})^2 \kappa (1-\kappa)}{4 N (V_\pi L_{\text{lc}} L_{\text{cd}})^2 L_{\text{mp}} L_{\text{up}}}. \qquad (4.11)$$

This last equation represents the *intrinsic receiver gain* of the beamformer.

Noise equivalent temperature of the OBFN system

In the 2-port system model, it was defined

$$T_{\text{sys}} = T_{\text{a}} + T_{\text{rec}}. \qquad (4.12)$$

The effective input noise temperature of the equivalent receiver, using Friis' formula [154], can be written as

$$T_{\text{rec}} = T_{\text{LNA}} + \frac{T_{\text{OBF}}}{G_{\text{LNA}}}, \qquad (4.13)$$

where T_{LNA} is the effective noise temperature at the input of the LNAs, and the contribution to the system noise temperature due to the noise in the optical beamformer is represented by $T_{\text{OBF}}/G_{\text{LNA}}$. T_{OBF} indicates the effective input noise temperature of the equivalent 2-port model of the beamformer described before, without LNAs. In [33] it was shown that T_{OBF} is given by

$$T_{\text{OBF}} = \frac{8 N V_\pi^2 L_{\text{lc}} L_{\text{cd}} L_{\text{mp}} (e \kappa R_{\text{pd}} P_{\text{o}} + I_{\text{rms}}^2 L_{\text{lc}} L_{\text{cd}} L_{\text{up}})}{k_{\text{B}} R_{\text{m}} (\pi R_{\text{pd}} P_{\text{o}})^2 \kappa (1-\kappa)}. \qquad (4.14)$$

Compression in the OBFN system

Due to the non-linearities in the MZM response, and in the hypotesis of low CNR of the signals reaching the individual antenna elements, it can be shown [33] that the total system gain G_{sys} expressed by Eq. (4.9) is reduced by a factor

$$\Delta G = \exp\left(-\frac{\pi^2 k_B (T_{AE} + T_{LNA}) B_{LNA} G_{LNA} R_m}{4 V_\pi^2}\right). \tag{4.15}$$

Carrier to noise ratio

Let us now suppose that the phased array antenna is employed in a telecommunication system with multiple channels. Each information channel will have an equivalent noise bandwidth B_{ch}. It is generally of interest to calculate the carrier-to-noise ratio (CNR) for one channel at the output of the phased array receiver, as this constitutes an important quality factor in telecommunication systems. Following from the equations derived in [33] and summarized before, the CNR is

$$\begin{aligned}
\mathrm{CNR} &= \frac{G_{sys} P_{in}}{G_{rec} k_B T_{sys} B_{ch}} = \frac{G_a}{T_{sys}} \frac{P_{in}}{k_B B_{ch}} \\
&= \frac{P_{in} G_{AE} \eta_t N}{k_B \left(T_a + T_{LNA} + T_{OBF} / (G_{LNA} \Delta G)\right) B_{ch}}
\end{aligned} \tag{4.16}$$

as a function of the quantities reported previously.

4.4 System Design

To describe the approach that has been used for the system design, we employ a practical example initially presented in [33]. An optically-fed phased array antenna is used to provide wideband reception of the Digital Video Broadcasting by satellite (DVB-S) band 10.7-12.75 GHz on mobile platforms (e.g. airplanes). This band lays partly over the X-band and partly over the K_u-band[3].

Within the Memphis project [155], the construction of a technology demonstrator for this type of application is one of the milestones for the "Advanced Optical Beam Forming Networks" work-package, in the framework of which this work has been funded. Therefore, a number of system requirements have been layed out before the design and construction of the technology demonstrator subsystems and their assembly (see Chapter 1). Based on those requirements, and using the system analysis results reported here, the design of the beamforming system has been realized and summarized in the following.

4.4.1 System requirements for DVB-S applications

ETSI standards define the requirements for the DVB-S receivers [156]. In particular the carrier to noise ratio at the front-end output should not be lower than

---

[3] as defined from the Radio Society of Great Britain (RSGB): X-band, 8-12 GHz; K_u-band, 12-18 GHz.

8 dB to be able to guarantee correct operation with a standard DVB-S back-end receiver/decoder. This CNR is defined over a single channel bandwidth of 33 MHz. It is assumed that the maximum reception angle in which the antenna will be used is in the order of, or lower than, ±60 degrees with respect to broadside (see Chapter 1 for the specifications and Chapter 2 for the definition).

4.4.2   Choice of the subsystem parameters

The system scenario and the corresponding system requirements impose a choice of the parameters of the subsystems that compose the phased array receiver system, as described in the following.

Antennas

The received power[4] from telecommunication satellites in Europe is in the order of -150 dBW. It is common to consider a safety margin to account for varying atmospheric conditions, which in this example will be chosen equal to 10 dB. We assume the LNAs used match the specifications of commercial low-noise block-downconverters (LNBs), with a gain of 70 dB and a noise figure of 0.7 dB (T_{LNA} = 50 K). With an assumption that the brightness temperature of the sky is T_{sky} = 50 K, from the results of the system analysis described before it is possible to derive a requirement on the minimum antenna gain G_a in the order of 35 dBi.

Let us now consider a planar array, with N elements placed on a rectangular lattice on the x and y axes of a cartesian reference coordinate system, as in Fig. 2.10. For the condition of absence of grating lobes for all scanning angles, which has been derived in Chapter 2, the inter-element spacing along the x and y axes is chosen to be lower than half-wavelength at the highest operating frequency (12.75 GHz). This results in a spacing of 11.8 mm. If we consider a maximum scanning angle of ±60 degrees as for the system requirements, and a uniform excitation (see Chapter 2), from the array factor calculations using the Eq. (2.79) it can be derived that the minimum number of radiating elements required to have sufficient antenna gain for all the scanning angles is 1830. Since in Section 4.2 we have motivated the use of a binary tree structure for the optical beamformer, it is desirable to round the number of AEs to a power of two, which in this case will be N=2048.

As for the current development status of the OBFN, it is not feasible to realize a photonic beamformer chip with thousands of delay channels. For this reason, a two-level modular configuration is proposed, as shown in Fig. 4.7. In this design 32 parallel OBFN chips with 64 inputs each (64 × 1) are used as a first beamforming stage. Their outputs are combined in a second stage consisting of a single OBFN chip with 32 inputs (32 × 1). RF amplifiers are added between the first and second stage to increase the total CNR.

---

[4]This value has been calculated using Friis' formula and the EIRP data available from the Astra satellite transponder description, available at [157].
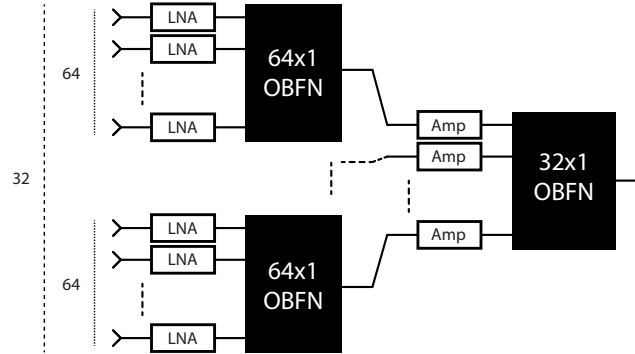
Figure 4.7: Modular architecture of the OBFN system

Optical Modulators

The optical modulators used in the system performance analysis here are MZMs. The insertion loss of the modulator (defined at the highest transmission point) is 2 dB and the RF half-wave voltage (V_π) is 1.0 V. This half-wave voltage can be regarded as the sensitivity of the MZM. Lower value indicates better sensitivity and performance. Note that the assumption made for the modulator characteristic, notably in terms of V_π is quite optimistic; currently only very limited commercial products that can provide this characteristic.

OBFN Chip

The required delay tuning ranges in each OBFN path can be determined based on the antenna geometry, the element spacing and the desired scan angle. In this example, we employ a planar array with separable illumination with AE spacing is 11.8 mm, which gives a maximum tuning range between adjacent elements of approximately 34 ps. In [158] we have presented a method to determine number of ORRs required in each delay unit based on the maximum delay tuning range in each path, ultimately determining the OBFN layout. The calculations for our example have been reported in Appendix B.

As for the optical losses in the OBFN chip, it is assumed that coupling losses from the laser and to the detector are in the order of 1 dB. We assume a waveguide loss of 0.05 dB/cm, which is seen as a realistic value considering the latest results [24]. Later on, we will simulate various values of the waveguide loss, in order to determine a range of values in which the system performs well. Assuming 0.05 dB/cm waveguide loss, it has been shown [33] that the total losses, in the path followed by the modulated signal, of the 64×1 and the 32×1 OBFNs are 4.7 dB and 3.5 dB, respectively.

Amplifiers

The LNAs and the RF amplifiers shown in Fig. 4.7 play an important role in the performance of the whole system. It can be shown that the optical beamformer does not degrade the performance of the receiver system in which it is applied, provided that proper amplifiers are used, and that the optical losses are kept sufficiently low. In Subsection 4.4.3 we will see that the LNA should provide at least 70 dB of amplification with a noise figure below 0.8 dB. The RF amplifiers at the second stage have lower constraints and a gain of 30 dB should suffice to achieve the desired 8 dB CNR. These amplifiers are not restricted to be low noise amplifiers.

Laser and Balanced Photodetector

The laser source in the system is a distributed feedback (DFB) laser with an output optical power of 100 mW and a relative intensity noise (RIN) of -150 dBm/Hz. It is assumed that the laser is temperature stabilized.

The balanced photodetector (BPD) has a responsivity of 0.8 A/W and a common-mode rejection ratio (CMRR) of 30 dB. The BPD output impedance is matched to 50 Ω.

The derived system parameters are summarized in Table 4.1, below.

Table 4.1: Key parameters of the OBFN system for DVB-S applications

Parameters	Symbol	Value	Unit
Frequency range	f_{range}	10.7 - 12.75	GHz
Number of AEs	N	2048	–
inter-element spacing	d	1.18	cm
sky temperature	T_{sky}	50	K
AE temperature	T_{AE}	150	K
Received RF power	P_{in}	-160	dBW
Minimum CNR (33 MHz BW)	CNR_{min}	8	dB
LNA gain	G_{LNA}	70	dB
LNA noise figure	NF_{LNA}	0.7	dB
Modulator insertion loss	L_{m}	2	dB
Modulator V_π	V_π	1.0	V
Optical waveguide loss		0.05	dB/cm
OSBF optical loss		0.25	dB
Second-stage amplification		30	dB
Input optical power		100	mW
BPD responsivity		0.8	A/W

4.4.3 Performance Analysis

Based on the parameters selected in the previous section, a performance analysis of the system has been performed in [153, 159] and the results are presented here. The system architecture together with the parameters from Table 4.1 are depicted in Fig. 4.8.
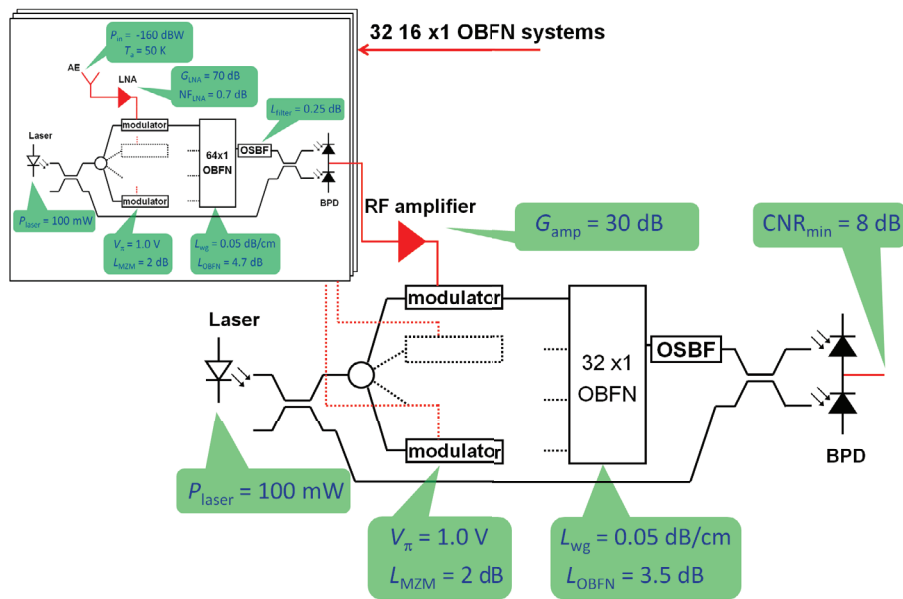
Figure 4.8: Two-level cascaded OBFN systems with the parameters (picture edited from [153], with permission)

In our analysis the system depicted above is simplified into a two-port cascaded systems as shown in Fig. 4.9. The contribution from the LNAs and the 64 × 1 OBFNs are incorporated in the equivalent receiver 1 with a gain and an effective input noise temperature of G_{rec1} and T_{rec1}, respectively. Correspondingly, the contribution of the 32 × 1 OBFN is included in the second equivalent receiver with a gain and an effective input noise temperature of G_{rec2} and T_{rec2}. The whole system can then be characterized as a two port system with a gain of $G_{\text{sys}} = G_a G_{\text{rec1}} G_{\text{rec2}}$ and an effective system noise temperature of $T_{\text{sys}} = T_a + T_{\text{rec1}} + T_{\text{rec2}}$, where G_a is the antenna gain and T_a antenna noise temperature. The details of this simplification are reported in [33].

This type of parametric performance analysis is very important in the design phase for the following reason. Based on this simplified model, a simulation of the CNR versus different system parameters is performed. When the value of the system parameters which are critical for the system performance are varied, this has a direct effect on the CNR. As a result of this analysis, it can be observed that a num-

ber of system parameters have a very strong effect on the overall performance. It is generally difficult to achieve low noise figure, high gain and low loss of the optical waveguide. Thus this analysis is crucial in the system design phase to determine within which boundaries the subsystem parameters can vary and still guarantee that the desired system specifications are satisfied. The figure of merit used is the CNR at the output which, as for the system requirements, should be at least be 8 dB in a 33 MHz channel bandwidth.
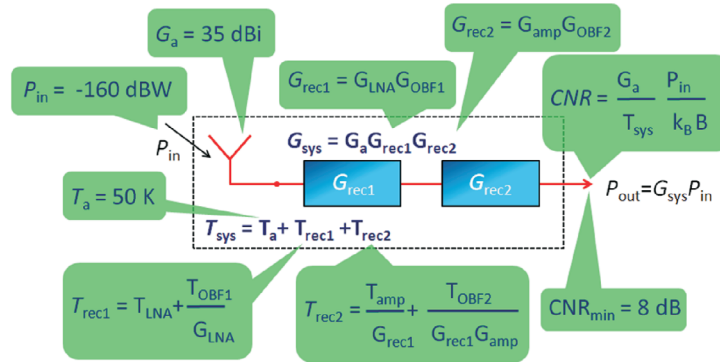
Figure 4.9: The equivalent two-port system model of the system depicted in Fig. 4.8
(picture edited from [153], with permission)

In Fig. 4.10, the CNR is depicted as function of the optical waveguide loss in dB/cm at three different conditions. First, the LNA gain and the modulator V_π are set at 70 dB and 1.0 V, respectively. These are, in fact, the target specification. With these parameters, the 8 dB CNR can be met for all waveguide loss values from 0 to 0.5 dB/cm (solid curve). But if the V_π increases to 4.0 V (which is the current status of the MZM modulator used in the system), the specified CNR can only be met with a waveguide loss below 0.2 dB/cm (dashed-curve). If now the LNA amplification is reduced to 60 dB, the CNR specification cannot be met even with lossless optical waveguides (dash-dotted curve). The graph depicts the importance of achieving low waveguide loss, high LNA gain and low modulator V_π. In these simulations, the LNA noise figure is set to 0.7 dB and the second-stage RF amplification is taken to be 30 dB, as suggested in Table 4.1.

In Fig. 4.11, the CNR is depicted as function of the LNA gain. As expected it shows a similar trend as the results in Fig. 4.10. The parametric study shows two groups of curves, the leftmost in the graph corresponding to $V_\pi = 1.0$ V, and the rightmost one to $V_\pi = 4.0$ V. For the intended specifications of $V_\pi = 1.0$ V and waveguide loss of 0.1 dB/cm, the required LNA gain is actually slightly above 50 dB (solid curve, leftmost group). This value increases to above 55 dB as the waveguide loss increases three-fold to 0.3 dB/cm (dash-dotted curve, leftmost group). As expected, higher amplification is needed if the V_π increases. For $V_\pi = 4.0$ V, the required LNA gain to achieve the 8 dB CNR is slightly more than 65 dB for 0.1 dB/cm waveguide
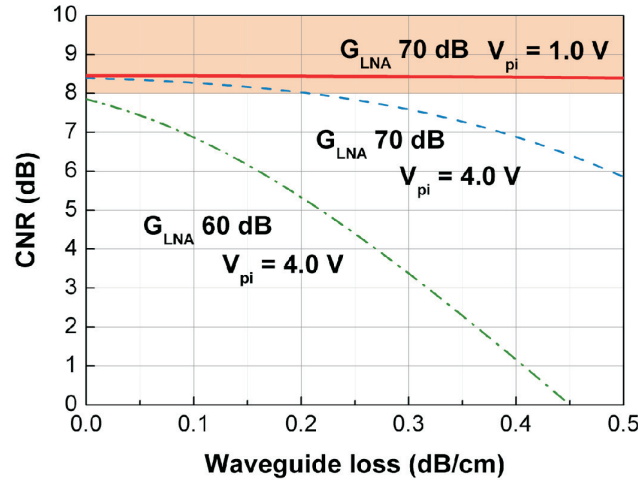
Figure 4.10: Simulated CNR for varying optical waveguide loss. The modulator half-wave voltage and the LNA gain are kept as parameters (picture edited from [153], with permission).

loss (solid curve, rightmost group), and even rises to 75 dB for a waveguide loss of 0.3 dB/cm (dash-dotted curve, lower group). Again, these results illustrate how the three parameters, the LNA gain, the waveguide loss and the modulator V_π values can be used to *complement each other* in order to meet the system specification.

In Fig 4.12, the impact of the LNA noise figure to the system CNR is shown. Here the LNA and the second-stage RF amplification gains are fixed respectively at 70 dB and at 30 dB. Four different conditions are considered: first, the waveguide loss of 0.2 dB/cm and the V_π of 1 V (solid curve). In this case, the minimum CNR of 8 dB can be achieved with an LNA noise figure lower than 0.8 dB. Deterioration in the modulator V_π (to 4.0 V in this case) limits the maximum acceptable LNA noise figure to a lower value of 0.7 dB (dashed curve). If further on the waveguide loss doubles to 0.4 dB/cm, the CNR specification cannot even be met with an LNA NF as low as 0.6 dB (dash-dotted curve).

For the sake of comparison, the case where the photonic part of the system is not the limiting factor is considered. In this case unrealistic parameters where the waveguide is lossless and the modulator V_π is very small (0.01 V) are used. Additionally, we also remove the laser relative intensity noise contribution of the laser, which was set to -150 dB/Hz in all other simulations. The resulting CNR as function of the LNA noise figure is shown as the dotted curve in Fig. 4.12. The curve does not deviate from the solid curve with realistic parameters of waveguide loss equal to 0.1 dB/cm and a V_π of 1.0 V. This result has a major implication that in the intended system architecture, that is, *the photonic section does not pose a limitation in the performance*. A second conclusion that we can draw is that *regardless of the*
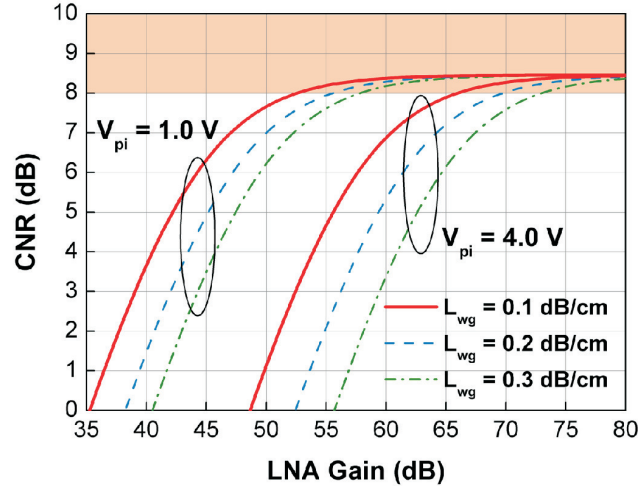
Figure 4.11: The CNR as a function of the LNA gain, for various waveguide loss and modulator V_π values (picture edited from [153], with permission).

*photonic system, a low LNA noise figure (below 0.8 dB) is required to achieve the CNR requirement.*

Finally in Fig. 4.13, the CNR as a function of the second-stage RF amplification is shown. The LNA gain and noise figure are set as 70 dB and 0.7 dB, respectively. As previously, the waveguide loss and the V_π values are varied. For $V_\pi = 1.0$ V and a waveguide loss of 0.1 dB/cm, the required CNR can be achieved without an additional amplification (solid curve, upper group). As the loss deteriorates to 0.2 dB/cm and subsequently to 0.3 dB/cm, the required amplification rises respectively to 3 dB (dashed curve, upper group) and 6 dB (dash-dotted curve, upper group). For the case of $V_\pi = 4.0$ V, the required amplification rises considerably. For low waveguide loss (solid curve, lower group), the minimum amplification should be slightly more than 20 dB. Doubling of this waveguide loss (dashed curve, lower group) increases the required amplification to at least 30 dB, and to at least 40 dB for a waveguide loss of 0.3 dB/cm. It can be concluded that for low V_π value the system is less sensitive to the deterioration of the waveguide loss.

The simulation results presented above show that there are very tight requirements for the LNA, modulator and the optical beamforming network. However, we have to emphasize on the fact that a safe margin of 10 dB has been taken into account on the received power from the satellite (-160 dBW instead of -150 dBW) in these simulations. Clearly, if the value of -150 dBW is used instead, all CNR values presented before will be raised by 10 dB, which considerably relaxes the system requirements. Thus, in the system requirement definition phase, it is imperative to accurately determine the realistic value of this received power.

Supposing that the power received by the antenna may vary between -160 dBW
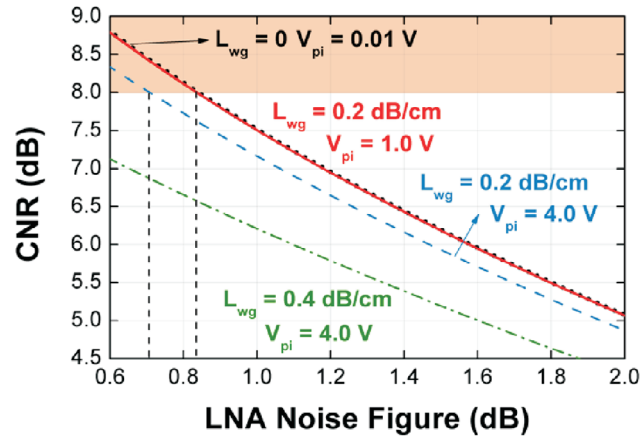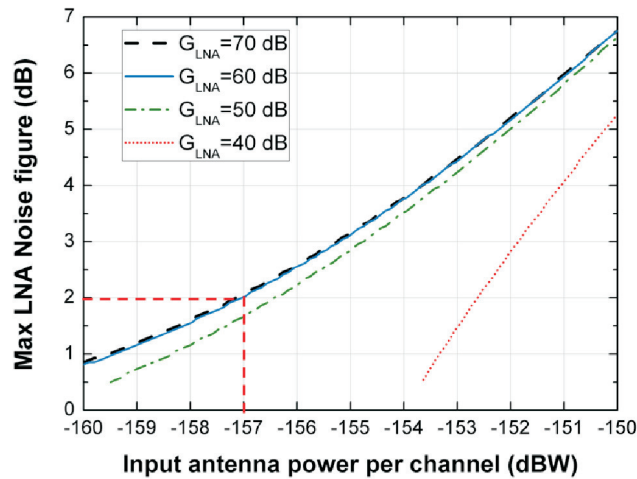
Figure 4.12: The CNR as a function of the LNA noise figure, for various waveguide loss and modulator V_π values (picture edited from [153], with permission).
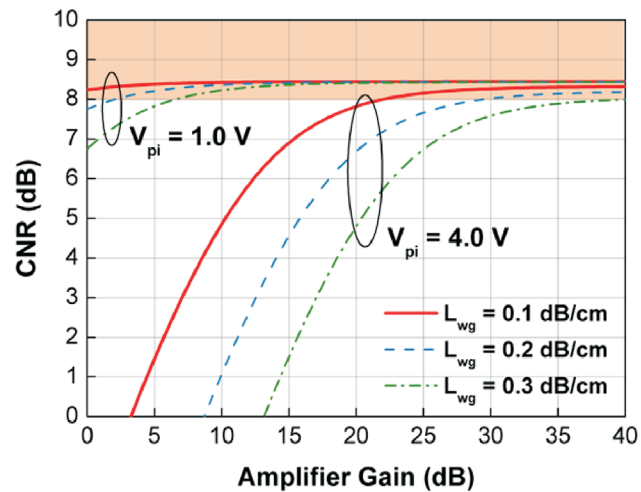
Figure 4.13: The CNR as a function of the second-stage RF amplifier gain, for various waveguide loss and modulator V_π values (picture edited from [153], with permission).

and -150 dBW, we can calculate the maximum allowed LNA noise figure for each received power, with the constraint to achieve at least 8 dB of CNR. In Fig. 4.14 this maximum LNA noise figure is depicted against the input power. Here we assume that the waveguide loss amounts to 0.1 dB/cm and the modulator V_π is 1.0 V. The figure shows that higher received power relaxes the LNA noise figure requirement quite considerably. For example, with a received power of -160 dBW and a LNA gain of 70 dB, the maximum allowed LNA noise figure to achieve the targeted CNR is around 0.7 dB. If now the received power is increased by 3 dB, i.e. the received power is -157 dBW, the maximum allowed noise figure goes up to 2 dB, which is substantially easier to achieve. This is indicated by the dashed red line in Fig. 4.14. Note that in this case the system still offers a 7 dB power margin from the assumed maximum received power of -150 dBW.

Figure 4.14: The maximum allowable LNA noise figure required to achieve a CNR of 8 dB depicted as a function of the received antenna power. The LNA gain is used as a parameter (picture edited from [153], with permission).

4.4.4   Alternative System Architecture

As mentioned earlier, the system performance investigations presented in this report have been performed in the architecture depicted in Fig. 4.16, where 32 OBFNs with a 64 × 1 architecture are used in the first stage.

However, the large scale of the 64 × 1 beamformer might pose a higher risk in system reliability, since the large OBFN should provide higher delay and might induce more loss. Furthermore, this system requires a large number of optical modulators (64) in one array which might lead to a low yield of the array. For this reason,
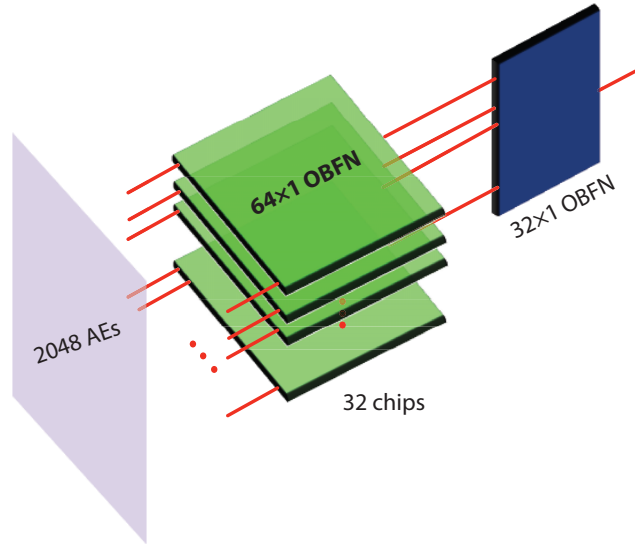
Figure 4.15: The original architecture of the OBFN system with 32 chips (each a 64×1 OBFN) at the first stage (picture edited from [153], with permission).
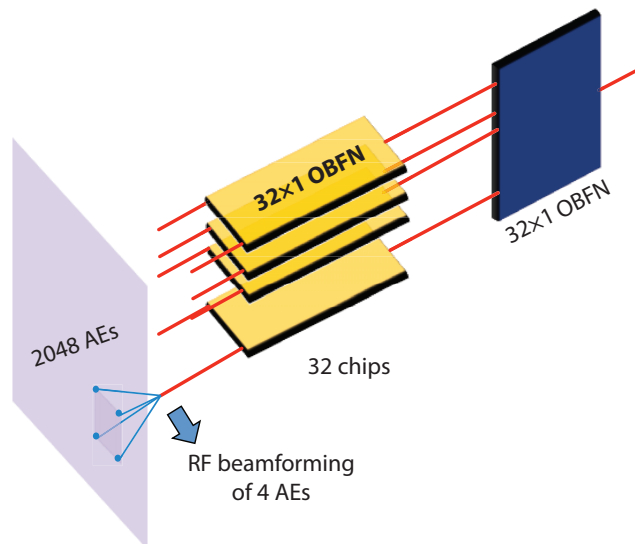
Figure 4.16: The alternative architecture with RF beamforming combined with optical beamforming. The first stage OBFNs can be simplified into 16 × 1 architectures (picture edited from [153], with permission).

an alternative architecture can be proposed, where RF beamforming of 4 antenna elements were performed prior to the first stage of the OBFN system (Fig. 4.16). This will reduce the size of the OBFNs in the first stage to 16×1 instead of 64×1. These smaller OBFNs would be more reliable and have already been realized and tested in other frameworks [160]. Moreover, the reduced number of modulators in one array (16 instead of 64) will also improve the yield. The RF beamforming prior to the OBFNs might be implemented in true-time delay elements or phase shifters [159]. The latter solution will induce a beam squint, as explained in Chapter 2, but its amount can be neglected since the required delay for neighboring antenna elements are small (in the order of 34 ps).

System Demonstration, Integration and Test

<div style="text-align: right; font-size: 3em;">5</div>

In this chapter[1] the realization and testing of the optical beamformers analyzed and designed previously are described. The characterization is conducted in subsequent steps of increasing complexity. First, an demonstration of the delay generation and of the coherent combining capabilities of the OBFN is performed. The beamformer system is then modelled as a multi-port microwave network, and characterized in terms of its measured s-parameters, that are, the RF-input to RF-output amplitude and phase transfers. The measured network parameters are then employed to simulate the radiation patterns that would be generated when the OBFN is employed to feed an antenna array. This allows to evaluate the performance of the network at a higher abstraction level, that is, as a feeding network for an antenna array. Finally, the ultimate characterization consisting in the integration of the OBFN in an antenna system is described. After a complete description of the system and of the OBFN tuning procedure, the radiation patterns are measured for multiple scanning angles and analyzed, in terms of their squint-free behaviour, to demonstrate the wideband capability of the optically-fed antenna array.

---

[1] *Published as:*

- M. Burla, M.R.H. Khan, L. Zhuang, D.A.I. Marpaung, C.G.H. Roeloffzen, P. Maat, K. Dijkstra, A. Leinse, M. Hoekman, R.G. Heideman, "System Integration and Radiation Pattern Measurements of a Phased Array Antenna employing an Integrated Photonic Beamformer for Radio Astronomy Applications," *Applied Optics*, vol. 51, no. 7, pp. 789-802, 2012.

- M. Burla, D. Marpaung, L. Zhuang, A. Leinse, M. Hoekman, R. Heideman, C. Roeloffzen, "Integrated Photonic K_u-Band Beamformer Chip with Continuous Amplitude and Delay Control," *IEEE Photonics Technology Letters*, vol. 25, no. 12, pp. 1145-1148, April 2013.

In the previous chapter, the system analysis of a photonic beamforming system for antenna arrays was described in detail, providing an estimation of the impact of the beamformer chip in the radio system in terms of gain, noise figure and dynamic range. A design example of was given for the case of a K_u-band TV-SAT application. The corresponding optical beamforming chip will be referred to as the "FLY" chip.

The designed optical beamforming network (OBFN) chip has been realized by LioniX B.V. [161] with LPCVD technology using a CMOS-compatible process. The realization has been described in detail in [143, 147].

The next step after realization has been the verification of the functionalities of the signal processing chip. In [147] and in [143] the authors have given a thorough description of the *optical characterization* and *RF characterization* of the realized OBFN photonic integrated circuit.

In this chapter, after a summary of those necessary characterization steps, the performance evaluation will be extended further towards the point of view of the final application as a feeding system for phased array antennas. The performance will be analyzed in two steps:

- *Radiation pattern simulation based on measured s-parameters*: the input-output characteristic of each OBFN channel will be represented by the scattering transmission parameter of an equivalent 2-port microwave network. Those transmission parameters are directly related to the excitation that the OBFN provides to the antenna array. The effects of the generated excitations on the radiation pattern will be evaluated by simulating the array factor based on the measured transmission parameters.

- *Antenna-OBFN system integration and testing (measured radiation patterns)*: The system integration of the OBFN system in a complete antenna system and the evaluation of its performance in terms of measured radiation patterns.

Those characterization steps will be described in detail in the following sections.

5.1   The *FLY* OBFN chip

5.1.1   OBFN chip schematic

The OBFN chip employed in the characterization has been realized in the framework of the SMART project [143]. The application aim is to realize a broadband optically-controlled phased array antenna for satellite television reception. The design of this beamformer has been described in [147]. The OBFN chip consists of three main sections: the delay-combine binary-tree section, the optical sideband filter (OSBF), and the carrier re-insertion coupler. The chip schematic is shown in Fig. 5.1.
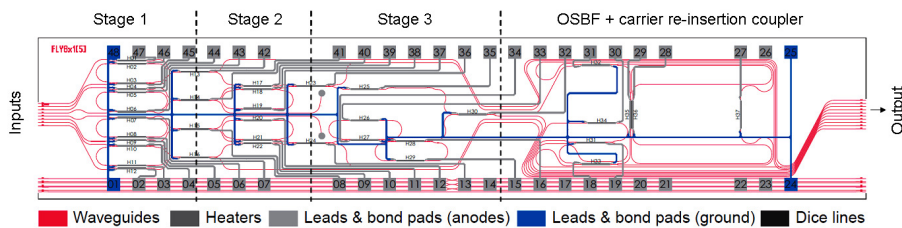
OBFN
inputs
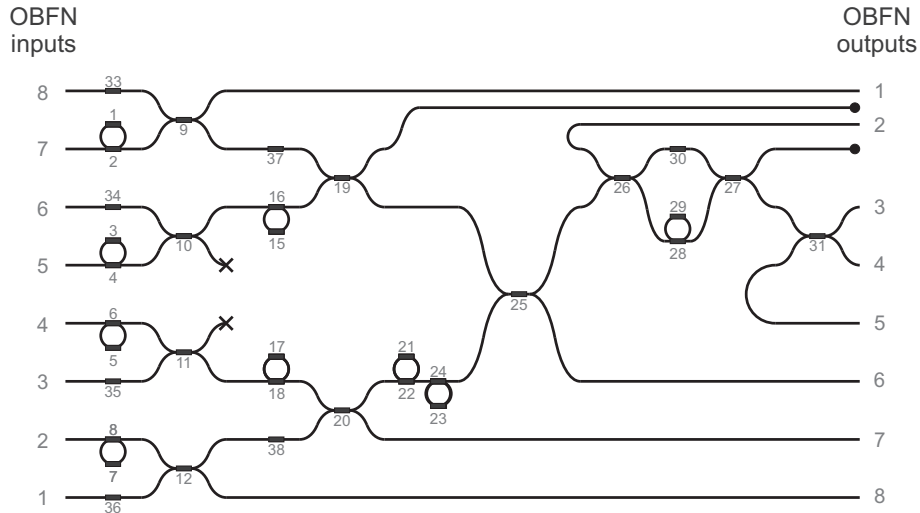
OBFN
outputs

Figure 5.1: FLY OBFN chip schematic. The black dashes overlapped to the waveguides represent the tuning elements.

5.1.2 OBFN chip layout

The OBFN described in this work and in the previous papers is integrated in a single-chip realized using a low-loss waveguide technology, produced with a CMOS compatible process [143]. For the particular technological choice of a silicon based substrate, thermo optical tuning is used by placing heaters on top of the waveguides sections to be tuned.

The 8x1 beamformer chip layout is shown in Fig. 5.2. The dye dimensions are 4.85 cm in length by 0.95 cm in width. In Fig. 5.2, the waveguide layout with the integrated optical ring resonators, the heaters used for thermo optical tuning, and the electrical leads and bond pads employed for OBFN control are visible.

Figure 5.2: Mask layout of FLY 8×1 OBFN chip (picture from [147])

For ease of operation, the OBFN chip has been pigtailed using commercial fiber

array units (FAU) at the input and at the output of the chip. Each FAU consists of an array of single-mode, polarization-maintaining fibers terminated with PM connectors. The input and output FAUs have been actively aligned to the input and output waveguide arrays on the OBFN chip. Each fiber of the FAU gives access to a specific input and output waveguide. This arrangement allows an easy access to the different OBFN ports and facilitates the mating-unmating operation of optical connectors during the OBFN chip tests.

The input-output response of the single channels can be programmed via electro optical effect, using chromium heaters which have been placed on specific locations of the chip in order to selectively heat up the desired waveguide sections. The use of tunable heater structures allows the implementation of tunable optical phase shifters, tunable optical couplers and tunable delay lines[2]. At a functional level, those tunable structures constitute the basic building blocks (BBB) for the optical beamformer. The tunability of the BBBs allows to electrically reconfigure the optical properties of the OBFN chip, which translate into electrically reconfigurable amplitude and delay coefficients constituting the complex excitation provided by the OBFN to each antenna element of the array. In this way it is possible to electrically program the optical behaviour of the programmable OBFN chip, and this will correspond to an electrically programmable array factor for the array. It is also possible to store the corresponding settings and recall them at a later time.

5.2   The OBFN system

Both the optical and the RF characterization of the OBFN chip performance require the PIC to be inserted into a suitable measurement setup. We refer to this setup as *OBFN system*, as opposed to *OBFN* or *OBFN chip* which refers to the PIC itself seen as the device under test (DUT).

Before starting with the three levels of performance demonstration introduced above, it must be noticed that the analysis of the *RF performance* of a microwave photonic system requires the possibility to compare magnitude and phase of the RF signals at the input and at the ouput of a 2-port microwave photonic (MWP) signal processor. As can be immediately noticed from the discussion so far, and as was introduced in Chapter 3, this requires: (1) suitable RF instrumentation, able to measure amplitude and phase of RF signals; (2) "interface" devices able to transfer signals between the *RF domain* to which the input and output signals belong to, and the *optical domain*, where the processor operates. Those two conversion processes are generally referred to as electrical-to-optical (E/O) conversion, and

---

[2]The heat flow through a certain waveguide section causes a change of its refractive index and, as a consequence, of its phase velocity, thus realizing a *tunable optical phase shifter*. When the optical phase shifter is inserted in an interferometric structure as a MZI coupler, the phase shift translates into a change in coupling ratio of the MZI, realizing a *tunable optical coupler*. Those components are also used to optically couple a ORR structure to a waveguide. As explained in Chapter 4, a change in the coupling ratio creates a corresponding change in the coupling factor to the ORR, thus a change in the quality factor of the resonator, that corresponds to a change in the group delay. This discussion shows how the implementation of a tunable phase shifter allows to realize a tunable optical coupler and, in turn, a *tunable delay line*.

optical-to-electrical (O/E) conversion. Since the distinction between what is commonly known as an RF signal and as an optical signal is simply a frequency range difference, in other words, it is required to have upconversion and downconversion devices that can operate the E/O and O/E conversions as desired. For this reason, the characterization of the performance of the MWP processor will be conducted using a modulator and a photodetector. In this thesis, the system composed by the cascade of (1) modulation device (one or more), (2) MWP processor and (3) photodetector (one or more) will be referred to as "microwave photonic (MWP) *system*". In the specific case of study where the MWP processor is an OBFN, we will indicate "optical beam forming network (OBFN) system" to distinguish it from OBFN, that is, the optical processor device only.

By recalling the description of a microwave photonic link (MPL) – or equivalently defined in literature as analog optical link (AOL) or analog photonic link (APL) – given in Chapter 3, and comparing it to the structure of the OBFN system, it becomes clear why the discussion on analog photonic links performance also applies in the case of the characterization of a MWP device, and why the MPL can be defined as the *workhorse* of any MWP signal processing system. In fact, in order to be able to characterize and ultimately to use a MWP processor, we first need to build an AOL, in which we insert the photonic processing section. In this example, the link consists of a modulator, an optical fiber, and a detector, employing an external laser source. At the time of this work, the current trend in MWP signal processing applications aims towards the realization of completely integrated systems [17], where optical source, modulation device, processing device and detector are either monolithically integrated on a single chip, or hybrid-integrated from different platforms, each optimized for a specific function (e.g. InP for sources and modulators, Si_3N_4 / SiO_2 for low-loss passive structures). This offers a number of crucial advantages, first of all cost reduction, compactness and increased performance, when compared to a solution based on system integration of commercial components. A glimpse on those advantages will be given by discussing the example of beamformer-antenna integration described in the following of this chapter. Still, in this type of integrated solution, it will always be possible to identify the components of an AOL, where the actual transmission media is a cascade of integrated waveguide structures instead of an optical fiber.

Ultimately, building a MWP system around a MWP device allows to have access to two or more RF ports: one or more RF input ports, and one or more RF output ports. Beyond those, the MWP system can be seen as a "black box" or as a 2-port microwave device, as explained in Chapter 3. This abstraction effort allows to consider it as any other microwave device that can be measured and characterized employing the common instrumentation available in a microwave laboratory. In particular, a vector network analyzer (VNA) will be used to characterize the magnitude and phase relation between the signals at the input and at the output of the MWP system. Before proceeding with the characterization of the OBFN, the performance of the basic AOL employed in the OBFN characterization will be analyzed in the following.

5.3   Analog optical link characterization

As mentioned in the previous section, the OBFN is inserted into an analog optical link (AOL) in order to provide the beamforming functionality. The first step towards the characterization of the OBFN performance is thus the analysis of the performance of the AOL employed. The characteristics of the link explained in Chapter 3 in terms of gain, noise and non-linear distortions are studied and reported in this section.

5.3.1   Link gain

The setup shown in Fig. 5.3 has been built. A DFB laser (DFB-LD, EM4 Inc.) feeds a Mach-Zehnder electro-optical modulator (MZM, Avanex FA20) via a polarization maintaining fiber (PMF). The output of the modulator is then connected to a high-power photodetector (PD, Discovery Semiconductor DSC710).
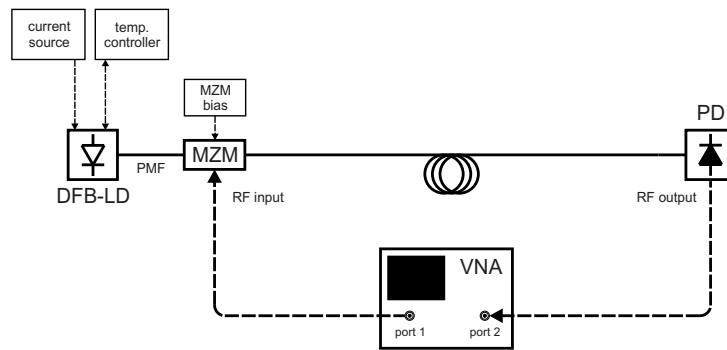
Figure 5.3: AOL setup for link gain measurements

First, a vector network analyzer (VNA, Agilent N5230A PNA-L) is employed to measure the broadband gain performance. The resulting magnitude and phase responses $\left(|s_{21}| \text{ and } \arg(s_{21})\right)$ are shown in Fig. 5.4, for two different PDs, the Discovery Semiconductor DSC30S (22 GHz bandwidth) and the Discovery Semiconductor DSC710 (balanced PD with 10 GHz bandwidth) [162]. In the following calculation we show that the measured gain is in good agreement with the theoretical value given by Eq. (3.7).

The laser output power P_{i} is set at +14.1 dBm by driving the DFB laser (EM4 Inc.) with 120.1 mA at a temperature of 25 degrees. The employed MZM has a $V_{\pi,\mathrm{DC}} = 6.4$ V, a $V_{\pi,\mathrm{RF}} = 3.8$ V, and the measured insertion loss is $L_{\mathrm{mod}} = 5.5$ dB. The modulator is biased at quadrature $(\phi_{\mathrm{B}} = \pi/2)$ and, according to the datasheet, the detector responsivity is 0.75 A/W. The source and the load resistances equal 50 Ω. An excess loss (L_{ex}) of approximately 1.1 dB is added by the fiber connectors between the LD and the MZM (0.5 dB) and between the MZM and PD (0.6 dB). The

total optical loss, L, in Eq. (3.7) amounts thus to $5.5 + 0.6 + 0.5 = 6.6\,$dB. The average optical power impinging on the PD is thus 7.5 dBm, and the measured average photocurrent at the PD output is 1.448 mA. The calculated link gain in decibels is $-27.21\,$dB, very close to the measured value of $-27.45\,$dB. The gain roll-off with frequency is attributed to the electro-optical response of the MZM and of the PD employed [163] in conjunction with the losses of the RF connectors which were not included in the initial calibration of the VNA. In particular, the gain dip and the corresponding 25 degrees phase transition around 7 GHz visible in Fig. 5.4, are attributed to the response of the specific MZM in use, since they are visible for both measurements with the DSC710 and the DSC30S.
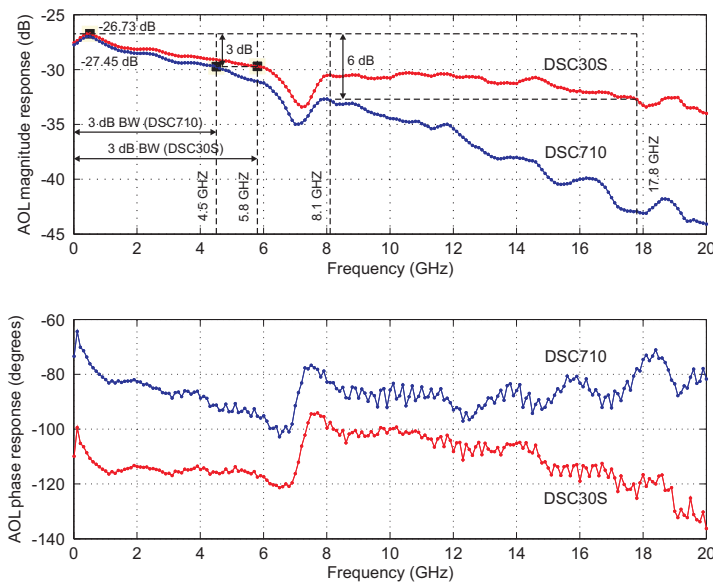
Figure 5.4: Measured magnitude response (gain) of the AOL in Fig. 5.3, with two different detectors

5.3.2 Noise and non-linear distortions

Following this test, the SFDR calculation has been performed graphically, as in Fig. 3.9. The FLY beamformer chip has been designed to operate on RF signals at L band, specifically at the IF DVB-S band (950-3100 MHz) [156], and also to be able to process modulated signal directly at K_u-band, specifically at the RF DVB-S band (10.7-12.75 GHz), before downconversion to the IF band. For this reason, the noise and linearity tests have been performed around 1 GHz and around 3 GHz. Nonlin-

earity tests at K_u-band could not be performed due to frequency limitations of the available photodetector. The measurement setup used for this characterization is shown in Fig. 5.5.
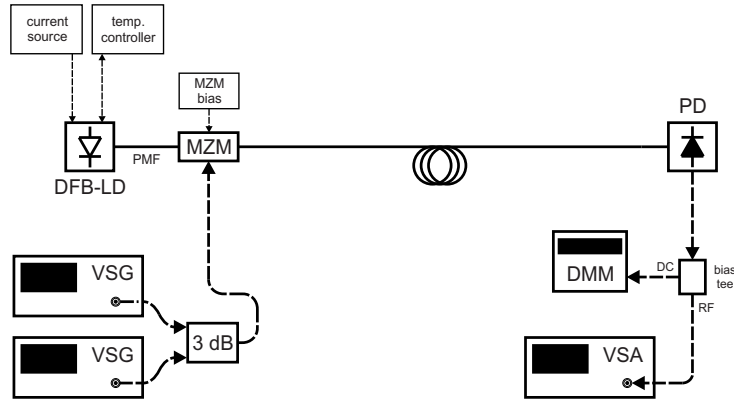
Figure 5.5: AOL setup for two-tone test

In order to measure the noise floor, a vector signal analyzer (VSA, Agilent MXA N9020A) is employed. It is important to notice that the VSA has to be set in such a way that the internally generated noise is negligible with respect to the noise power available at the output of the AOL. For this reason, the mechanical attenuation option of the VSA is manually set to 0 dB, and the internal broadband pre-amplifier (20 Hz to 26.5 GHz) is switched on. In those conditions, the displayed average noise level (DANL) is -165 dBm/Hz and the noise power density of the AOL can be measured to be -163.27 dBm/Hz at 1 GHz and -159.97 dBm/Hz at 3 GHz.

Two vector signal generators (VSG, Agilent E8267D PSG and Agilent E4438C ESG) have been used to generate tones at 0.95 GHz and at 1.05 GHz. The outputs of those VSGs have been combined using a broadband 3 dB coupler and fed to the input of the MZM. The PD output is connected to the VSA. The power of the fundamental tones, of the second-order (IMD2) and of the third order intermodulation distortions (IMD3) measured at the output of the MWP link is reported in Fig. 5.6 with respect to the power of the corresponding input fundamental tones. From this graph, it is possible to deduce the gain, the input and output intercept points and the SFDR of the link.

When the MZM is biased in quadrature, it is possible to theoretically predict the value of the OIP3 very simply by measuring the average photocurrent I_{av} and employing the equation [22]

$$\text{OIP3}_{\text{MZM,quad}} = I_{av}^2 R \tag{5.1}$$

where R is the load resistance of the PD. The average photocurrent can be easily measured by connecting a bias-tee at the electrical output of the PD, in such a way
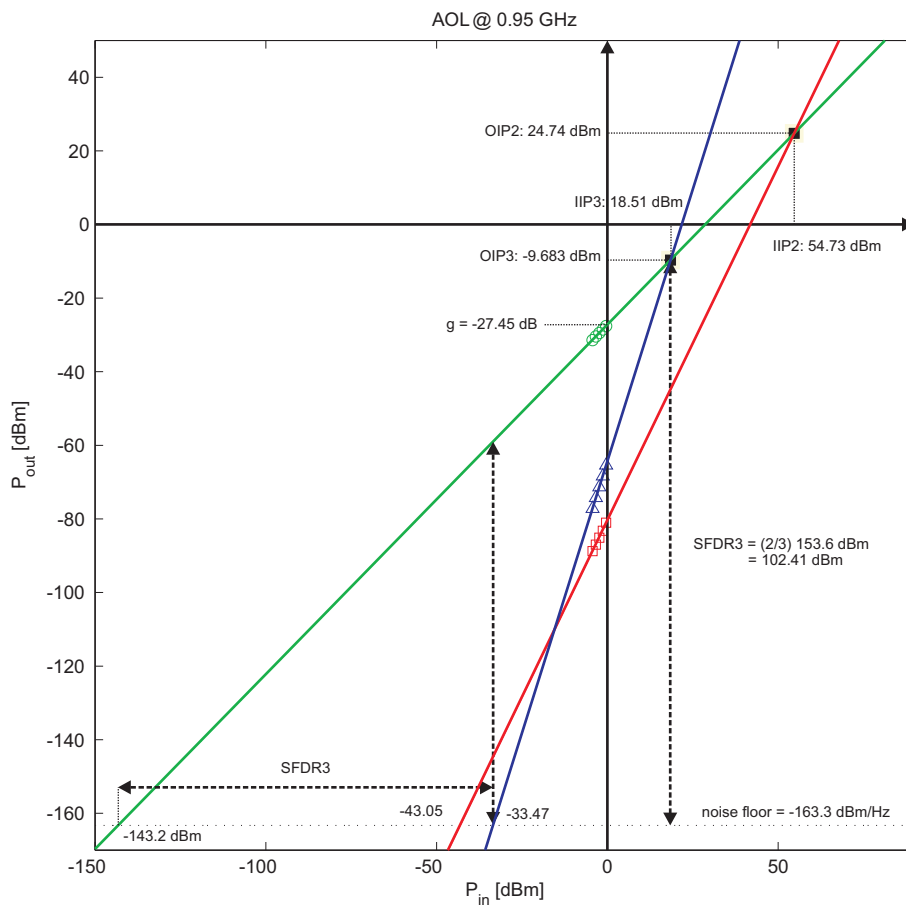
Figure 5.6: AOL performance (two-tone test at 950 MHz and 1050 MHz)

to separate the RF output signal, measured with the VSA, from the DC signal, which can be measured using a digital multimeter (DMM, Fig. 5.5). In the experiment, for +4.1 dBm of optical power impinging on the PD, the measured average photocurrent is 1.45 mA. Considering the load resistance of 50 Ω offered by the VSA, the OIP3 is approximately −9.8 dBm, in good agreement with the result of the graphical analysis reported in Fig. 5.6 and 5.7.

Ideally, by biasing the MZM in quadrature, the OIP2 is infinite, since no IMD2 should be seen thanks to the perfectly odd-symmetry of the MZM power response at the quadrature point. In the figure it is possible to see that the OIP2 value is high but not infinite. This is attributed to a possible drift of the MZM bias point during the measurement, being the optical power to the PD too low to attribute the distortion to the PD non-linearity [162].

Similarly, the test has been repeated around 3 GHz, using two tones respectively at 2.950 GHz and at 3.050 GHz. The result is graphically shown in Fig. 5.7.
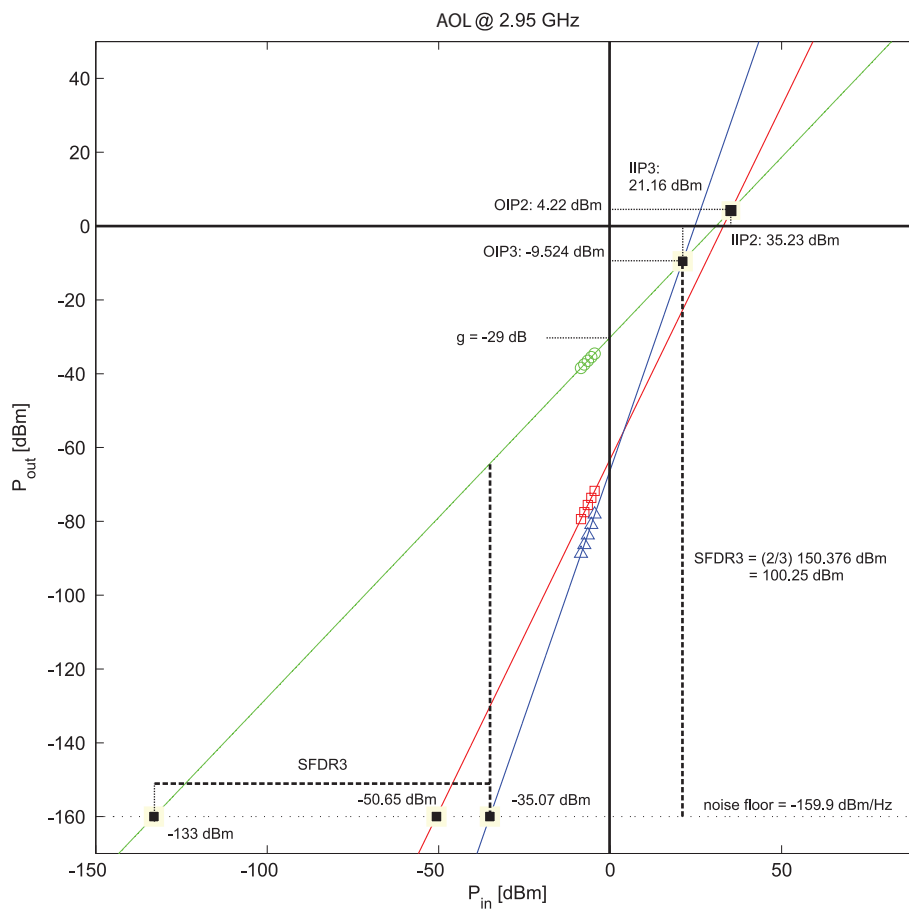
Figure 5.7: AOL performance (two-tone test at 2950 MHz and 3050 MHz)

5.3.3   AOL with carrier re-insertion

In Chapter 4 the modulation formats to be employed in the OBFN system have been discussed. In particular, a DSB-SC modulation can be implemented using external modulation with an MZM biased at its minimum transmission, in order to suppress the carrier and minimize the IMD3, the RIN and the shot noise. Further, it has been shown how it can be advantageous to suppress one of the sidebands, that is, to use a SSB-SC modulation format in order to reduce the delay bandwidth required and, in turn, the OBFN complexity. A filter-based approach to suppress the undesired sideband can be implemented in a straightforward manner by adding an optical sideband filter (OSBF) within the same chip of the OBFN and using the same basic building blocks. Carrier re-insertion can be employed in order to realize direct detection. Finally, balanced photodetection can be used to reduce the total link noise by using balanced photodetection to suppress the RIN of the laser.

At this stage, it is thus interesting to analyze the performance of the same type of AOL that will be actually used in the operation of the OBFN system. For this reason, in the following sections we built an analog photonic link implementing the type of modulation format described above. First, a DSB-SC modulation with carrier re-insertion and direct detection is realized, and then the sideband filter in the OBFN chip is used to produce an SSB-SC modulation. Then we analyze the challenges in its fiber-optic based implementation and propose possible solutions.

5.3.4   Double-sideband suppressed-carrier (DSB-SC) with carrier re-insertion

The setup shown in Fig. 5.8 has been built to test the AOL with DSB-SC modulation and carrier re-insertion. Besides the components employed before in the two-tone test setup, shown in Fig. 5.5, a 90:10 optical polarization-maintaining coupler is used to direct part of the laser power towards the carrier lead-around path, and which will be used for re-insertion before direct photodetection. The MZM is biased at minimum in order to suppress the carrier and thus modulate the RF signal originating from the VSG in DSB-SC format. The modulated signal enters the OBFN chip from input 7 to output 6 (see OBFN chip schematic, Fig. 5.1). The insertion of the chip introduces an additional loss of approximately 15 dB, due to combined effects of fiber-to-chip coupling at both input and output of the chip, and light propagation in the integrated waveguide. And erbium-doped fiber amplifier (EDFA, Firmstein Inc.) is employed to compensate for these losses. An EDFA is also inserted in the carrier lead-around path, followed by a variable optical attenuator (VOA, HP 8157A). Note that the RF input of the lower MZM is not used in this test. By tuning the attenuation it is possible to equalize the optical power of the carrier with the one of the modulated optical signal. A 50:50 optical coupler is employed to recombine the DSB-SC signal with the unmodulated carrier before entering the photodetector. It is important to note that the OBFN chip includes a carrier re-insertion coupler, rendering the use of an external coupler not necessary during OBFN operation. In this setup a separate coupler was initially employed for ease of reconfigurability. In addition to that, unbalanced detection is employed for

simplicity. The use of balanced detection would allow a suppression of the RIN, beyond the scope of this specific test, by matching the microwave path lengths.
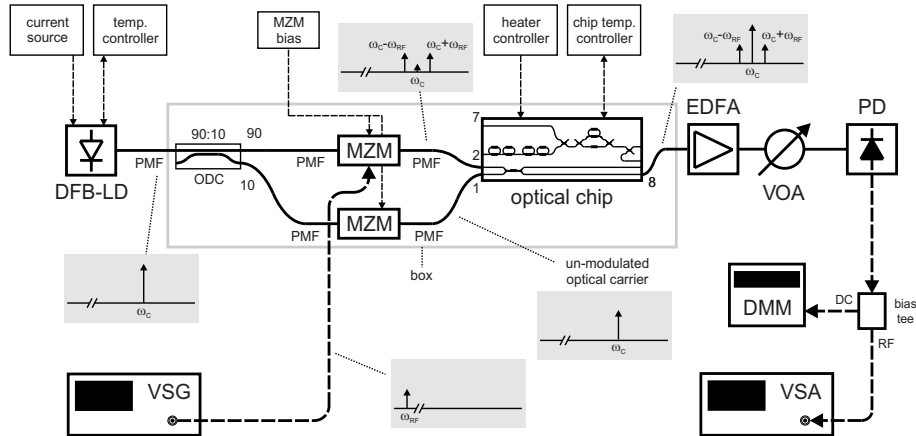
Figure 5.8: AOL setup for DSB-SC with carrier re-insertion test

The first test made with this setup has been a single tone test. A 1 GHz, 0 dBm RF signal is generated by the VSG. The modulator bias is set to the minimum optical power transmission. The VOA is set in such a way to equalize the optical powers of the modulated optical signal with respect to the unmodulated carrier before entering the carrier re-insertion coupler. The signal at the PD output is shown in Fig. 5.9. It is important to note that the amplitude of the RF signal is not stable, but fluctuates rapidly. For this reason, in Fig. 5.9 two traces are shown, one obtained by setting the max-hold function on the VSA, and the other by setting the min-hold function. In this way, it has been possible to analyze the extent of variation of the RF signal power.

The observed fluctuations can be simply explained by considering the setup and the optical signals propagating through the different parts of it, represented in phasor form on the complex plane. Fig. 5.10 shows 12 diagrams; let us first analyze diagram (1a). This represents the three E-field components of the optical signal impinging on the photodetector: the optical carrier originating from the carrier re-insertion path (E_C), the upper sideband (E_{USB}) and the lower sideband (E_{LSB}). The carrier can be represented as a vector rotating on the complex plane with angular velocity equal to ω_C. The upper sideband and the lower sideband are also represented as vectors, rotating respectively with angular velocity $\omega_C + \omega_{RF}$ and $\omega_C - \omega_{RF}$. The angular positions of the three vectors represent the initial phase of the carrier (φ_C, 90 degrees in the figure), the upper sideband (φ_{USB}, 135 degrees) and the lower sideband (φ_{LSB}, 45 degrees) at an arbitrary time instant t_0. The sum of these three vectors represents the actual optical field impinging on the PD. The PD, in turn, will translate the magnitude variations of the vector (that correspond to changes in optical field) to photocurrent variations, according to the following relation [164]:
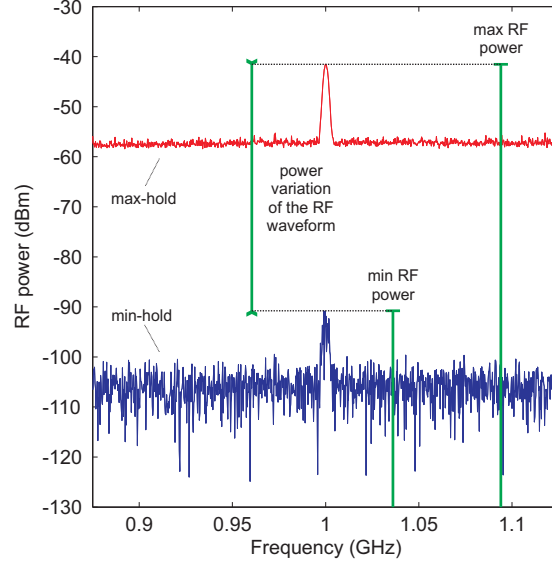
Figure 5.9: Max-hold and min-hold of the observed RF signal at the output of the AOL with DSB-SC and carrier re-insertion

$$I_{\text{det}}(t) = r_{\text{PD}} \left(E_{\text{C}}(t) + E_{\text{USB}}(t) + E_{\text{LSB}}(t) \right) \left(E_{\text{C}}(t) + E_{\text{USB}}(t) + E_{\text{LSB}}(t) \right)^{*}$$

$$= r_{\text{PD}} \left| E_{\text{C}}(t) + E_{\text{USB}}(t) + E_{\text{LSB}}(t) \right|^{2}$$

$$= r_{\text{PD}} P_{\text{det}}(t) \tag{5.2}$$

where I_{det} represents the detected photocurrent, r_{PD} the responsivity of the photodetector, and $E_{\text{C}}(t)$, $E_{\text{USB}}(t)$ and $E_{\text{LSB}}(t)$ indicate the E-field components of the optical carrier, the upper and the lower sideband, respectively. P_{det} is the total optical power impinging on the photodetector. The star (*) represents the operation of complex conjugation. Each of the optical E-field terms is proportional to the square root of the corresponding optical power, according to the following relations [33]:

$$E_{\text{C}}(t) = \sqrt{2 P_{\text{C}}} \exp[\, j \omega_{\text{C}} t + \varphi_{\text{C}} \,] \tag{5.3}$$

$$E_{\text{USB}}(t) = \sqrt{2 P_{\text{USB}}} \exp[\, j(\omega_{\text{C}} + \omega_{\text{RF}}) t + \varphi_{\text{USB}} \,] \tag{5.4}$$

$$E_{\text{LSB}}(t) = \sqrt{2 P_{\text{LSB}}} \exp[\, j(\omega_{\text{C}} - \omega_{\text{RF}}) t + \varphi_{\text{LSB}} \,] \tag{5.5}$$

where P_{C}, P_{USB} and P_{LSB} are, respectively, the power of the optical carrier, of the USB and of the LSB. The RF power delivered to the load (in this case, the VSA) is thus related to the E-fields component by the following relation

$$P_{\mathrm{RF}} = I_{\mathrm{PD}}^2\, \mathrm{R_L}$$
$$= \left(r_{\mathrm{PD}} \left| E_{\mathrm{C}}(t) + E_{\mathrm{USB}}(t) + E_{\mathrm{LSB}}(t) \right|^2 \right)^2\, \mathrm{R_L}$$
$$= \left(r_{\mathrm{PD}} P_{\mathrm{det}}(t) \right)^2\, \mathrm{R_L}$$
$$= r_{\mathrm{PD}}^2 P_{\mathrm{det}}^2(t)\, \mathrm{R_L} \tag{5.6}$$

The latter equation formally relates the amplitude of the E-field terms in the phasor diagrams in Figs. 5.10 and 5.14 with the RF power P_{RF} measured by the VSA in our setup.

Let us suppose we are not interested in phase of the of the RF signal at the PD output; thus, to predict its magnitude, we should analyze the magnitude variations of the sum vector. Since it is not obvious to visualize the vector sum of three rotating vectors at once, in diagram (1b) we display the angular velocity of the sidebands relative to the angular velocity of the carrier. In other words, we imagine that the observer rotates with the carrier. Such an observer will see the upper and the lower sideband to respectively rotate counterclockwise and clockwise, with angular velocities $+\omega_{\mathrm{RF}}$ and $-\omega_{\mathrm{RF}}$ with respect to the carrier, respectively. Thus it is now easier to imagine the resulting vector: it will oscillate in amplitude along the vertical axis, as in diagram (1c), between a max and a min, as in diagram (1d). The RF E-field amplitude will be the difference between the max and the min values.

Let us now imagine that, for some reason, the initial phase relation between the carrier and the sidebands varies. In particular let us suppose the carrier receives an extra 45 degrees phase shift compared to case (1a) while the sideband phases are not varied. The new situation is shown in diagram (2a). Again, by displaying the relative rotation of the sidebands with respect to the carrier (2b) shows that the resultant varies between two extreme points indicated by the upper and lower arrows in (2c). In (2d), the resulting maximum and minimum vectors are shown. Due to the misalignment between the carrier phase and the sum of the sideband vectors, the phase of the resultant will also change in time. Again, we suppose we are interested in the amplitude variation only; it can be seen that the amplitude variation is still visible but it is reduced with respect to the case of diagram (1d).

Finally, let us analyze the case in which the initial phase of the carrier is 90 degrees (3a). In this situation, the resultant of the sidebands is always orthogonal to the carrier (3c). The resulting vector is now oscillating between the two vectors shown in diagram (3d). This limits the amplitude to a much lower value when compared to the one in diagram (2b), and even lower than the one in (1d).

The relative phase variation experienced by the carrier with respect to the sidebands is what occurs in our AOL setup shown in Fig. 5.8. In fact, between the 90:10 splitter and the 50:50 coupler, the carrier travels on a separate fiber with respect to the sideband. Any minimum temperature variation, airflow or mechanical fluctuation of the fibers will create a variation of the optical phase shift along the whole length of the fiber. For this reason, the optical signal impinging on the photodetector can be seen as continuously fluctuating between the states represented
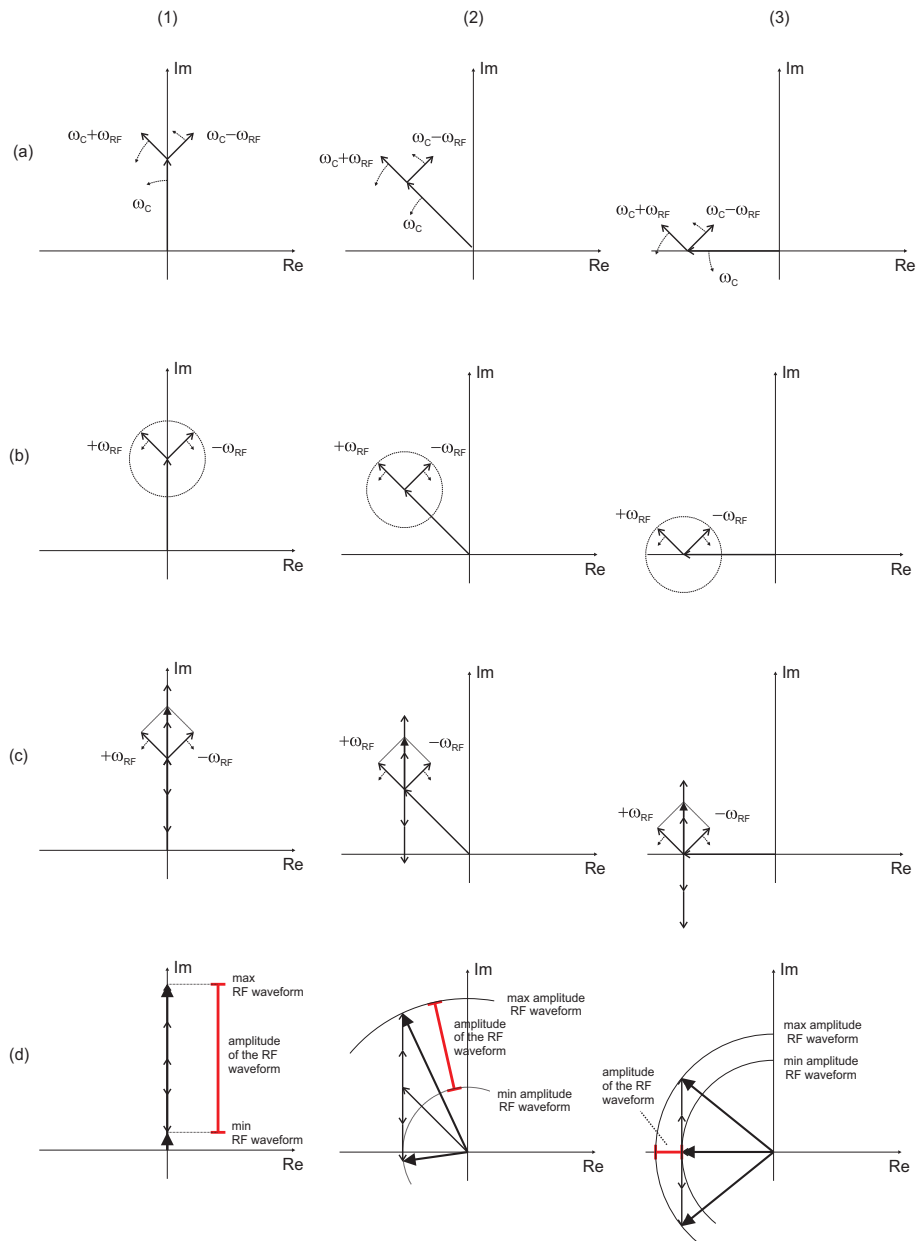
Figure 5.10: Phasor diagram for DSB-SC with carrier re-insertion test

in diagram (1a) and (3a), thus creating a continuous fluctuation of the power of the RF signal at the PD output, as in diagrams (1d) to (3d).

In order to solve this issue, we must make sure that the optical carrier and sidebands always have a constant phase relation among them. This can be achieved, for example, by integrating splitter, optical paths and carrier re-insertion couplers on an integrated waveguide platform. In this way, it will be possible to control much more accurately and keep stable the optical phase relation between carrier and sidebands, since the length of the paths will be largely reduced and the temperature of the waveguides can be easily controlled and kept stable.

5.3.5 Single-sideband suppressed-carrier (SSB-SC) with carrier re-insertion

Let us now analyze the behaviour of the AOL employing SSB-SC modulation with carrier re-insertion. The only difference when compared to the previous DBS-SC case is that one sideband is suppressed by the optical sideband filter (OSBF) on the OBFN chip. The setup is show in Fig. 5.11, and is the same as in Fig. 5.8 except for the fact that now the modulated optical path goes through a different OBFN channel in order to insert the OSBF on the path to suppress one sideband.
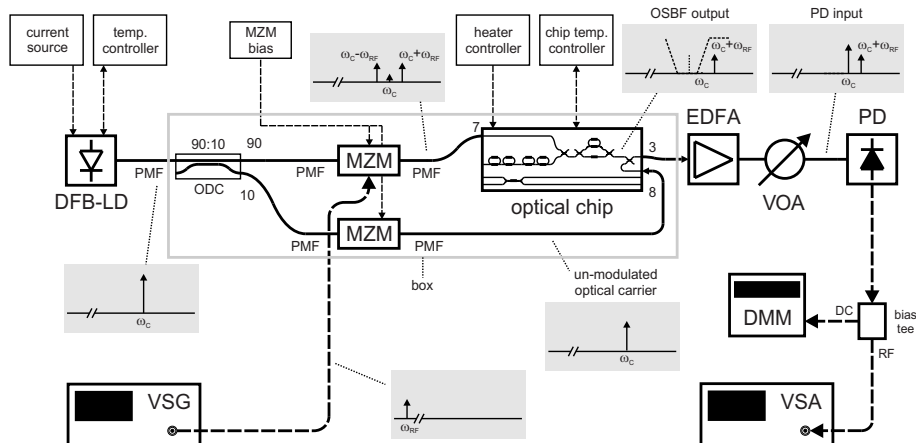
Figure 5.11: AOL setup for SSB-SC with carrier re-insertion test

The VSG generates a tone at 1.5 GHz with 10 dBm power. The free-spectral-range of the OSBF is 6.7 GHz. The frequency was increased to 1.5 GHz to make sure one sideband falls in one of the minima of the OSBF stopband, as depicted graphically in Fig. 5.12. An increased RF power was needed in order to compensate for the extra losses due to the insertion of the OSBF in the optical path.

At the PD output we can now see an RF signal, which shows a much lower fluctuation when compared to the DSB-SC case. The max-hold and the min-hold traces
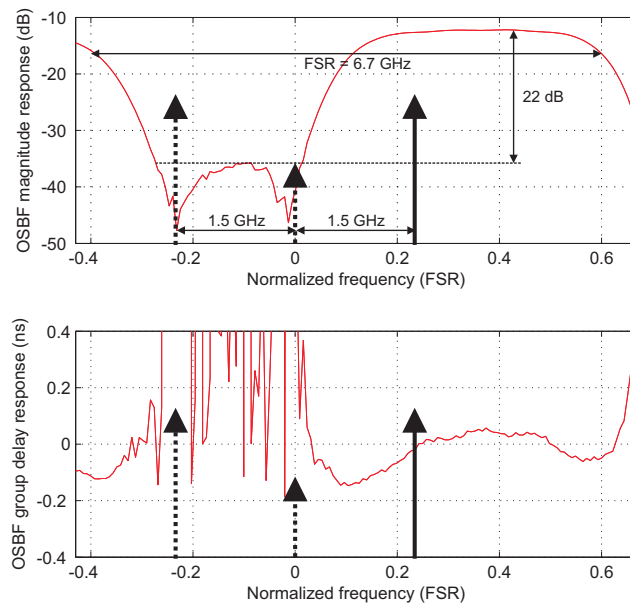
Figure 5.12: OSBF response and position of the sidebands

obtained with the VSA are shown in Fig. 5.13.
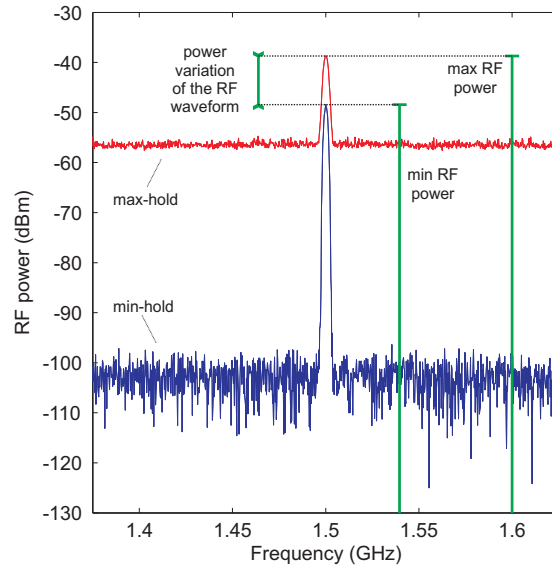
Figure 5.13: Max-hold and min-hold of the observed RF signal at the output of the AOL with SSB-SC and carrier re-insertion

Again, also in this case the RF signal behaviour can be explained by analyzing the optical signal impinging on the PD in the phasor domain. The same discussion done for the DSB-SC case holds, except for the fact that in this case, only one sideband is left. This means that, whichever the initial phase relation between carrier and sideband is, the resultant phasor will always have the same amplitude. In practice, the residual ripple visible in Fig. 5.13 is attributed to a non-perfect suppression of the undesired sideband by the OSBF, resulting in a small but visible vector for the lower sideband in the phasor plane that creates an RF amplitude fluctuation as in the DSB-SC case. Nonetheless, it is important to note the dramatic reduction of maximum power fluctuation from 50 dB of the DSB-SC case (Fig. 5.9) to approximately 10 dB obtained with SSB-SC (Fig. 5.13). The relative phase variation are again attributed to the different and random phase variation of the carrier with respect to the modulated optical path due to the presence of long optical fibers between the splitting and combining points, and are expected to disappear once the carrier re-insertion system will be fully-integrated on-chip.

The SSB-SC case shows an improved robustness when compared to the DSB-SC case. Nonetheless, this does not solve the problem for beamforming applications. In fact, in beamforming it is crucial to keep control not only on the RF magnitude but also on the input-output RF phase relation of the AOL, which determines the beam pointing direction as largely discussed in Chapter 2. Again, photonic integration appears as the most immediate solution in order to keep control on the optical
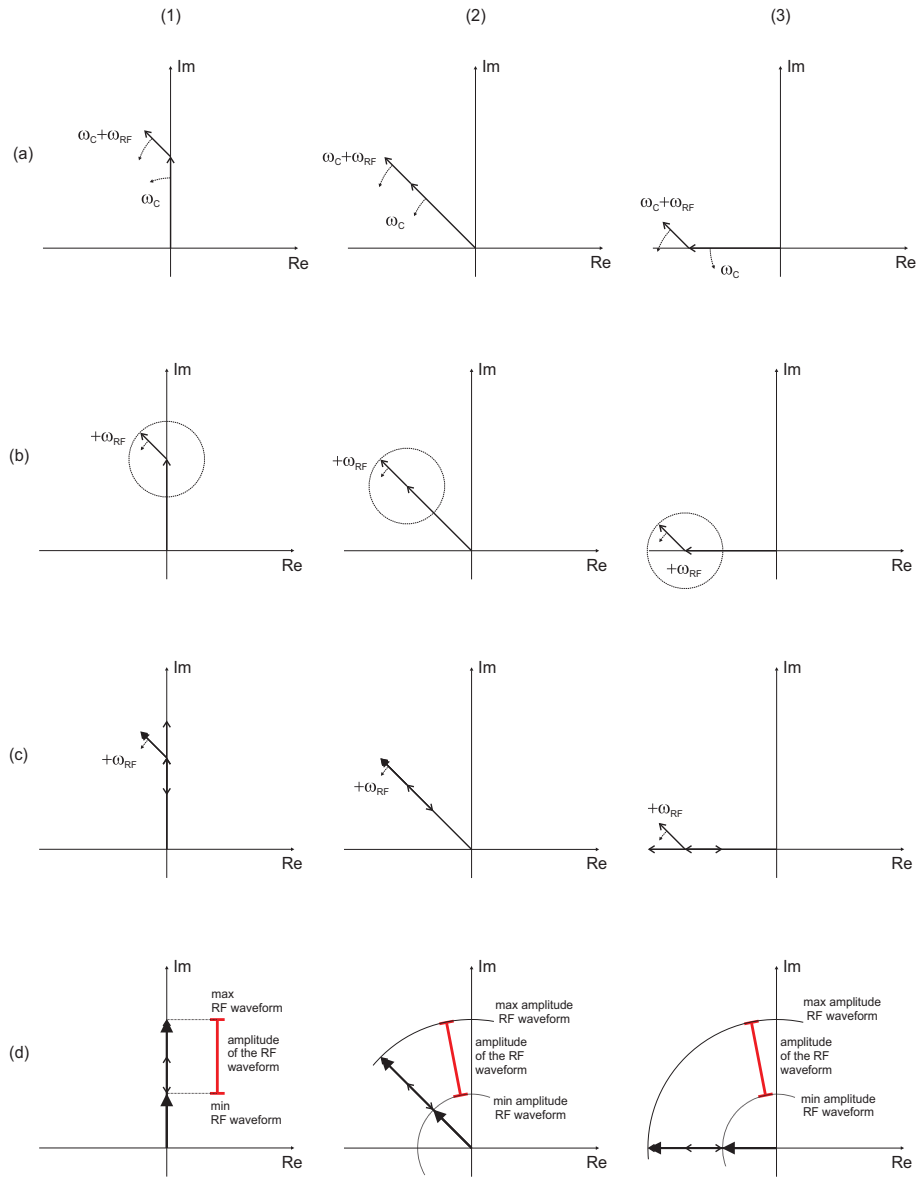
Figure 5.14: Phasor diagram for SSB-SC with carrier re-insertion test

phase of the optical coherent system analyzed in this section.

5.4 Optical characterization

This section summarizes the results of the optical characterization of the *FLY* OBFN chip, which has been performed and published by Zhuang et al. in [147] and in [143]. First the capability of the OBFN chip to generate optical group delay will be demonstrated, followed by the measurement of the optical power transfer of the OSBF. Finally, a discussion on the optical losses will be given and compared to the latest results.

5.4.1 Measurement setup for optical characterization

As mentioned in the previous section, the first step for the optical characterization consists in inserting the chip into a suitable measurement setup. The aim of the optical characterization is to measure the optical power responses and the group delay offered by each optical path.

In principle, to measure an optical power response it would be sufficient to use an optical spectrum analyzer (OSA) with a sufficiently low resolution (below 1 GHz) to accurately characterize the frequency response of the OSBF. In practice such an instrument was not available, and a different solution known as *phase-shift method* (see [165, 166]) has been employed. This technique is beneficial to our application since, in addition to the power response, it also allows to easily measure the group delay response. The corresponding measurement setup is shown in Fig. 5.15.
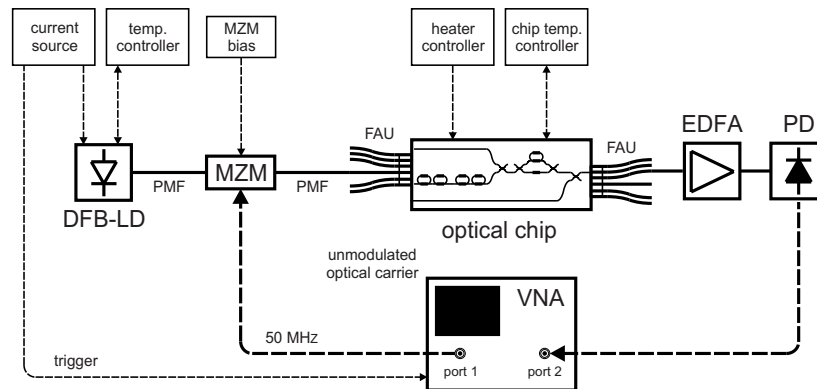
Figure 5.15: Schematic of the measurement setup for optical characterization of the OBFN chip

A vector network analyzer (VNA, Agilent N5230A PNA-L) is used to generate a 50 MHz signal, at -5 dBm RF power, from port 1. A high-power distributed feedback laser diode (DFB-LD, EM4 Inc.), operating in the 1550 nm wavelength range,

is used to generate the optical carrier which is modulated by the 50 MHz RF signal using a Mach-Zehnder modulator (MZM, Avanex PowerLog FA-20). By means of polarization-maintaining fibers the laser is connected to the MZM, and the MZM to the optical chip under test. This type of fibers are used to make sure the laser light enters the chip with the desired transverse-electric (TE) polarization. In fact, the waveguide technology employed in the realization of the chip has a polarization dependent behaviour, and has been optimized for the propagation of TE-polarized light. After propagation through the optical chip, the light at the OBFN output is amplified using an erbium-doped fiber amplifier (EDFA), due to the high losses of this particular chip, before entering a high-power photodetector (PD, Emcore R2860E). The RF output of the photodetector is connected to port 2 of the network analyzer. The DFB-LD is kept at stable temperature by a dedicated controller, and the wavelength is swept over by varying the laser current using a low noise current source operated in sweeping mode. The current ramp range has been set to sweep between 1549.97 nm to 1550.03 nm. In this way, a double-side band optical modulation of the 50 MHz RF signal is obtained. By sweeping the laser wavelength, also the modulated sidebands are swept. By using the VNA to compare the RF signal at port 1 and the RF signal at the photodetector output, it is possible to analyze the optical power and phase response of a 2 port optical network by using an RF instrument instead of optical instrumentation.

This setup has been used both in the group delay measurement and in the OSBF power response characterization, as described in the following.

5.4.2   Optical delay generation

According to the functional design given in Chapter 4, each OBFN channel must be capable of generating a tunable amount of group delay. Thanks to the construction based on a binary tree structure built using tunable MZI optical couplers, it is possible to reconfigure the input-output optical path that the light undergoes on-chip after entering a particular OBFN input. In particular it is possible to optically connect each of the inputs (1 to 8) to the OBFN output alternatively. This allows to separately characterize the delay characteristic of each OBFN channel. Seven OBFN on-chip delay paths have been measured by connecting the output fiber of the MZM to the corresponding input fiber (i.e. fiber of the input FAU) of the chip. First, the optical response of the ORRs in each path have been set using the thermo-optical tuning mechanism, in such a way to provide a flat and minimum amount of delay. This characteristic has been used as a reference in the corresponding group delay plot.

Using the phase-shift method introduced before, the optical wavelength is swept over the range of interest. The VNA can then be used to measure the phase difference $\Delta\phi(\lambda)$ between the input and the output RF signal for multiple values λ of the laser wavelength. The group delay response $\tau_g(\lambda)$ of the optical path can be estimated by normalization with respect to the RF modulating frequency f_{RF} as

$$\tau_g(\lambda) = \frac{\Delta\phi(\lambda)}{2\pi f_{\text{RF}}} \tag{5.7}$$

First, the OBFN was programmed in order to achieve the minimum delay for each path. Those are generally different, due to the different number of ORRs in each of the optical paths. Nonetheless, the resulting delays can be equalized by adding a suitable length of transmission line, either in the optical or in the RF domain (fiber optic or a coaxial cable, respectively). In this way, when the OBFN is used to feed a 8-elements linear array, the first beam setting can be used to provide a uniform delay excitation to the elements, resulting in a broadside beam pointing direction. Then, the OBFN has been programmed to provide two sets of linearly increasing delays from input 1 to 8. The first offers a 40 ps delay difference between adjacent elements, and the other a 80 ps delay difference. The corresponding delay characteristics are shown in Fig. 5.16 and Fig. 5.17, respectively. Those delay settings will generate two different beam pointing directions for the antenna. In this discussion we have assumed a *phase only weighting* beamsteering, that is, the antenna elements of the antenna array are excited with uniform amplitudes. This can be provided by equalizing the RF-to-RF power transfer, either acting on the optical transmission, or the RF transmission.
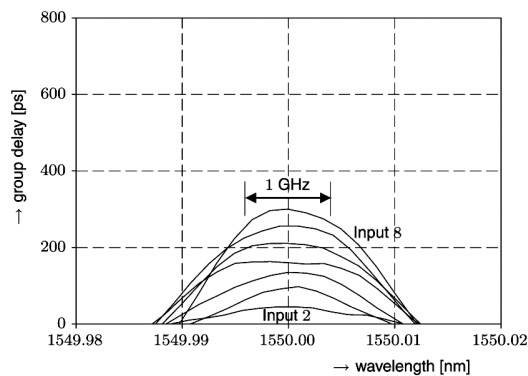
Figure 5.16: Group delay response, setting 1 (from [147])

5.4.3 Optical sideband filter response

The same measurement setup employed for the delay characterization has been also used to characterize the optical power transfer of the filter used to remove the carrier and one of the sideband from the modulated optical signal. The OSBF can be accessed separately from the OBFN using dedicated input and output test waveguides on the optical chip, and reconfiguring the on-chip optical couplers accordingly. The VNA has been used to measure the RF power transfer between the modulator input and the photodetector output, when the RF signal is at a constant frequency of 50 MHz and the laser wavelength is swept between 1549.97 nm and 1550.03 nm. Based on the quadratic relation between the optical power and pho-
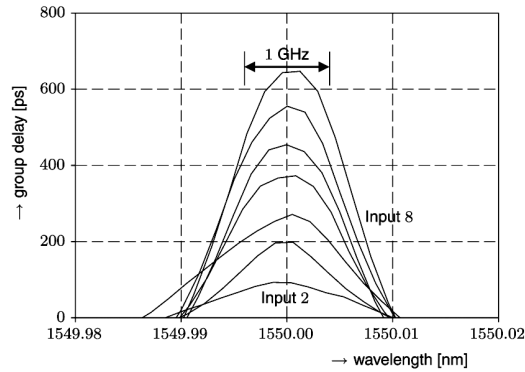
Figure 5.17: Group delay response, setting 2 (from [147])

tocurrent in a photodetector (see Chapter 3), the measured RF power transfer is the squared version of the optical power transfer. Thus, the optical power transfer in dB scale can be simply obtained by the RF power transfer by dividing by two the transfer value in dB. This measurement has been reported in Fig. 5.18, normalized with respect to the transfer of the chip, when the optical path is programmed in such a way to have no filter in the optical path. In this way it is possible to exclude from the power response the effects of coupling losses between fibers and chip.
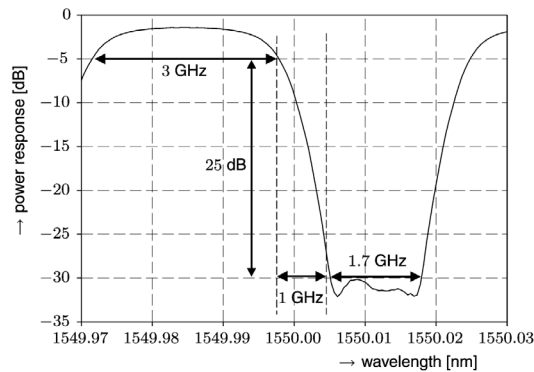
Figure 5.18: OSBF response (from [147])

The graph shows the values of the achieved passband width (3 GHz), stopband width (1.7 GHz) and transition band width (1 GHz), when the filter response is programmed in order to have 25 dB of optical suppression, as desired by design (see Chapter 4). The stopband width is smaller when compared to the design (2.05 GHz). In fact, due to realization inaccuracies, the FSR of the ORR in the realized OSBF is

not exactly half of the FSR of the MZI. This reduced the performance of the filter in terms of optical suppression. Due to the complete filter reconfigurability, it has been possible to still achieve the desired 25 dB of attenuation simply by reducing the stopband width to a lower value, but still acceptable when compared to the sideband width for the desired TV-SAT application (1.2 GHz).

5.5 RF-to-RF characterization

The RF-to-RF characterization work aims at demonstrating the capability of the optical beamformer chip to operate the three fundamental functions in antenna array beamforming. Those are

- RF signal delay generation

- RF signal amplitude tapering

- RF signal combining

This can be seen by analyzing the basic beamforming equation, Eq. (2.47), where the summation symbol indicates that the individual contributions from the single antenna elements have to be combined to form the desired array factor and, in turn, the desired beam pattern according to the principle of pattern multiplication, also explained in Chapter 2. C_i indicates the amplitude excitation and α_i is the phase term of the i-th antenna element.

The beamformer demonstration consists of showing the combining, amplitude tapering and delay tapering capabilities of the OBFN chip.

5.5.1 Measurement setup for RF characterization

The first step towards the demonstration is the construction of the measurement setup, as shown in Fig. 5.19 and described in the following.

A vector network analyzer (VNA, Agilent N5230) has been used to measure the amplitude and phase relation between the input and the output of the OBFN system, over a band of 1 GHz. Port 1 of the VNA generates an RF signal sweeping between 1 and 2 GHz, at constant power of -30 dBm. This signal is applied to the RF input of a Mach-Zehnder modulator (MZM, Avanex FA-20, 3 dB bandwidth of 20 GHz) to modulate the optical carrier generated by a high-power laser (DFB-LD, EM4 Inc.), operating in the 1550 nm band, generating 100 mW of optical output power. The modulated optical signal obtained can then be injected into any of the OBFN inputs (Fig. 5.1).

Part of the light generated by the laser is extracted by means of a 90:10 optical directional coupler (ODC) placed before the MZM, and injected into the carrier re-insertion input of the beamformer (labeled as "output 5" in Fig. 5.1). This unmodulated laser light is used for the coherent detection of the RF signal after the single-sideband suppressed carrier (SSB-SC) modulation and the optical processing.
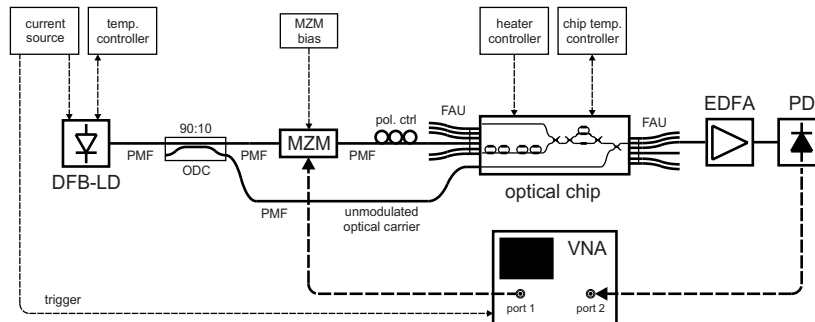
Figure 5.19: Schematic of the measurement setup for RF-to-RF characterization of the OBFN chip

All the components used in this setup are connected using polarization maintaining, single-mode optical fibers (PMF) with PM connectors. This is done to make sure the laser light enters the chip with the desired polarization. In fact, the waveguide technology employed in the realization of the chip has a polarization dependent behaviour [143].

The light at the output of the OBFN was amplified by an erbium-doped fiber amplifier (EDFA), before entering a high-power 10 GHz balanced photodetector (PD, Discovery Semiconductor DSC 710). The detected signal is routed to the Port 2 of the network analyzer. The EDFA is used to compensate for the optical losses introduced by the insertion of the OBFN chip in the AOL. The main sources of loss consist of (1) fiber-to-chip coupling losses at the input and at the output interfaces between the OBFN chip and the FAUs, and (2) waveguide propagation losses onchip. The bending losses are kept to a negligible value by choosing a sufficiently high value for the bending radius in the layout design phase. For this chip, the minimum bend radius was chosen around 700 μm. The most recent technology employs a different type of waveguide geometry which allows to lower the bending radius of almost an order of magnitude by keeping negligible waveguide losses, as described in detail in [24].

5.5.2   Phase response (delay generation)

The MZM output is connected to OBFN input 8 using a PM fiber. The eighth OBFN branch (Fig. 5.1) was first set to minimum delay and the corresponding measured phase response was used as a reference (0 ns delay). After that, more delay settings were made and the corresponding phase responses were measured with respect to the reference: the results are shown in Fig. 5.20 for 0.4 and 0.63 ns branch delays. The measured results show good agreement with the theoretical results expected, apart from a slight ripple that is mainly attributed to small reflections generated by the various fiber connectors present in the optical signal path. The future fully-

integrated implementation is expected to completely solve this problem.
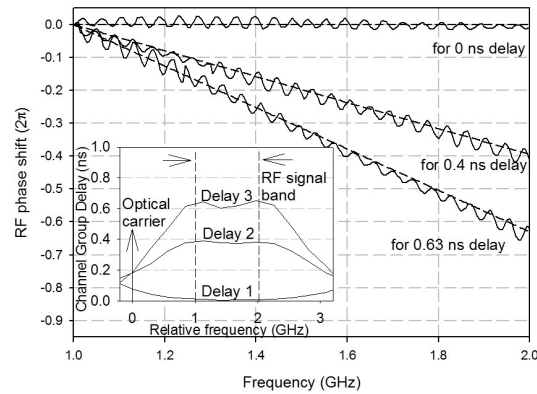
Figure 5.20: Measurement results of the RF-to-RF phase response of one OBFN channel, for three different delay settings. The minimum delay setting is used as reference 0 ns delay. The dashed lines indicate the ideal linear phase responses (picture from [167]).

Though not shown in the figure, the magnitude responses corresponding to the delay settings were also measured. In all cases, they showed a flat trend over the signal band but with larger losses for higher delay, due to the total optical loss increase with increased delay.

5.5.3 Power reponse (coherent combining)

For a complete RF-to-RF characterization of the optical chip, the coherent combining capability of the beamformer has also been measured. A similar setup has been used, while for this test three RF splitters and three directional fiber couplers have been added to split the 1-2 GHz signal and the laser output, respectively. Each couple of the four resulting outputs was then routed to four MZMs, whose outputs were in turn connected to the Inputs number 1, 2, 4 and 8 of the OBFN (Fig. 1). Four signal paths resulted then between the two ports of the network analyzer. The delays in each line have been synchronized by properly tuning the ORR-based delay elements and, to assure coherent combining, the optical phases were also aligned by manually tuning the dedicated phase shifters before the combiners in such a way to achieve the maximum output power. A promising research has also been carried out to implement a system for automatic phase synchronization [152] (see also Section 4.3.1). The resulting RF-to-RF power transfer was then measured in the injected RF band and plot in Fig. 5.21 (top line).

A coherent combining in the OBFN would produce a decrease of 6 dB of the RF power level each time the number of combined signals is halved. This was proved
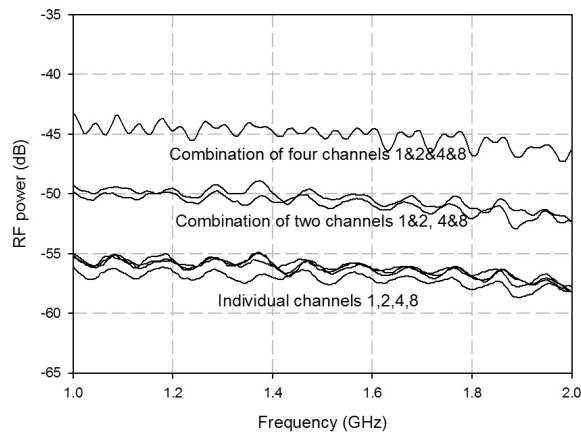
Figure 5.21: Measurement results of the RF-to-RF power response when one (bottom), two (middle) and four RF inputs (top) are connected to the OBFN. The 6 dB increase at each doubling of the number of inputs demonstrates the OBFN coherent combining capability (picture from [167]).

by alternatively disconnecting two couples of RF inputs to the MZMs and by connecting them to matched loads, while keeping the same total RF input power. The same test was repeated by leaving only a single RF input at a time and terminating the remaining ones. Fig. 4 shows that, at each of these steps, the RF power is actually decreasing by 6 dB as expected and this demonstrates the coherent combining capability of the OBFN system.

5.6   Radiation pattern simulation

In Chapter 2, it has been shown how the radiation pattern of an antenna array directly depends on the complex excitations, provided by the so called beamforming network (BFN), to the individual antenna elements constituting the array. In fact, we have proven that the ability to reconfigure those excitations allows to modify important radiation characteristics of the antenna array, as the spatial pointing direction of the main antenna beam, its shape, the levels of the sidelobes, the possibility to place nulls of radiations in desired directions, and more. This gives a large degree of flexibility when compared to individual antennas, making arrays highly desirable in many applications within the field of wireless communications.

To characterize the performance of any beamforming network, it is very useful to analyze the characteristics of the radiation pattern generated when this feeding network is connected to an actual antenna array. In general, this type of test re-

quires the integration of the OBFN with an antenna system, in an anechoic chamber or another suitable environment, using a complex measurement setup, leading to a characterization process which might be expensive and not trivial to realize.

An attractive solution to facilitate the initial test of the performance of the OBFN before integration is to *simulate* the array factor, based on the *measured* complex excitations provided by the realized beamformer. This is a common approach used by several authors [168], [52].

In this section, we report the simulation of the array factor generated by the *FLY* optical beamformer, based on the measured RF-to-RF characteristics that are obtained when the OBFN is programmed for two different beam settings. For this purpose a computer application was implemented to automatize the procedure [169]. The software operates the automatic measurement of the transmission parameters s_{i1} of an equivalent $N+1$ ports microwave network (N antenna ports + 1 beam port), each corresponding to the complex excitation of an individual (i-th) antenna element of the array. The measured excitations are used to simulate the array factor generated by the optical beamformer and to analyze it in terms of maximum directivity, sidelobe levels and wideband behaviour. The software provides a useful tool to test the wideband performance of the network, the effects of excitation inaccuracies, and a straightforward evaluation of the effects of amplitude and phase weighting for beam shaping.

The aim of the software application is twofold. First, it creates a communication between the measurement instrument (a vector network analyzer, VNA) and the computer to automate the measurement of the OBFN transmission parameters, corresponding to the antenna excitations. After that, the acquired data are used to calculate the simulated array factor generated by the optical beamformer. This can be done for both linear (1-D) and planar (2-D) arrays. The program allows to display the array factor in various forms and to analyze different important quality parameters, included its frequency dependent behaviour.

5.6.1   Modelling a beamformer as a microwave network

When the OBFN is integrated in a system with electro-optical modulators and photodetectors, as described in Section 5.5.1, it can be used to generate the complex excitations required to feed the individual elements of the antenna array. Those excitations can be directly related to the s-parameters of an equivalent microwave network which has as many inputs as the number of antenna elements, and as many outputs as the number of beams generated by the OBFN. For more information about the S-matrix description of a microwave network, the reader may refer to [170].

Let us consider an optical beamformer with N antenna ports and M beam ports. When integrated with modulators and photodetectors, this OBFN can be modelled as an N-by-M microwave circuit, where the n-th input-output response (that is, the nm-th transmission parameter, s_{mn}) corresponds to the complex excitation provided to the n-th antenna element of the array (C_n) when exciting the m-th beam port:

$$\underbrace{C_n = |C_n|e^{-j\varphi_n}}_{\text{beam}\,m} \quad \text{is equivalent to} \quad s_{mn} = [S]_{m,n} \quad n \in [1,...,N]\,, \; m \in [1,...,M] \quad (5.8)$$

Magnitudes ($|C_n|$) and phases (ϕ_n) of the s-parameters can be measured over the frequency range of interest using a VNA. The measured data can be employed to calculate the array factor of a linear array, at a specific frequency, by implementing the relation (2.98)

$$F(\psi, f) = \sum_{n=0}^{N} C_n e^{j\alpha_n} e^{jn\frac{2\pi f}{c_0}d\cos\psi} \qquad (5.9)$$

where f is the frequency, ψ is the pointing angle, and d is the inter-element distance of the array. A similar formula is implemented for the case of a planar array (see Section 2.4.3).
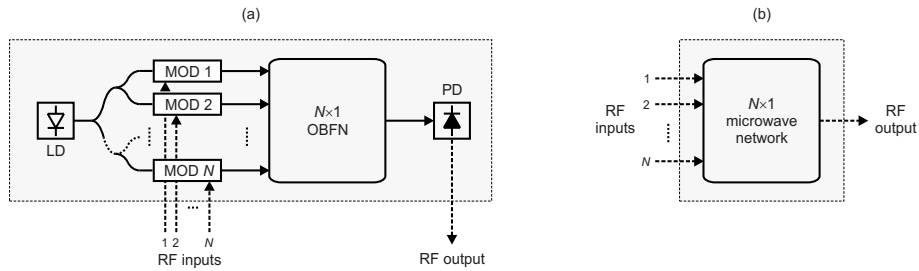
Figure 5.22: Equivalence between an $N \times 1$ optical beamforming network and a $N \times 1$ microwave network

An application has been developed, in the LabView® programming environment, to assist the measurement of the s-parameters and to calculate and display the array factor originated by the corresponding excitations. An interactive graphical interface allows first to select the array configuration (linear or planar) and then to specify the array parameters: operating frequency range, inter-element spacing d and desired beam direction ψ.

Through the VISA communication protocol, the LabView application implements an automatic instrument control. First, it sets the network analyzer to the specific frequency range, and then it remotely measures magnitude and phase of the complex network transmission coefficient s_{mn}, specified by the user, over the frequency range of interest. The measured data are then acquired in the computer and displayed in the user interface for comparison with the desired behaviour. The user can select the desired display format as when directly operating on the VNA interface. The data can be saved in *Touchstone*[3] format and recalled, with the same application, for further offline processing.

---

[3]Touchstone was originally a proprietary file format from EEsof (now owned by Agilent Technologies) and later became a *de facto* industry-standard file format for measurement equipment (e.g. vector net-

A MatLab® script is placed within the LabView structure to simulate the array factor, which can then be plotted (in 2-D) with respect to steering angle, for a specific frequency (to analyze the array factor characteristic in comparison with theory at a specific frequency), both in linear and polar coordinates, or (in 3-D) with respect to both angle and frequency, to analyze the frequency dependent behaviour, the presence of grating lobes or frequency squint [4]. The application has been reported and demonstrated in [169].

5.6.2   Measured s-parameters

The first step towards the OBFN performance evaluation based on the analysis of the array factor, is to configure of the OBFN input-output responses. The same setup used in the RF-to-RF characterization of Section 5.5 has been used for this test.

Differently from what has been described in Section 5.5, where a single input-output response has been configured to demonstrate three different delay settings, it is now needed to configure multiple input-output responses corresponding to the different OBFN channels, in order to provide N input-output transfers with a linearly increasing delay that can be used to feed a linear antenna array (see Section 2.4.1). The result of such a configuration will be referred to as a *beam setting*. When associated to a uniform amplitude response, a certain beam setting would form a beam pattern with a main lobe in direction ψ_0, according to Eq. (2.53) given in Chapter 2.

The scope of this test is to check that the beam pointing direction is as desired, and to prove the wideband performance of the beamformer by showing its capability to generate a squint-free radiation pattern over the whole band of interest. It is also desired to show the seamless beamsteering capability of the ORR-based OBFN, for this reason several *arbitrary* beam pointing directions will be chosen, and the corresponding beam settings will be set and demonstrated.

5.6.3   Reference OBFN setting and delay equalization

As a start, it is desirable to consider a *reference* OBFN setting. It is convenient to choose a delay setting in which the ORRs of the different delay units are all set to their minimum quality factor. This condition will be referred to as the *out of resonance* condition. According to the theory introduced in Chapter 4, in this state each ORR will introduce a delay equal to its round trip time T. In practice, due to the imperfections in the realization of the optical couplers that couple the light in and out of the ring waveguide, in many cases the ORRs resonances cannot be completely flattened, causing the delay in the resonance band to be slightly higher (and, out of band, slightly lower) than T. In those cases, the effect of the residual resonance condition will be minimized by shifting the resonance frequency of the ORRs out of the band of interest.

---

work analyzers), and then an EIA standard as part of the Input/output Buffer Information Specification (IBIS) project [171].

The setting described here can be conveniently used as a reference since it provides the widest possible band of operation, being ideally independent from the ORR resonance bandwidth limitation that will be encountered when programming the ORRs to increase the group delay.

In practice, this setting does not necessarily provide either a uniform or a linear delay distribution across the N OBFN ports, as would be required to form a beam in direction ψ_0 according to Eq. (2.53). In fact, different delay paths may contain a different number of ORRs, each of them giving an offset delay equal to a round trip time T. In addition to that, the optical waveguides paths on chip have different lengths. Finally, the optical fiber pigtails at the output of different MZMs and the fibers constituting the input FAU might have different lengths as well. This situation is likely to result in a non-uniform or a non-linear distribution of delay across the OBFN channels.

Nonetheless, the delay differences can be equalized by adding a suitable length of transmission line (optical fiber or coaxial line) to each input-output channel of the OBFN system. This process is generally undesired since it requires a customized modification of the system. For this reason, the novel chip implementations described in the following of this thesis aim at solving the problem of unequal RF delay paths by (1) building a OBFN layout with the same number of ORRs in each channel, and with equal optical path lengths (*symmetrical* OBFN), and by (2) eliminating optical fibers from the setup by hybrid integration of a modulator array with the OBFN chip.

5.6.4 Beam settings

After equalization, the described reference OBFN setting offers a uniform delay distribution across the OBFN channels, which corresponds to a broadside beam pointing direction for the antenna array. The beamformer can be conveniently tuned to provide linearly increasing delays at the OBFN ports. The correspondance between delay progression and beam pointing direction depends on several factors, as RF frequency and the inter-element antenna spacing, and can be described by a simple expression derived from Chapter 2. In that chapter, we have defined the pointing direction ψ_0 as the angle between the axis of the array and the direction of the main lobe. For convenience we now define the pointing direction as $\theta_0 \doteq \pi/2 - \psi_0$, that is the angle between the broadside direction and the direction of the main lobe of radiation.

For a linear array, the phase excitation α_n of element n required to create a beam pattern with a maximum in direction ψ_0 is as in Eq. (2.52)

$$
\begin{aligned}
\alpha_n &= -nk_0 d \cos\psi_0 \\
&= -nk_0 d \sin\theta_0
\end{aligned}
\tag{5.10}
$$

at frequency $f_0 = k_0 c/2\pi$. The phase shift increment between adjacent elements is thus

$$\Delta\alpha = \alpha_n - \alpha_{n-1} = k_0 d \sin\theta_0 \tag{5.11}$$

The required phase shift given by Eq. (5.10) corresponds to a group delay

$$\tau_n = \frac{-nd\sin\theta_0}{c_0} \tag{5.12}$$

where we have substituted $k_0 = 2\pi/\lambda_0$ and $\tau = L/c_0 = \Delta\alpha/k_0 c_0$.

This in turn gives that the group delay increment between adjacent elements must be

$$\Delta\tau = \tau_n - \tau_{n-1} = \frac{d\sin\theta_0}{c_0} \tag{5.13}$$

The relation between delay increment (or phase shift increment at the operating frequency) and beam direction is immediately clear by observing Fig. 5.23.

Based on this theory, let us create two beam settings corresponding to array beam directions of $\theta_0 = +30$ degrees and $\theta_0 = +60$ degrees. Let us consider an antenna array operating at K_u-band, in the TV-SAT band 10.7-12.75 GHz, as in the OBFN design in Chapter 4. The central frequency will be 11.725 GHz. To avoid grating lobes for all frequencies and all scanning angles, we refer to the sufficient condition given by Eq. (2.67) and we choose an inter-element distance of

$$d \le \frac{\lambda_{\min}}{2} = \frac{c_0}{2f_{\max}} \approx 11.8 \text{ mm} \tag{5.14}$$

where $f_{\max} = 12.75\,\text{GHz}$ and $\lambda_{\min} = (30/12.75)\,\text{cm} \approx 2.353\,\text{cm}$.

Beam setting 1

In order to form a beam in direction $\sin\theta_0 = 30$ degrees, the phases should be

$$\alpha_n = -nk_0 d\sin\theta_0 = -n\Delta\alpha = -n \cdot 1.24 \cdot 10^{-10} f \text{ (deg)} \tag{5.15}$$

and the corresponding group delays should be

$$\tau_n = \frac{-nd\sin\theta_0}{c_0} = -n\Delta\tau = -n \cdot 19.67 \text{ (ps)}. \tag{5.16}$$

Beam setting 2

The simulation and OBFN setting operation are repeated for a beam pointing direction of $\theta_0 = 60$ degrees. In order to form a beam in this direction, the phases should now be

$$\alpha_n = -nk_0 d\sin\theta_0 = -n\Delta\alpha = -n \cdot 2.14 \cdot 10^{-10} f \text{ [deg]} \tag{5.17}$$

And the corresponding group delays should be

$$\tau_n = \frac{-nd\sin\theta_0}{c_0} = -n\Delta\tau = -n \cdot 34.06 \text{ ps} \tag{5.18}$$
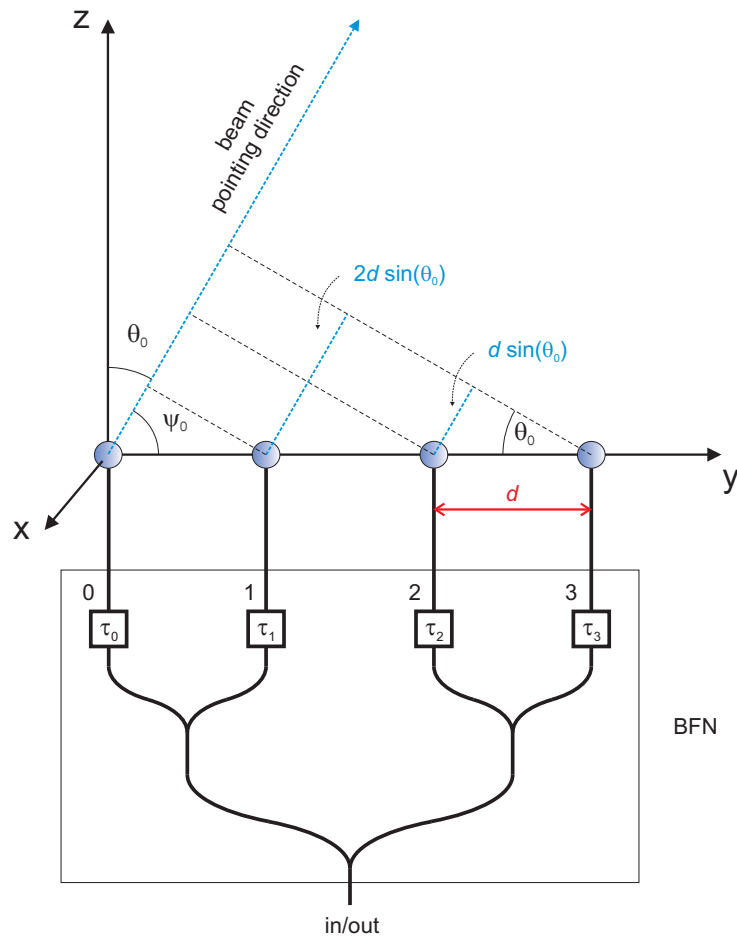
Figure 5.23: Graphical representation of the relation between the pointing angle ψ_0 and the delay increment between adjacent elements
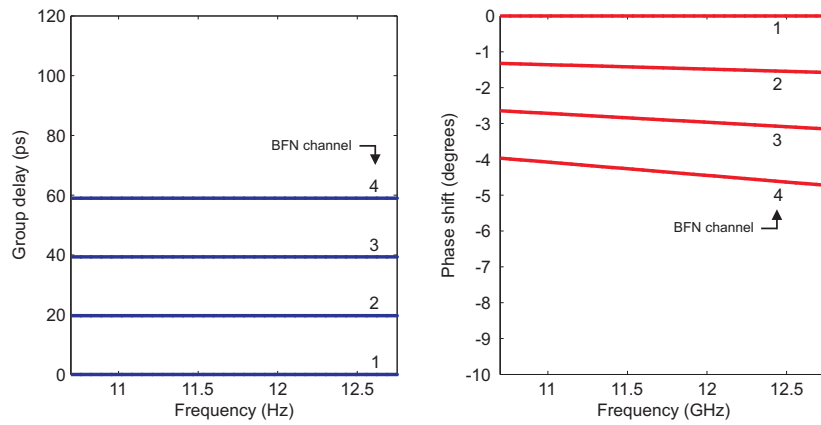
Figure 5.24: Simulated delay (left) and phase (right) responses of the 30 degrees beam setting
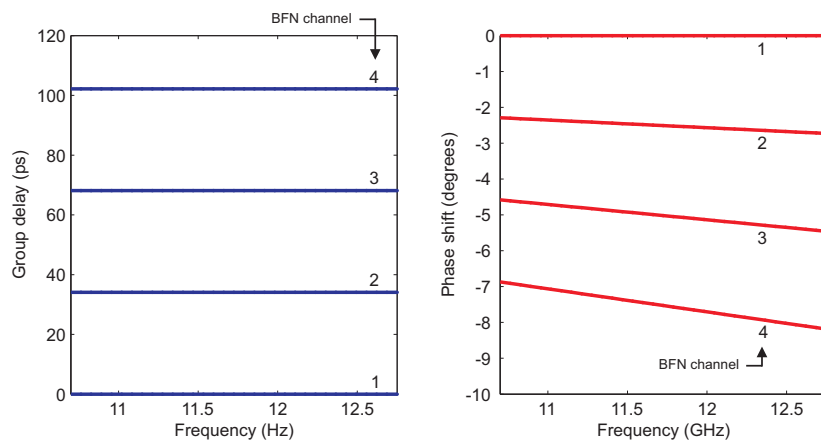
**Figure 5.25:** Simulated delay (left) and phase (right) responses of the 60 degrees beam setting

5.6.5   Simulated array factor vs frequency (squint analysis)

Fig. 5.26 and Fig. 5.27 show a 3-D plot where the array factor is given versus both pointing angle and frequency, over the band of interest, respectively for the 30 degrees beam setting and for the 60 degrees beam setting.
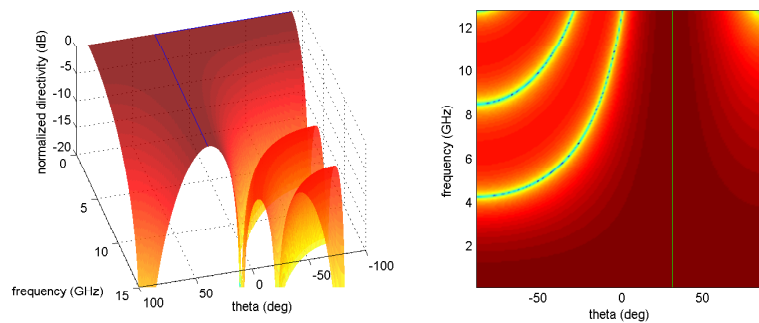
Figure 5.26: Simulated array factor versus pointing angle and frequency. Beam setting: 30 degrees. Left: 3D view. Right, spectrogram (top view).
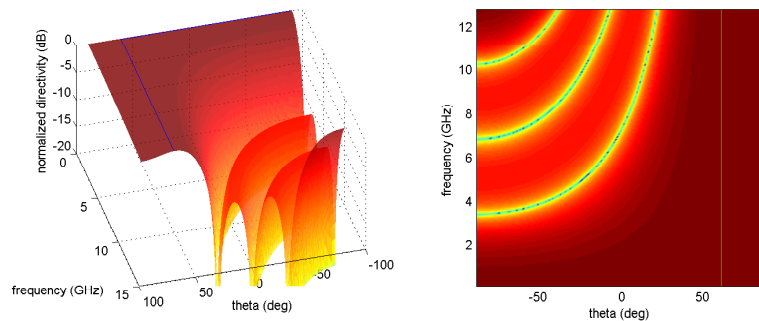
Figure 5.27: Simulated array factor versus pointing angle and frequency. Beam setting: 60 degrees. Left: 3D view. Right, spectrogram (top view).

The latter graph (Fig. 5.27) shows two important aspects:

- the main lobe direction does not vary with frequency (the maximum beam pointing direction is emphasized by the green line): ideal delay lines, capable of providing a perfectly linear phase response over frequency, allow the squint-free operation of the antenna (see Chapter 2);

- the grating lobe does not appear in the considered frequency range. In fact, in Eq. (5.14) we had set the inter-element distance in order to satisfy condition of absence of grating lobes for all scanning angles. The first grating lobe will start to become visible only at frequencies above 12.75 GHz, when the condition given by Eq. (2.67) will no longer be satisfied.

5.6.6 Simulated array factor based on measured *s*-parameters

In the present section, we evaluate the OBFN performance by analyzing the effect that the optically-generated delays have on the array factor of a linear array. To do this, we measure the s-parameters of 4 delay channels of the OBFN and we analyze the effect that the corresponding antenna excitations have on the shape of the array factor and on the pointing direction (frequency squint).

It is important to note that, in this study, we assume that the *mutual coupling* between the elements of the array [172] is negligible. For a real array, this is generally not true, and it has to be taken into account when designing antenna arrays. Mutual coupling is responsible of severe modifications in the radiation diagram with respect to the ideal case and problems like the so-called *scan blindness*. Nonetheless, large amount of research has been performed on this aspect [172], and in general it is possible to design the array taking into account the effects of mutual coupling between elements and avoid or reduce the relative issues. Thus, we can accept this assumption and proceed in the analysis of the simulated array factor as an accurate indication of the characteristics of the radiation pattern of a real array. We start with the following case study.

Case study: 16-elements linear array

Let us now consider a 16-elements linear array operating in the DVB-S band ($10.7 - 12.75\,$GHz). Let us also consider for example that the desired pointing angle for the antenna beam is 30 degrees. According to Eq. (5.18), in order to have a beam pointing direction at $\psi_0 = 30$ deg the required delay progression along the antenna elements is given by Eq. (5.12), as shown in Fig. 5.28.

Let us consider a binary-tree architecture for the beamformer. The 16-elements linear array can be divided into 4 subarrays of 4 elements each, as shown in Fig. 5.29. In particular, we consider the common case in which, at subarray level, the beamforming is performed by 4 electronic beamformers placed in the antenna front-ends. This is an advantage employed in many practical cases, e.g. in the transmit/receive (T/R) elements in active electronic scanning arrays (AESA) [5], [173]. Since our scope is to characterize the performance of the OBFN only, we assume that the front-ends have an ideal performance (flat delay response, magnitude response equal to unity) over the complete band of interest. The optical beamformer is placed in the back-end, to provide the larger delays needed to feed the subarrays. As shown in the previous sections, in fact, the OBFN is capable of providing large delays in the order of few nanoseconds, over bandwidths in excess of 2 GHz [144].

In the specific case of the Memphis project (Chapter 1), a similar approach is employed. In demonstrator 1 (optically-controlled phased array for radio astro-
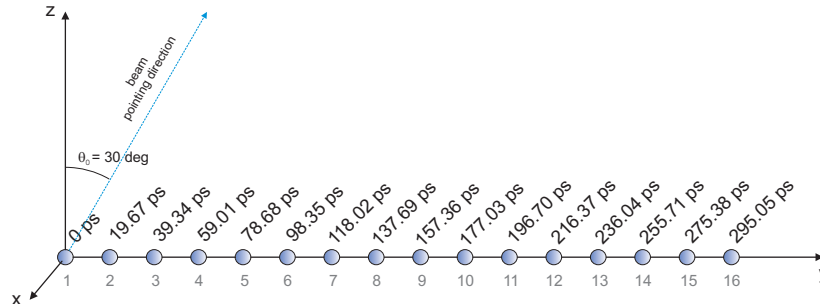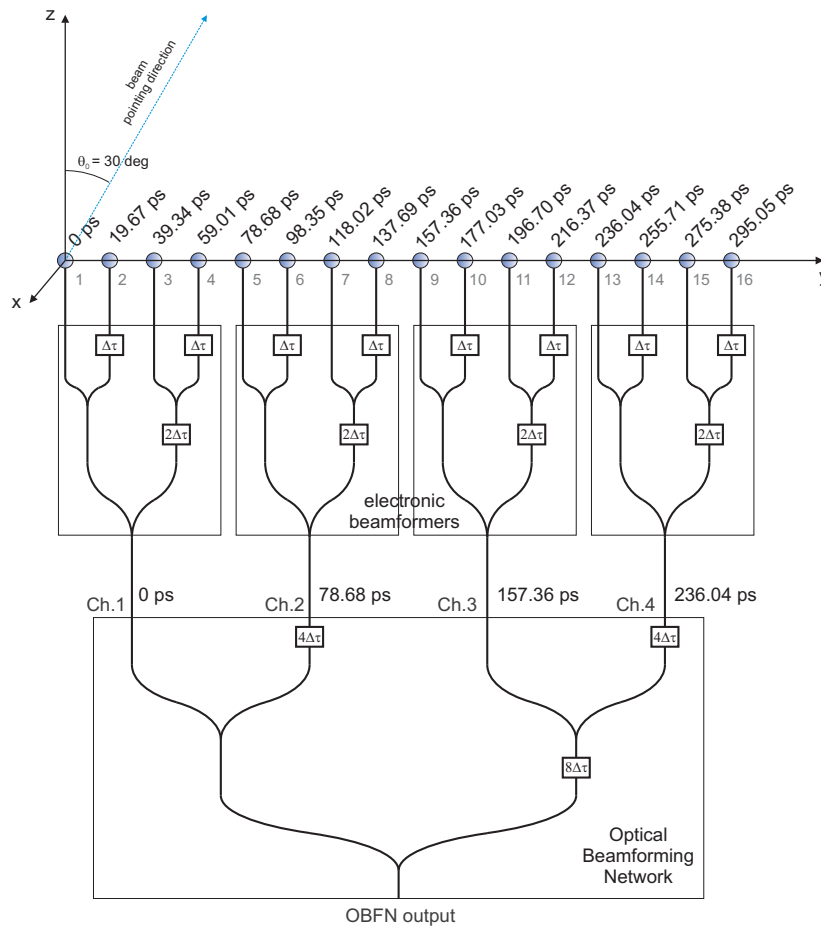
Figure 5.28: Delays required for 30 degrees beamsteering on a 16-elements linear array

nomy applications), in fact, the OBFN will feed an 8×8 connected-type array [174], which is electronically beamformed at subarray level (one microwave monolithic integrated circuit (MMIC) beamforming chip for each 2×2 subarray), and then the remaining 16 outputs are beamformed optically. In demonstrator 2, the airborne antenna for satellite reception is composed by 25 tiles of 8×8 antenna elements each, as shown in the schematic in Fig. 5.30, providing sufficient receiving surface in order to achieve the desired signal-to-noise ratio required for the targeted satellite communication applications (see the analysis in Chapter 4 and in [33]). Again, each 2×2 subarray is electronically beamformed, and the remaining 16 channels are beamformed optically by the proposed OBFN. In the present case study, for simplicity, we limit our analysis to a 16-element linear array. In the envisioned application, instead, an array of up to 7 tiles in a row is produced, corresponding to 56 antenna elements in a single row, with the advantage of a much higher directivity than in this example.

For this beam setting, the delays that have to be provided at the channels 1, 2, 3 and 4 of the OBFN are 0, 4, 8 and 12 times $\Delta\tau$, that are, 0 ps, 78.68 ps, 157.36 ps and 236.04 ps, respectively (see Fig. 5.29). Once the required delays are known, it is possible to display the delay and phase responses required for the OBFN. Those have been respectively calculated according to Eq. (5.12) and Eq. (5.10), and are displayed in Fig. 5.31.

Measured amplitude and phase responses

The OBFN has been tuned employing the measurement setup shown in Fig. 5.19, in order to match the desired phase responses. This setup has been preferred to the one employing carrier re-insertion (Section 5.5) in order to simplify the measurement process. In fact, as seen in Section 5.3.5, the SSB-SC with carrier reinsertion still suffers amplitude and phase fluctuations due to the presence of optical fibers in the setup. This simplified setup, instead, still allows to evaluate the phase and amplitude excitations, without the added instability due to carrier reinsertion. It is

Figure 5.29: Delays required in the binary tree beamformer for 30 degrees beam-steering on a 16-elements linear array

complete array
(25 tiles)

single
antenna tile
(8 x 8 AEs)

11.8 mm

94.4 mm
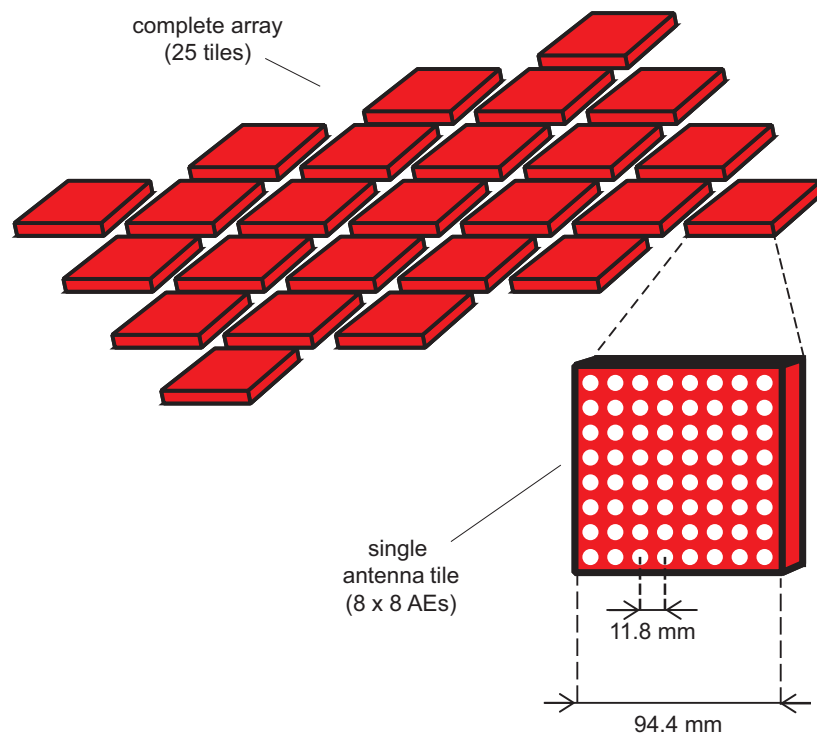
Figure 5.30: Schematic of the satcom antenna array for the Memphis demonstra-
tor 2. In this array, 25 tiles of 8×8 elements each are arranged in a
diamond-like layout.
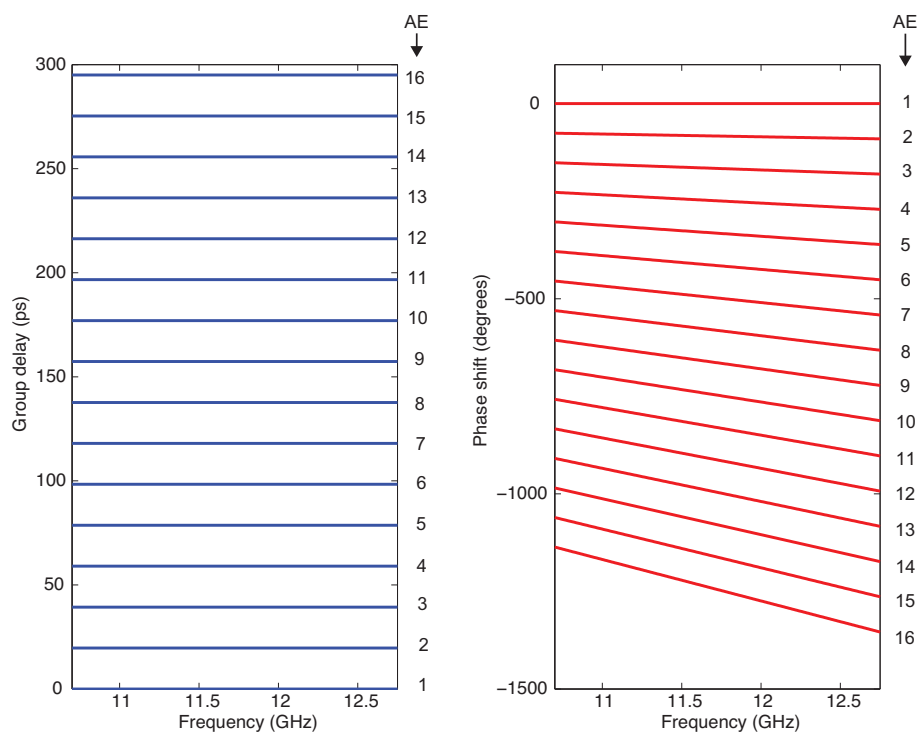
Figure 5.31: Ideal delays (left) and phase responses (right) required for 30 degrees beamsteering on the 16-elements linear array in Fig. 5.29

important to note that such an instability is only due to the presence of fibers within the coherent optical system, and is expected to be completely solved once the system will be realized in an integrated manner as in the final scope of the Memphis project (Chapter 1). With this setup, the RF phase can be given the desired offset by adding a length of coaxial cable or of optical fiber, as discussed in the previous sections, or by employing the separate carrier tuning (SCT) technique, as will be thoroughly explained in Chapter 6. The measured responses are shown in Fig. 5.32. Since we considered the front-ends to be ideal, they will not attenuate the signal and add exactly the desired delays to the output of the OBFN. The responses of all the outputs are shown in Fig. 5.32.

The measured phase responses show a very good match with the desired values. This has been possible by tuning the κ and ϕ factors of the ORRs in the corresponding OBFN path in such a way to approximate with the highest accuracy the ideal delays shown in Fig. 5.31 (left). A residual phase fluctuation is attributed to the presence of slight reflections in the system setup, e.g. at the fiber-to-chip coupling points at the input and at the output of the OBFN chip, and are due to the absence of spot-size converters in this specific chip, which gives optical power losses as high as 6 dB/facet. In the current chip implementations (see Chapter 7), this problem has been solved by the insertion of suitable spot-size converters on-chip which can reduce the loss down to 0.5 dB/facet according to simulations results.

The amplitude responses of the OBFN channels show an increasing attenuation when increasing the delay, as expected, due to the longer propagation time in the waveguide. The amplitude unbalance has been equalized using the tunable couplers available on the OBFN chip at each of the combining points (see Fig. 5.1). The resulting responses shown in Fig. 5.32 have been normalized in order to show the residual amplitude ripple after equalization. The responses are close to the desired unit value but present a ripple of approximately 2 dB, which has been attributed to the non-perfectly flat magnitude response of the optical sideband filter on-chip used in this setup to generate OSSB-FC modulation.

Wideband performance analysis

After having set the amplitude and phase responses of the individual channels, we now can start our analysis from the point of view of the *array factor* that would be generated when the beamformer is connected to the array. As shown in the previous section, the array factor can be computed on the basis of the measured s-parameters of the microwave network equivalent to the OBFN system. A MatLab script is used to implement the calculations, and the results are shown in the following figures.

Fig. 5.33 depicts the array factor with respect to both the angle θ and the RF frequency, in the band $10.7 - 12.75$ GHz. The top figure represents the result obtained by employing the ideal magnitude and delay excitations for the AEs of the array. The bottom graph, instead, is obtained when the measured amplitudes and phases displayed in Fig. 5.32 are fed to the AEs. In the present analysis, the *normalized* value of directivity has been plotted; this is a common choice in all cases in
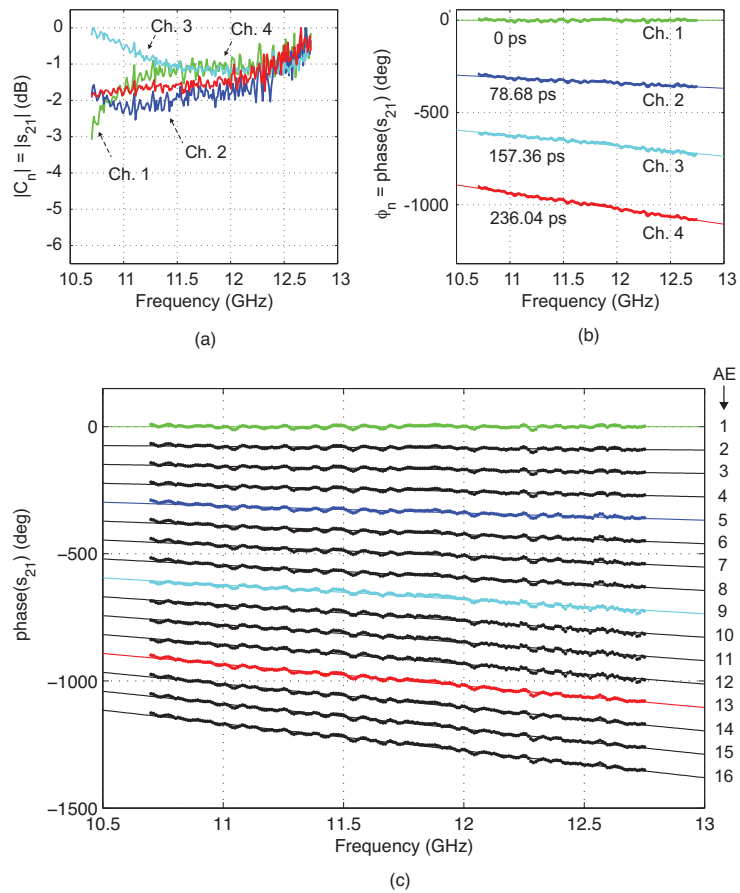
Figure 5.32: Measured amplitude response (a) and phase response (b) compared with the theoretical amplitude (a, solid line) and phase responses (b, solid lines) to be provided by the OBFN in Fig. 5.29 in order to provide 30 degrees beamsteering on a 16-elements linear array. In (c) are shown the phase responses that would be obtained at each antenna element when ideal electronic delay lines would be used (Fig. 5.29).

which the main interest is to compare the beam shape and the relative position of the main lobe and of the sidelobes at different frequencies, rather than the antenna gain, which ultimately is very much dependent on the number of elements and the array size.

It can be noted immediately that the highest portion of the surface represents the main lobe of radiation, which is pointed in the desired direction $\theta_0 = 30\,\text{deg}$ at all frequencies. Parallel to this main lobe, additional local maxima are visible, separated from each other by sharp dips. Those local maxima represent the sidelobes of the array, while the dips indicate the position of the minima (or nulls) of radiation. When observing the depth of the minima, a noticeable difference can already be seen between the ideal case and the measured case: the depth of the nulls tends to become more shallow and irregular in the measured case. This is most likely due to the non-perfect amplitude equalization among the AEs, which in turn does not allow complete cancellation in correspondence of the minima of radiation observed in the ideal case. Nonetheless, most of the nulls have depths of at least 30 dB and all of them show values of at least 20 dB or higher, which can be considered sufficient for the target applications [153]. In fact, we must consider that for the final application to both satellite communication and radio astronomy, suitable amplitude tapering techniques will be employed, which are possible thanks to the complete reconfigurability of the OBFN and which allow a further sidelobe level and null depth suppression [2]. In addition to that, it is expected that the system integration will provide improved stability in the measurement of the response, allowing a higher degree of accuracy in the amplitude tuning procedure and, in turn, in the shape of the generated antenna patterns.

In this analysis, however, our main interest is the wideband performance of the beamformer. For this reason, in Fig. 5.34 the calculated array factor is plotted in a color-coded graph. The horizontal axis shows the pointing angle, while the scale on the vertical axis indicates the RF frequency. The values of the array factor are visible via color coding as indicated in the color bar on the right. This type of plot allows to clearly identify the angular position of the main lobe, the sidelobes and the nulls of radiation by observing the color intensity, and to effectively analyze their variation across frequency. It can be seen that the main lobe of radiation is again around 30 deg as expected; in addition to that, this graph allows to see clearly that the direction of the main lobe does not vary in frequency, neither in the case of using ideal true-time-delays (top) nor for the measured case (bottom). This demonstrates that the OBFN performs in a squint-free manner as desired, over the complete DVB-S band. Other noticeable differences between the two plots are the less sharp color transition between the sidelobes and the nulls of radiation, especially approaching the lowest frequency range. This again confirms that the feeding inaccuracies create the a so-called *filling effect* of the nulls of radiation.

Figures 5.33 and 5.34 are effective in graphically showing the overall performance of the OBFN with respect to frequency. It is now desirable to give a more accurate and quantitative evaluation of this performance, as well as an analysis of the array factor degradation due to the non-ideal excitations. For this scope, it is useful to represent the array factor versus the angle θ for different RF frequencies,
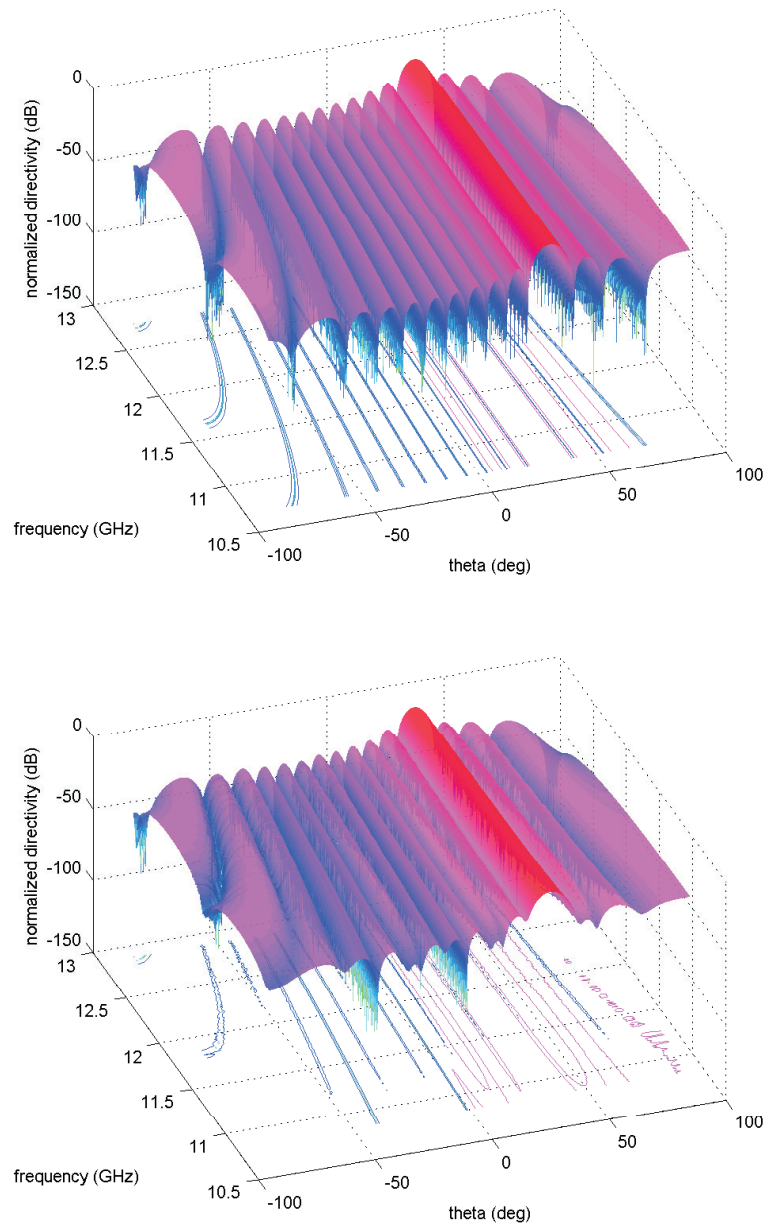
Figure 5.33: Simulated array factor of the 16-elements array versus angle θ and versus frequency, for the ideal AE excitations (top) and the measured AE excitations (bottom)
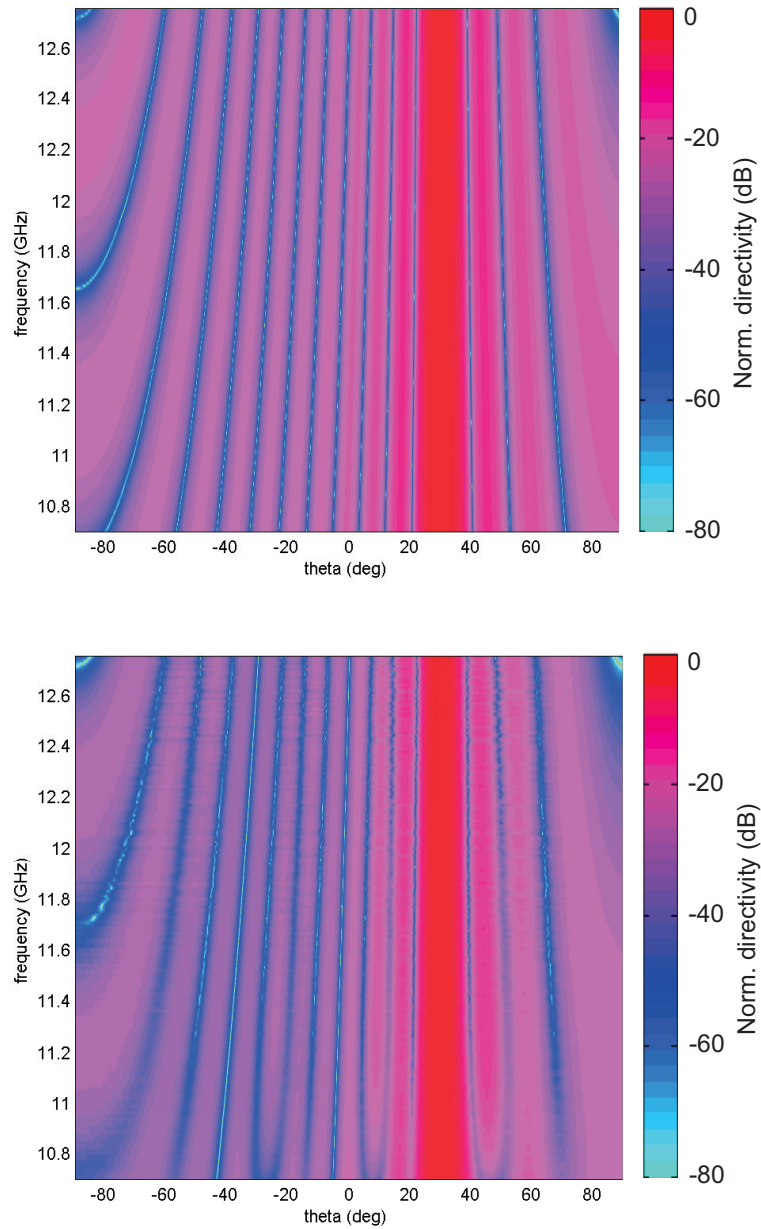
Figure 5.34: Simulated array factor of the 16-elements array versus angle θ and versus frequency, for the ideal AE excitations (top) and the measured AE excitations (bottom). The color scale codes the value of the normalized directivity (in dB).

that is, by analyzing multiple "cuts" of the previous figures at those specific RF frequencies. This is done in Fig. 5.35 for five frequency points equally spaced over the whole band (10.7 GHz, 11.2125 GHz, 11.725 GHz, 12.2375 GHz and 12.75 GHz).

From the analysis of Fig. 5.35 it can be observed that the pattern generated using the optical beamformer are very accurate with respect to the ideal patterns at most of the frequencies. A more sensitive deviation can be seen towards the low band. In particular, at 10.7 GHz there is a broadening of the main lobe and an observable null-filling effect for most of the radiation nulls. In addition to that, some of the sidelobes appear to be lower than expected, a fact that generally indicates the presence of phase errors. Considering the amplitude excitation coefficients given in Fig. 5.32, it can be observed that in the low band the amplitude of channel 3 of the OBF appears approximately 2 dB higher than the others, while the amplitudes tend to become more uniform at higher frequencies. This can explain the deviation from ideality observed only at low frequencies, and on the broadening of the main lobe.

The right column in Fig. 5.35 shows a zoomed portion of the corresponding diagram on the left, in proximity of the main lobe. This allows an accurate diagnosis of the squint problem. For the high frequencies, the error in the pointing direction is very low, in the order of a hundredth of a degree (0.02 degrees at 11.2125 GHz, 0.04 degrees at 11.725 GHz, 0.015 degrees at 12.2375 GHz and at 12.75 GHz), which corresponds to the 0.034%. At 10.7 GHz, the error rises to 0.2 degrees, which is still as low as the 0.67% of the total beamsteering angle (30 degrees).

Comparison with phase shifter-based beamsteering

It is important to note how this compares with the case in which phase shifter based beamforming would be used. Assuming the phase shift is calculated to generate a beam with 30-degrees pointing direction at mid-band, that is, 11.725 GHz, the phases would be the ones shown in Fig. 5.36.

The corresponding array factor would be as shown in Fig. 5.37 (top). The comparison with the array factor obtained using the measured OBFN response (bottom) shows that for the phase shifter case the main lobe moves sensibly across frequency.

A clearer view is obtained when displaying the array factors at different frequencies as in Fig. 5.38. From this figure it can be seen that the use of phase shifters would create a strong beam squint, that is, a strong variation of the pointing direction across the frequency band. Fig. 5.39 shows the amount of beam squint: the pointing angle varies from 27.3 deg at 10.7 GHz through 33.15 deg at 12.75 GHz. The absolute errors would then become 2.7 deg (9 %) at 10.7 GHz and 3.15 deg (10.5 %) at 12.75 GHz, each two orders of magnitude larger than the ones obtained with the proposed true-time-delay OBFN. As will be further discussed in Sec. 5.6.7, the phase-shifter-based approach is inadequate to provide a solution to the broadband beamsteering problem for the desired satellite communication application of demonstrator 1. On the contrary, it will be shown that this result proves the effectiveness of the OBFN to solve the squint problem in K_u-band phased array antenna
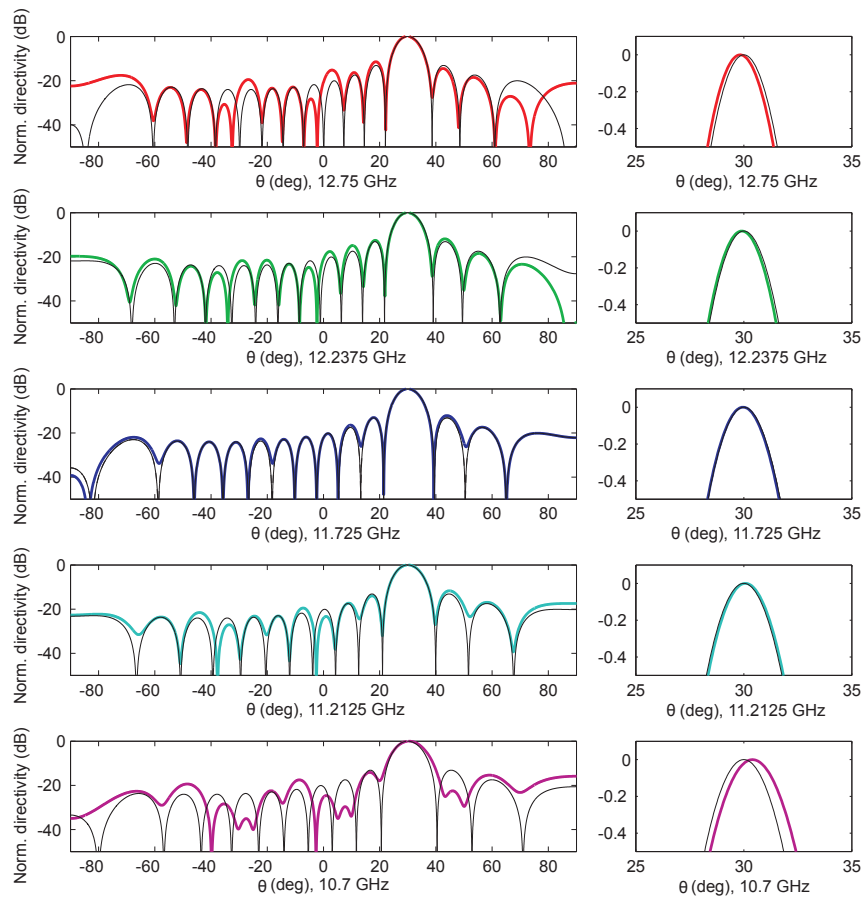
Figure 5.35: Simulated array factor of the 16-elements array versus angle θ, for the
ideal AE excitations (solid, black) and the measured AE excitations
(solid, color). The corresponding frequency is indicated on the θ-axis.
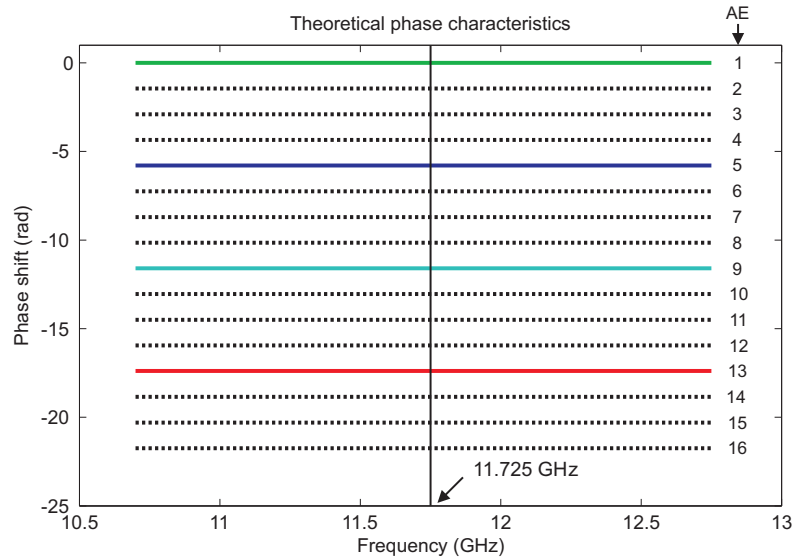
Figure 5.36: Ideal phase responses required for 30 degrees beamsteering at 11.725 GHz, for antenna elements (AE) 1 to 16

beamsteering.

An even more effective way of showing this result is to display, on the same graph, the maximum pointing angle versus frequency for the three cases of (1) simulated beam pointing angle based on measured excitations, versus (2) ideal delays and (3) pure phase shift beamsteering. Fig. 5.40 shows this comparison. The variation of pointing direction across frequency due to the measured excitations follows closely the ideal true-time-delay case, showing the squint-free beamsteering capabilities of the proposed OBFN. The deviation towards lower frequency can be attributed to the unbalanced amplitude response among the different channels, visible in Fig. 5.32, as explained before in this section.

5.6.7 Bandwidth analysis

By observing Fig. 5.37 one may object that the squint observed in case of using phase shifter is not dramatic, since the desired pointing direction (+30 degrees) appears to be comprised within the angular aperture of the main lobe of radiation at all frequency, at least for the considered case of a 16-elements array. In this section, we will discuss this objection in detail, by analyzing the effect of the use of phase shifters on the fractional bandwidth of the array, with respect to the system requirements given by the Memphis demonstrator. In particular, we will demonstrate that the fractional bandwidth provided by the use of phase shifters is not sufficient for the desired application, while the use of the proposed OBFN effectively solves the
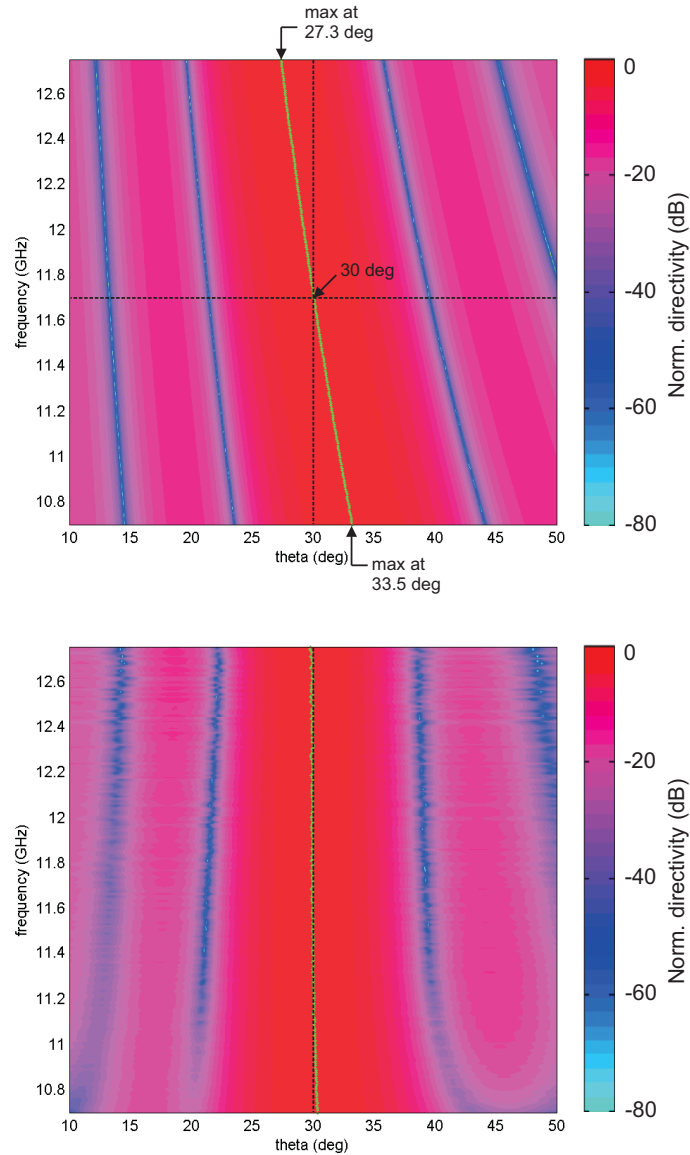
Figure 5.37: Simulated array factor of the 16-elements array versus angle θ and versus frequency, for the case of phase shifter-based AE excitations (top) and the measured AE excitations (bottom). The color scale codes the value of the normalized directivity (in dB). Note the large change in the main beam direction across frequency in the phase shifter case, as expected from Eq. (2.103), compared to the negligible variation for the measured case.
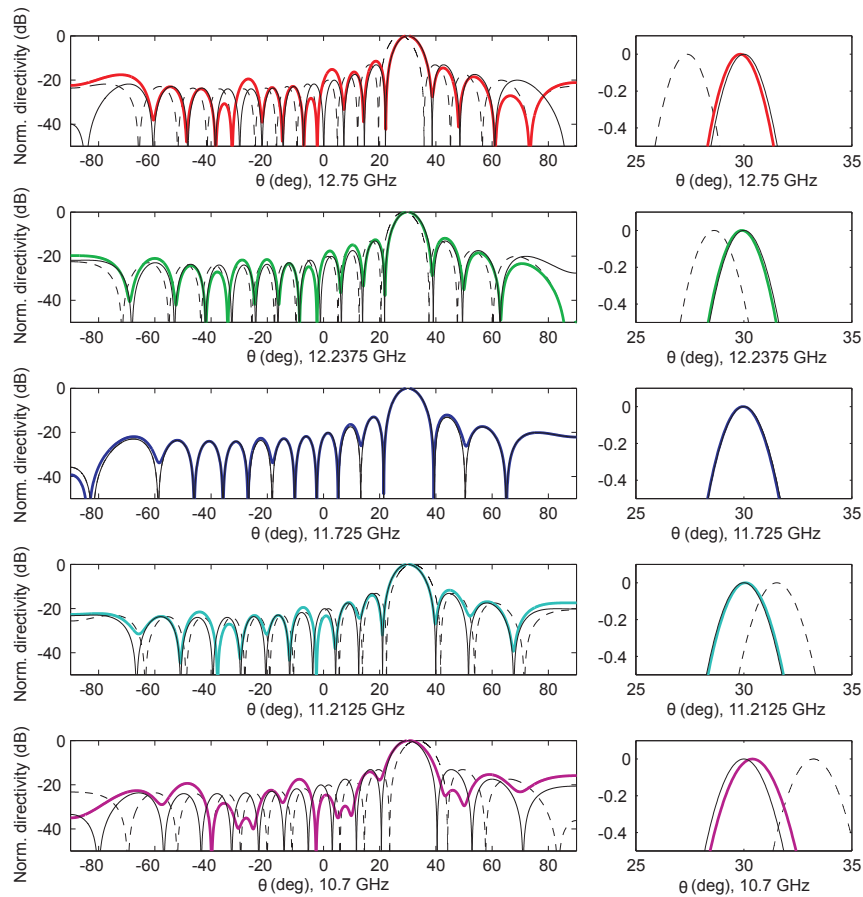
Figure 5.38: Simulated array factor of the 16-elements array versus angle θ, for the phase-shifter based AE excitations (dashed), the ideal TTD-based AE excitations (solid, thin) and the measured AE excitations using the OBFN (solid, thick colored curves). The corresponding frequency is indicated on the θ-axis.
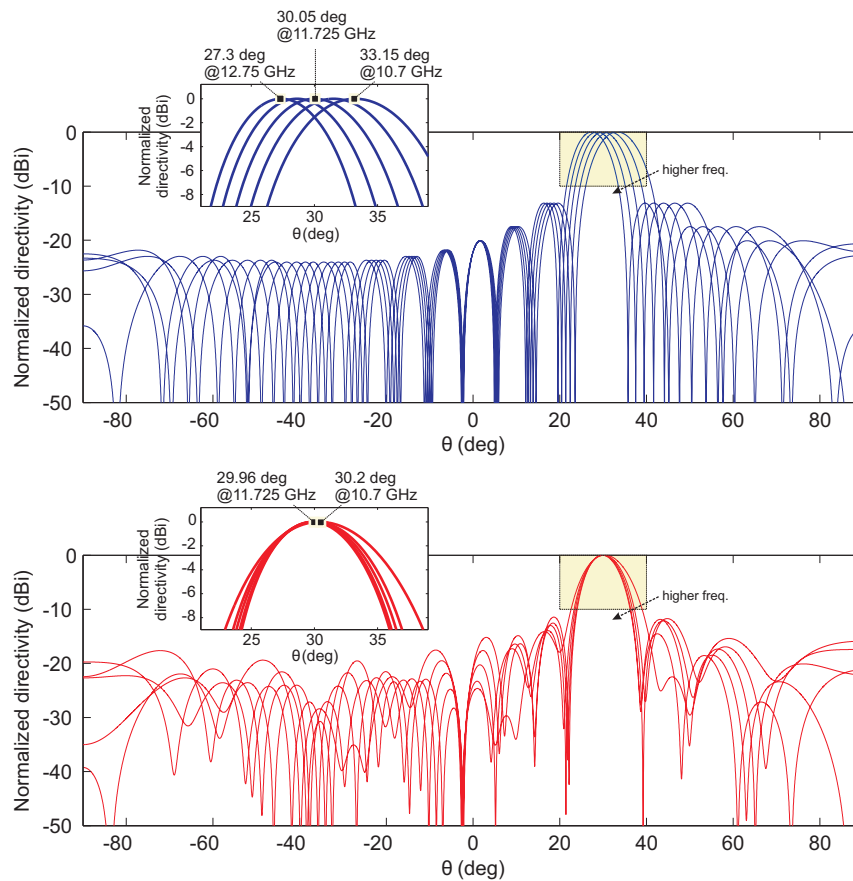
Figure 5.39: Array factor variation across frequency for the phase shifter based
beamforming case (top), with zoom on the main lobe (top inset), and
for the measured OBFN case (bottom) with zoom on the main lobe
(bottom inset)
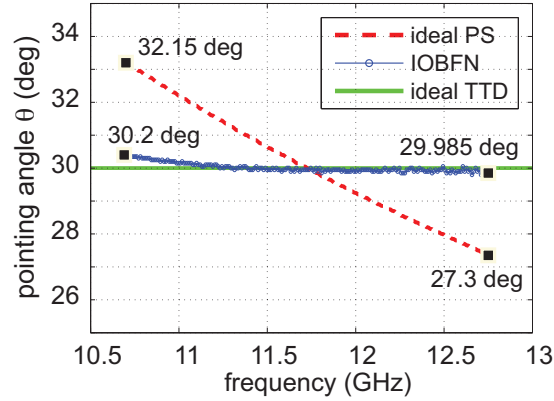
Figure 5.40: Maximum directivity versus frequency for the three cases of (1) ideal true-time-delay beamsteering (green solid line), (2) phase-shift beamsteering (red dashed line), (3) measured excitations with OBFN (blue circled line)

problem.

Let us consider the definition of array bandwidth given by Mailloux [2]. The bandwidth Δf of an array is defined as the interval comprised between the frequency limits at which the gain is reduced by half power. The resulting fractional bandwidth is given by:

$$\frac{\Delta f}{f} = \frac{\vartheta_{3,\text{broadside}}}{\sin(\vartheta_0)} = 0.866 B_b \left(\frac{\lambda}{L \sin(\vartheta_0)} \right) \tag{5.19}$$

where $\vartheta_{3,\text{broadside}}$ is the half-power beam width (HPBW) of the array at broadside, which in turn is defined as [2]

$$\vartheta_{3,\text{broadside}} = 0.866 B_b \left(\frac{\lambda}{L} \right) \tag{5.20}$$

L is the effective array length, which for a linear array is defined as $L = Nd_x$, and for a planar array is the dimension of the array along the principal plane considered. B_b is called the beam broadening factor which models the beam broadening effect due to non-uniform array illumination, e.g. in the case of amplitude tapering for sidelobe level reduction or beam shaping (see Chapter 2). $B_b = 1$ for uniformly illuminated arrays. For large arrays, the HPBW increases with the scan angle ϑ_0 as

$$\vartheta_3 = \frac{\vartheta_{3,\text{broadside}}}{\cos(\vartheta_0)} \tag{5.21}$$

Fig. 5.41 shows the reduction of fractional bandwidth when the dimension of the array L or the scan angle ϑ_0 increase.
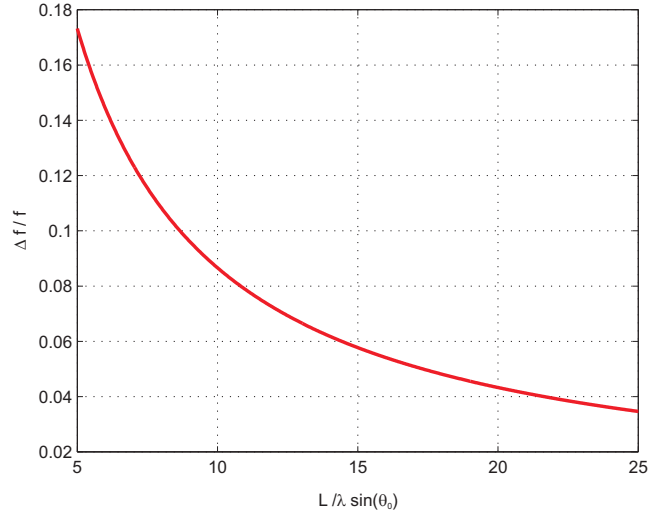
Figure 5.41: Fractional bandwidth of an array versus dimension of the array L and scan angle ϑ_0, in case of beamsteering based on phase shifters only

To better understand the implications of this result with respect to the case of study, let us consider the following examples. The first example analyses the reduction of the fractional array bandwidth with the increase of the scan angle, while the second example shows the bandwidth reduction when the antenna size increases.

Example 5.1

A single tile of the Memphis demonstrator is composed by an 8×8 square array with inter-element spacing of 11.8 mm. Let us imagine to place two of those tiles close to one another, in order to calculate the HPBW along one of the principal directions (e.g. the x-axis) according to Eq. (5.21). The dimension L will be $L = Nd_x = 16 \cdot 11.8$ mm $= 188.8$ mm. The central operating frequency of the array is $f = 11.725$ GHz. Using those values we can specify Eq. (5.19) and plot the absolute bandwidth Δf with respect to the scan angle ϑ_0 only, as in Fig. 5.42. From this plot we can observe that, for a pointing angle of $30°$ as in the previous discussion, the fractional bandwidth is approximately 23.47%, corresponding to an absolute bandwidth of 2.752 GHz. As soon as the pointing angle goes beyond approximately $42°$, the bandwidth of the array falls below the minimum required bandwidth (2.05 GHz) required for the Memphis demonstrator. For the maximum scan angle of $60°$, the bandwidth reduces to 13.55%, corresponding to 1.589 GHz. □

Example 5.2

In the Memphis demonstrator, the architecture of the complete antenna array is as shown in Fig. 5.30. In the principal directions (x or y), 7 tiles of 8×8 antenna
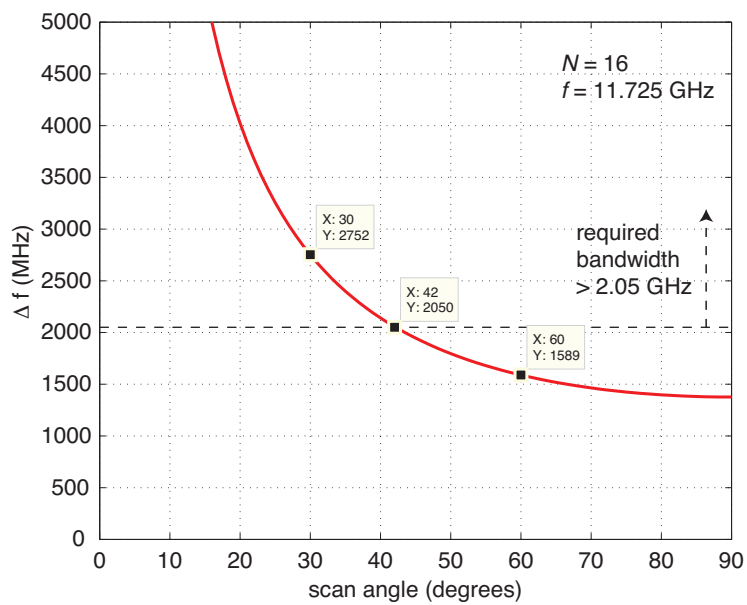
Figure 5.42: Array bandwidth versus scan angle for a 16-elements linear array ($L =$ 188.8 mm, $f = 11.725$ GHz), in case of beamsteering based on phase shifters only

elements are placed adjacent to each other, thus forming an array with $7 \cdot 8 = 56$ antenna elements in the principal direction. The total dimension of the array along this principal plane is thus $L = Nd_x = 56 \cdot 11.8$ mm $= 660.8$ mm, comparable to the size of a standard satellite dish for DVB-S. Fig. 5.43 shows the bandwidth of this array with respect to the steering angle. Compared to the previous example,
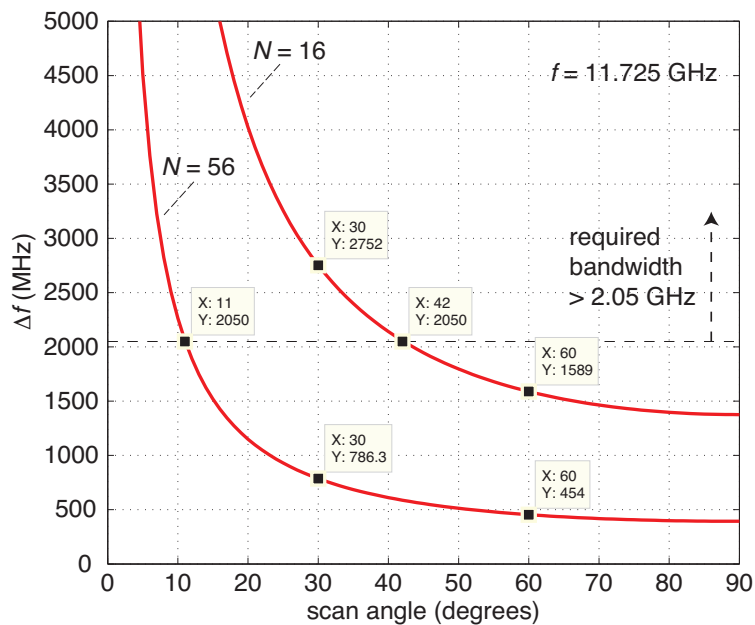
Figure 5.43: Array bandwidth versus scan angle for an 56-elements linear array ($L = 660.8$ mm) and for a 16-element linear array ($L = 188.8$ mm), in case of beamsteering based on phase shifters only (center frequency $f = 11.725$ GHz)

from this plot we can observe that, keeping the same array parameters (frequency, antenna element spacing and steering angle), an increase in the dimension of the array leads to a reduction in the fractional bandwidth. In fact, the bandwidth is now only 6.71% (786.3 MHz) at 30 degrees, and only 3.87% (454 MHz) at 60 degrees, and stays beneath the 2.05 GHz required by the application only up to a steering angle of 11 degrees.

An additional interesting observation is the plot of the bandwidth with respect to the number of antenna elements, for a fixed steering angle, as in Fig. 5.44. This figure shows that, assuming phase-shifter based beamforming, given a maximum desired steering angle, the number of elements of the array cannot exceed a certain

maximum number, which in our case is 22 if we limit the steering to ± 30 degrees and only 12 for the complete steering to ± 60 degrees.
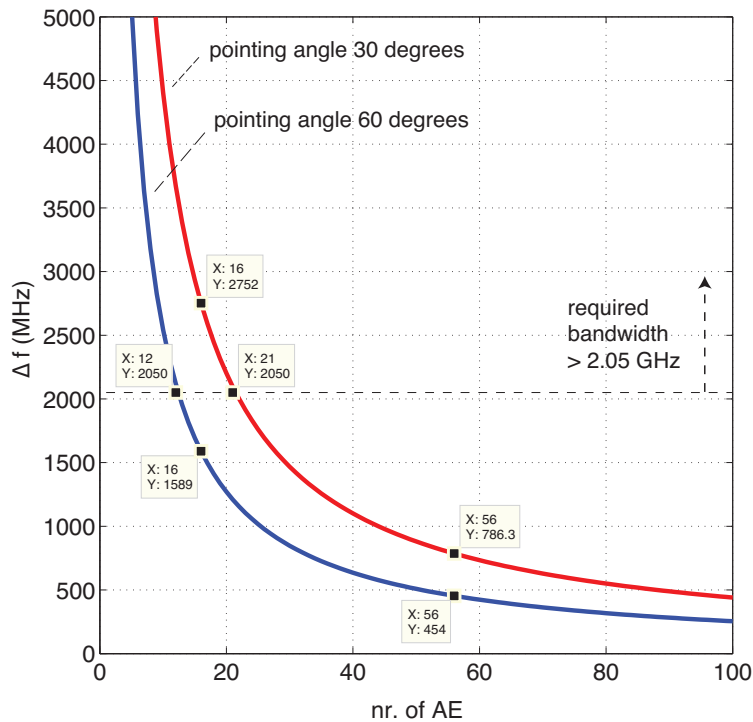
Figure 5.44: Array bandwidth versus number of antenna elements, for a beam-steering of 30 degrees (right, red) and 60 degrees (left, blue), in case of beamsteering based on phase shifters only ($f = 11.725$ GHz)

More in general, a direct relation between actual bandwidth and array size can be derived [2] from Eq. (5.19):

$$L\sin(\vartheta_0) = 0.886 B_b \frac{300}{\Delta f_{\mathrm{MHz}}} \tag{5.22}$$

This equation generally shows that, given a certain required bandwidth, the dimension of an array only using phase shifters cannot be larger than a certain upper limit. In many cases, especially for telecommunication applications, the antenna dimensions are determined by other factors besides the bandwidth, e.g. the antenna gain, the G/T, etc [2]. This shows that the use of true-time delay beamformers for the realization of the feeding network is imperative in many cases, especially for low-power, high-frequency future telecommunication applications.

Interference from adjacent satellites

In the previous section we have discussed how the use of phase shifters limits the number of elements (thus the size), the steering angle and the bandwidth of the array. This brings to the conclusion that true-time-delay beamforming is necessary to guarantee the desired performance to the antenna system.

In addition to that, it is important to consider another fundamental requirement for the antennas employed in telecommunication applications, that is the rejection of interference signals. In particular, when dealing with satellite communications, the requirements on interference are particularly stringent due to the very low power involved [33]. From the beam pattern point of view, this discussion leads to the consideration that it is important that the radiation pattern of the array should present a maximum of radiation pointed towards the direction of the desired satellite, and minima of radiation in the direction of any sources of interference, for example other satellites on geosynchronous earth orbit. The use of antenna arrays is particularly advantageous for the flexibility it provides in terms of antenna pattern shaping. Relatively simple amplitude and phase weighting techniques [2, 148] can be implemented in order to reduce the amplitude of the side-lobes (see Chapter 2). More advanced and well established techniques allow an active interference rejection via adaptive nulling [175]. A large amount of scientific literature deals with the evolution of this specific topic, which is beyond the scope of this research. In our study, however, we can already derive a simple condition to show again the necessity of use of true-time-delay beamforming.

In order to avoid interference from adjacent satellites, it is of fundamental importance that the main contribution to the incoming power comes from the desired satellite transmitter. This in turn implies that the main lobe of radiation from the array shall point to the desired satellite over the whole operating bandwidth.

By means of the simplified example of the 16-elements linear array, we have shown that the use of true time delays allows a squint-free behaviour, in contrast with the phase shifter based approach. If we consider that adjacent satellites have an azimut spacing of approximately 2 degrees, it is important that the main lobe of radiation stays within this angular range. To assure that, we will first calculate the HPBW of the satellite array envisioned for the Memphis demonstrator, and subsequently we will combine this result with the information on the inter-satellite azimut spacing in order to derive a condition for the maximum allowable squint in band.

Considering Eq. (5.20) and Eq. (5.21) we can calculate the HPBW at broadside for the 56-elements array of Example 5.2 as

$$
\begin{aligned}
\text{HPBW}_{\text{broadside}} &= 0.866 B_b \left(\frac{\lambda}{L} \right) \\
&\approx 0.866 \cdot 1 \cdot \left(\frac{0.02554}{0.66} \right) \\
&= 0.03354 \text{rad} \approx 1.9215 \text{deg}
\end{aligned}
\tag{5.23}
$$

and at the limit angle $\vartheta_0 = 60\,\text{degrees}$

$$\begin{aligned} \text{HPBW}_{60\,\text{deg}} &= \frac{\text{HPBW}_{\text{broadside}}}{\cos(\vartheta_0)} \\ &\approx \frac{0.03354}{0.5} \\ &= 0.06708\text{rad} \approx 3.8434\text{deg} \end{aligned} \tag{5.24}$$

After having calculated the HPBW at 60 degrees beamsteering, let us analyze the amount of squint experienced by the array which, according to Eq. (2.103) in Chapter 2 is

$$\begin{aligned} \vartheta(f) &= \arccos\left[\frac{f_0}{f}\cos\vartheta_0\right] \\ &= \arccos\left[\frac{11.725\text{GHz}}{f}\cos(60\text{deg})\right] \end{aligned} \tag{5.25}$$

Let us consider the worst case where the beam squint will occur on the same plane as the azimuth angle, meaning that, across frequency, the pointing direction will move from one satellite towards the other due to squint. If we now plot the actual pointing direction (affected by squint) with respect to frequency (Fig. 5.45), it is possible to see at which point the beam squint can no longer be tolerated. In fact, on the same figure, we also indicate the azimuth position of the desired satellite (60 degrees) and the neighboring satellites (at 58 and 62 degrees), assuming an inter-satellite azimuth spacing of 2 degrees. Two other lines indicate the intermediate angular positions, between the main satellite and its immediate neighbor. As soon as the main beam crosses this line, it can be said that the power from the interferer becomes stronger than the power from the desired satellite. The figure shows that this would occur at the frequencies of 11.38 GHz and 12.09 GHz, for a total usable bandwidth of only 710 MHz, versus the desired 2.05 GHz. It must be considered that, in this analysis, we assumed the very simple hypothesis that, to avoid interference, the main beam direction shall be closer to the direction of the desired satellite than to the ones of the neighboring satellites. In practice, this assumption is more stringent, further reducing the usable bandwidth.

Employing true time delays would allow a strong reduction (or, ideally, a complete elimination) of the squint phenomenon, thus reducing the problem of inter-satellite interference to an acceptable limit.
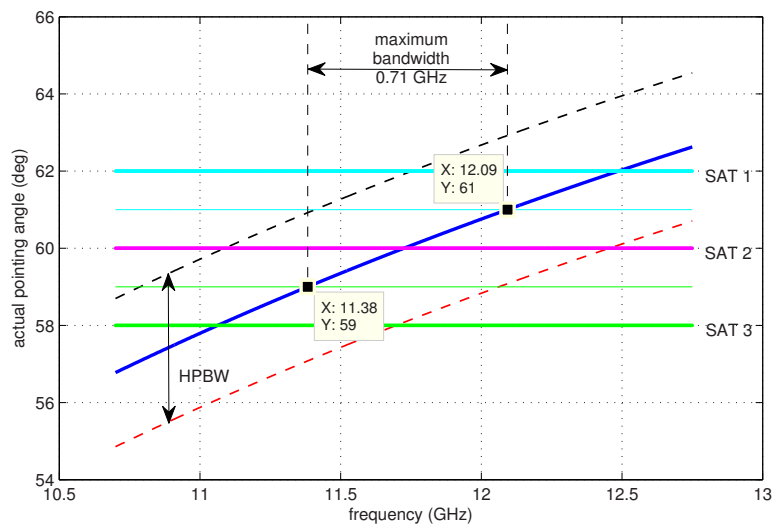
Figure 5.45: Pointing direction versus frequency for a 56-elements array for satel-
lite communications, fed by phase-shifer beamforming. The position
of the target satellite is at 60 degrees of azimuth angle. Neighboring
satellites are at 58 degrees and 62 degrees, and act as interferers. The
squint phenomenon due to the use of phase shifter would limit the
usable bandwidth to 710 MHz.

5.7 System integration and pattern measurements

In this section will be described the system integration and the experimental demonstration of a photonically beamformed, 4-elements receiving array antenna for radio astronomy applications. This work represents the first demonstration of the squint-free, continuously tunable beamsteering capability offered by an integrated photonic beamformer based on optical ring resonator true time delay units, via analysis of the measured radiation patterns. The integrated beamformer is realized in a low-loss optical waveguide technology, realized by LioniX B.V. with a CMOS compatible process. The measurements show a wideband, continuous beamsteering operation over a steering angle of 23.5 degrees and an instantaneous bandwidth of 500 MHz limited only by the measurement setup.

For the system integration, a new OBFN chip has been designed, realized and characterized. This new chip will be used to feed a 4×4 planar array for radio astronomy applications. For this reason, this chip is designed to process the signals of 16 different antenna elements of the planar array. This OBFN chip will be referred to as the "SKY" chip.

The specific application described in this section used a 4×4 planar array for the complete 400 to 1500 MHz frequency band [176], for which the architecture shown in Fig. 5.46 has been designed. The total bandwidth (beyond 100%: see Chapter 2 for the definition of percentage bandwidth) can now be processed at once by the optical beamformer, while in the full electronic system it had to be divided into 40 MHz-wide instantaneous sub-bands [177]. Such a large percentage bandwidth is made possible by the properties of ORR-based delay units, as discussed in Section 6.1. The network (Fig. 5.46) has 16 optical inputs, corresponding to the individual antenna elements of the 4×4 array, and 1 optical output. The signals received by the individual antenna elements are converted into the optical domain by employing an array of 16 Mach-Zehnder electro-optical modulators (MZM). The optical carrier for each modulator is provided by a single laser source via a 1×16 optical splitter. The received RF signals, once transferred to the optical domain, are processed and coherently combined by the beamformer chip. The optical combiners described in Subsection 4.1.2 are placed in such a way to form a binary tree structure, as shown in Fig. 5.46. The inputs of the horizontal subarrays, or rows (Fig. 5.46, left side) are combined by the left section (horizontal beamforming). Their outputs are combined by the right section (vertical beamforming). The optical output is then fed to a photodetector, to recover the RF signal. The details on the integration of the OBFN in the system setup will be described in Section 5.8.

5.7.1 Optical technology and chip realization

The beamformer chip has been realized by LioniX B.V. on a silicon substrate. The design of the optical waveguides is based on the TriPleX™ technology, which has been optimized for low loss and minimum chip area occupation, as described in [144, 147, 178]. In this design, the limiting factor to footprint reduction was the minimum bend radius of 700 μm, needed to ensure negligible bending losses. In
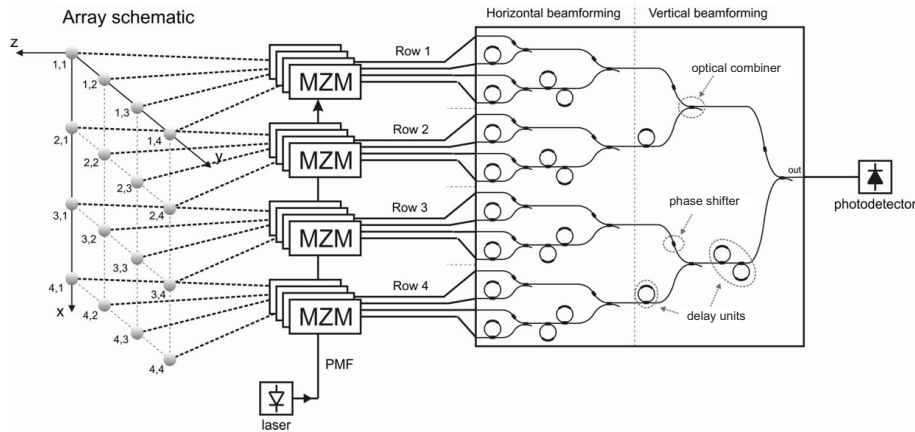
**Figure 5.46:** 16×1 OBFN schematic (right), corresponding to a 4×4 planar array
(left). The position of the ORR delay elements, optical phase shifters
and combiners and their connections are displayed. (From [160])

present implementations, the minimum bend radius that can be used before bend-
ing losses start to play a significant role has been reduced by almost a factor 10 [24].
The low propagation losses, which are as low as 0.2 dB/cm for the most recently
measured chip [159], assure that the insertion of the beamformer in the receiver
has negligible effect on the system performance. The effects at system level of the
insertion of the described optical beamforming chip in the receiver have been the-
oretically analyzed in [33] and for a more general case in [179].

The programmability of the delays produced by the ORR units is based on the
same thermo-optical tuning mechanism employed in the FLY chip [147].

The layout of the optical beamformer is shown in Fig. 5.47, where the optical
waveguide layout is overlapped with the electrical leads layout. The input wavegui-
des (left) fan out to the inputs of the first beamformer section, where it is possible
to recognize the eight ORRs placed on every other input, as shown in the schematic
of Fig. 5.47. The OBFN section 2 contains four pairs of two ORRs each. Sections 3
and 4 contain four rings in total. The optical filter included in the layout is not used
in this application and is bypassed during operation. The heater sections used to
tune the OBFN are connected to the ground line at one side and to a specific bond
pad at the other side, allowing independent control of all the heater elements.

The chip is relatively compact, measuring 13×70 mm. It has been pigtailed with
two fiber array units (FAU) for ease of testing. The input and the output FAUs con-
tain 16 polarization maintaining single mode fiber pigtails each, which provide an
easy access to all the inputs and outputs of the chip. A picture of the packaged chip
is shown in Fig. 5.48, where the input FAU can also be seen.
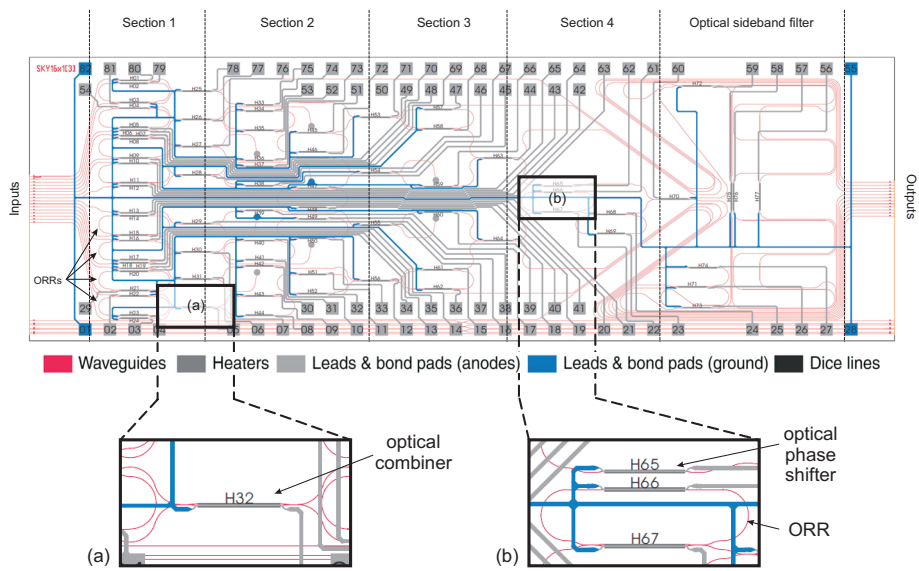
Figure 5.47: Overview of the 16×1 OBFN chip layout (13×70 mm). Waveguides, heaters for electro optical tuning, bond pads and lines for electrical control are visible. The insets provide a closer view of the tunable combiner (a), of the phase shifter and of the optical ring resonator (b). (From [160])
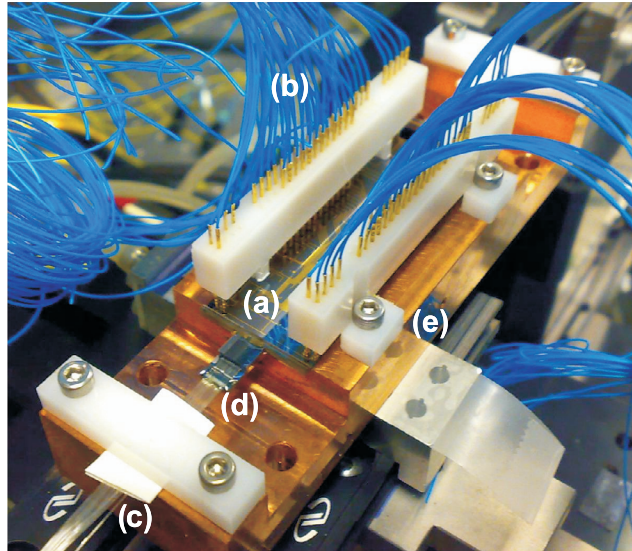
Figure 5.48: Photograph of the packaged chip (a), with electrical (b) and optical (c) connections. The fiber array unit (d) and the copper block used as support and heat sink (e) are also visible. (From [160])

5.8   Description of the RF photonic integrated system

The wideband, continuous beamsteering capability of the proposed beamformer structure has been demonstrated by a measurement in the near field antenna test range facility of The Netherlands Institute for Radio Astronomy (ASTRON). The OBFN subsystem has been integrated on the antenna array. The integration and the experimental results are described in the following sections.

5.8.1   Antenna array and front-end

The antenna employed for the demonstration consists of a 4×4 elements array of Vivaldi antennas, operating in the 400 to 1500 MHz frequency band [176]. This type of radiating element allows ease of integration and exhibits an active reflection co-efficient below -10 dB over the whole frequency band. The 4×4 rectangular subarray is a subsection of the EMBRACE tile [177], shown in Fig. 5.49, left. Fig. 5.49, right indicates the position of the 4×4 rectangular subarray with respect to the complete tile.

Each antenna element is connected to a low noise amplifier (LNA), based on a commercially available active device, designed for minimum noise figure and allowing a total system noise temperature well below 100 K [177].
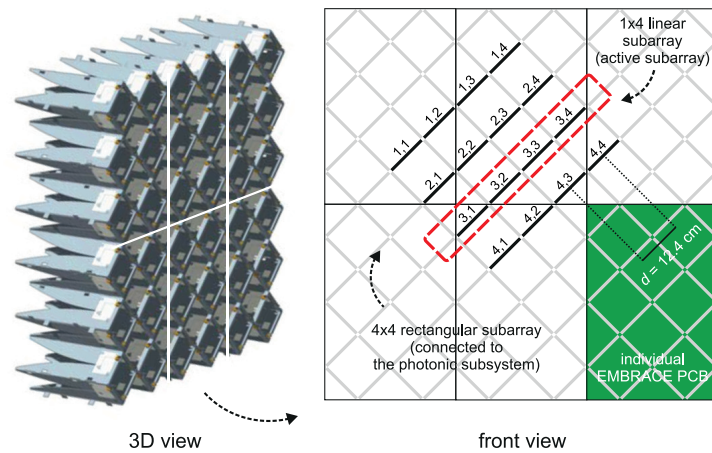
3D view   front view

Figure 5.49: Schematic representation of the antenna tile: 3D view (left), front view
(right). The complete tile is built out of 6 individual PCBs. In the front
view, each diagonal segment represents one of the Vivaldi antenna el-
ements. The 16 numbered elements are the ones which have been
connected to the photonic subsystem (4×4 rectangular subarray). The
4-element linear subarray used for the demonstration is the one sur-
rounded by the dashed line (1×4 linear subarray - active subarray). Its
position and orientation with respect to the complete tile are visible
here. (From [160]) (3D view: edited from http://www.skads-eu.org)

5.8.2 Photonic subsystem

For the demonstration presented here, a 1×4 linear subarray of the realized 4×4 rectangular subarray has been tested. The direction of the 1×4 linear subarray forms an angle of 45 degrees with the sides of the tile, and its position in the complete tile is shown in Fig. 5.49, right. The corresponding RF photonic integrated system is schematically represented in Fig. 5.50 and described below.
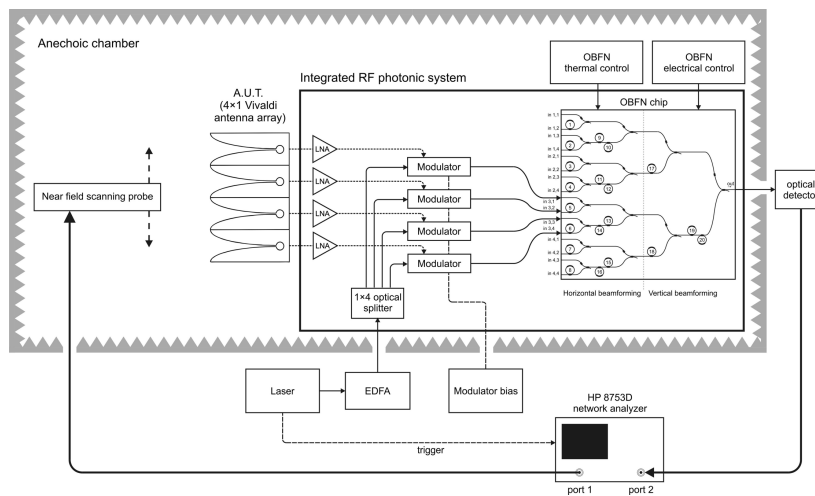
Figure 5.50: Setup used in the radiation pattern measurements (From [160])

The photonic subsystem (Fig. 5.50) consists of the following main components: laser; erbium-doped fiber amplifier (EDFA); optical splitter array; modulator array; optical beamformer chip; detector; control and bias electronics.

The RF circuit boards connecting the antenna elements to the active front ends have been modified to allow the integration of the photonic components (Fig. 5.51). In particular, each of the LNA outputs has been connected to a Mach-Zehnder modulator (Photline MXAN-LN-10), mounted on the same PCB as the LNAs, via SMA connectors. The modulators come in a package with single mode, polarization maintaining (PM) input and output fibers. All the optical components used between the laser and the beamformer employ PM fibers. They have been individually tested and characterized prior to assembling, and their fiber lengths have been equalized by the manufacturer, upon request, for the specific application. This equalization process has been performed in order to match the lengths (thus the delays) among the different channels. The residual unavoidable length differences have been compensated using the programmable delays included in the photonic chip. The measured optical insertion loss of each modulator is approximately 4 dB and the value of half-wave voltage ($V_{\pi,\mathrm{RF}}$) is around 5 V. Slight differences in the optical insertion loss have been observed among the different modulators as well as

among the different channels of the 1×4 optical splitter array. During assembly, an effort has been made to minimize the imbalances among the different beamformer channels, by careful selection of the MZMs to be connected to the individual outputs of the optical splitter array, thus maximizing the amplitude matching of the beamformer. Any residual amplitude unbalance among the channels was compensated by using the continuously tunable combiners. After the delay and combining processing in the OBFN, the resulting signal is detected with a photodetector (Agere 2560A, 3 dB bandwidth of 13 GHz and responsivity of 0.8 A/W).

The optical carrier is provided by a high-stability tunable laser (ANDO AQ4321D), set to an optical output power of 4.9 dBm and whose wavelength has been tuned to lie in the center of the optical delay band. The output of the laser is then split into 4 optical carrier signals by a 1×4 optical splitter array (Fig. 5.50).

The fiber-chip coupling at the input and output of the OBFN introduces a coupling loss of around 6 dB per facet due to the absence of a spot size converter at the fiber-chip interface. An EDFA (gain = 22 dB) is used immediately after the laser to compensate this loss. In future implementations, suitable spot size converters will be introduced to reduce the coupling losses thus removing the need for optical amplification.

A network analyzer (HP 8753D) is used to measure the RF-to-RF responses (s_{21} parameter) of the individual OBFN paths. Port 1 of the network analyzer is connected to the probe antenna, and the output of the photodetector is connected to port 2 (Fig. 5.50).
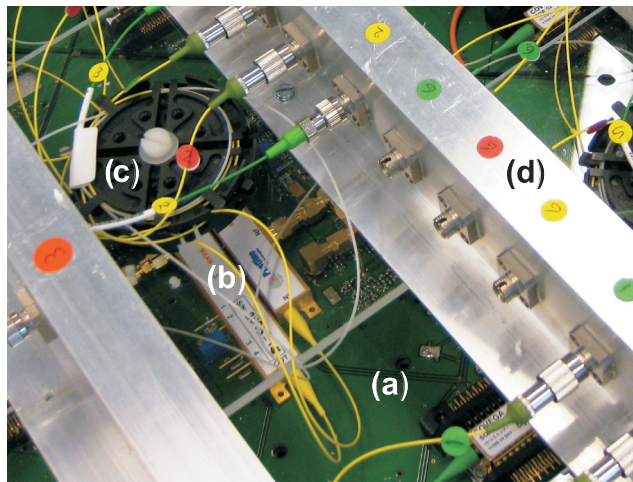
Figure 5.51: Detail of the back side of the antenna tile. The discrete optical components are mounted on the same PCB as the LNAs (a). Note the modulators (b), the reels (c) for the mechanical support of the fibers and the panels (d) supporting the optical connectors. (From [160])

5.9   Experiment

The optical beamformer can be tuned as desired by using dedicated software. Details on the tuning technique can be found in [147]. The preliminary step for the OBFN tuning consists in setting the desired bias point for each of the MZM modulators. In this test, a double sideband full carrier (DSB-FC) modulation has been achieved by biasing the modulators at their quadrature point [33]. The required bias voltages have been determined manually for each of the modulators.

5.9.1   Delay settings

Once the bias point has been set for all the modulators, the optical chip can then be tuned to give the proper amplitude and delay settings required to implement the desired beam pattern.

First, a single optical path is isolated by properly tuning the optical combiners to separately set its delay response. A test tone at the frequency of 1000 MHz and power of -30 dBm is generated with the network analyzer and fed into the modulators via the probe antenna. The RF power is set to this value to ensure that the LNAs operate in linear region.

The first step is tuning the delay elements. Given the desired steering angle ϑ for the main lobe, the corresponding required delay difference to be set between adjacent antenna elements is calculated as [148, 180]

$$\Delta\tau = \frac{d\cos(\vartheta)}{c_0} \tag{5.26}$$

where d is the inter-element distance shown in Fig. 5.49, and c_0 the speed of light in vacuum.

The desired delay is then set by employing the ORR-based delay units previously described and visible (with numbering) in Fig. 5.52. Sweeping the laser wavelength, the resonance frequency of the ORRs can be easily identified and subsequently tuned to match the modulated RF signal band (phase-shift method [165, 166]).

The desired delay difference $\Delta\tau$ given by Eq. (5.26) can be obtained by setting the corresponding phase difference at the frequency f of operation, using the relation

$$\Delta\phi_f = 2\pi f \Delta\tau \tag{5.27}$$

The OBFN paths connected to the subarray in use are the (3,1)-(3,4) as indicated in Fig. 5.49. First (Fig. 5.52), the path corresponding to input (3,1) can be isolated by tuning the combiners C5, C11 and C14. The RF phase response of this path is set to 0 degrees and used as a convenient reference for tuning the relative phases of the remaining inputs.

The other paths are then isolated and tuned one at a time. First ring number 5 in the path corresponding to input (3,2) is tuned to give the phase shift $\Delta\phi_{1\text{GHz}}$, calculated with Eq. (5.27), compared to the reference path of input (3,1). Then, with the same procedure, rings 13 and 14 are tuned to set the phase shift to be $2\Delta\phi_{1\text{GHz}}$
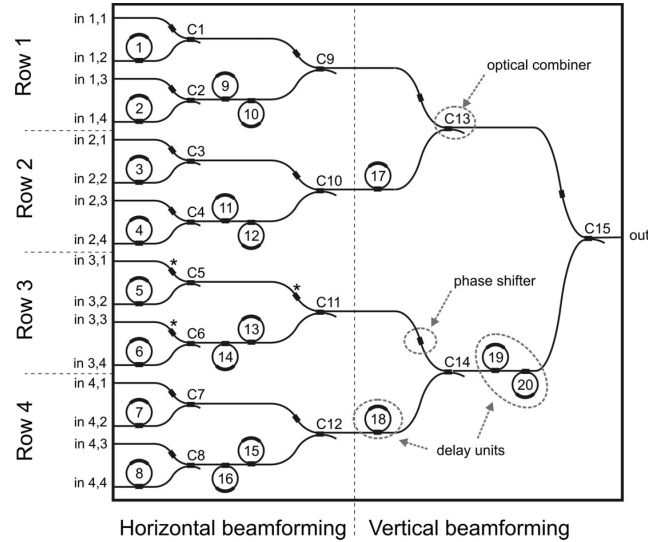
Figure 5.52: 16×1 OBFN schematic. Numbering of inputs, optical combiners and ORRs is indicated. (From [160])

desired for path (3,3). Similarly, ring 6 is then tuned to add enough delay to achieve in path (3,4) a phase shift of $3\Delta\phi_{1\text{GHz}}$.

The method described here allows the beamformer to be programmed to generate a main array beam at an arbitrary pointing angle.

The possibility to achieve good isolation among the different channels is important to guarantee high accuracy for the operation of delay tuning. The isolation provided with the MZI combiners was tested prior to integration to be in the order of 30 dB, thus adequate for an accurate calibration of the individual channels. A very high repeatability and stability of the combiner settings was also demonstrated and reported in our previous work [147]. This allowed the combiner settings to be determined prior to integration and then recalled in the calibration phase of the integrated system. (Any slight residual deviation from the desired isolation could be compensated for by an additional and highly accurate isolation procedure. This procedure consisted in observing any residual optical interference between the isolated channel and the remaining ones, and in fine-tuning the coupling ratio of the combiners to remove this residual interference, thus providing the best possible isolation among the channels.)

5.9.2 Amplitude settings

After the delays have been set as desired with the procedure described above, the second step is the equalization of the amplitude. The individual input-output paths are again isolated and the magnitude of the s_{21} is compared for the different inputs.

Due to the binary tree architecture of the OBFN, adjacent pairs of channels can be equalized by setting a single combiner. That is, the pairs of inputs (3,1)-(3,2) and (3,3)-(3,4) can be equalized in power by using the couplers C5 and C6 in Fig. 5.52, respectively. Once those pairs have been individually equalized, the coupler C11 can be used to set the same value for the magnitude of the optical link gain (s_{21}) in the four channels. In this way it is possible to obtain a uniform amplitude excitation.

5.9.3   Calibration accuracy, stability and repeatibility

In this demonstration, the beamformer channels have been manually tuned in amplitude and phase for each beam setting. With the described procedure, the amplitude and phase match achieved among the four channels is within 0.5-1 dB in amplitude and below 5 degrees in phase difference (at 1 GHz). For the off-broadside beams, the same high degree of accuracy in the calibration was obtained between the measured and the desired phase differences among the channels, calculated using Eq. (5.27).

The calibration settings obtained with the described manual tuning approach are stable, and can be saved and recalled at any time. Multiple tests of the same beam setting were repeated at several days of distance from each other and showed very consistent results, giving a further proof of the repeatability of the settings and of the reliability of the thermal stabilization mechanism employed.

In the real application scenario, a software program for automatic calibration has been implemented on a microprocessor-based platform and is currently being tested. Through an initial, one-time calibration procedure, this software also allows to include corrections for amplitude and phase deviations of the measured OBFN components and for the measured electrical and thermal crosstalk that might occur in the OBFN chip, due to unavoidable inaccuracies in the chip realization. This approach will allow even higher accuracy in the calibration procedure and will remove the need for the cumbersome manual calibration process.

5.9.4   Optical phase synchronization

An aspect which had to be properly considered while performing the measurement was to guarantee the so-called constructive optical interference condition. The presented optical beamformer is a coherent system, meaning that the optical signals have to be combined in phase. Failure to maintain this condition will lead to a loss of the optical signal and, thus, of the RF signal. For this reason, the beamformer includes tunable optical phase shifters before each combining point (see Fig. 5.52) to adjust the optical phase in each branch in order to achieve constructive interference. Keeping a constructive interference condition at all times can become an issue when using the OBFN in setups where optical fibers are used between the splitting and the combining points, since any mechanical stress and temperature variations on the fibers can create fluctuations of the optical phase, thus an instability problem, as previously discussed in Chapter 4.

By careful design of the mechanical support and of an enclosure for the fibers, the system is made to work. The following countermeasures have been taken: (1) all the fibers in the setup were fixed using reels and panel mounted connectors with the scope to minimize mechanical vibrations (see Fig. 5.51); (2) the demonstrator was placed in an air conditioned anechoic room (Fig. 5.53) at stable temperature; (3) the whole fiber setup was enclosed in a Plexiglas structure, visible in Fig. 5.53 (b) and (c), which allowed sufficient thermal insulation and avoided fiber vibrations that might have been caused by the airflow present inside the anechoic room due to the air conditioning system. This solution allowed to keep the system setup stable for the whole duration of the antenna pattern measurement.

Currently a novel system is being developed aiming at the integration of the modulators with the OBFN. In this solution, all the signal paths will be integrated on-chip, hence solving the problem of phase instability created by the presence of optical fibers.
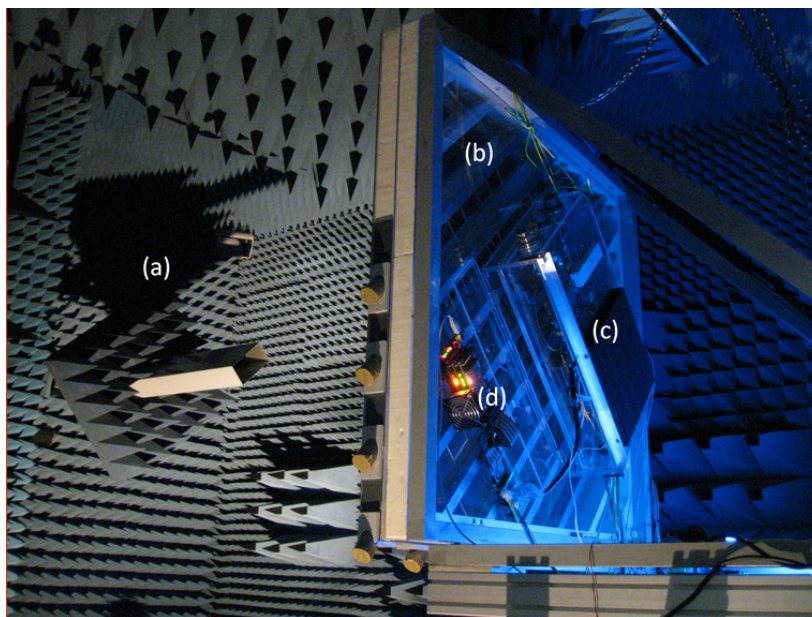
Figure 5.53: Integrated system mounted in the antenna test range. Left, near-field 2-axes scanning probe (a). Right, vertically-mounted integrated antenna demonstrator (b, c, d). Different parts of the integrated system are visible. Back side of the antenna tile with integrated RF photonic devices (b). The OBFN chip is inserted in the transparent box visible on the back side of the integrated demonstrator (c). OBFN control electronics (d). (Picture from [160])

5.10   Antenna pattern measurements

Antenna pattern measurements are used to validate the performance of the OBFN. This approach takes into account the setup non idealities, in contrast to other works that used simulated radiation patterns based on measured scattering parameters [56,168,181]. The latter approach does not take into account several non idealities, such as the effects of frequency dependence of the beam shape which do not directly depend on the beamformer (e.g. the mutual coupling between the elements, the change in the active reflection coefficient of the antenna with frequency and the element beamwidth variations), as described in [4].

The integrated array system (OBFN + antenna) was mounted inside the anechoic chamber on a support which could be rotated on the horizontal plane and whose distance from the scanning plane of the near field probe could be adjusted, in order to measure the radiation patterns (Fig. 5.53, right). The distance between the probe and the antenna under test has been optimized in order to obtain an accurate measurement of the radiation pattern. The near field probe is driven by a computer controlled 2-axes positioner for automatic near field scanning (Fig. 5.53, left). Several test scans have been conducted in order to find the optimal parameters in terms of scanning range and accuracy, i.e. number of measurement points per scanning direction.

The measurement results are depicted in Fig. 5.54. Our aim was to test the RF photonic system over the whole band for which it was designed, that is, 400 to 1500 MHz. However, due to limitation in the measurement setup, it was not possible to measure patterns below 1 GHz which corresponds to the lowest cutoff frequency of the waveguide probes available. For this reason, 4 frequency points between 1 GHz and 1.5 GHz were measured.

5.11   Discussion

The measurements have been performed at the frequencies of 1000 MHz, 1150 MHz, 1300 MHz and 1500 MHz, for three different beam pointing directions (0, -11.5, -23.5 degrees) chosen to illustrate the squint-free operation.

The measured radiation patterns are displayed in Fig. 5.54, normalized to the maximum value. They show a very good agreement with the simulation results (shown by the solid lines) obtained by considering the effect of ideal delays, as in Eq. (2.47). In particular, it is important to note how the position of the main lobe of radiation (indicated by the arrows) does not change across the band, for the three different beam pointing directions, thus demonstrating the desired squint-free, or wideband, beamsteering. In the following subsections a complete analysis of the beam patterns is described, taking also into account the influence of parasitic, to demonstrate the squint-free beamsteering.
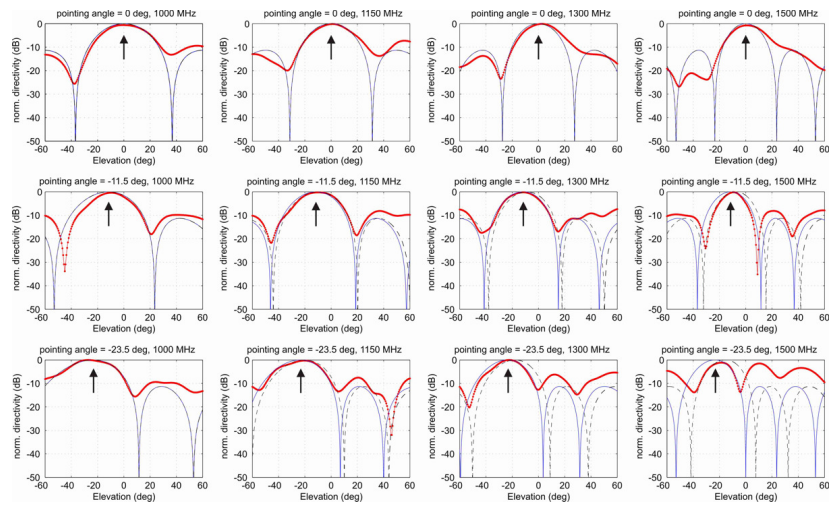
Figure 5.54: Measured (thick lines) vs simulated (thin solid lines) radiation patterns (E-plane) for three different pointing angles of the main beam: 0 degrees (top), -11.5 degrees (centre) and -23.5 degrees (bottom). The measurements are also compared with the patterns that would be obtained in case phase shifters are used (dashed lines). Measurements at four frequencies (left to right: 1000 MHz, 1150 MHz, 1300 MHz, 1500 MHz) show the absence of beam squinting for the main lobe (indicated by the arrows) over the whole frequency range. Note the shift to the right of the leftmost null of radiation and the irregular shape assumed by the main lobe, in several of the measured patterns, as a consequence of parasitic in the measurement setup. (From [160])

5.11.1   Parasitic effects in beam pattern measurements

For the broadside beam (0 degrees pointing angle) the sidelobe levels are particularly low, and another interesting phenomenon can be observed. Instead of the expected perfect symmetry around the 0 degrees elevation angle, the sidelobes show lower values for negative pointing angles, when compared to theory, and slightly higher values towards the positive angles, with a corresponding null filling effect that becomes more visible moving towards higher frequencies.

The accuracy of the amplitude and phase matching, resulting from the accurate calibration phase described in Section 6.4, led us to exclude phase errors as the main cause of the non ideality of the measured radiation patterns. Instead, this asymmetric offset phenomenon is attributed to the parasitic coupling effects, which could not be completely avoided, between the scanning probe and the metal ground plane on which the Vivaldi antenna elements are mounted for structural reasons. The fact that the subarray under test is not in the exact center of the metal plane (as visible in Fig. 5.49), creates the observed asymmetry with respect to the elevation angle. At higher frequencies and steering angles, where the system becomes more sensitive to the described non idealities and asymmetries of the setup, the parasitic coupling creates higher sidelobe levels and a shift of the leftmost null of radiation which also affects the shape of the main lobe.

An additional source of pattern degradation is likely to have originated from the mutual coupling between the active array and the unused antenna elements of the tile. The latter were connected to their corresponding low noise amplifiers, which were kept biased in the ON state in order to provide the desired terminating impedance to the antenna elements and thus minimize reflections. Nonetheless, not all the antenna elements of the array could be put in place during the measurements. This was due to the structural modifications that had to be performed in order to accommodate the photonic components on the antenna PCBs. The absence of several antenna elements is likely to have had a detrimental effects on the beam pattern and to have been an additional factor to their mentioned asymmetry and null filling effect.

5.11.2   Beam analysis

The discussion described so far clearly shows that the measurements are heavily affected by serious parasitic phenomena, that unfortunately could not be removed because intrinsic to the measurement setup. The presence of those non-idealities must be carefully considered when analyzing the measured array beam patterns. Given those conditions, to objectively evaluate the performance of the proposed beamformer it is important to isolate as much as possible the effect of those parasitic effects from the analysis of the generated beams. For this scope, we can observe that the non ideal effects on the beam patterns (namely, a shift of the leftmost null of radiation, accompanied by an irregular, asymmetrical shape of the main lobe) are particularly visible for elevation angles around and below -20 degrees, in most of the graphs. This leads us to consider this range as the least reliable to judge the behavior of the array. As a consequence, we need to observe the graphs in the

range that shows the patterns being less affected by parasitic, thus providing the best possible degree of trustworthiness. For this scope, Fig. 5.55 shows a magnified view of the non broadside beams at -23.5 degrees over the elevation range between -20 and +60 degrees. In this way we can evidence the pattern shape in the elevation range which was less affected by the setup non-idealities, that is, at the right of the main lobe. In this region, the parasitic do not disrupt the shape of the main lobe, and the sidelobes are higher but in the expected position. From these plots is immediately evident how the measured response (solid thick line + dots) (which at those angles is less influenced by the effect of parasitic) shows a good match with the ideal response (solid line), both in terms of position and shape of the main lobe, position of sidelobes and nulls of radiation, and evidences instead a large and clear difference when compared with the squinted response that would be obtained using phase shifters only (dashed line). This gives a proof of the benefit of using time-delay steering even with a steering angle limited to -23.5 degrees from broadside.
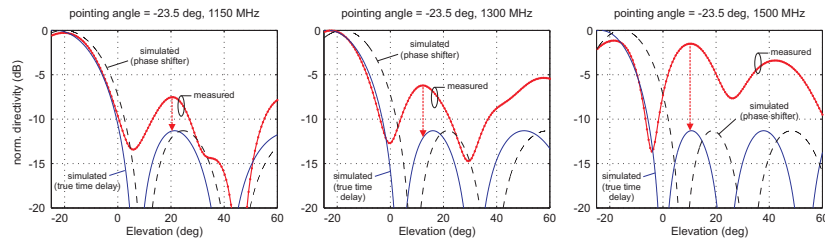
Figure 5.55: Beam analysis: the measured beam patterns (thick solid lines + dots) are observed and compared with simulations in the elevation range less affected by parasitic effects (-20 to +60 degrees). The comparison shows that the shape of the main lobe and the position of the sidelobes of the measured patterns coincide with the ideal true-time-delay patterns (thin solid lines), and do not show the squint effect suffered by phase shifter based beamforming (dashed lines). This result shows the absence of beam squinting and the utility of true-time-delay beamforming. (From [160])

In general, a comparison of the pointing direction of the main lobe is the most evident proof of squint-free behaviour. Nonetheless, for the same reasons described above, if the effects of parasitic are not carefully considered, a misleading result might originate from this analysis. In particular, in Fig. 5.54 we can observe that the main lobe is affected by asymmetry in shape, showing a clear "bump-like" deviation from its regular quasi-parabolic shape. At -23.5 degrees, this effect moves the maximum to the left (at 1000 MHz) or to the right (at 1150 and 1300 MHz) compared to the position of the maximum that would be expected observing the overall shape of the main lobe. At 1500 MHz the shift of the leftmost null, due to parasitic, completely changes the shape of the lobe. For this reason, the asymmetrical shape of the main lobe would lead to misleading conclusions when the main lobes
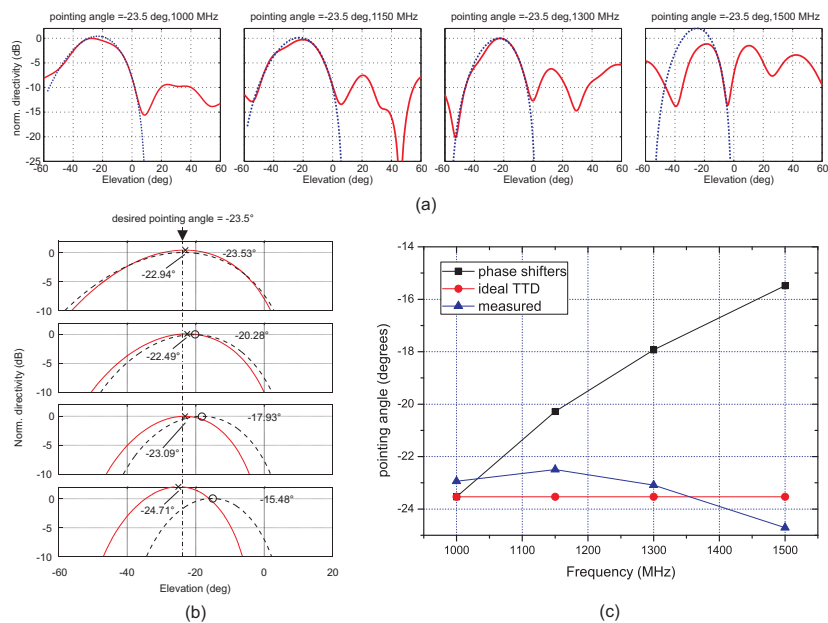
Figure 5.56: Beam analysis: (a) the asymmetry in the main lobe of radiation caused by parasitic (solid line) can be compensated by interpolation (dotted line). (b) The interpolated beams (solid lines) are overlaid on the same angular scale to evaluate the pointing direction at different frequencies, and for comparison with the beams that would be obtained using phase shifters (dashed lines). (c) The pointing direction versus frequency show a very limited amount of squint when compared to the one that would be obtained using a beamformer based on phase shifters. (From [160])

maxima would be compared without trying to mitigate the effect of this parasitic. The actual pointing direction of the pattern generated by the array can more accurately be estimated by analyzing the overall shape of the lobe, instead of its absolute maximum that has been shown to be affected by the setup non idealities (misleadingly moved to the left or to the right). Thus, in Fig. 5.56 (a) we estimate the actual main lobe pointing direction by interpolation of the measured point of the complete main lobe (at 1500 MHz, the interpolation is based on the right part of the main lobe, the left part being strongly affected by the shift of the leftmost null of radiation mentioned before.) At this point, in Fig. 5.56 (b) we can overlay the beams on the same angular scale to evaluate the pointing direction at different frequencies. In Fig. 5.56 (c) the actual pointing direction are compared with the ones that would be generated by using phase shifters, showing the squint reduction and thus the utility of the true time delay beamformer.

From Fig. 5.56, it is immediately visible how the percentage variation of the achieved beam pointing direction is much lower than the one for the squinted beams, giving a further proof of the advantage of time delay beamsteering compared to the use of a phase shifter based beamformer.

These observations demonstrate that the asymmetric behavior is only due to setup non idealities and that the beamformer is capable of squint-free beamsteering. This is shown over an instantaneous bandwidth of 500 MHz, for a beamsteering of 23.5 degrees, corresponding to approximately 495 ps delay difference among the opposite elements of the array, or 14.94 cm distance in air. The bandwidth is only limited by the measurement setup, and is expected to be over 100% (400-1500 MHz by design) if this limitation were removed.

5.12 Conclusion

In this work we have reported the system integration and demonstration of a photonically controlled antenna system where the integrated beamformer chip is based on optical ring resonator delay units.

The measured radiation patterns show that the beamformer chip is capable of wideband operation. The instantaneous bandwidth is at least 500 MHz and is limited only by the measurement setup.

Future implementations aim to develop a novel fully integrated RF photonic system, eliminating the need for fiber-based components and optical amplification. This will provide prominent benefits in terms of optical phase stability, compactness and cost.

6

Separate Carrier Tuning Technique

In this chapter[1] we report an integrated photonic signal processor consisting of a reconfigurable optical delay line (ODL) with a separate carrier tuning (SCT) unit and an optical sideband filter on a single CMOS compatible photonic chip. The processing functionalities are carried out with optical ring resonators as building blocks. We show that the integrated approach together with the use of SCT technique allows the implementation of a wideband, fully-tunable ODL with reduced complexity. To highlight the functionalities of the processor, we demonstrate a reconfigurable microwave photonic filter where the ODL has been configured in a bandwidth over 1 GHz.

6.1   Introduction

In Chapter 3 we have discussed how, in recent years, the use of photonic technology for control of phased array antennas has been proposed as an attractive solution in the cases where high performance in terms of bandwidth, multibeam capability or fast reconfigurable operation are needed [31, 53]. Various approaches have been proposed to implement reconfigurable true time delay (TTD) lines employing photonic crystals [183], semiconductor waveguides [184–186] or exploiting nonlinear effects in optical fibers, such as the stimulated Brillouin scattering (SBS) [187–189]. Several authors have proposed and demonstrated the advantages that can be obtained by employing integrated variable optical delay lines (ODL) based on cascaded optical ring resonators (ORR) [99, 144, 190, 191]. The main advantages of this approach are the large instantaneous bandwidth, continuous delay tunability, compactness and CMOS compatibility of the technology given by the integrated photonic approach [192–195]. In some cases, all this can be achieved with low loss (as low as $0.1 \, \text{dB/cm}$ with a waveguide bending radius of $70 \, \mu\text{m}$, as reported in [24]), which is a particularly important aspect in the common practical situation where the optical beam former (OBFN) is placed in the front-end of low noise receiver systems, e.g. in the case of application of phased arrays to satellite signal reception or radio astronomy.

Many solutions, however, suffer a tradeoff between maximum achievable delay, operating frequency and bandwidth. For MWP signal processing schemes like filtering or beamforming it is advantageous to employ a single sideband with carrier (OSSB+C) modulation scheme to limit the delay bandwidth [188, 194, 196] without resorting to coherent detection scheme where the optical carrier is completely removed. For an OSSB+C modulation scheme what is needed in order to have the correct group delay for the demodulated signal is to make sure that the phase response is (*i*) linear across the sideband, with slope equal in magnitude to the desired group delay and (*ii*) such that the optical carrier experiences the same phase shift that it would experience when the phase response were linear over the whole frequency range. Now, possibly for simplicity, imposing a linear phase response over the *whole* frequency range is what is most commonly done in literature for tunable optical delay lines. Thus, in this scheme, one would need to employ a delay line that imposes a linear phase response over the *whole* frequency range comprised between the optical carrier and the highest frequency component of the RF sideband (shown as the solid line in Fig. 6.1(a)). In this case the delay bandwidth, defined as the frequency range where the linear phase response of the ODL is obtained, *depends strongly on the absolute frequency of the RF signal (ω_{RF} in the figure)*.

The *separate carrier tuning* (SCT) *technique* [13–14, 19–20] can be used to relax this stringent requirement on the ODL. In this scheme, basically, the ODL would impose a linear phase response over the RF sideband only (see Fig. 6.1(b)). As for the optical carrier, a separate component is used to apply the correct phase shift as it would experience when an ideal delay unit with a linear phase slope over the whole frequency range is employed (Fig. 6.3). With this scheme, the delay band-

width of the ODL is independent of the absolute RF frequency. In this research work we have proposed and experimentally demonstrated a scheme where the ODL, the SCT and the optical sideband filter (OSBF) necessary to create the OSSB+C spectrum are integrated in a single CMOS compatible photonic chip. This approach brings advantages in terms of compactness together with wideband performance and full tunability. The functionality in terms of full-2π carrier phase shift and continuously tunable delay is demonstrated by implementing a reconfigurable 2-tap complex-coefficients microwave photonic notch filter.
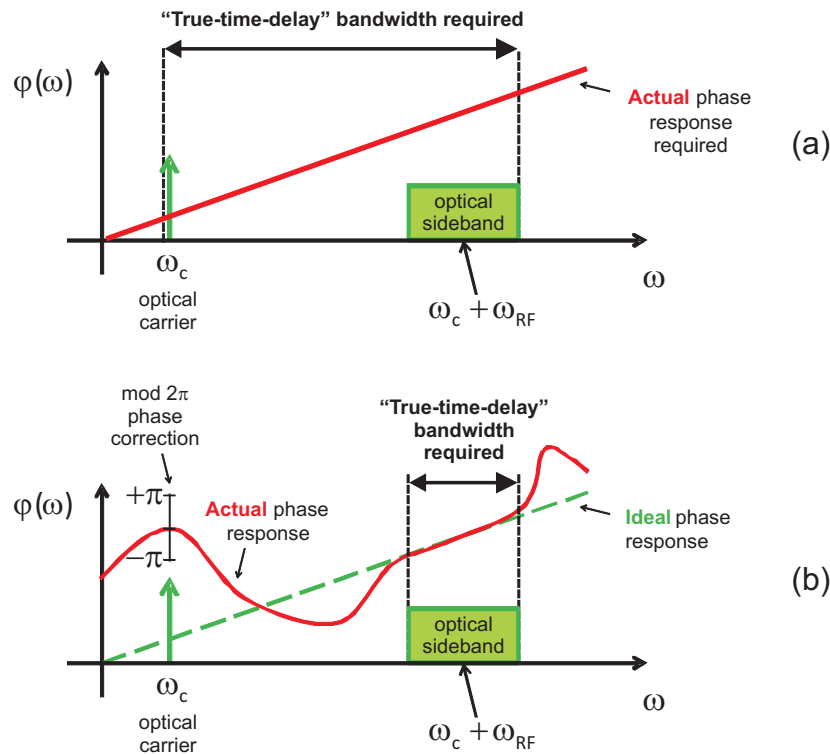
Figure 6.1: Comparison of the *required* delay bandwidths for (a) OSSB+C (b) OSSB+C *with separate carrier tuning* (SCT)

In Chapters 4 and 5 we have proposed and demonstrated a beamformer based on ORRs delay units. The system is based on an optical single sideband suppressed carrier (OSSB-SC) modulation scheme, which allows to reduce the required delay bandwidth to the one of a single sideband, with advantages in terms of reduced complexity for the delay units. This technique implements a *coherent* beamformer approach; it requires a single laser source, where a portion of the light is tapped off and used for carrier re-insertion before direct detection can be realized.

Nonetheless, as already mentioned, there are a variety of cases in which it is

desired to avoid carrier re-insertion. For example, there are a number of cases where an *incoherent* beamforming approach could be of interest, for example for the possibility of employing multiple laser sources instead of a single one, direct modulation instead of external modulation, or to use separate carrier wavelengths to implement a wavelength division multiplexing (WDM) based beamformer as proposed for example in [9] (Fig. 6.2). In those non-coherent optical systems, the OSSB-SC operation with single carrier re-insertion described in [7], used to simplify the complexity of the delay units, can no longer be used, due to the fact that the separate signals do not share the same coherent carrier any longer.

Again, the separate carrier tuning (SCT) technique proposed in several recent works [188, 196] appears again as an ideal solution for the delay elements to be employed in all the cases where a non-coherent OBFN is used, in order to keep the advantage, in terms of ODL complexity reduction given by the SSB modulation, and still allowing the use of a simple, unbalanced detection scheme.
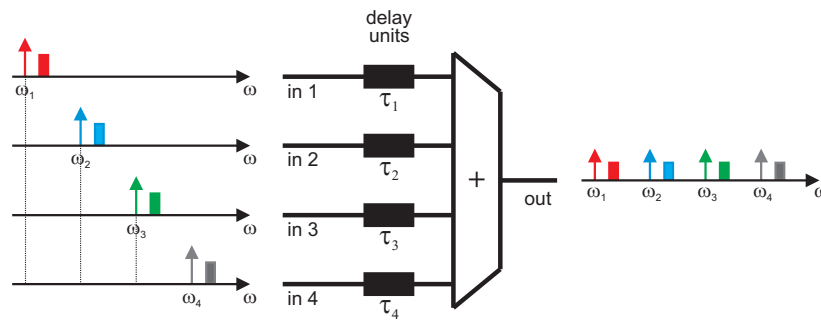
Figure 6.2: Example of a 4-channel, non-coherent OBFN based on wavelength division multiplexing (WDM)

Many efforts are currently being done in order to implement a tunable delay line which is continuously tunable and independent of the operating RF frequency, in a compact integrated format. In this chapter, after a theoretical introduction on the SCT technique (Section 6.2), we describe the implementation of a SCT delay unit (Section 6.3) in which the carrier tuner (CT), the delay element and the optical sideband filter (OSBF), used to generate the optical single sideband full carrier (OSSB+FC) modulation, are integrated on the same optical chip. In Section 6.4 we demonstrate its functionality in terms of generation of SSB modulation, full-2π carrier phase shift and continuously tunable delay. This type of reconfigurable optical delay lines (ODL), together with tunable phase shifters, have primary importance in a number of microwave photonic (MWP) signal processing applications like filtering [1–4], arbitrary waveform generation [195] or control of wideband phased-array antennas [33, 147]. For the scope of this thesis, the proposed delay unit will be employed in a WDM-based incoherent beamformer as proposed in [9] and reported in Chapter 7.

6.2 Theory of separate carrier tuning

Let us consider OSSB+C modulation where only the upper sideband is kept, as in Fig. 6.3.
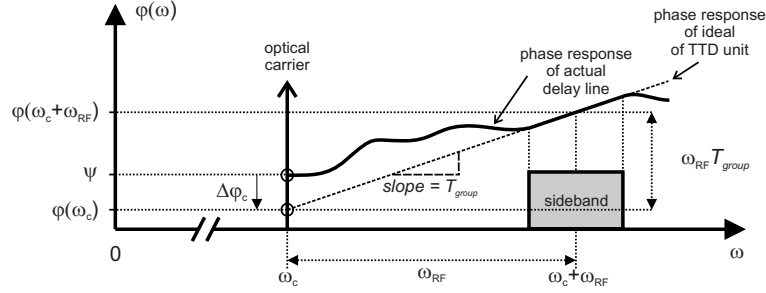
Figure 6.3: Principle of operation of an optical true time delay unit with separate carrier tuning

The group delay T_{group} applied to the signal at frequency $\omega_c + \omega_{\text{RF}}$ is given by the slope of the optical phase characteristic at the same frequency:

$$T_{\text{group}} = \frac{\partial \varphi(\omega)}{\partial \omega}\bigg|_{\omega_c + \omega_{\text{RF}}} \tag{6.1}$$

For TTD operation, the desired carrier phase should be

$$\varphi(\omega_c) = \varphi(\omega_c + \omega_{\text{RF}}) - \omega_{\text{RF}} \frac{\partial \varphi(\omega)}{\partial \omega}\bigg|_{\omega_c + \omega_{\text{RF}}} \tag{6.2}$$

which, as discussed in the introduction of this chapter, is generally achieved by imposing that the RF phase response should be a linear function of frequency over the whole frequency range [196], with the slope T_{group}. If a dispersive device is used to add a constant phase slope to the sideband, as in (6.1), the carrier phase will assume a certain value ψ, which can deviate from the desired phase $\varphi(\omega_c)$, as illustrated in Fig. 6.3. Based on the separate carrier tuning approach, to achieve TTD operation, the carrier phase should be adjusted to the value given by (6.2), by adding a phase shift to the carrier equal to

$$\Delta \varphi_c = \varphi(\omega_c) - \psi \tag{6.3}$$

It should be kept in mind that the carrier phase adjustment can be applied modulus of 2π since the carrier is monochromatic. The details on SCT technique applied to delay lines based on SBS in optical fibers can be found in [188].

6.3 Principle of operation and device realization

The schematic of the MWP processor consisting of the OSBF, the reconfigurable ODL and the SCT unit is depicted in Fig. 6.4. The OSBF is an asymmetric Mach-

Zehnder interferometer loaded with an optical ring resonator in one of its arms
(i.e. MZI + ring type) (Fig. 6.4(a)).
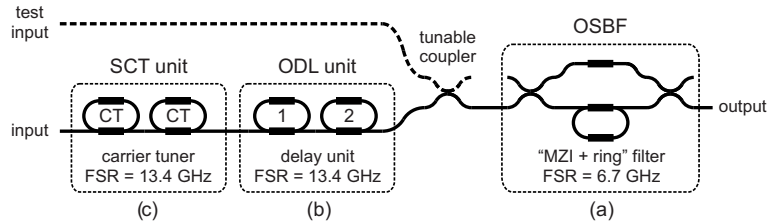
Figure 6.4: Schematic of the delay structure employed to demonstrate the single-
chip SCT-based optical delay line: (a) optical sideband filter (OSBF); (b)
optical delay line (ODL) unit; (c) separate carrier tuning (SCT) unit

The OSBF is used to remove one of the RF sidebands (in this case the lower side-
band) of a double sideband with carrier (DSB+C) modulation signal generated from
an intensity modulation of the optical carrier. For a modulation signal between 1.2
and 2.2 GHz, the achievable lower side band (LSB) suppression is 22 dB. The DSB+C
spectrum and the magnitude response of the OSBF is depicted in Fig. 6.5(a). The
detail of the OSBF design has been reported elsewhere [33].

The reconfigurable ODL consists a pair of cascaded all-pass ORRs [99] as shown
in Fig. 6.4(b). These ORRs can be tuned in such a way to approximate a linear phase
response over the sideband, with the specific slope (6.1) that gives the desired group
delay T_{group}. The desired phase response is shown in Fig. 6.5(b).

The SCT unit is implemented using a pair of cascaded ORRs, exploiting the re-
gion of phase transition of the resonator [196, 197]. This is characterized by a 2π
optical phase transition centered at the resonant wavelength. The separate tuning
is thus obtained by tuning the phase transition of an ORR and then simply adjust-
ing the position of its resonant frequency with respect to the carrier wavelength (see
Fig. 6.5(c)). This approach was demonstrated in [197] where an RF phase shift up
to $336°$ was obtained employing a tunable silicon-on-insulator (SOI) microring res-
onator (MRR). Nonetheless, this solution may require a detuning of the resonance
of the MRR in the order of several GHz. Here we use two optical ring resonators, as
shown in Fig. 6.4(c), in order to achieve a sharper transition in the phase transfer
around the resonance frequency, as visible in Fig. 6.5(c). This permits to give a com-
plete $360°$ phase shift to the carrier with moderate detuning of the resonant fre-
quency, thus limiting the phase shift effect only in the vicinity of the desired wave-
length, without sensibly affecting the linear phase transfer desired in the spectral
region occupied by the sideband (Fig. 6.5(c)). In addition to that, using two ORRs
allows to keep a relatively low quality factor for the resonators, thus minimizing
their insertion loss.

The structure in Fig. 6.4 is realized in a low-loss CMOS compatible TriPleX™ wa-
veguide technology [198]. The realized ORRs have a free spectral range of 13.4 GHz
and the OSBF has an FSR of 6.7 GHz. The ORRs and the OSBF are fully tunable
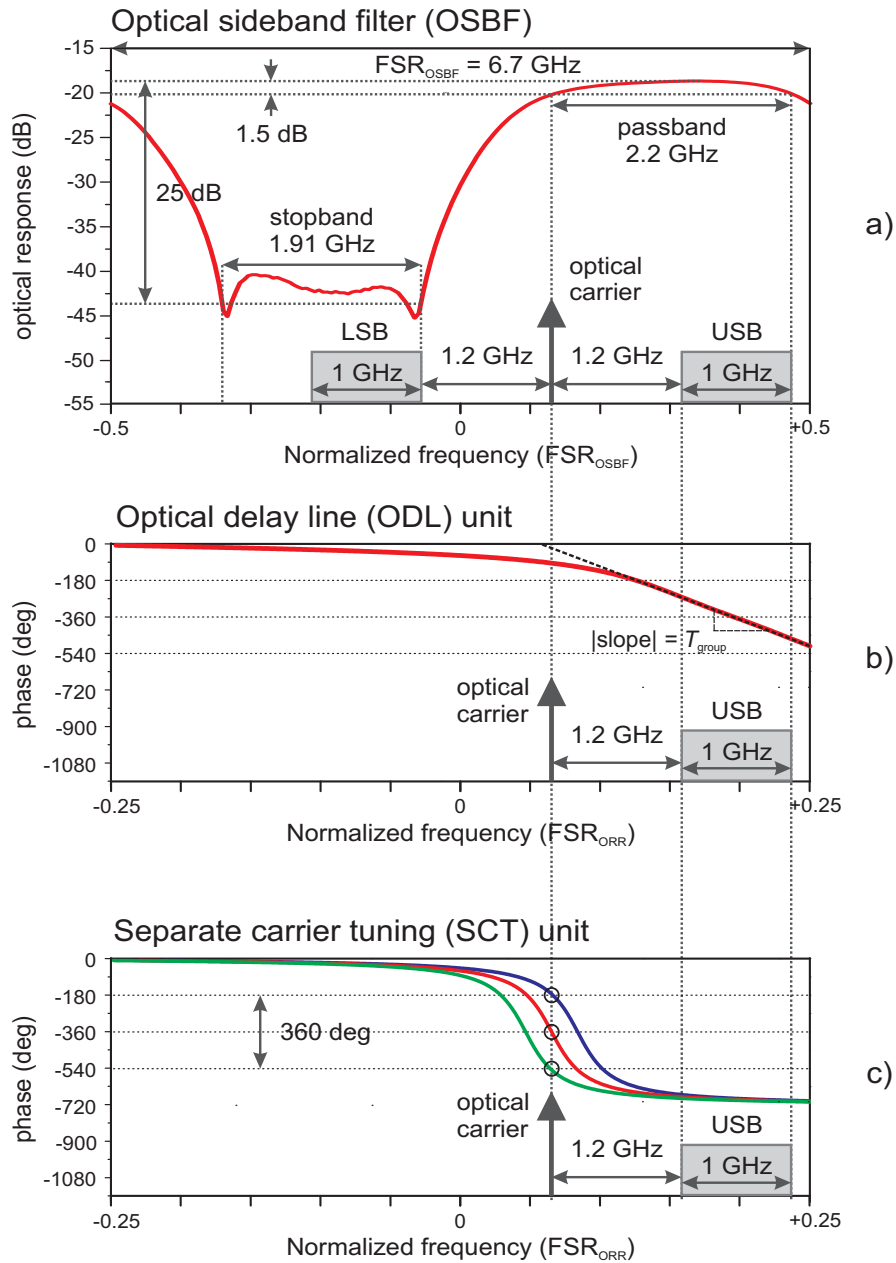
Figure 6.5: Measured frequency response of subsection (a) and simulated responses of subsections (b) and (c) of the optical delay line in Fig. 6.4, over half the FSR of the ORR (6.7 GHz)

using thermo-optical tuning with chromium heaters that have been deposited on the optical chip. Using these heaters, the ORRs can be fully tuned in terms of their resonance frequencies and their Q-factors as will be explained in the next section.

6.4   Experiment

The measurement setup in Fig. 6.6 is used to analyze the performance of the OSBF, the ODL and the SCT sections. We use a DFB laser with an optical power of 100 mW (EM4 Inc.), a Mach-Zehnder modulator (MZM, Avanex FA20), an erbium-doped fiber amplifier (EDFA) and a 10 GHz photodetector (PD, Discovery Semiconductor DSC 710). A vector network analyzer (VNA, Agilent N5230) is used for the amplitude and phase transfer measurements; the optical responses can be displayed on the VNA by using the phase shift method [165], which is a similar method to the one implemented in a lightwave component analyzer [183].
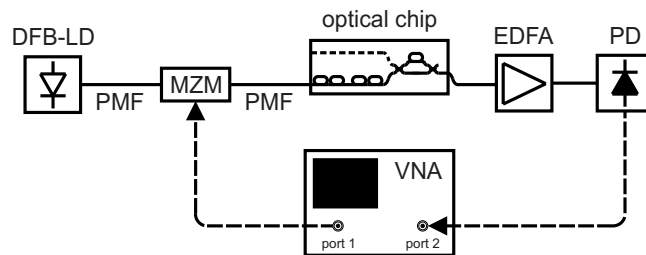
Figure 6.6: Schematic of the measurement setup. Polarization maintaining optical fibers (PMF) are used for the interconnection of laser, modulator and optical chip.

Fig. 6.5(a) shows the measured magnitude response of the OSBF, in comparison with a schematic representation of the DSB+C signal spectrum to be processed. Assuming an optical suppression of at least 22 dB for the undesired sideband, the usable bandwidth in which it is possible to achieve OSSB+C modulation for the RF signal is between 1.2 GHz and 2.2 GHz as illustrated in Fig. 6.5(a).

In Fig. 6.7 we show how the integrated delay line can be used to provide different values of group delay to the signal sideband (visible as different slopes of the phase response, Fig. 6.7(a)) and arbitrary phase shifting to the optical carrier (Fig. 6.7(b)).

The amount of time delay (i.e. the slope of the phase response) of the ODL unit can be varied with continuity by means of tuning the resonance frequencies and the coupling factor (hence the Q-factor) of the ORRs in Fig. 6.4(b). By properly cascading the ORRs (i.e. adding their group delay response) in principle a large and wideband true time delay can be achieved. The detail of this principle is reported in [144, 147]. The phase responses obtained with the ODL are displayed in Fig. 6.7(a), and show good agreement with their theoretical responses. In the measurements, the electrical delay function of the VNA has been employed to compensate for the additional group delay given by the transmission path external to the tunable ODL
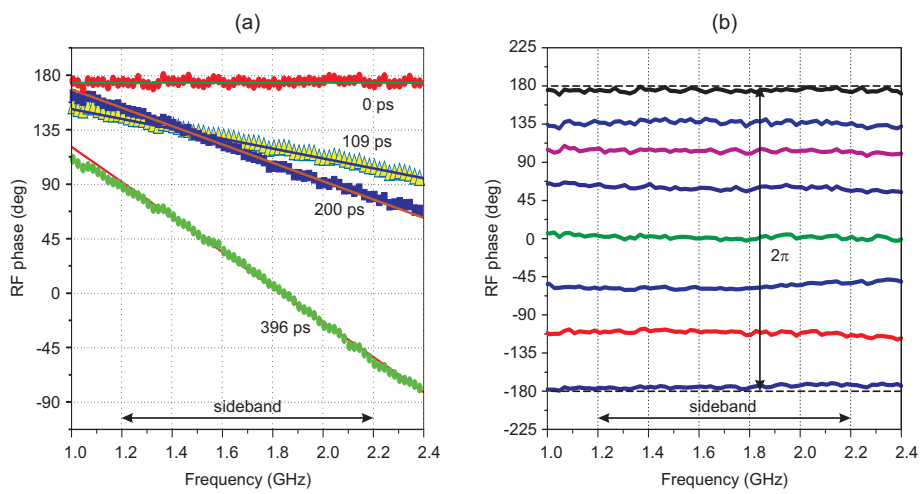
Figure 6.7: (a) Measured (symbols) and theoretical (solid lines) phase responses over the signal sideband. Different slopes (corresponding to different delays) can be set using the ODL unit. (b) Phase shift of the RF phase responses. A phase shift over 2π is achieved by changing the phase of the optical carrier employing the SCT unit. The constant slope for all traces shows that the amount of delay is not influenced by the carrier tuning.

(e.g. coax. cables, fibers, EDFA), in such a way that the slope of the phase response in Fig. 6.7(a) would represent the delay provided by the integrated ODL only.

In order to demonstrate the effectiveness of the SCT unit, in Fig. 6.7(b) we show measured RF phase characteristics on the detected sideband when a variable phase shift (PS) between 0 and 2π is imposed to the optical carrier via the ORRs of the CT unit in Fig. 6.4(c). In a OSSB+C modulation scheme, the phase shift imparted on the optical carrier generates an equal phase shift on the detected electrical signal, constant with respect to RF frequency [199]. This effect is visible in Fig. 6.7(b), where the constant phase shift over the detected sideband shows that the carrier phase is effectively being shifted over the whole 2π range, and the fact that the slope does not change confirms that the carrier phase can be tuned without affecting the linear phase response at the delay band as suggested in Fig. 6.5.

6.5   Microwave photonic filter demonstration

To demonstrate the functionality of the delay line when employed in a specific application, we built a 2-tap reconfigurable microwave photonic filter (MPF) with complex coefficients. For 2-taps, the general expression of the transfer function [4, 13, 25–27] reduces to

$$H(\omega) = a_0 + a_1 e^{-j\omega T} \tag{6.4}$$

where ω is the microwave frequency, $a_0 = |a_0|e^{-j0}$, $a_1 = |a_1|e^{-j\varphi}$ are the complex tap coefficients, T is the basic delay [194] of the MPF and φ the phase difference between the taps. In this demonstration we use the ODL unit to change the MPF basic delay and the SCT unit to adjust the φ, thereby fully reconfiguring the MPF response.
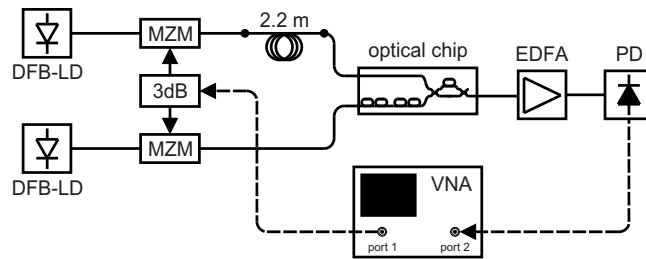
Figure 6.8: Schematic of the 2-tap microwave photonic filter

The schematic of the incoherent MPF is shown in Fig. 6.8. The optical frequencies were generated using two DFB laser diodes (DFB-LDs). The laser wavelengths have been set to have an offset over 1 nm (corresponding to approximately 125 GHz of frequency difference between the DFB-LDs) to prevent that a possible beating frequency might fall in the passband of the photodetector and create signal distortions. The two taps have a length imbalance of 2.2 m, which gives a delay differ-
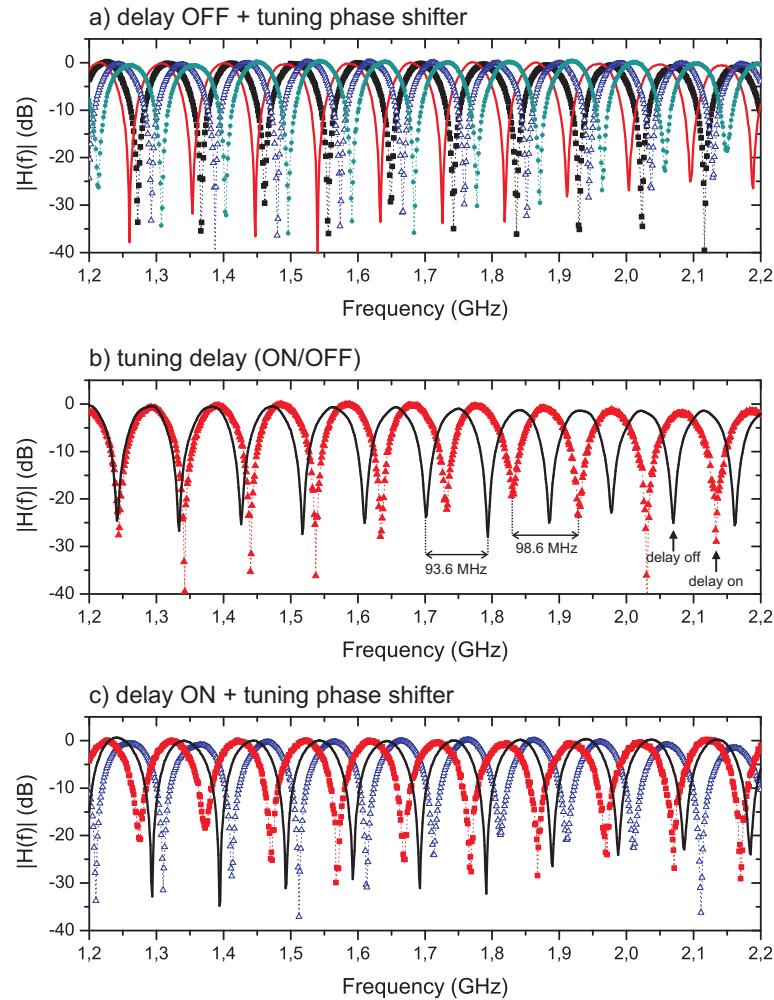
Figure 6.9: Measured magnitude responses of the MPF. A continuous 100% fractional tuning can be achieved by the SCT unit, without changing the FSR (a). The FSR can be changed from 93.6 MHz to 98.6 MHz by setting the tunable delay to 540 ps (b). The fact that the FSR of the MPF does not vary when shifting the response, shows that operating the carrier tuner does not disrupt the delay response imposed over the sideband by the delay unit (c).

ence of approximately 10.68 ns and free-spectral range of 93.6 MHz. One signal tap propagates through the ODL while the other one enters the chip from the OSBF test input port, thereby bypassing the ODL and the SCT. These taps are combined using a tunable coupler prior to entering the OSBF, as depicted in Fig. 6.4. In this way, if

desired, a single OSBF can be used to suppress the lower sideband for both taps. This is possible by exploiting the periodic response of the integrated OSBF, by simply setting the frequency spacing between the carrier wavelenghts to be a multiple of the FSR of the OSBF. The filter taps amplitudes a_0 and a_1 can be equalized by modifying the coupling ratio of the tunable coupler.

By operating the SCT unit and the ODL, as in Fig. 6.9, the notch positions and the FSR of the MPF can be tuned independently. In particular, Fig. 6.9(a) shows how the MPF notch positions can be shifted by 360 degrees by operating the SCT unit in Fig. 6.4(c). A 100% tunability can be achieved, as expected from the the phase shift capability of the ODL shown in Fig. 6.7(b). The equal shape of the individual responses and their constant FSR demonstrates that the carrier phase tuning does not influence neither the amplitude nor the delay in the passband, as expected from the principle of operation of the SCT unit represented in Fig. 6.5(c).

Fig. 6.9(b) shows the capability the ODL to impose a tunable group delay over the entire sideband. The solid line represents the MPF response when no delay is applied to the tunable tap (0 ps line in Fig. 6.7(a)). This condition is indicated as "delay off". The dotted line shows how the response is modified when a group delay of approximately 540 ps is set in the ODL ("delay on"). The application of this amount of delay reduces the basic delay T of the MPF from 10.68 ns to 10.14 ns, with a corresponding increase the FSR from 93.6 MHz to 98.6 MHz.

In Fig. 6.9(c) different measured MPF responses are depicted, when both the ODL and the SCT units are active simultaneously. As described before, here the ODL has been kept on the "delay on" condition in all traces. It is possible to see that the FSR keeps to the 98.6 MHz value, independently by the absolute position of the MPF notches, which can be set applying a phase shift to the carrier via the SCT section as in Fig. 6.9(a). This latter measurement confirms that the SCT section can be operated without affecting the amount of delay in the ODL section.

6.6 Conclusion

We have experimentally demonstrated a reconfigurable ODL based on the SCT technique where, for the first time, all the required components are integrated on a single photonic chip. The functionality was demonstrated over a bandwidth in excess of 1 GHz by employing the ODL to fully reconfigure the response of a 2-tap complex-valued MPF. The operating bandwidth can be readily extended just by adding more ORRs in the delay section of the ODL and simply increasing the FSR of the OSBF by design.

The ODL proposed here opens a path towards the implementation of a wideband and fully reconfigurable MPF with multiple taps monolithically integrated on a single chip. The number of taps can be increased by multiplying the delay sections and SCT units, while sharing a single OSBF. A schematic of a possible implementation is shown in Fig. 6.10.
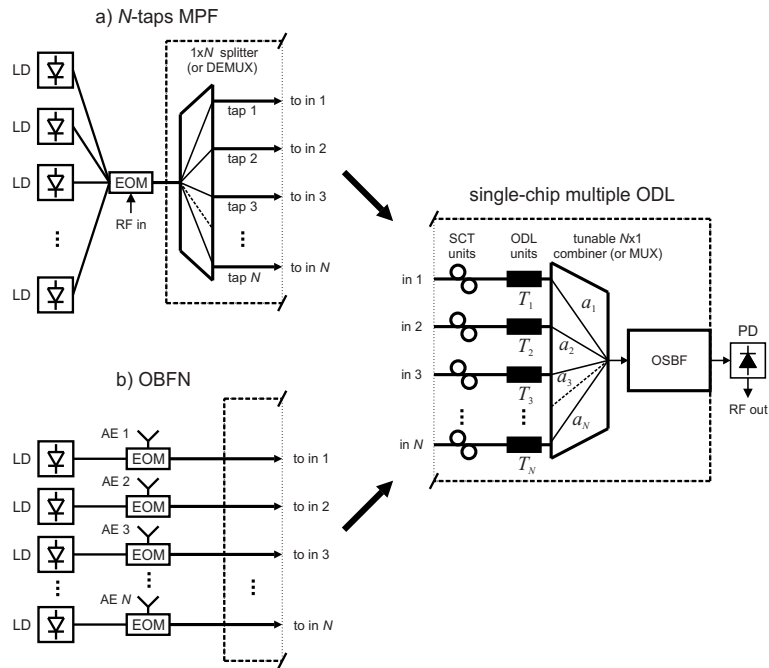
Figure 6.10: Schematic example of a multiple optical delay line (right). This structure could be used, for example, to implement (a) an incoherent multi-tap microwave photonic filter with complex coefficients, or (b) an optical beamforming network (OBFN) for phased array antennas.

Notably, the same multiple ODL structure could also be operated as an integrated optical beamforming network (OBFN) for the control of phased array antenna systems, according to the schematic displayed in Fig. 6.10(b). In this case, the individual delay lines are used to give the desired time difference to the RF signals originating from the individual antenna elements (AE) of the array. This OBFN could use multiple laser sources, each of them acting as a carrier for the RF signal originated from a different antenna element.

7

Multi-Wavelength Beamformers

In the previous chapters, the advantages offered by integrated optical beam forming networks (OBFNs) for phased array applications have been described. ORR-based true-time-delay units can be cascaded in a binary tree topology and tuned for continuously adjustable broadband time delay. Nonetheless, with a large number of antenna elements, the OBFN may become very complex. In this chapter, a novel idea is proposed to exploit the frequency periodicity of the ORRs and the WDM technique to achieve multiple signal paths on a single beamformer, thus reducing complexity and costs. The idea has been translated into a physical design, and the resulting multi-wavelength beamformer has been realized and tested[1] . The use of high index contrast waveguides in Si-compatible technology further reduces chip footprint and allows the use of integrated OBFNs for large arrays and multi-beam applications.

---

[1] *To be submitted as:* M. Burla, L. Zhuang, D. A. I. Marpaung, M. R. H. Khan, A. Leinse, W. Beeker, M. Hoekman, R. G. Heideman, and C. G. H. Roeloffzen, "On-chip hardware-compressive integrated photonic beam forming network based on wavelength division multiplexing", *Optics Letters*.

7.1   OBFN limitations for large arrays

In the previous chapters, it has been shown that phased arrays antennas offer a number of advantages when compared to other single antenna systems, namely, low profile, electronic beamforming (beam shaping and beam steering), multibeaming and interference nulling capability. In practice, we have seen how their performance is limited by the characteristics of the beam forming network (BFN) used. As a solution, we have proposed that a possible improvement to the limitations of all-electronic BFNs can be achieved by integrating electronics and photonics by realizing an OBFN which can provide large bandwidths, RF frequency transparency, true-time-delay (squint-free) characteristic over the band of interest, EMI immunity, compactness and light weight, thus extending the application of smart antennas to domains where size and weight are critical (e.g. aerospace).

In many typical applications of phased-array antennas, like space communications and radioastronomy, the signal powers are typically very low, and also a narrow antenna beam is required. This requires a large receiving surface, that is, large arrays with many elements, since grating lobes may appear for certain scanning angles (in conventional arrays) if the distance between the elements goes beyond half-wavelength, as theoretically demonstrated in Chapter 2. In this case, even using a binary-tree topology, as motivated in Sec. 4.2, the OBFN may become very complex, especially considering the total number of heaters required for chip control. The same problem appears when a system capable of multiple, independent beams is desired (multi-beam OBFN), as will be described in the next chapter.

7.2   Complexity reduction using multiple wavelengths

To overcome the limitations described above, the challenge is to modify the binary-tree topology in such a way to realize an OBFN capable to be scaled to hundreds or thousands of antenna radiators, while keeping a low system complexity and cost. Several ideas have been proposed in literature that make use of multiple wavelengths for the realization of hardware-compressive beamformers (see Chapter 2). For the first time to our knowledge, we propose a solution employing multiple wavelengths aimed at the realization of a beamformer in an integrated manner, as a photonic integrated circuit (PIC).

7.2.1   OBFN based on ORRs and multiple wavelengths

The basic idea is to *create multiple signal paths on a single beamformer channel*. In this way, a single delay line carries the signals originating from different antenna elements, thus significantly reducing the network complexity and, in turn, the number of rings and heaters required.

This concept can be considered as a multiplexing technique, and it can be applied in the very common situation of arrays with separable illumination (Chapter 2). The idea is based on the fact that the proposed optical beamformers are devices operating on a modulated optical signal, and on the exploitation of the

frequency-periodic behaviour of the ORRs used as TTD units. The initial idea has been reported in [200]. A detailed description of this concept is given in the following.

7.2.2 Operating principle

Let us consider an M-by-N planar array with separable illumination. This configuration is employed in many practical applications of antenna arrays and, as seen in Chapter 2, in this case the array factor $F(\vartheta, \varphi)$ can be written as the product of the array factors of two linear subarrays, as in Eq. (2.96)[2]

$$F(\vartheta, \varphi) = \sum_{m=0}^{M-1} |A_m| e^{j\alpha_m + jk_0(md_x \sin\vartheta \cos\varphi)} \cdot \sum_{n=0}^{N-1} |B_n| e^{j\alpha_n + jk_0(nd_y \sin\vartheta \sin\varphi)}$$
$$= F_x(\vartheta, \varphi) \cdot F_y(\vartheta, \varphi) \tag{7.1}$$

This means that the array factor can be defined by separately defining the delays between the vertical subarrays (thus providing horizontal beamsteering), and then between the horizontal subarrays (for vertical beamsteering), as described in Sec. 2.4.3. The physical meaning of the separable illumination can more easily be shown by using Fig. 7.1, where $M = N = 4$ has been chosen without loss of generality.
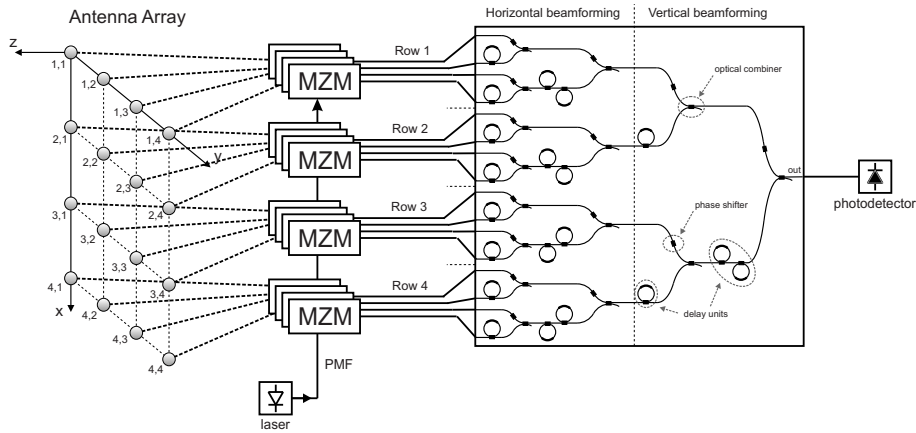
Figure 7.1: 4×4 array with separable illumination and corresponding beamformer (from [160])

Fig. 7.1 shows a rectangular array with elements placed on a 4×4 rectangular lattice laying on the xy plane and indicated as "m, n" in Eq. (7.1) corresponding to the column and row indexes. The elements are connected to an optical beamformer

---

[2]Equation (7.1) is identical to the (2.96) apart from the dimension of the array, which here (to simplify the notation) is chosen as $M \times N$ instead of $(M + 1) \times (N + 1)$.

via a corresponding array of modulators (each indicated as MZM). A common laser and photodetector complete the optical beamforming system, as explained in detail in the previous chapter.

Let us analyze the beamformer architecture. The horizontal beamforming section Fig. 7.1 is used to provide the required delays and amplitude relation among the elements of each row of the array in the y direction. This will provide beamsteering in the horizontal direction, that is, on the yz plane. This section implements the rightmost sum in Eq. (7.1) and corresponds to the $F_y(\vartheta, \varphi)$ term. Note that, in this term, the amplitude and delay coefficients only depend on n, that is, the position on the y axis, and are independent on m, which indicates the position of the antenna elements on the x axis. Nonetheless, note also that the beamformer contains *one* 4×1 binary tree section *for each row* of the array. Those have been emphasized in Fig. 7.2 with different colors. This means that, during operation, each of those sections will have the same delay settings. This redundancy will be removed employing the proposed multi-wavelength solution which will be described in the following.
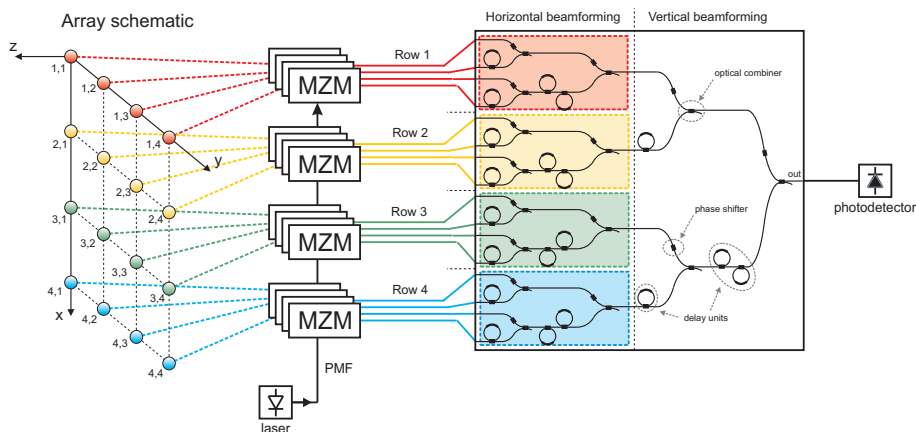
Figure 7.2: 4×4 array with separable illumination and corresponding beamformer. The horizontal beamforming sections corresponding to different rows have been indicated with different colors.

The vertical beamforming section is used to provide the desired delays and amplitude tapering coefficients between the individual rows. Applying delays between the rows corresponds to a beamsteering function in the vertical direction, that is, on the xz plane in Fig. 7.1. This beamformer section is composed by a 4×1 binary tree section, combining the outputs of the horizontal beamforming section. It implements the leftmost sum in Eq. (7.1) and corresponds to the $F_x(\vartheta, \varphi)$ term.

The previous discussion shows that the conceptual *product* between the two sum terms in Eq. (7.1) can be translated into a hardware architecture as the *cascade* of a horizontal and a vertical beamforming section. This concept was used already
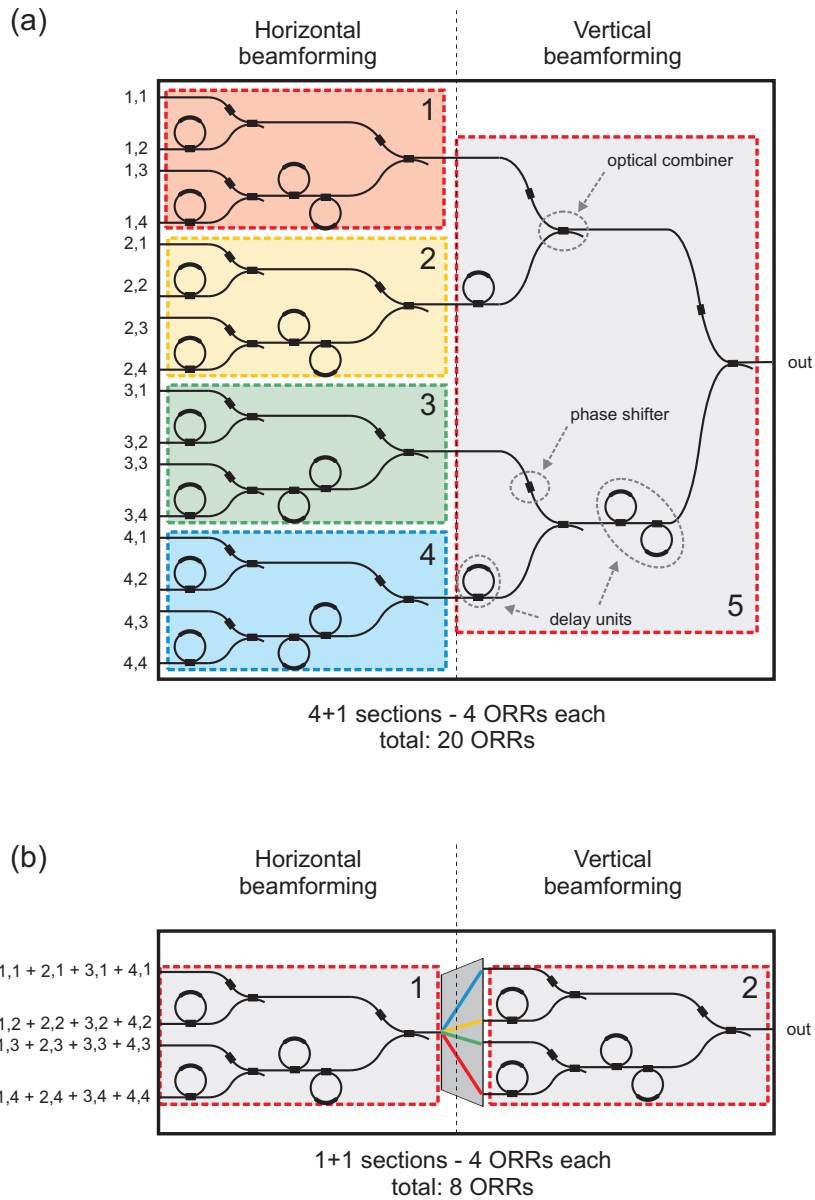
in the single wavelength architecture proposed in Chapter 4. In Fig. 4.4, sections 1 and 2 correspond to the horizontal beamforming section, whose 4 outputs are "beamformed" (combined and delayed) by sections 3 and 4, which together form the vertical beamforming section.

In the previous discussion referred to the architecture of the OBFN in Fig. 7.1 we have seen that there are 4 sub-sections of the OBFN that are supposed to provide the same delay relation between their inputs, that is, the delay among the subarrays in vertical direction. Those OBFN sections have been indicated with colors in Fig. 7.2. In principle, then, those 4 sub-sections could be "folded" into one, in which the signals originating from elements $(1, n)$, $(2, n)$, $(3, n)$ and $(4, n)$, that are, the elements of each column, could be *multiplexed* and undergo the same amount of delay simply using *a single* 4×1 binary tree section. In this way, the architecture of the beamformer can be greatly simplified applying the described WDM technique, as schematically represented in Fig. 7.3 for the case of a 4×4 array. This simplfication in the structure allows to reduce the number of ORRs from 20 to only 8. Considering the number of tuning elements, assuming 2 tuners per ring, 1 per combiner and 1 per phase shifter, the number of heaters required reduces from 70 to only 28, with an equal reduction of power dissipation in case thermal tuning is used. The complexity reduction becomes more and more visible as the dimension of the array increases. A complete complexity analysis is reported in Subsec. 7.2.3.

The use of a WDM approach is made possible by two facts:

- The proposed optical beamformers are devices operating on *modulated optical signals*. The modulation carrier frequency can be selected and used to multiplex multiple signals on the same optical path, using a wavelength-division multiplexing (WDM) approach, thus reusing the same delay elements for multiple RF signals.

- The ORRs used as TTD units offer a *frequency-periodic response*. As seen before, in this respect a ring is characterized by its FSR, that is fixed by the round trip time RTT. In this sense, the ring is frequency "transparent", meaning that it is capable of delaying the signals in each of its resonance frequency bands, which are spaced by the FSR, of the same amount, independently of the RF frequency, that is, the frequency spacing between the optical carrier and the sideband to be delayed. By using a multi-wavelength laser source (or a laser array and a multiplexer) and fast integrated modulators, it is possible to multiplex signals originating from *different* antenna elements on a *single* path, delaying them by the same amount. This technique is an example of application of optical wavelength-division multiplexing (WDM) to an optical beamforming PIC.

As can be seen in the schematic in Fig. 7.3, this technique allows a dramatic reduction in the number of rings required, especially in the case of large number of elements N. As a direct consequence, we achieve a reduction in complexity, in area occupation (the ring dimensions are the limiting factor), in power and heat dissipation (drop in the number of heaters). The only additional hardware required

(a)

Horizontal beamforming

Vertical beamforming

1,1
1,2
1,3
1,4
2,1
2,2
2,3
2,4
3,1
3,2
3,3
3,4
4,1
4,2
4,3
4,4

1

2

3

4

optical combiner

phase shifter

delay units

5

out

4+1 sections - 4 ORRs each
total: 20 ORRs

(b)

Horizontal beamforming

Vertical beamforming

1,1 + 2,1 + 3,1 + 4,1

1,2 + 2,2 + 3,2 + 4,2
1,3 + 2,3 + 3,3 + 4,3

1,4 + 2,4 + 3,4 + 4,4

1

2

out

1+1 sections - 4 ORRs each
total: 8 ORRs

Figure 7.3: Layout comparison between the traditional binary-tree (a) and the multi-wavelength, mutiple signal path OBFN (b), for a 4×4 planar array. Note the dramatic reduction in the number of ORRs, area and heaters required. This reduction will be more and more dramatic by increasing the number of inputs, as described in Sec. 7.2.3.

consists of the multiplexers needed to combine the wavelengths in the single waveguides, in the first stage, and the de-multiplexer used to split them before the second stage. In the following of this chapter, we will discuss the functional design of the combiner in the second stage, that will need to be capable of combining the RF signals carried by the different optical carriers λ_1, λ_2, λ_3, λ_4, and the design of the input multiplexers and of the demultiplexer.

7.2.3 Complexity

In this section we analyze the reduction of the OBFN *complexity* allowed by adopting the proposed WDM approach. In this discussion, we would like to slightly force the precise definition of the term complexity, from the one given in computational complexity theory[3]. In particular, our definition is similar to the one of space complexity, where we replace the "volume of memory used by an algorithm" with the *wafer area* as a function of the size of the array.

By observing the layout of the beamformers proposed in the previous chapters, it can be seen that the largest part of the wafer area is occupied by the ORR delay structures. For this reason, we limit our analysis by considering the number of ORRs as the dominating factor with respect to the beamformer complexity, intended as space occupation on the wafer. For the analysis, we consider the following assumptions:

- The antenna array is planar and square ($N \times N$), with $d_x = d_y = d$.

- N is a power of 2 ($N = 2^n, n \in \mathbb{N}$)

- The antenna array is of the separable illumination type, that is, the array factor can be written as in Eq. (7.1).

- We assume that the steering angle and the operating bandwidth are such that 1 ORR filter is sufficient to provide the required delay difference between AEs which are at distance d from each other. This implies that the OBFN stages will have 1 ORR on the first stage, 2 ORRs on the second stage, and so on.

With those assumptions, we can compare the complexity of the single-wavelength (SWL) binary-tree OBFN with the complexity of the proposed multi-wavelength (MWL) WDM-based OBFN. Both beamformers can be divided in a horizontal beamforming and a vertical beamforming section. As visible in Fig. 7.3, the basic difference between those architectures is that:

- in the single-wavelength OBFN, N equal OBFN sections, with N inputs each, are required for the horizontal beamforming (see Fig. 7.2), plus another section (also equal) for vertical beamforming (as in Fig. 7.3a);

---

[3]In computational complexity theory, the *time complexity* of a problem equals to the number of steps that it takes to solve an instance of the problem as a function of the size of the input (usually measured in bits), using the most efficient algorithm. The *space complexity* of a problem, instead, equals to the volume of the memory used by the algorithm (e.g., cells of the tape) that it takes to solve an instance of the problem as a function of the size of the input (usually measured in bits), using the most efficient algorithm.

- in the multi-wavelength OBFN, only 1 OBFN section, with N inputs, is required for the horizontal beamforming (see Fig. 7.2), plus another section (also equal) for vertical beamforming (as in Fig. 7.3b).

To better understand the impact on the asymptotic complexity of this novel architecture, and thus the performance for large scale arrays, it is possible to fill the following Table 7.1 with some examples[4].

Table 7.1: Complexity comparison between SWL and MWL OBFNs

N	AEs	Sections	ORRs/section	ORRs (SWL)	ORRs (MWL)
$2^0 = 1$	1	–	–	–	–
$2^1 = 2$	4	3	1	3	2
$2^2 = 4$	16	5	4	20	8
$2^3 = 8$	64	9	12	108	24
$2^4 = 16$	256	17	32	544	64
$\vdots$	$\vdots$	$\vdots$	$\vdots$	$\vdots$	$\vdots$
$2^n = N$	N^2	$N+1$	$\left(\frac{N}{2}\right)\log_2 N$	$(N+1)\left[\left(\frac{N}{2}\right)\log_2 N\right]$	$2\left[\left(\frac{N}{2}\right)\log_2 N\right]$

The number of antenna elements (second column of Table 7.1) is equal to N^2, since the array is square with N elements on each side. The number of sections for the SWL OBFN can be calculated considering the architecture presented in Fig. 7.2. From the figure it can be seen that there is a section for each horizontal subarray, implementing the horizontal beamforming function, plus one additional section that combines the output of the previous sections and implements the vertical beamforming function. Thus the total number of section is $N+1$ (see the third column of Table 7.1). Instead, for the MWL OBFN, there is only one section for the vertical beamforming and one for horizontal beamforming, connected by a demultiplexer. Thus the total number of sections is 2, independently of N.

The number of ORRs per section (fourth column of Table 7.1) can be obtained by multiplying the number of stages by the total number of ORRs in each stage. The number of stages is $\log_2 N$, while the number of ORRs is the same in each stage and equal to $N/2$. Thus, the *total number of ORRs per stage* is

$$\text{ORRs/stage} = \left(\frac{N}{2}\right)\log_2 N \tag{7.2}$$

Based on the description given before, the difference in complexity between the SWL and the MWL OBFN is mainly in the *number of stages*, which are $(N + 1)$ and

---

[4]Note that the case $N = 1$ is the degenerate case of the 1-element array, for which the number of ORRs cannot be defined.

2, respectively. Thus the total number of ORRs for a SWL OBFN and the number of ORRs for a MWL OBFN are respectively given by the equations

$$ORR_{\text{SWL}} = (N+1) \left[\left(\frac{N}{2} \right) \log_2(N) \right] \in O(N^2 \log_2 N) \tag{7.3}$$

and

$$ORR_{\text{MWL}} = (2) \left[\left(\frac{N}{2} \right) \log_2(N) \right] \in O(N \log_2 N). \tag{7.4}$$

which have been obtained multiplying the number of stages with the number of ORRs per stage (term in square brakets). In Eqs. (7.3) and (7.4) the big O notation[5] has been used to represent in simpler terms the speed of growth of the two functions with respect to N. In particular, the number of ORRs for the SWL case grows faster than quadratic with N. Instead, employing the MWL technique, allows to reduce the speed of growth down to a so-called *linearithmic* (also known as loglinear, or quasilinear) with N. This is the same speed of growth as for example in the fast Fourier transform (FFT) algorithm.

The extreme importance of this result can be better understood by plotting the growth of number of ORRs required versus the array dimension, N, as in Fig. 7.4.
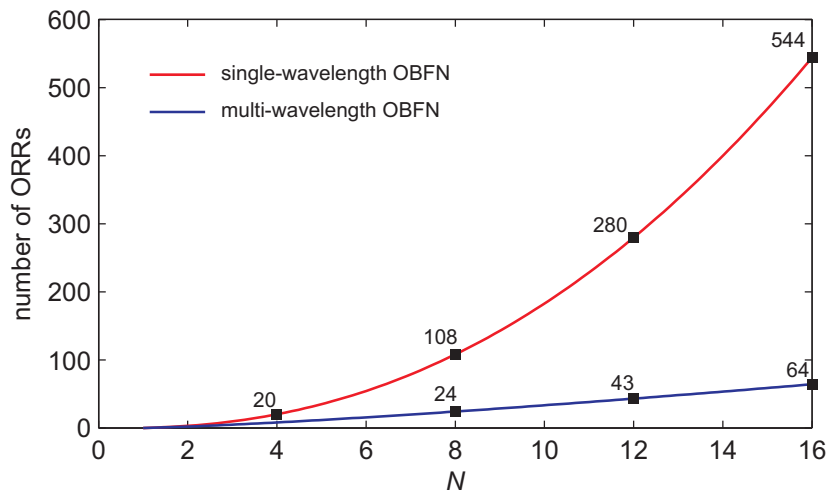
Figure 7.4: Comparison of the growth of number of ORRs required versus the array dimension N, in the case of single-wavelength OBFN (red) and of multi-wavelength OBFN (blue)

For SWL OBFN, as soon as the array size grows beyond 5×5 or 6×6, the number of ORRs required surpasses 50. The largest number of ORRs ever realized on

---

[5]Typical of mathematic or computer science, the big O notation is used to indicate the limiting behavior of a function when the argument tends towards infinity, usually in terms of simpler functions [201].

a single OBFN chip is 40, for the OBFN shown in Chapter 4. This means that the programmable chip should have at least 100 heaters only for the ORRs, plus all the tuning elements required for the combiners and the optical phase shifters, which should be all independently programmable. This creates a large chip footprint and generates a high level of complexity for the control system. In this example, using the MWL OBFN, a beamformer with approximately the same complexity would be able to control a phased array which is already *four times* the size (only 64 ORRs would be required to control a 256-elements array). This difference would increase by increasing the array size. If we used a traditional SWL OBFN, we would have needed more than 500 ORRs, meaning a number of heaters beyond one thousand, which would be impossible to realize with the current technology. Area and cost also receive benefit by reducing the number of required ORRs; in fact, the area is linear with number of ORRs, and the cost is linear with area. Besides this clear implication on cost, it is important to notice that the ability to keep the OBFN area limited to the wafer size allows to solve the beamforming problem using only one OBFN chip. This avoids the need of connection between multiple chips which, as analyzed in Chapter 4, sensibly increases the system costs and can also degrade system performance in the cases where multiple optical-to-electrical conversions are needed.

Note that in this discussion the presence of the multiplexer and demultiplexer stages, required in the MWL architecture, have been neglected in the complexity calculation. Nonetheless, as will be seen in the following, those components do not include ORRs which are considered in this study as the most impactful elements on the system complexity, in terms of tuning and required dye area occupation, and thus have a limited impact on the fractional complexity, especially for large numbers of N which the use of the multi-wavelength technique is aimed for.

To fully understand the true hardware compressive potential of this architecture, it is also important to note that the complexity of a MWL OBFN used to feed a 2-D antenna of $N \times N$ elements, has the same complexity, besides a factor 2, of a single-wavelength beamformer used for a 1-D linear antenna of N elements. In fact, a linear array would employ an OBFN which is equal to a single stage of a 2-D array, thus employing a number of ORRs given by Eq. (7.2). Thus the introduction of the MWL technique allows to reduce the complexity of a 2-D problem of N^2 size to the one of a 1-D problem of size N. In other words the beamformer, instead of growing more than quadratic with N, would be only twice as large as the one for a linear array.

7.3   System architecture

After having described the operating principle, in the present section we show the architecture of an OBFN system based on a MWL beamformer, and we analyze the characteristics of each component.

This OBFN has been designed, realized and tested for integration in demonstrator 1 of the "workpackage" A2 of the Memphis project. As described in Chapter 1, the project aims at integration of photonics and electronics in integrated systems.
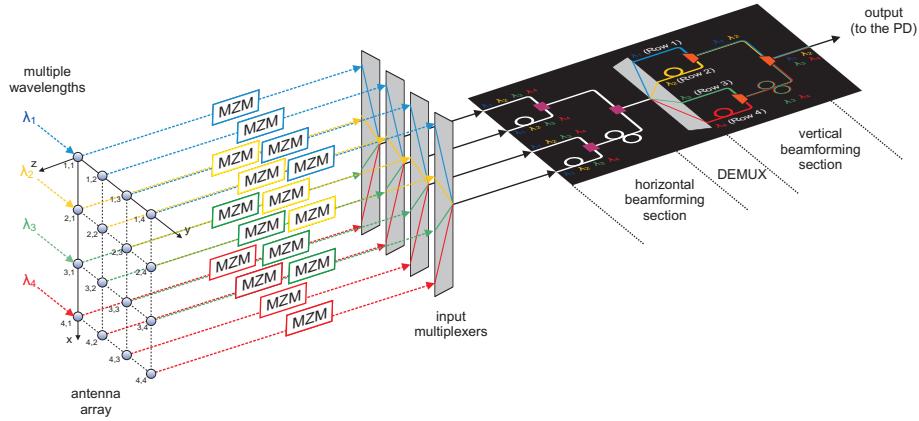
Figure 7.5: Block diagram representing the connection between a 4 × 4 antenna array and the OBFN chip

A more detailed impression of the aimed form for the demonstrator will be reported at the end of this chapter, in Subsec. 7.12.

The OBFN is composed of the following sections. Details on the function of each of them will be given in Sec. 7.4.

1. Optical phase shifter section 1

2. Horizontal beamforming section

3. Optical demultiplexer

4. Separate carrier tuning section

5. Optical phase shifter section 2

6. Vertical beamforming section

7. Optical filter

The multi-wavelength optical beamformer (MWL-OBFN) block diagram is represented in Fig. 7.6.
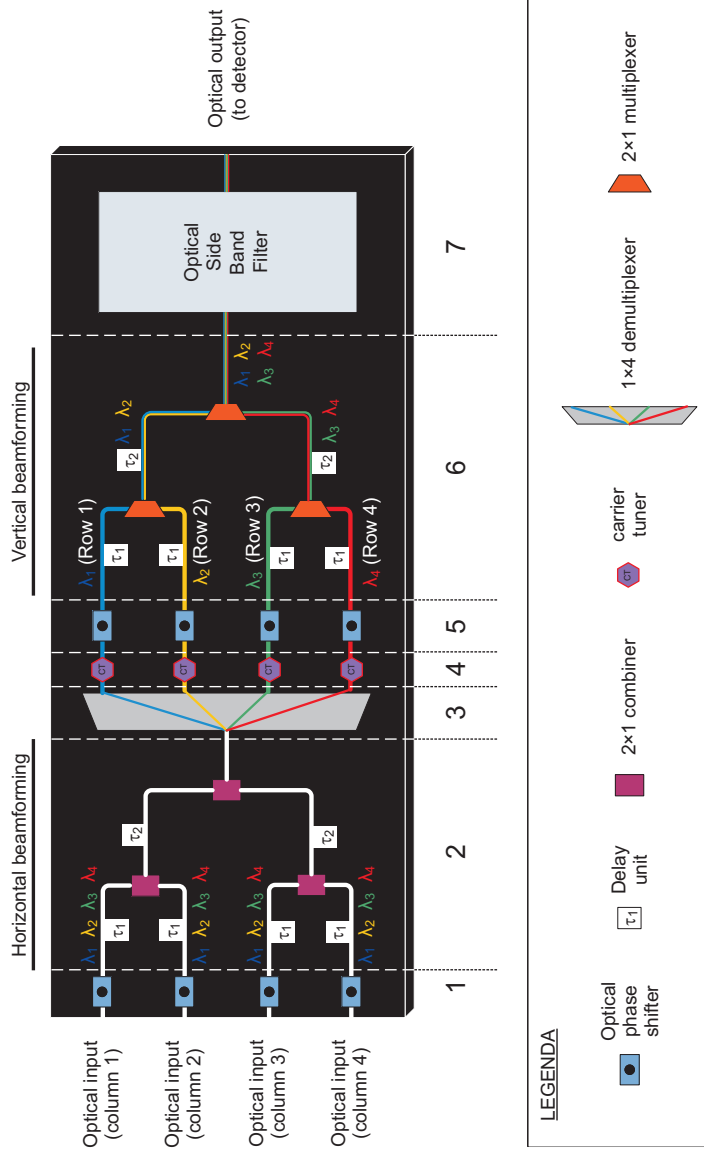
Figure 7.6: Schematic representation of the of the multi-wavelength, mutiple-signal-path OBFN, for a 4×4 planar array. The separate sections are indicated by the numbers as: (1) Phase shifter section 1; (2) Horizontal beamforming section; (3) Optical demultiplexer; (4) Carrier tuning section; (5) Phase shifter section 2; (6) Vertical beamforming section; (7) Optical filter.

7.4 Building blocks

The multi-wavelength OBFN represented in Fig. 7.6 has 4 inputs, each of them carrying the signals originating from 4 different antenna elements, which have been wavelength-multiplexed[6] using different optical carriers (spacing $\Delta f = 100$ GHz, corresponding to $\Delta\lambda \approx 0.8$ nm @ 1550 nm). In the **horizontal beamforming section**, those signals are delayed with respect to each other by the delay units τ_1 and τ_2 and then optically combined. This allows *horizontal beamsteering* (i.e. in the direction of the rows of the array) of the main lobe of the generated antenna pattern.

The output is then applied to a 1×4 **demultiplexer**. Each wavelength has been used to modulate the signals of the same row: as a consequence, each output of the demultiplexer carries the combination of signals received by the antenna elements of the same row. Those signals are then applied to the second part of the MWL-OBFN, namely the **vertical beamforming section**, where they are delayed with respect to each other by the delay units τ_1 and τ_2. This operation corresponds to the *vertical beamsteering* (i.e. in the direction of the columns of the array). As in Memphis A2 demonstrator 2, the horizontal and vertical beamsteering sections have two distinctive characteristics:

- *Binary tree architecture:* couples of adjacent inputs to a stage combine into a single output of that stage, which correspond to the input of the following stage.

- *Symmetric architecture:* every path between each input and the output contains the same number of basic delay units (see Fig. 7.6).

The **optical side band and carrier filter (OSBCF)** is used to select only one sideband plus the optical carrier, for each of the laser wavelengths. The elimination of one sideband allows to reduce the required delay band, and the carrier is kept to allow direct detection of the RF signals.

The **delay units** are designed to delay the remaining sideband of the information signal after optical sideband filtering. For a complete description of the operation of the delay units, refer to Chapter 4, and to Chapter 6 for the specific signal processing technique used.

The **carrier tuner** is placed at each output of the optical demultiplexer. It consists of a separate couple of optical ring resonators whose resonant wavelengths will be tuned in such a way to modify the phase of the carrier frequency only, *separately* from and without affecting the one of the information signal. In particular, this component is used to realign the phase of the optical carrier to the desired value, after the ORR-based delays have been used to tune the delay of the sideband only. In particular, the phase of the carrier must be made equal to the one that it would have experienced in case broadband ideal delays had been used. The concept of SCT (separate carrier tuning) using optical ring resonators has been described in detail in Chapter 6.

---

[6]In the implementation phase, two versions of the chip have been realized: one of them includes additional on-chip input multiplexers before each input.

7.5 OBFN Functional Design

Here the design of the sections of the OBFN chip is described. The system design of the optical filter is discussed separately in Sec. 7.7.

7.5.1 Optical phase shifter section 1

Optical phase shifters are placed at each input of the chip. This will allow to use the first stage of the MWL OBFN as a single-wavelength, 4×1 OBFN. This is useful to easily test the basic functionality as well as the bandwidth capability of the system.

It is important to note that, for the actual operation, it is important to realize constructive coherent combining of each of the four wavelengths in the horizontal beamforming stage. For this purpose, two conditions should be satisfied.

1. The system is supposed to operate as a coherent system, where multiple wavelengths are employed. As a consequence, the combining waves for one specific wavelength should originate from the same cavity.

2. Individual optical phase shifters will be placed on each optical path which carries the signals originating from each antenna element. Tuning those phase shifters will allow to independently change the carrier phases and realize the desired constructive coherent combining among RF signals modulated on the same wavelength carrier[7]. Those phase shifters will be shown in Fig. 7.25 in Sec. 7.8.

7.5.2 Horizontal beamforming stage

This section of the chip allows (*i*) combination and (*ii*) delay of the signals originating from the different columns of the antenna array (Fig. 7.6). A binary tree structure is employed, with ORR delay units placed symmetrically on the tree branches. The number of ORRs in this section is determined based on the procedure described in Sec. 7.6. The different branches are combined using symmetric Mach-Zehnder interferometer (MZI) combiners (Fig. 7.7).

- Each wavelength needs to be combined coherently and constructively. For this reason optical phase shifters are introduced before multiplexing as described in Sec. 7.5.1.

- Note that this structure needs to delay signals generated by modulation from multiple carrier wavelengths ($\lambda_1, \lambda_2, \lambda_3, \lambda_4$). In addition to that, the delay elements should provide the same amount of delay to the RF signals modulated using each wavelength carrier (which encodes a specific row of the array, as visible in Fig. 7.2), to make sure that the maximum of radiation from each horizontal subarray will point in the same direction on the yz plane. This is made possible by exploiting the frequency periodic behaviour of the optical

---

[7]To realign the RF phases, instead, the separate carrier tuning section described in Sec. 7.5.5 will be employed.
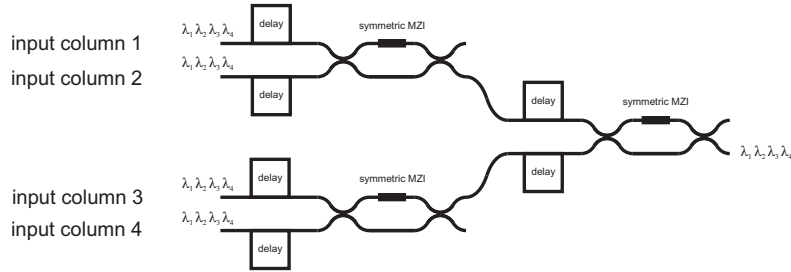
Figure 7.7: Block diagram of the horizontal beamforming section

ring resonator used as optical delay units, to delay the RF signals modulated on the different optical bands. This concept is shown in Fig 7.8. For this reason, the channel spacing (Δf = 100 GHz) must be an integer multiple of the FSR of the ORRs used in the delay elements: the FSR has then to be chosen accordingly.

Accuracy of the FSR. In the proposed beamformer architecture, the frequency periodicity of the ORRs is exploited to implement a WDM OBFN (that is, multiple bands are delayed by the different bands of the same ORR). For this reason, it is very important that the FSR value is implemented with high accuracy. In fact, an error on the FSR will accumulate and create a large error at the band at $3\Delta f$ distance (Fig. 4.2). In principle, the FSR accuracy must then be high enough to assure that all the four bands will be included in the minimum delay band of the ORRs (achieved at the maximum required delay).
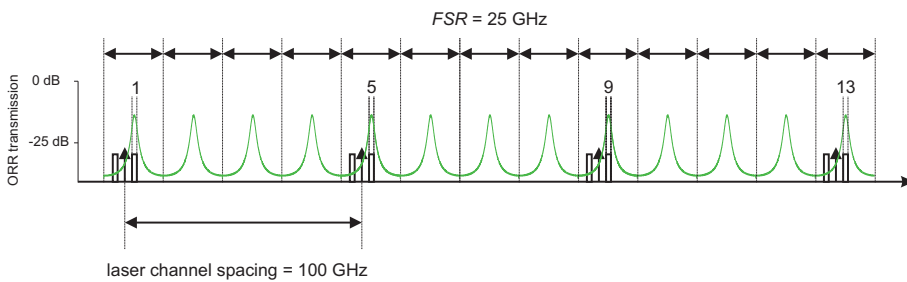
Figure 7.8: The periodic response of the ORRs is exploited to delay multiple wavelength-multiplexed signals using a single structure

By analyzing Fig. 7.8, it can be seen that the maximum tolerance on the FSR is given by this expression:

$$\Delta FSR_{\max} = \pm \frac{BW - BW_{\min}}{(n_\lambda - 1) \cdot n_\lambda + 1} \tag{7.5}$$

where n_λ is the number of wavelengths, BW is the delay bandwidth and $BW_{\min}$ is the minimum required delay bandwidth given by the specifications, which will be the same as the bandwidth of the sideband representing the information signal.

Example 7.1

From the specifications given in Memphis A2 demonstrator 1 (reported in Sec. 7.12, the bandwidth of the required information signal is 2 GHz. From the antenna element spacing (37.5 mm) and from the maximum steering angle (+30 degrees for both ϑ and φ), it is possible to derive the maximum delay required for each ORR. Assuming a choice of the FSR of 25 GHz, and the use of a single ORR per delay unit, the maximum delay will be 13.375 RTT, where RTT is the round-trip-time of the ORR (which, in turn, is defined as the inverse of the FSR). By simulations, it can be proven that, this delay can be achieved with a phase error below $\pi/16$ over a maximum bandwidth of 2.39 GHz. If we substitute the obtained values in Eq. (7.5) above, we obtain

$$\Delta FSR_{\max} = \pm \frac{2.39\,\text{GHz} - 2\,\text{GHz}}{(4-1)\cdot 4 + 1} = \pm \frac{0.39\,\text{GHz}}{13} = \pm 30\,\text{MHz} \qquad (7.6)$$

This is a challenging tolerance to be achieved with the available production process. In practice, assuming the possibility to independently tune the carrier wavelengths separately, this stringent requirement can be largely relaxed.

Optical phase synchronization. For coherent combining operation, the optical phases of the 4 individual wavelengths in the multiplexed OBFN paths must be synchronized in such a way to obtain constructive coherent combining for each wavelength, as discussed in Sec. 7.5.1 before. Since the 4 wavelength are already multiplexed when they enter the OBFN chip, the required phase synchronization shall be performed externally to the OBFN chip, before the multiplexing, using independently-controllable optical phase shifters, as shown for example in Fig. 7.9. Those optical phase shifters are included in the realized version of the chip, as will be shown in Fig. 7.25. In the Memphis project demonstrator, the optical multiplexing occurs already on the InP chip containing the multiwavelength lasers and integrated modulators, reported by Zhao et al. in [202]. In this case, the phase shifters can be easily added, in the design phase, on the MWL laser chip itself.

7.5.3 Demultiplexer

The optical demultiplexer has a binary tree structure based on asymmetric MZIs (AMZIs) [203], with different values of free spectral range (FSR), as shown in [204]. The FSR of an AMZI is determined by the difference in path length between the branches of the interferometer. The FSR has to be chosen in order to separate the four wavelengths of the four lasers (λ_1, λ_2, λ_3, λ_4) which, in the example of the Memphis demonstrator, have a channel spacing Δf of 100 GHz. The resulting structure and the choice of the FSR for the different AMZIs is shown in Fig. 7.10.
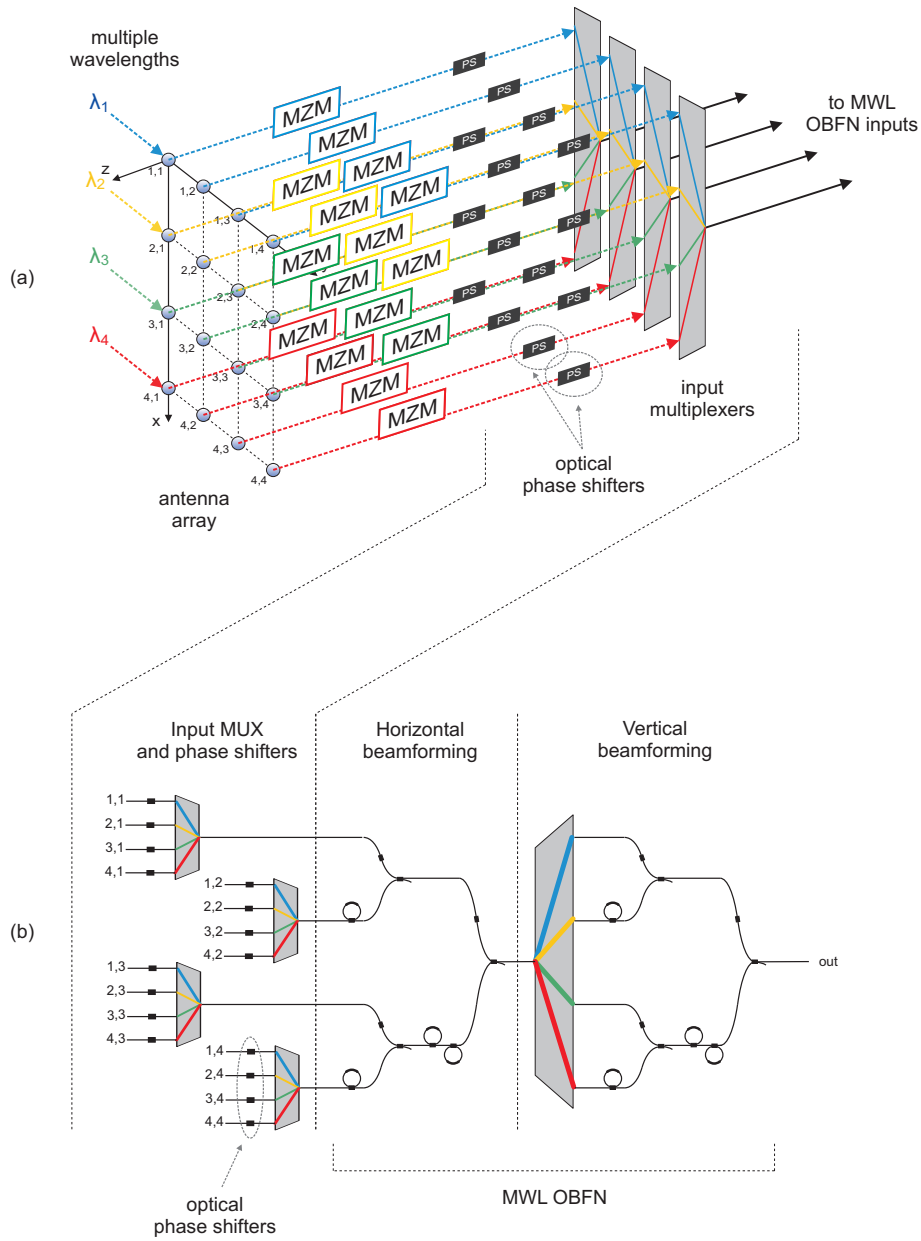
Figure 7.9: Possible arrangement of external optical phase shifters for optical phase synchronization and constructive coherent combining; (a) functional schematic, (b) example of a possible planar layout.
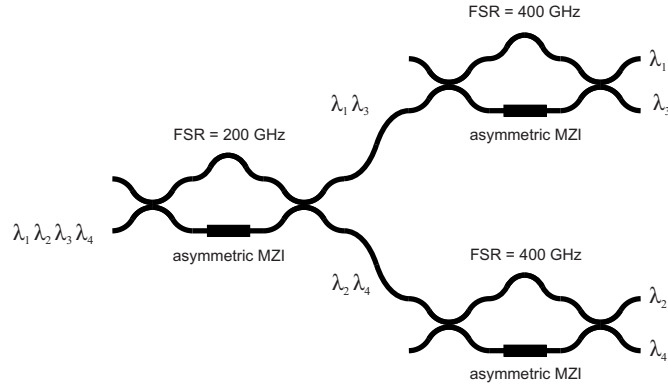
Figure 7.10: Block diagram of the 1×4 demultiplexer

The demultiplexer is composed of two stages. The first stage contains an AMZI with an $FSR = 200$ GHz, used to separates the four wavelengths into the two couples of channels (λ_1, λ_3) and (λ_2, λ_4). The second stage contains two AMZIs with an $FSR = 400$ GHz. This will be used to separate the individual wavelengths as shown in Fig. 7.11.

Note that the order of the outputs is (top to bottom): λ_1, λ_2, λ_3, λ_4. It will be sufficient to swap channels 2 and 3 at the antenna-modulator connection side to still achieve the desired beam pointing with a linear delay profile in the vertical beamformer section (following the demultiplexer).

7.5.4   Optical phase shifter 2

During operation of the MWL OBFN in nominal conditions, the phase shifters in this section are not used. Nonetheless, the thermo-optical tuning allows a complete reconfigurability of the chip. The vertical beamforming stage can then be used to implement a non-coherent, multi-tap microwave photonic filter (MPF) based on separate carrier tuning delay lines, as described in Chapter 6 and graphically represented in Fig. 6.10(a). In this case the n-th phase shifter can be used to change the phase of the n-th complex coefficient $a_n = |a_n|e^{-j\varphi}$ of the MPF, as expressed by Eq. (6.4), and correspondingly reconfigure the MPF response.

7.5.5   Separate carrier tuner

The separate carrier tuner is an array of four couples of ring resonators (Fig. 7.12) used to realign the phase of the optical carrier to the desired one after delay of the sideband. The theory of separate carrier tuning has been described in detail in Chapter 6 and its application to our system is detailed below.
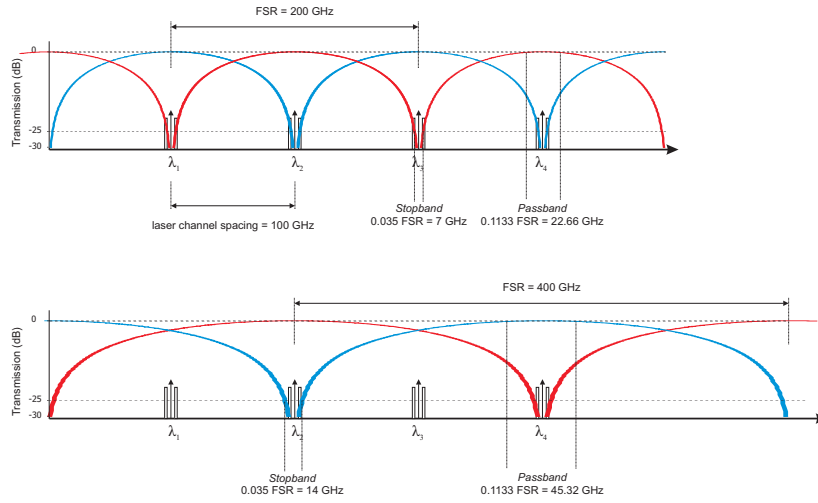
Figure 7.11: Response comparison of the AMZIs in the 1×4 demultiplexer: first stage, *FSR* = 200 GHz (above); second stage, *FSR* = 400 GHz (below)
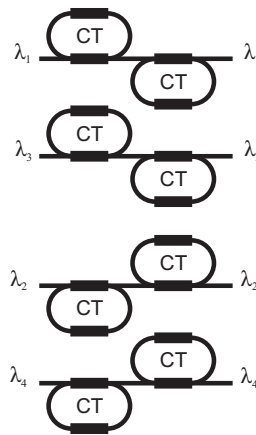
Figure 7.12: Block diagram of the carrier tuner
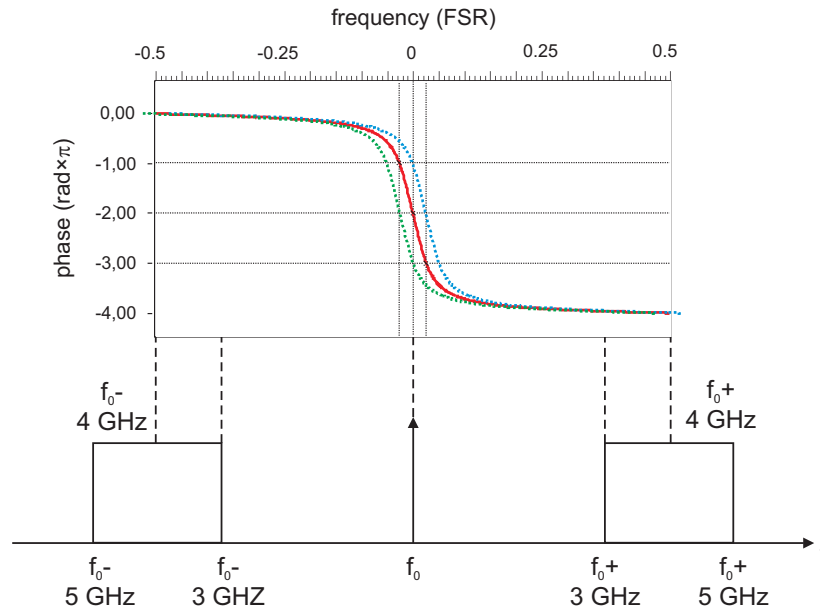
Figure 7.13: Phase response of the separate carrier tuner

Fig. 7.13 shows the operation of the CT section. The resonance frequency of the ORRs composing the CT is shifted around the frequency of the optical carrier. In this way, it is possible to provide the desired phase shift to the carrier in the complete range from 0 to 2π radians. Tuning the Q-factor of the ring resonators to a sufficiently high value, as shown in Fig. 7.13, it is possible to achieve an approximately flat phase characteristic over the sidebands, thus without disrupting the phase characteristic imposed by the ORRs delay sections. Maximum flatness of the phase characteristic of the CT rings is achieved at half-*FSR* distance from the resonance (around +0.5 *FSR* and -0.5 *FSR* in the graph). This imposes that the *FSR* of the ORRs used in the CT section shall be equal to twice the central RF frequency of the sideband. In our case, from the specifications of the Memphis demonstrator, the sideband is comprised between 3 GHz and 5 GHz, thus with a central RF frequency of 4 GHz, which gives *FSR* = 8 GHz.

7.5.6   Vertical beamforming stage

The vertical beamformer stage has both the function to delay and to multiplex the signals carried by the different wavelengths (those, as we have seen in the previous stage, encode the different rows of the phased array). For this reason, it can be realized with the same structure as the demultiplexer, but reversed with respect to input-output direction. In addition to that, delays have been added to the branches, as in Fig. 7.14. As a consequence, this section of the beamformer is very

similar to the horizontal beamforming stage. Instead of the wideband combiners, which in the horizontal beamforming section have been realized with symmetric MZIs, here multiplexers are used, which are realized with AMZIs as in the demultiplexer stage.
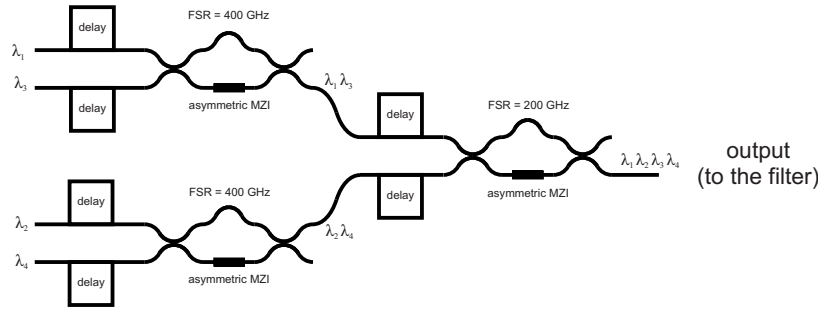
Figure 7.14: Block diagram of the vertical beamforming section (4×1 multiplexer including delay units)

7.6 Tunable delay units design

Tunable delay units are realized using cascaded basic tunable delay units. A basic tunable delay unit consists of an optical ring resonator (ORR). As described in Chapter 4, the ORRs delay units show an inherent tradeoff between (*i*) bandwidth, (*ii*) maximum delay, (*iii*) delay ripple (or phase error) and (*iv*) number of ORRs. As a consequence, in the design of the MWL-OBFN, the number of ORRs required in each delay unit has to be determined on the basis of the following parameters:

- the RF signal bandwidth;

- the maximum delay required;

- the maximum allowed beam pointing fluctuation within the complete band (which, in turn, translates into a requirement on the maximum phase error allowed in the band of interest [158]).

To determine the number of ORRs, it is also important to consider the free spectral range (*FSR*) of the ORRs and the ring losses.

RF bandwidth and maximum phase error allowed are given by the OBFN specifications (see Chapter 1). The maximum delay required can be obtained from the specifications by considering:

- the maximum scan angle;

- the distance between the subarrays on x and y axes of the antenna plane.

The calculation of the minimum number of ORR needed in each delay section is performed via simulation of the phase response of a delay unit (using a Lab-View [205] model) and its comparison with the simulated phase response of a corresponding ideal delay line. The number of required rings is then determined based on the procedure which has been described in detail in [158] and reported in Appendix B.

An important parameter for the simulation of the delay units is the FSR of the ORR. As discussed in Section 4.1.1, the value of this parameter depends on technological considerations and constraints (trade-off between chip area occupation and minimum bending radius reliably reproducible with acceptable losses) and is fixed once the chip has been realized. Nonetheless, it has effect on the design procedure and, being a non-tunable design parameter, must be calculated and considered as a fixed value in the design procedure. According to the specifications from the layout designers [161], the maximum FSR that could be reliably realized at the time of this design was 25 GHz.

The ring losses have been evaluated based on the measurement procedure detailed in [24], and introduced in a later stage of the design to account for the possible deviations from ideality they might introduce.

7.6.1   Calculation of the maximum delay in each OBFN path

Given the array architecture and the required scanning angle, and given the beamformer architecture and its connection to the array (Fig. 3.2), it is possible to determine the required maximum delay in each path and, from that, the number of ORRs needed in each delay stage.

In our example, we have:

- Scan angle ($\pm\vartheta_{max}$): $\pm$ 30 degrees

- Distance between adjacent antenna elements: 37.5 mm

- Array architecture: 8×8 elements, separable illumination

The array architecture is of the separable illumination type; this means that the array factor $F(\vartheta,\varphi)$ produced by such a beamformer can be obtained as the simple product of the array factor $F_x(\vartheta,\varphi)$ of the x-direction subarrays and the array factor $F_y(\vartheta,\varphi)$ of the y-direction subarrays (see Section 2.4.3). In turn, this means that, for the required scan angle, it is possible to calculate the maximum delay to be introduced by the beamformer between the x-direction subarrays and the y-direction subarrays. For this purpose, we use Fig. 7.15, where a side view (either in the xz or the xy planes) of a portion of the array is depicted.

Let d be the spacing between the antenna elements and ϑ_{max} the maximum angle that the desired beam forms with the z axis. For the considered system it follows that the maximum delay to be provided by the beamformer (between two adjacent delay elements, both in x and y direction) shall be the one given by

$$\Delta l_{max} = d\sin\vartheta_{max} = \pm 18.75 \text{ mm} \tag{7.7}$$

$$\Delta\tau_{max} = \Delta l_{max}/c_0 \ \ = \pm 62.5 \text{ ps} \tag{7.8}$$
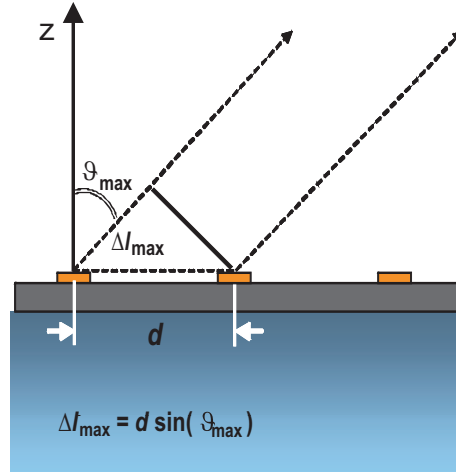
Figure 7.15: Calculation of required delay based on the subarray spacing (d) and the maximum desired steering angle ($\vartheta_{\max}$)

The beamformer delays are designed according to the highest delay case. This occurs in the case the pointing angle is $\vartheta_{\max}$ both in the xz and in the xy plane. In this case, every couple of adjacent elements both in the x and in the y direction must have the delay difference given by the (7.8). The resulting delay profile across the array is depicted in Fig. 7.16.

From the delay values in Fig. 7.16, by routing each delay to the corresponding beamformer path (see Fig. 7.5), we obtain the desired delay profile for maximum beamsteering shown in Fig. 7.17. This delay profile allows a beam tilting of $+\vartheta_{\max}$ both in the xz and in the xy plane. For a beam tilting of $-\vartheta_{\max}$ in the same planes, the delay profile needed is symmetrical with respect to the axis of symmetry of the OBFN geometry.

From the particular structure of the OBFN (symmetric binary tree) it follows that the required maximum delays for the delay elements in each stage (Fig. 7.17) are

$$\tau_2 = 2\tau_1 \tag{7.9}$$

Note that, thanks to the symmetry of the beamformer structure, the determination of the number of ORRs required can be performed considering one direction of beam tilting only, and then symmetrically replicated.

7.6.2 Calculation of required number of ORRs per delay element

In principle, once the delay distribution is known, it would be sufficient to calculate the delays τ_1 and τ_2 in order to specify the number of basic delay units (ORRs) needed in each section of the beamformer in Fig. 7.17. In practice, the basic delay
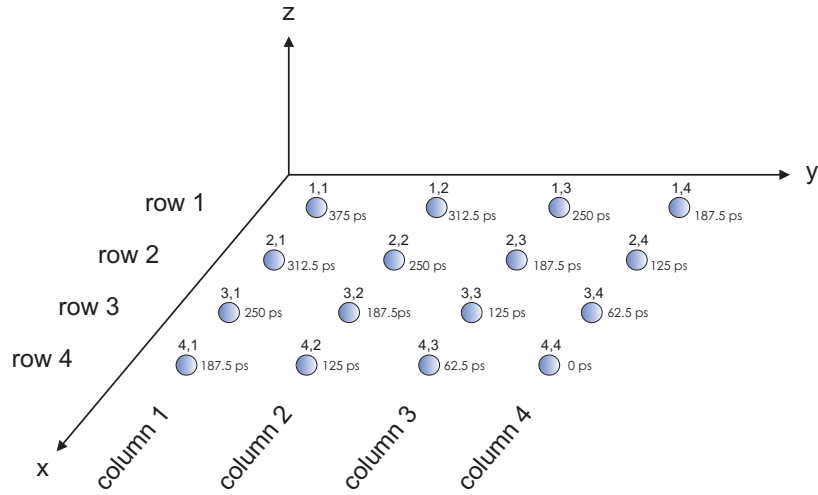
Figure 7.16: Required delay profile for the maximum desired steering angle ($\vartheta_{\max}$) both in x and y directions. The spheres represent the positions of the antenna elements.
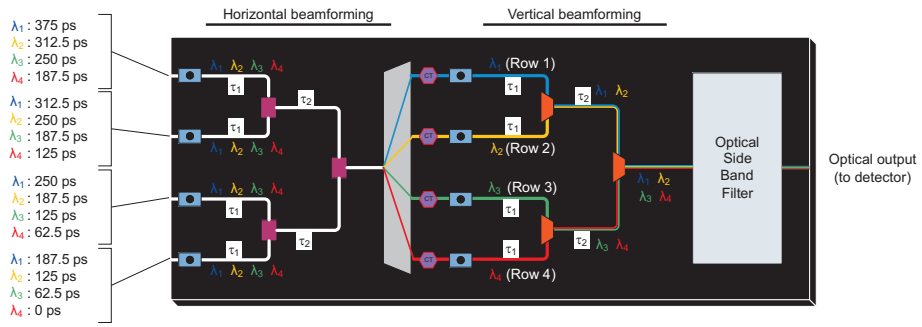
Figure 7.17: Required maximum delays in each stage of the optical beamformer. The squares represent the delay units, which shall be tunable between a minimum delay (equal to the sum of the RTT of all the ring resonators composing the delay element) and the value (λ_1, λ_2, λ_3 or λ_4) indicated.

units are not *ideal* delays, in the sense that they introduce a frequency-dependent delay error which has to be accounted for when cascading multiple basic delay units, as it happens in the binary tree structure of the beamformer. For this reason the simulation described in Appendix B allows to consider those delay error effects and, with a further analysis, their consequences on the beam shape and pointing direction.

Performing the analysis described in this paragraph, the simulation showed that, in the situation of Fig. 7.18, one ORR per stage is sufficient to implement a beamformer with a phase ripple in the passband below $\pi/16$ over a bandwidth of 2.39 GHz, as from specification (min. required bandwidth: 2 GHz). The specification on the maximum phase error was derived by simulations performed within the Memphis framework (see Chapter 1) by the National Aerospace Laboratory (NLR) [206] on the pointing direction tolerance. Those simulations showed that for the desired array configuration (i.e. a 2-dimensional array operating at Ku-band, composed by 25 tiles of 8×8 elements each), phase errors up to this specified amount are sufficiently low to guarantee that the main beam pointing direction is not sensibly disrupted for the aim of communication with geostationary telecommunication satellites.

7.6.3 Final layout

As a safety margin towards fabrication tolerances and for added system flexibility, it is desirable to add an extra ring resonator in the second stage of the OBFN, that is, duplicating the rings sections 1, 4, 7, 10 (see the figure for the numbering). The resulting system level layout is shown in Fig. 7.19. From the LabView simulations, this architecture gives an instantaneous bandwidth of 6.74 GHz.
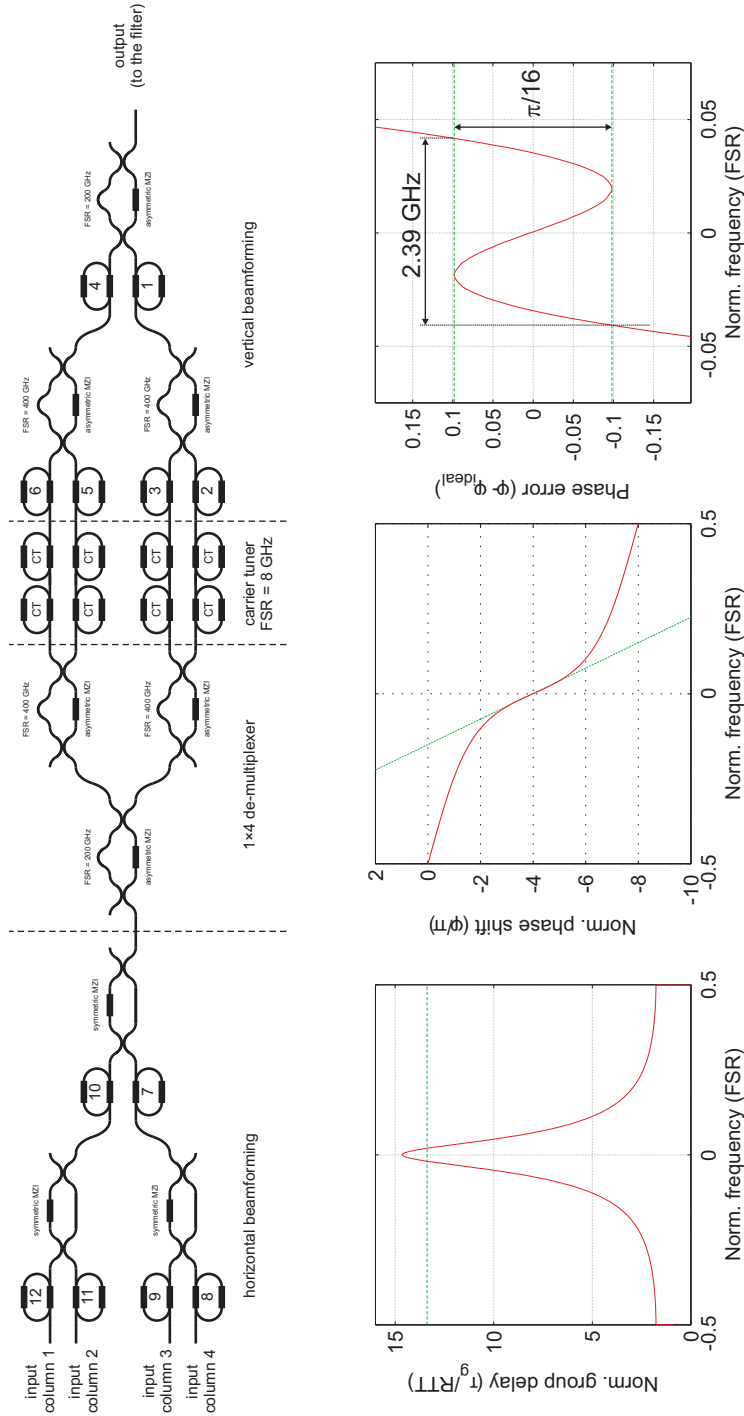
Figure 7.18: Proposed OBFN architecture with 1 ORR per stage, in all delay sections. Resulting bandwidth: 2.39 GHz
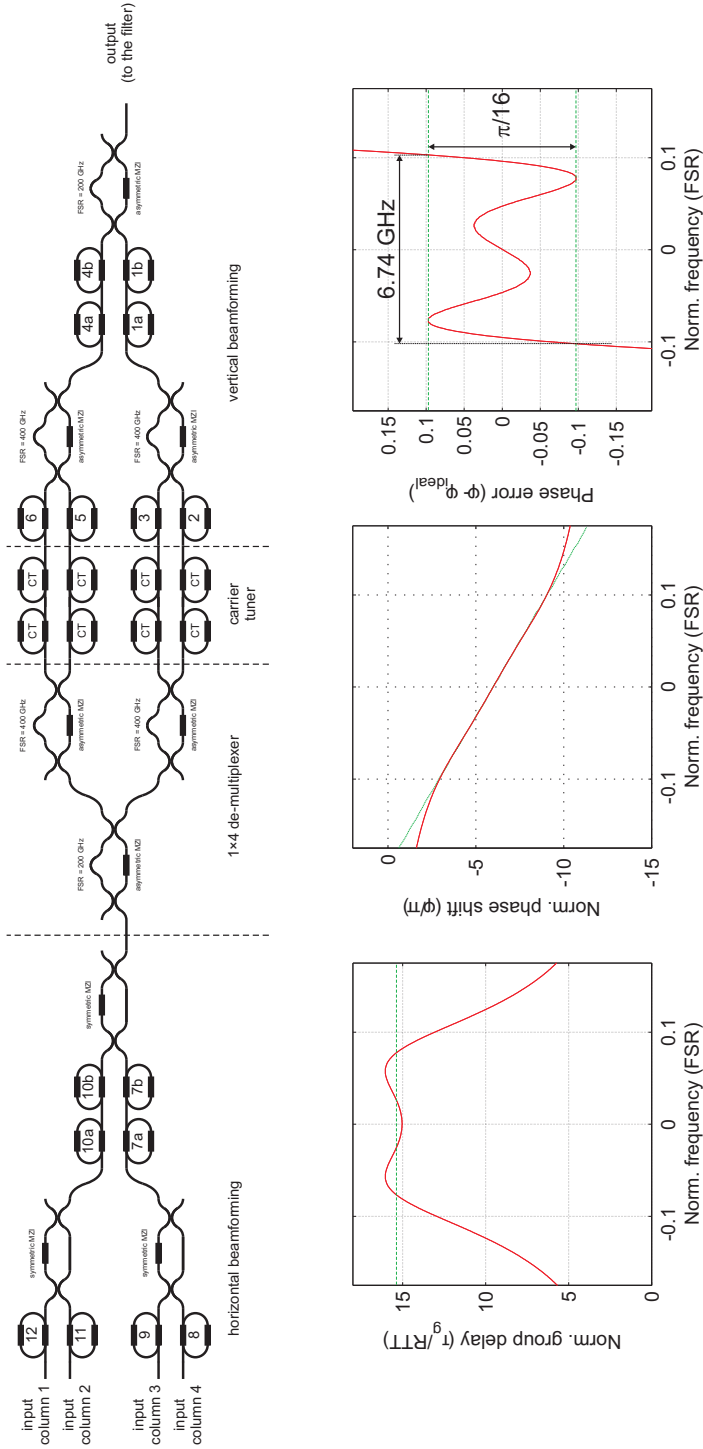
Figure 7.19: Proposed OBFN architecture as in Fig. 7.18, with extra rings added in sections 1, 4, 7 and 10. Resulting bandwidth: 6.74 GHz

7.6.4   Wideband Design (2–10 GHz)

In an optical ring resonator based OBFN, the delay-bandwidth product does not have inherent limitations, provided that the FSR of the ORRs is sufficiently wider than the RF band of interest. Increasing the number of rings in the layout, we aim to demonstrate that the instantaneous bandwidth can be improved to fit the initial A2 demonstrator 1 design specification of 2-10 GHz. For this reason, a wideband architecture has been designed as shown below.

To determine the number of ORRs needed in each stage in order to accommodate this new bandwidth requirement, we follow the same procedure described above and in Appendix B. Using 2 + 2 ORRs in the horizontal beamforming stage, and 2 + 2 ORRs in the vertical beamforming stage, from the OBFN simulations, for the individual paths we obtain the delay bandwidths reported in Table 7.2. The first column represents the optical path, where the numbers indicate the ORR section indicated as for the numbering in Fig. 7.20. The second column indicates the required delay according to the values reported previously in Fig. 7.16. The third column indicates the RF bandwidth of the delay, according to the $\pi/16$ maximum phase error criterion [158]. Finally, the last column indicates the values of κ and ϕ of the ORRs (see Chapter 4 for the definitions) that have to be set in order to achieve the desired delay response in the corresponding delay section.

Table 7.2: Channel bandwidths for the wideband MWL-OBFN architecture in Fig. 7.20

Optical path	Required delay	Bandwidth	κ, ϕ of the ORRs
8-7-5-4	125 ps ($3.125RTT$)	10.7422 GHz	$\kappa = 0.736, \phi = 0.879$
8-7-6-4	187.5 ps ($4.688RTT$)	11.1328 GHz	$\kappa = 0.985, \phi = 0.383$
11-10-6-4	312.5 ps ($7.813RTT$)	9.4727 GHz	$\kappa = 0.826, \phi = 0.104$
12-10-6-4	375 ps ($9.375RTT$)	9.7656 GHz	$\kappa = 0.981, \phi = 0.360$

The required values for κ of the ORRs in stage 4 and 12 are very close to 1 (0.985, 0.981, as in Table 7.2). This might not be a realizable condition in the actual chip, due to the possible non idealities of the 50:50 couplers used to fabricate the variable MZI couplers. For this reason, we may add 1 ring to both horizontal and vertical beamforming sections in order to relax the specification on the accuracy of the couplers. We obtain the proposed architecture shown in Fig. 7.20.
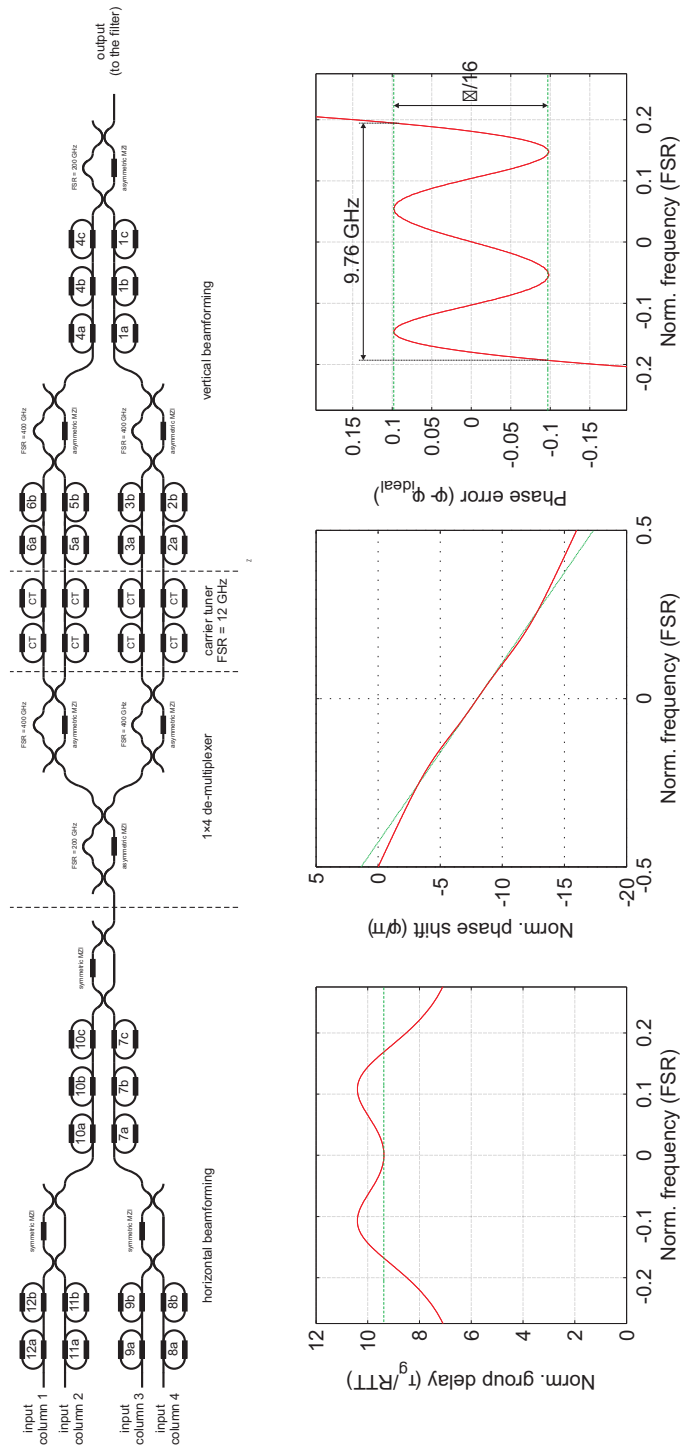
Figure 7.20: Wideband (2-10 GHz) OBFN architecture. Bandwidth: 9.76 GHz

7.7 Modulation technique and optical filter design

7.7.1 SSB-FC modulation

The multi wavelength approach used in this design required a careful choice of the most convenient modulation technique. A SSB-SC modulation, with carrier re-insertion and balanced detection, used in previous single-wavelength OBFN designs [33], is not convenient in this case because it requires the availability of the unmodulated carrier for all the wavelengths (not guaranteed in the Memphis demonstrator for which the system is built). Moreover, this would require to add carrier re-insertion points which would complicate the structure of the MWL-OBFN. Thus, the chosen optical modulation technique for the optical beamformer design is single sideband with full carrier (SSB-FC). This technique does not require the availability of the unmodulated carrier signal and allows the use of direct detection. Together with the separate carrier tuning (SCT) technique (Chapter 6), it allows to reduce the delay element complexity, thus also its area occupation on chip (compared to a DSB modulation scheme) by reducing the required RF delay band to a single sideband, as in the case of SSB-SC [33]. SSB-FC modulation has been implemented using a filter-based approach. The filter passes one of the sidebands and the optical carrier, and suppresses the remaining sideband, as shown in Fig. 7.22. The filter will be indicated in the following as *optical side-band plus carrier filter* (OSBCF). The carrier will be phase shifted before direct detection by a dedicated carrier tuner, as described in Sec. 7.5.5, and the sideband will be delayed by the ORR-based delay elements.

7.7.2 Filter architecture: MZI + 2 ORRs

The selected optical filter architecture is an MZI loaded with 2 ORR (Fig. 7.21). This kind of filter allows to satisfy all the requirements imposed by the design specifications, can be realized using the same building blocks (directional couplers, phase shifters and ORRs) as the MWL-OBFN and can be easily integrated on the same optical chip.
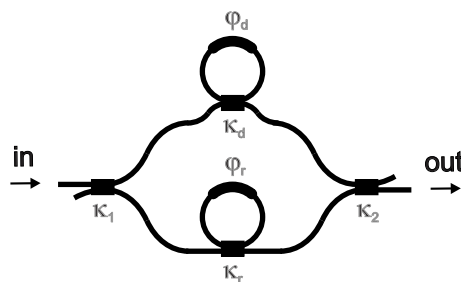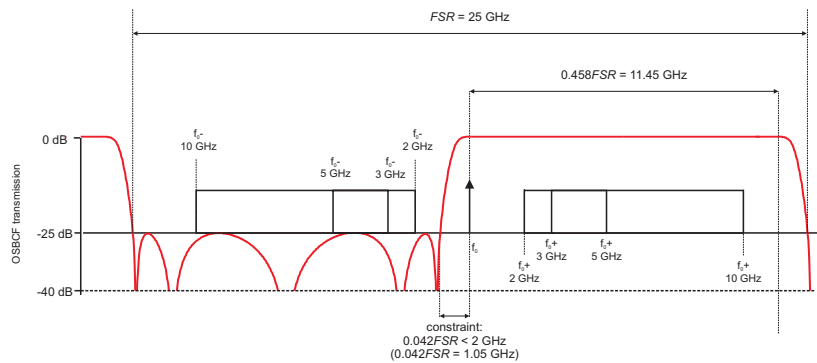

Figure 7.21: MZI + 2 rings optical filter

Choice of the filter FSR

Let us assume the lower sideband (LSB) is the one to be suppressed. The free spectral range of the filter shall be chosen in such a way that four conditions are satisfied:

1. ≥ 25 dB suppression of the undesired sideband (LSB);

2. the filter shall be used at the four wavelengths at the same time;

3. The transition between passband and stopband shall be narrower than 3 GHz, that is, the distance between the carrier and the highest frequency component of the LSB;

4. The passband and stopband shall be wide enough to (respectively) suppress the LSB and minimize the effect over the USB as desired.

Condition 2 imposes that the filter FSR should be a submultiple of the laser channels spacing. Using the LabView simulator, it is possible to tune the filter in order to have the widest possible band, keeping the stopband attenuation above 25 dB. The simulated response obtained is represented in red in Fig. 7.23. It results that choosing an $FSR = 25$ GHz allows the four conditions to be satisfied, as graphically shown in Figg. 7.22, 7.23.

Figure 7.22: MZI + 2 rings optical filter response tuned for LSB suppression

From Fig. 7.22 and 7.23 it can be noticed that this filter would allow to process signals whose RF band is as wide as 8 GHz, from 2 to 10 GHz, as in the wideband beamformer design described in Sec. 7.6.4, or even wider.

7.7.3 Filter FSR accuracy requirements

Similarly to the case of the ORR delay units, the periodic response of the filter is also exploited to add compactness to the structure by employing the same filter for all
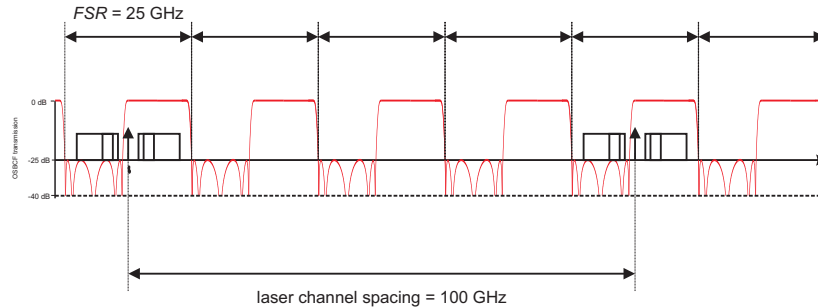
Figure 7.23: Periodicity of the MZI + 2 rings optical filter response and comparison
with the laser channel spacing

the wavelength carriers. This adds a requirement on the accuracy of the *FSR* of the
OSBCF. As in the case of the ORR based delay units, in fact, an error on the *FSR* will
accumulate and create a large error at the band at $3\Delta f$ distance. Here we analyze
this issue for the filter and derive the requirement on the FSR accuracy.

Since the FSR of the filter (25 GHz) is 0.25 times the wavelength spacing (100
GHz), the passbands used are the 1st, the 5th, the 9th and the 13th. Let us consider
the situation in which the filter is used to remove the lower side band, as in Fig. 7.22.
If the rightmost edge of the stopband to be suppressed is aligned with the rightmost
edge of the LSB, the margin between the leftmost edge of the passband and the
carrier is 2 GHz - 1.05 GHz = 0.95 GHz. An error on the filter *FSR* equal to ΔFSR
will translate into an error in the uppermost band (13th band) equal to 13 times the
error ΔFSR. This leads to the condition

$$13 \cdot |\Delta FSR_{\text{OSBCF}}| \leq 0.95 \text{ GHz} \qquad (7.10)$$

which, in turn, gives

$$|\Delta FSR_{\text{OSBCF,max}}| \approx \pm 73.8 \text{ MHz.} \qquad (7.11)$$

The measured characteristic of the same filter structure, but having an FSR of
6.7 GHz, has been reported by Zhuang et al. in [24].

7.8   Chip Layout

Considering the complexity of the OBFN chip, it is important that the different sub-
sections of the MWL-OBFN are made available and accessible at the external opti-
cal interfaces. Keeping this requirement in mind, the functional schematic repre-
sented in Fig. 7.20 has been translated into the layout represented in Fig. 7.25 by
LioniX BV [161].

In the following we will analyze the layout of the different OBFN sections sepa-
rately.
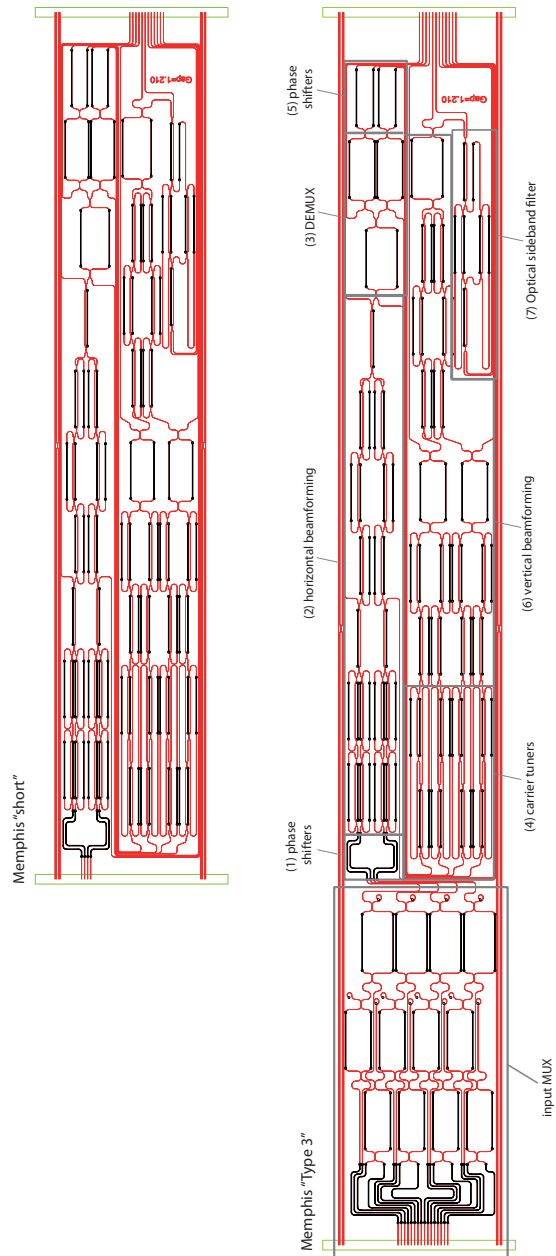
Figure 7.24: MWL-OBFN layouts: OBFN without input multiplexers (a), OBFN with including four 4×1 input multiplexers (b)

input MUX

to (1)
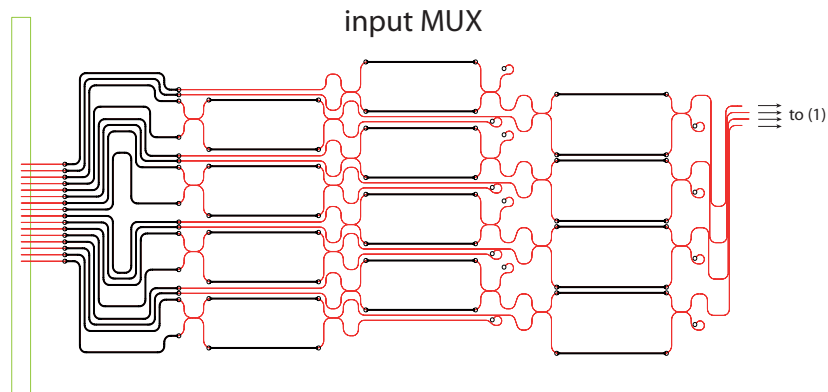
Figure 7.25: Detailed layout of the input multiplexer of the MWL-OBFN in
              Fig. 7.25(b)

7.9   Measurement of BBBs Characteristics

To demonstrate the basic functionality of the chip, the optical demultiplexer has
been tested and its performance compared with the simulation results.

The MWL OBFN described in this chapter contains a number of building blocks
which are novel when compared to the OBFN chips analyzed previously. In partic-
ular, three sections are different:

- the multiplexer/demultiplexers;

- the OSBF (which is now of the type MZI loaded with two ORRs instead of
  one);

- stringent specifications on the FSR periodicity are given.

In this section we report the test results needed to characterize the novel build-
ing blocks or to test if the novel performance requirements are met.

7.9.1   System setup for bare chip characterization

In the previous chapters, we have shown how the OBFN chips were connected to
a fiber array unit (FAU) in order to be able to easily access all the useful input and
output waveguides simply by means of optical connectors. In fact, as soon as the
photonic chips are produced and diced off the wafer, an initial characterization
must be performed in order to test the basic chip functionalities, and the correct
operation of the basic building blocks. This type of test is divided in electrical test
and optical test. The electrical tests include the verification of the electrical conti-
nuity for each individual control lines, the test of the ohmic resistance of the ground
lines, and the test of the ohmic resistance of the heaters. The optical test includes
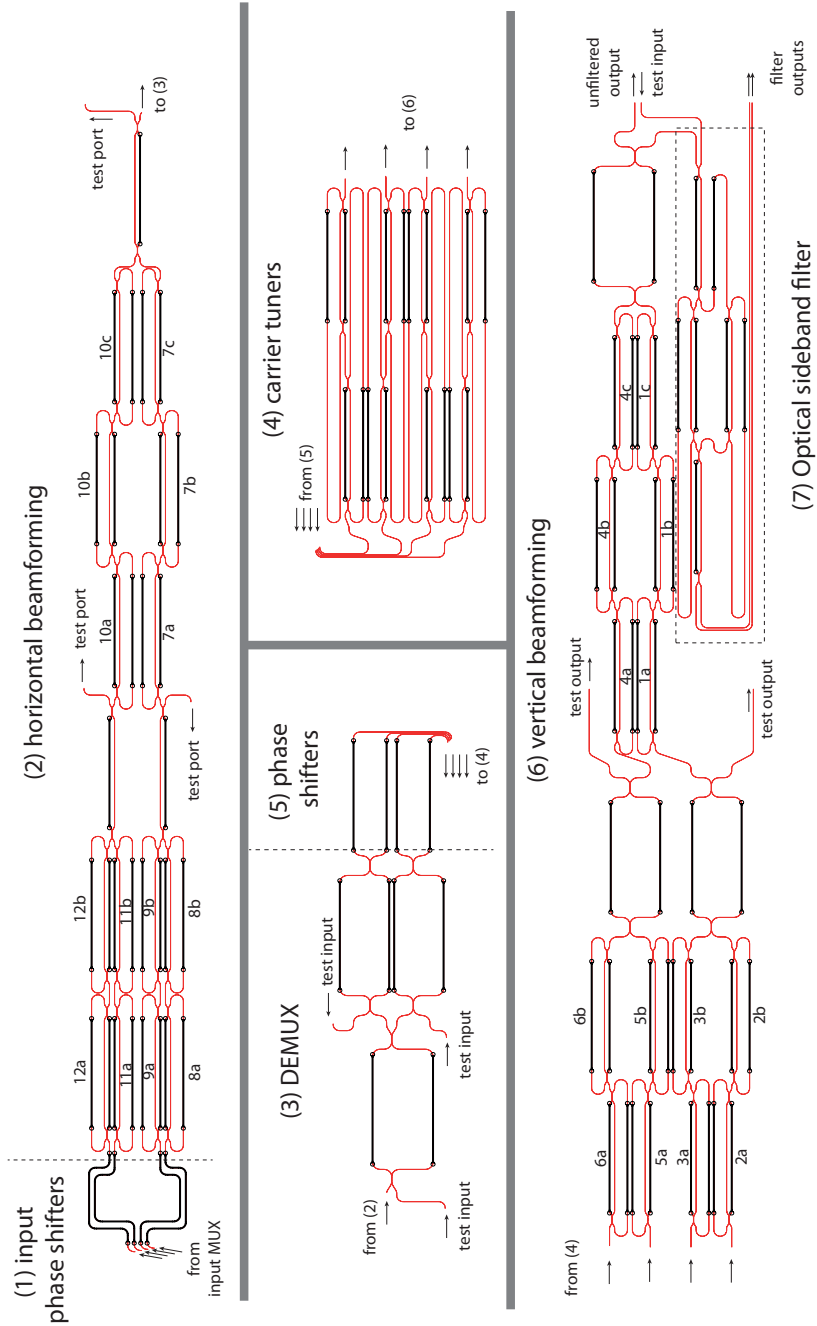
Figure 7.26: Detailed layouts of the different sections of the MWL-OBFN. Each section is numbered (in brackets) as in Fig. 7.6, while the ORRs are labeled as in Fig. 7.20.

and starts with the measurement of the fiber to chip coupling losses and the test of the main building block that is the 50:50 directional coupler. In general, each waveguide mask contains three complete replicas of the whole set of desired structures, which differ only in the coupling gap of the directional couplers contained in the functional structures. One value is the nominal one obtained by simulations, and the other two are chosen as a safety margin to compensate for fabrication inaccuracies. In this way, the probability to obtain a set of functioning structures from the specific mask is higher, thus increasing the robustness of the process with respect to deviations in the complex fabrication process.

After this test, a specific gap is selected as the one that provides the correct coupling ratio in the directional couplers, and the corresponding structures undergo packaging via fiber pigtailing by means of FAUs, butt-coupling with other optical chips, and wire bonding of the electrical connections. A packaged chip appears as in Fig. 7.27.
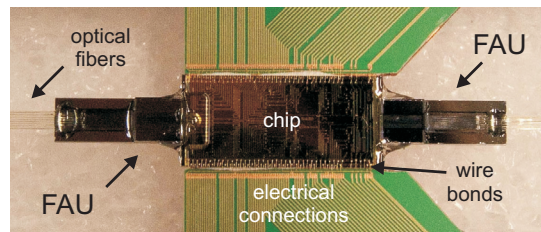
Figure 7.27: Example of an OBFN with wire bonds (for the electrical connections) and fiber pigtails (for the optical connections)

Another very important parameter which is tested is the waveguide loss. As discussed in Chapter 4, the waveguide loss has a very strong impact on the overall system performance of the optical beamformer system. When the structures include optical ring resonators, this test can be conveniently and accurately done by means of the procedure described in [24].

In order to test the optical performance of the optical structures, it is necessary to access the chip waveguides before connecting FAUs. This can be done by mounting the optical chip on a chuck, which includes thermal control via a Peltier element and a temperature sensor, and by aligning bare fibers to the waveguides to be accessed by using a suitable fiber alignment stage, featuring micrometric three-axis control of the fiber position. The schematic of the setup employed for the bare chip characterization is displayed in Fig. 7.28, and a picture of the MWL OBFN chip mounted on this setup is shown in Fig. 7.29.

7.9.2 Multiplexer/demultiplexer characterization

In the MWL OBFN run, a test chip was included in the realized mask. This test chip contains a number of test structures, among them an exact replica of the MUX that
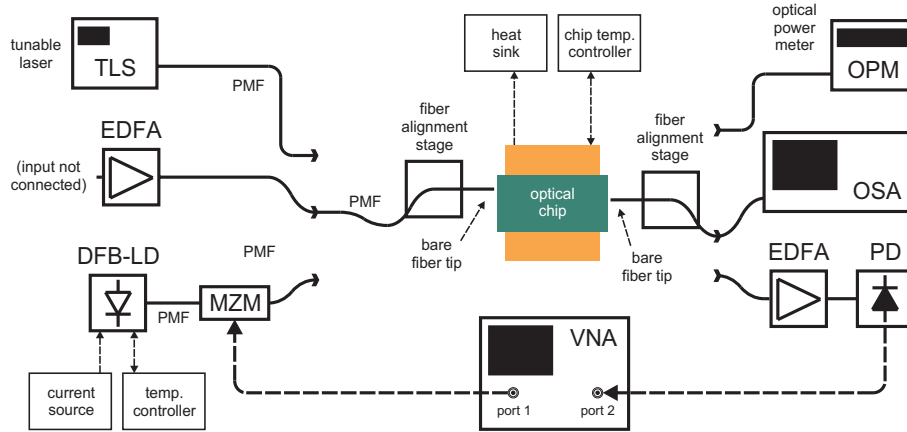
Figure 7.28: Setup employed for the characterization of bare (un-packaged) optical chips

has been included in the final multiwavelength chip[8]. This device includes 2 inputs and 4 outputs which are all accessible by using bare fibers and the alignment setup shown in Fig. 7.28 and Fig. 7.29.

The layout of the chip containing the test structures is shown in Fig. 7.30, and a picture at the microscope is visible in Fig. 7.31.

By connecting the tunable laser source (TLS) to the input of the optical chip, and the power meter at one of the outputs, it is possible to measure the optical transmission of the selected input-output path with respect to wavelength, this can be done by scanning the wavelength of the laser and measuring the optical power impinging on the optical power meter. In the case of the DEMUX, the TLS was connected to the DEMUX input in the left of Fig. 7.30, and the output bare fiber has been aligned sequentially to each of the outputs.

As seen in Fig. 7.10, the DEMUX is composed of two sections: one consisting of an AMZI with 200 GHz FSR, whose output are connected to the inputs of two AMZI with 400 GHz FSR. Tunable voltages were applied to the heaters that control the phase shifters on the branches of the three AMZIs which form the DEMUX, as visible in Fig. 7.31. (*i*) first, the 400 GHz AMZIs are tuned, taking advantage of the test ports on the chip visible in Fig. 7.30; (*ii*) then, the 200 GHz is tuned. This procedure allowed a fine tuning of the frequency response of the complete 1×4 DEMUX and a good matching with the desired response. The measurement results are shown in Fig. 7.32, in comparison with the simulated responses of each DEMUX channel.

From the measurement it can be observed that the positions of the passbands

---

[8]The MUX and DEMUX have exactly the same architecture, the only difference being that the inputs of the DEMUX are the outputs of the MUX and vice versa. Thus each can implement both functionalities. From now on, we will call the tested device DEMUX.
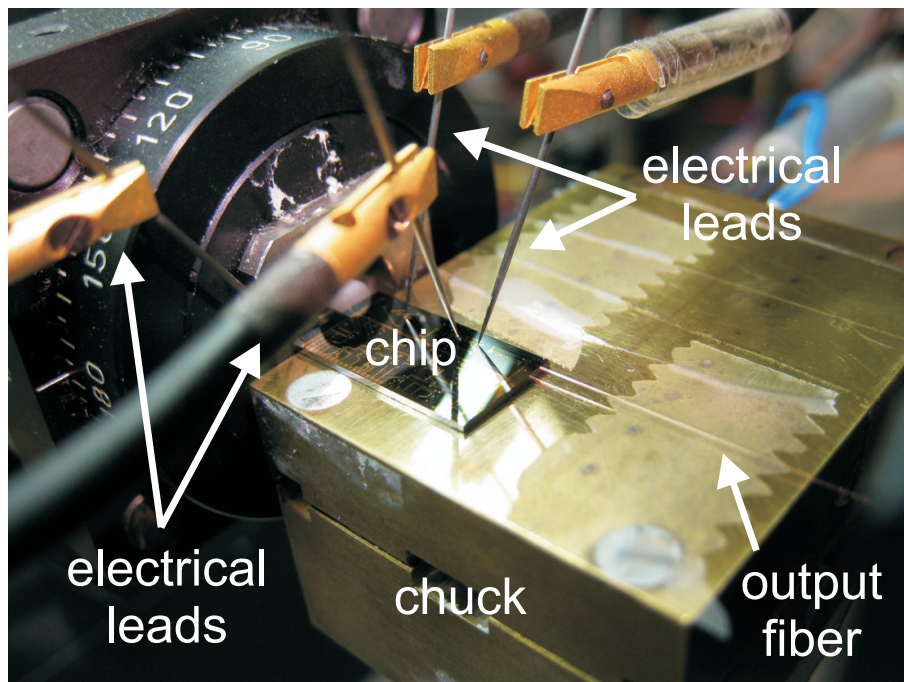
Figure 7.29: Example of an optical chip on the bare fiber alignment setup. The chuck (providing support and heat sink), the tungsten leads (for the electrical connections) and one bare fiber (for the optical connection) are also visible.
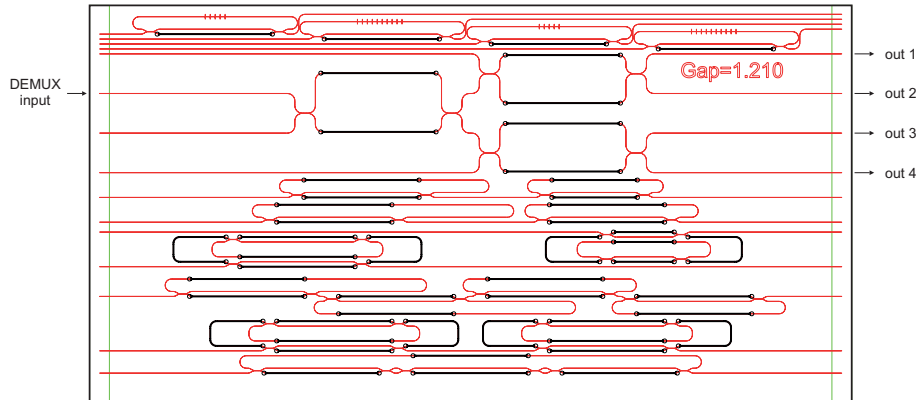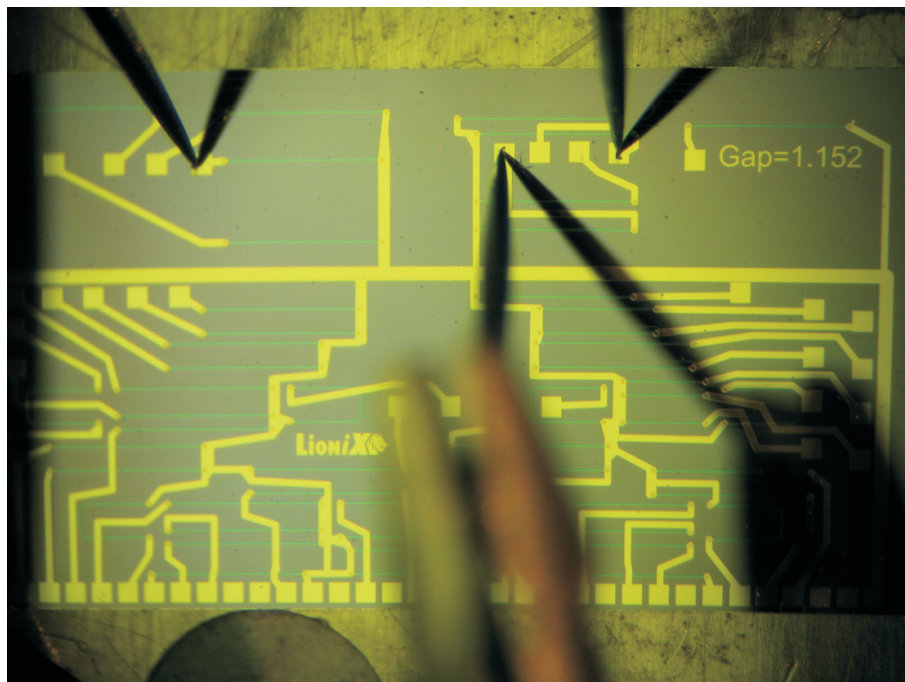
Figure 7.30: Layout of the optical chip containing the test structures for the MWL
OBFN. The input and the outputs of the DEMUX employed in the char-
acterization are indicated.

and of the stopbands are matching very well with the simulated ones, for all of the
four channels. This is partcularly evident by looking at the frequency position of
the zeroes of transmission with respect to the simulated response. Nonetheless, as
expected, the analysis of the zeroes of transmission shows as well that the depth
of the zeroes is not equal across all the DEMUX channels. Specifically, when input
1 of the DEMUX is used, as in this case, channels 3 and 4 which are connected to
the input via the *cross* port of the input AMZI, show a similar performance, both
having a high suppression in their stopbands. On the contrary, channels 1 and 2
suffer a lower suppression in stopband, a fact which is particularly visible for chan-
nel 2, being this directly connected to the DEMUX input via the bar port of both
the first-stage and of the second-stage AMZIs. This translates into a non-perfect
suppression of the undesired sidebands, which in the worst case (for port 2) can be
as low as 13.58 dB. This non-ideal suppression is due to the fact that the directional
couplers employed in the design have slight variations with respect to their perfect
50:50 splitting ratio; this, in turn, creates an unbalance in the routing of the optical
power between the bar and the cross ports, making impossible to route all the op-
tical power from the input to the cross port, thus leaving a residual optical power in
the bar port.

It is also important to note that the measured traces in Fig. 7.32 have been scaled
to match the same maximum transmission. In fact, the maximum transmission
varies across the channels, being highest for the bar-bar port 2, and lowest for the
cross-cross port 4. This can again be attributed to the non perfectly balanced split-
ting ratio in the directional couplers, which results in a non-perfect out of band
isolation by the AMZI. Nonetheless, the residual power unbalance can be compen-
sated for by properly adjusting the transmission of the tunable multiplexer in the
following vertical beamforming stage of the MWL OBFN, visible in Fig. 7.14.

Figure 7.31: Photograph of the optical chip containing the test structures for the MWL OBFN, as visible at the optical microscope. The needles visible are used to draw current through the heaters for tuning the responses of the optical structures.
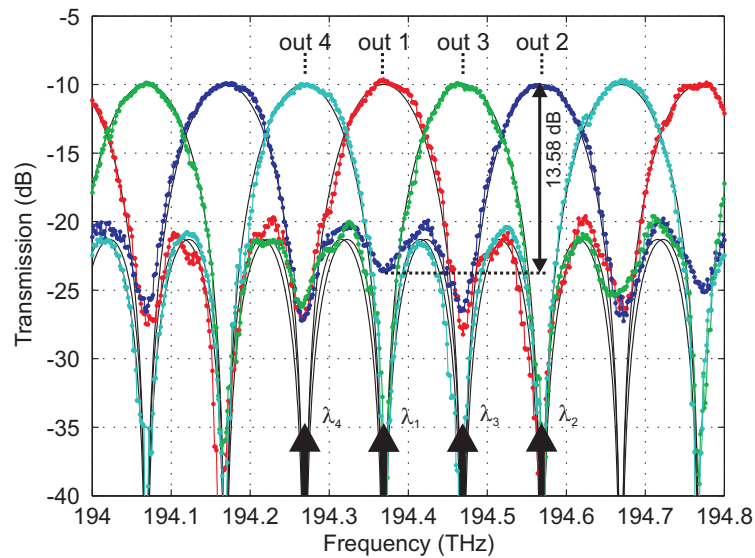
Figure 7.32: Measured (dotted lines) and simulated (solid lines) optical transmission of the DEMUX channels 1, 2, 3 and 4

Fig. 7.33 shows the DEMUX response over a wider frequency band. The transmission characteristic keeps a high degree of accuracy over a large bandwidth, making possible to accommodate wavelengths at different central frequencies; this is also a proof that the fabrication procedure is sufficiently accurate and the proposed multi-wavelength approach could be extended to a much larger number of wavelengths.

The FSR of the DEMUX can be measured and appears to be equal to 402.3 GHz ($\approx$ 400 GHz by design. Percentage variation: $\approx 0.575\%$).

7.10 Demonstration of Basic Functionalities

The main target of the test described in this section is the demonstration of the basic functionality of the MWL-OBFN, that is, the capability of implementing the functions of selectively delaying and combining RF signals carried by different optical wavelengths. For that purpose we designed and realized a set of tests on a subsection of the MWL-OBFN chip. In particular, the aim is to:

- create two IM signals with different optical carrier frequencies, spaced of approx. 200 GHz

- route the two IM signals to a single input of the MWL-OBFN
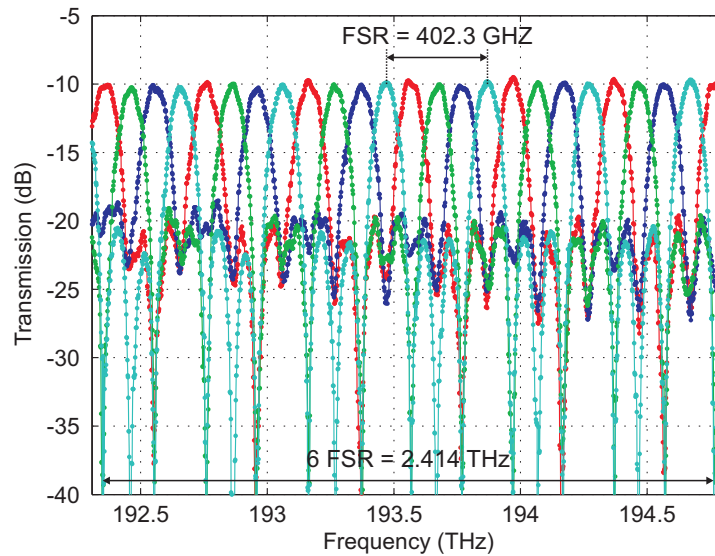
Figure 7.33: Measured (dotted line) and simulated (solid line) optical transmission of the DEMUX channels 1, 2, 3 and 4

- de-multiplex the two signals to separate paths on the chip

- show the *group delay* applied selectively to only one of the two signals

- show the *multiplexing (combining)* of the two signals

For this demonstration, the simplest structure required consists of a 1×2 DE-MUX, whose outputs are connected to two separate waveguides, containing independently tunable delay sections, being then combined by a MUX. This structure is schematically represented in Fig. 7.34.

7.10.1   Modifications to the alignment setup

For purpose of the demonstration described before, we consider a subsection of the MWL-OBFN shown in Fig. 7.25(a). This is the simplest structure available on-chip that contains the basic components required for the test. Such structure can be accessed by two test ports, which have been added by design for those type of tests and have been made available at the output facet of the chip. The proposed test requires transmission measurements, thus both ports have to be accessible simultaneously. Nonetheless, the measurement setup shown in Fig. 7.28 and Fig. 7.29 allows to access only one port per facet at a time. The setup has been modified for this specific test by modifying the alignment stage at the output facet of the chip,
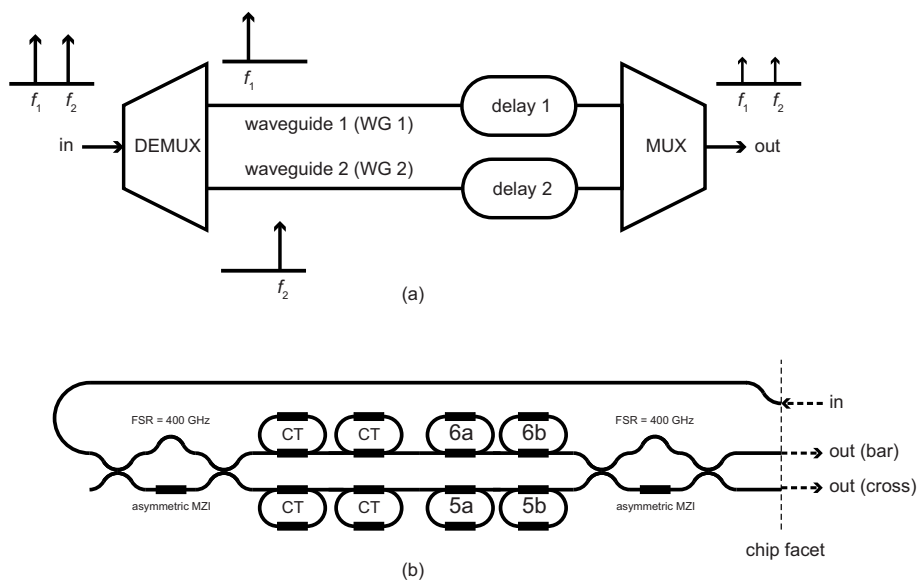
Figure 7.34: Schematic of the portion of the MWL-OBFN used for the functionality tests: 1×2 DEMUX, cascaded to two separate waveguides (including separate tunable delay sections), combined by a MUX (a). Corresponding schematic of the selected section on the MWL-OBFN chip (b).

by replacing the single bare fiber with a fiber array unit from OZ Optics Ltd. This FAU includes 4 PM fibers, whose cores are horizontally spaced 125 μm, which corresponds to the pitch separation between the output waveguides on the chip. In this way, a single FAU could be used to access as many as four adjacent ports of the output facet simultaneously. Since the desired test ports are ports 1 and 2, the 4-fibers FAU is sufficient for the desired test. For future tests that may require to access arbitrary test ports, the FAU could simply be replaced with a larger one (i.e. including a larger number of fiber pigtails). The FAU has been mounted on a "goniometer", which in turn has been mounted on the three-axes alignment stage. The goniometer allows the yaw-movement needed to align the plane of the waveguides (i.e. the plane of the chip) with the plane of the fiber pigtails of the FAU. In this way it has been possible to maximize the optical transmission between the test ports, acting both on the xyz alignment stage controls and on the yaw angle of the FAU. Fig. 7.35 shows a picture of the alignment stage including the goniometer and the FAU.

7.10.2   Optical characterization of the cascade of two AMZIs

The first step towards the functionality demonstration of the MWL-OBFN is the optical input-output characterization of the device under test, that is, the chip section in Fig. 7.34(a). In particular, we are interested in the optical response of the bar port, as in Fig. 7.34(b). Ideally, when the free spectral ranges of the individual AMZIs are equal, and when the connecting waveguides have equal length, the cascade of the two AMZIs has a response which is independent of the optical frequency. The simulated bar and cross port responses are shown in Fig. 7.37 and in Fig. 7.38, for different values of the phase shift applied to the longer arm of the AMZI 1. Thanks to the symmetry of the structure, applying an equal phase shift to AMZI 2 instead of to AMZI 1 would produce exactly the same effect.
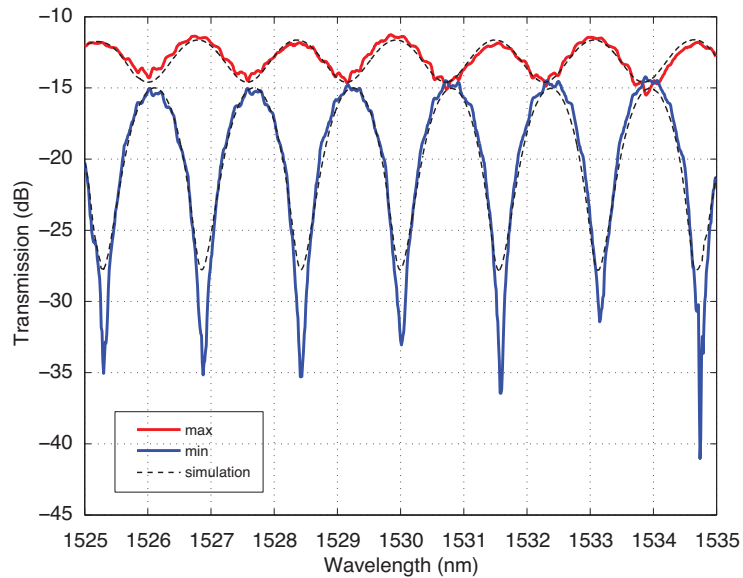
The LabView simulations of the structure under test reported in Fig. 7.39 and in Fig. 7.40 show also that there is a deviation from the ideal response as soon as the directional couplers (DC) become non ideal (i.e. have a splitting ratio not exactly equal to 0.5) or when there is an amplitude unbalance between the two waveguides connecting the DEMUX and the MUX (waveguide 1 and waveguide 2, indicated respectively as WG 1 and WG 2 in the following). In particular, a ripple is introduced in the amplitude response as soon as there is an amplitude transfer unbalance between the two arms (waveguide 1 and waveguide 2). The ripple changes in depth when changing the phase shift of either arm of AMZI 1. In Fig. 7.36, the measured bar response is shown for two different voltages applied to the phase shifter on the longer arm of AMZI 1. The ripple variation predicted by the simulations is clearly visible.

For the sake of this experiment, our scope is to make sure that the frequencies of two optical carriers, spaced 125 GHz apart, are chosen in such a way that one of them propagates in the upper arm (WG 1) and the other propagates on the lower arm (WG 2). Unfortunately, we do not have access to the separate waveguides, thus a method has to be found to identify the transfer of each path by only measuring
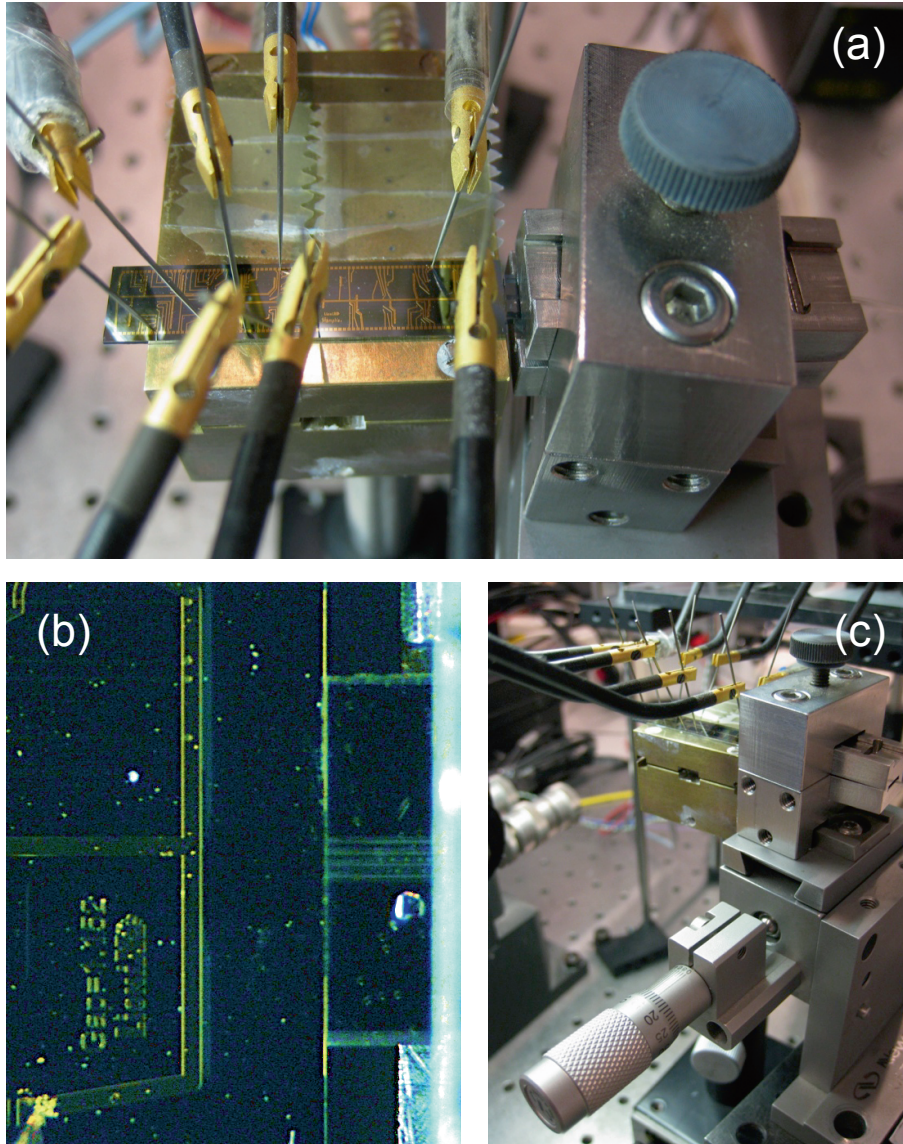
Figure 7.35: Alignment stage including the FAU used to access multiple waveguide ports on the right facet of the MWL-OBFN chip in Fig. 7.25(a). The FAU containing 4 fiber pigtails has been aligned to the optical waveguides (b). Note the presence of the goniometer used to align the plane of the fiber array to the plane of the chip (c).

the bar response of the complete structure under test. It is not possible to determine which bands propagate to the upper and to the lower arm by simply analyzing the shape of the response without prior knowledge on the loss of each branch (WG 1 and WG 2). In fact, when the proper phase condition is satisfied, the power in the two waveguide arms ideally combine constructively to produce the desired all-pass response at the bar output. Thus, any amplitude unbalance between the arms (e.g. due to a non perfect DC splitting ratio, or to different losses in the waveguides) would produce a non-uniform response at the bar port. As expected, this is confirmed from the simulations, where it appears that the maxima of the overall transfer function can be corresponding either to the maxima of the bar arm (WG 1), or to the maxima of the cross arm (WG 2), dependently on whether the attenuation is higher in the lower or in the higher arm, respectively. Fig. 7.37 through Fig. 7.40 show the simulation results to graphically represent this phenomenon.


Figure 7.36: Measured bar responses of the structure under test shown in Fig. 7.34, compared to the simulated responses obtained by uniform excitation at the input, for different values of phase shift applied to the upper arm of AMZI1.
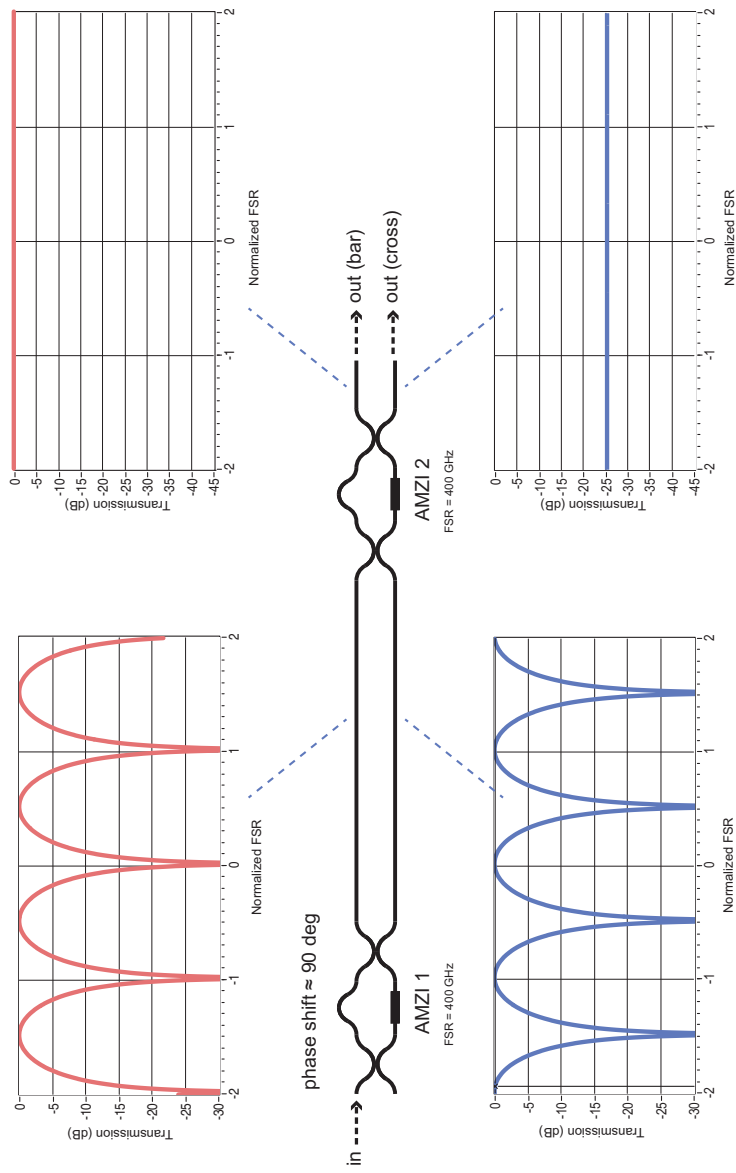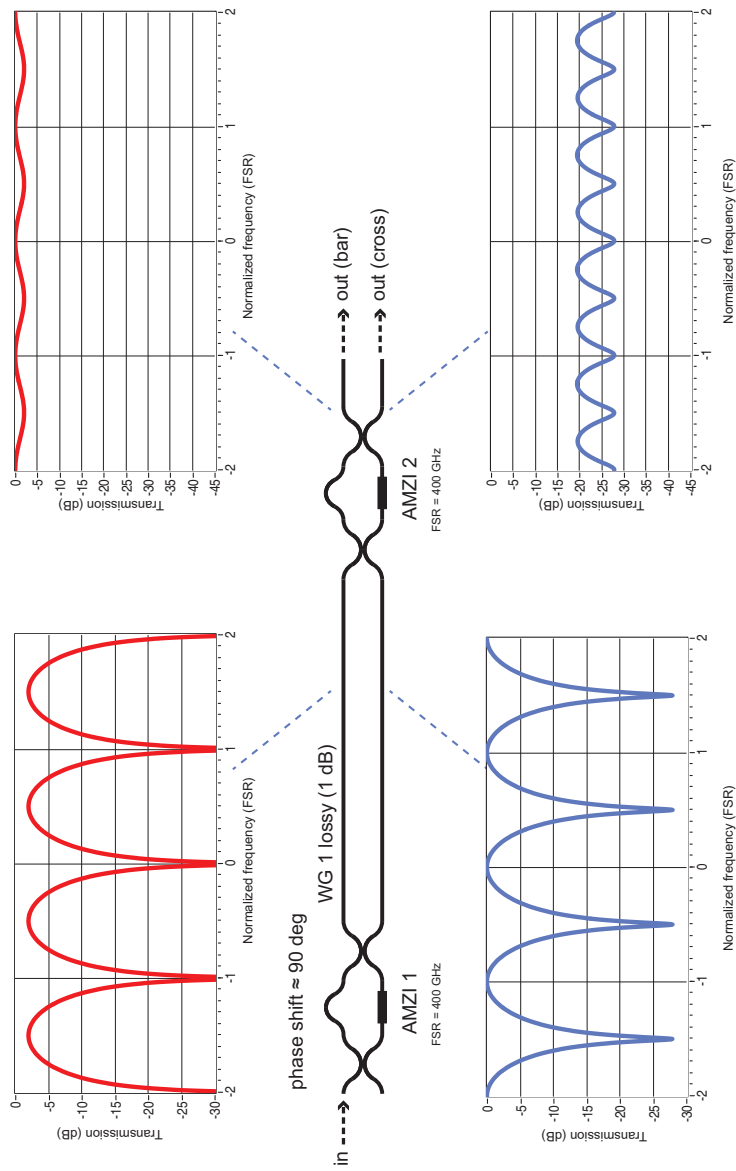
Figure 7.37: Simulated response of the structure under test obtained by uniform excitation at the input. The additional phase shift applied to the upper arm of AMZI1 is approximately 90 degrees.
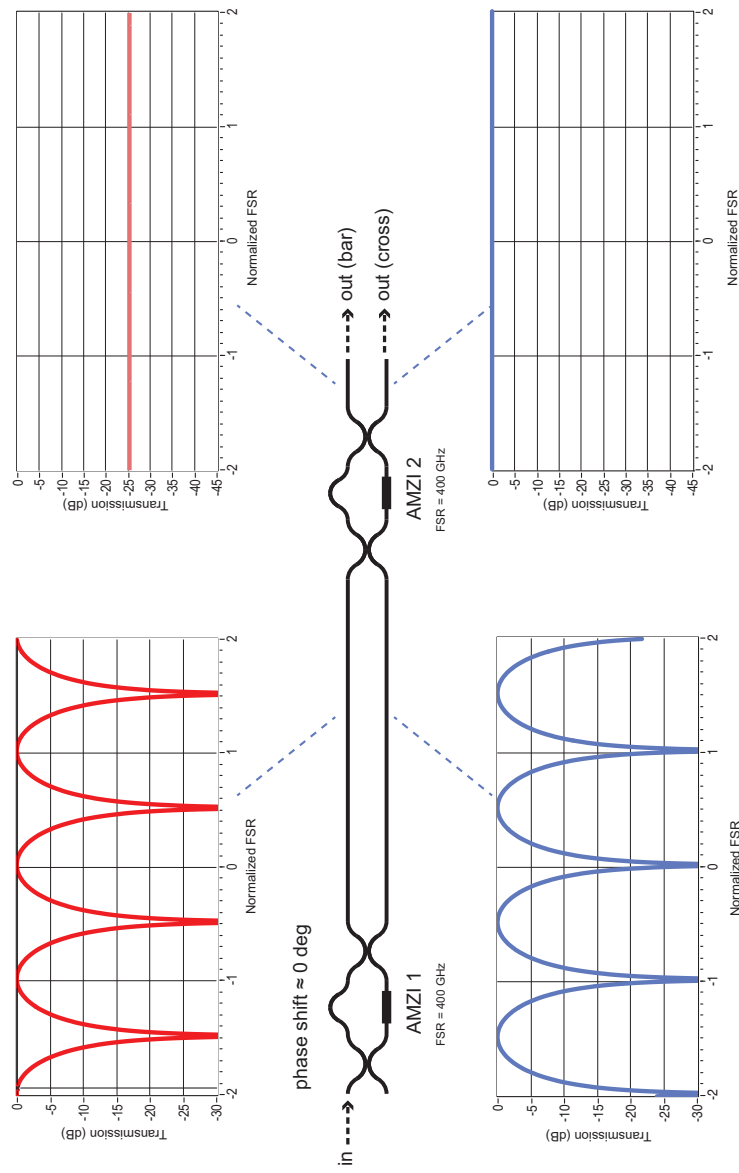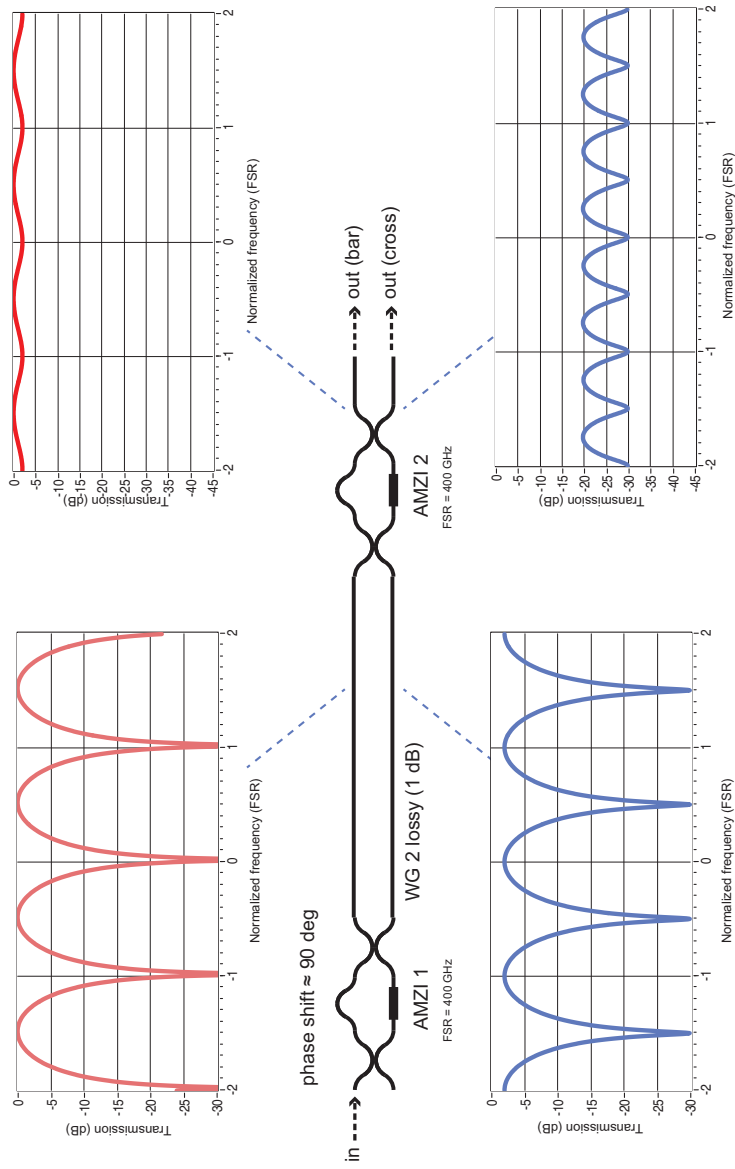
Figure 7.38: Simulated response of the structure under test obtained by uniform excitation at the input. The additional phase shift applied to the upper arm of AMZI1 is approximately 0 degrees.

Figure 7.39: Simulated response of the structure under test obtained by uniform excitation at the input. The additional phase shift applied to the upper arm of AMZI1 equals approximately 90 degrees. WG 1 introduces 1 dB optical loss. The DCs in the AMZIs have a coupling factor of 0.48 instead of the ideal 0.5 value. Note that the *maxima* of the bar response of the AMZI1-AMZI2 cascade correspond to the *minima* of the AMZI1 response.

Figure 7.40: Simulated response of the structure under test obtained by uniform excitation at the input. The additional phase shift applied to the upper arm of AMZI1 equals approximately 90 degrees. WG 2 introduces 1 dB optical loss. The DCs in the AMZIs have a coupling factor of 0.48 instead of the ideal 0.5 value. Note that the *maxima* of the bar response of the AMZI1-AMZI2 cascade correspond also to the *maxima* of the AMZI1 response.
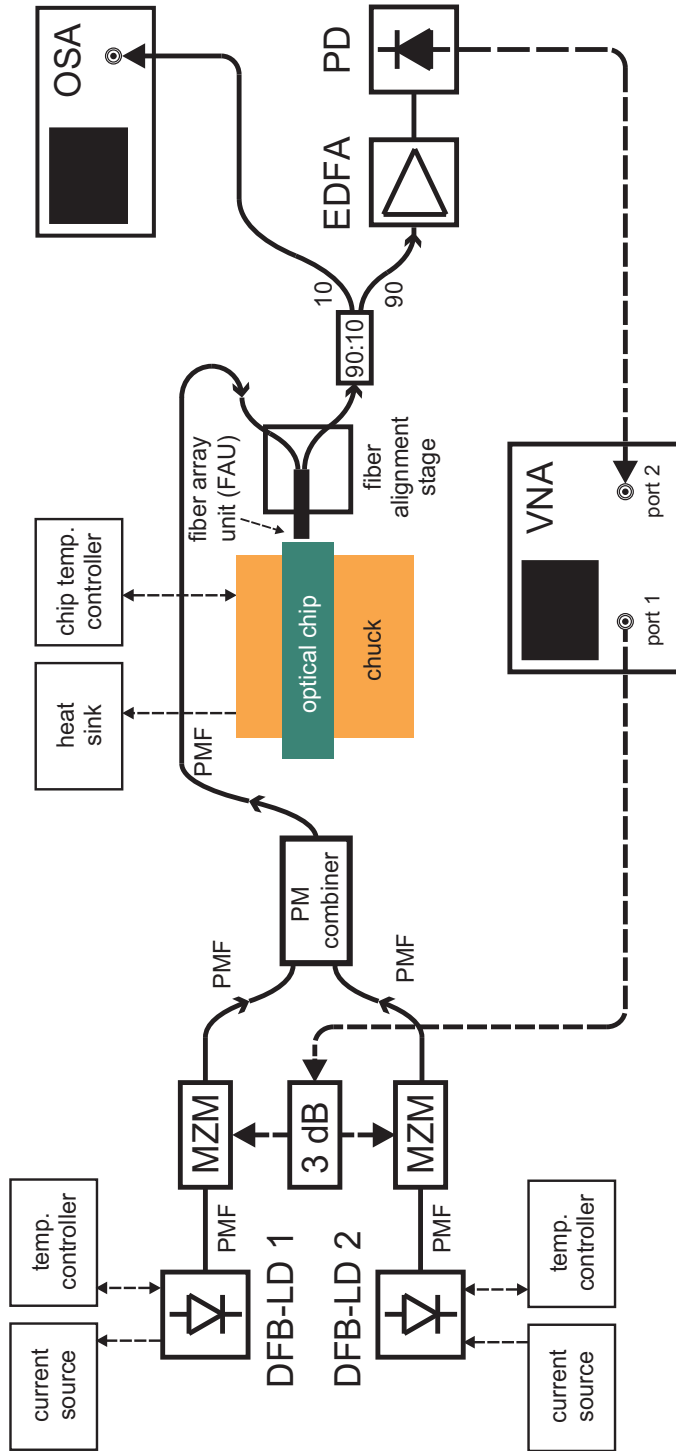
Figure 7.41: Setup employed for the basic functionality demonstration of the MWL-OBFN

7.10.3   Identification of the paths and laser wavelength selection

In order to perform the delaying and combining tests mentioned in the previous sections, it is necessary to know which wavelength inserted at the input of the test section in Fig. 7.34 will be propagated through the upper branch (WG 1) and which ones to the lower branch (WG 2). As demonstrated in the previous section, it is not possible to know the bar and cross responses of AMZI 1 only from the observation of the transfer function of the cascade AMZI 1 - AMZI 2, without prior knowledge on the attenuation of the two arms. For this reason, a different technique has to be introduced for the scope to identify which wavelengths propagate in the upper branch (WG 1) and which ones in the lower branch (WG 2).

The idea is to employ the tunable ORRs present in each branch to identify the bar and cross responses of AMZI 1. In fact, by changing the coupling of the ORRs to the waveguides, their respective quality factor will change, thus affecting the transfer function of the corresponding branch. This change can be observed by measuring the bar response of the complete test section, provided that the instrument used has sufficient spectral resolution to identify at least large changes in the ORRs responses. The OSA employed in the tests has a minimum resolution bandwidth of 0.1 nm (approx. 12.5 GHz) which allows to observe the ORRs responses (with a FSR of 25 GHz) as a ripple overlapped to the response of the complete structure.

Fig. 7.42 shows the bar transfer obtained when all ORRs are tuned in such a way to minimize their resonance (referred to as "ORR off"), overlapped with the transfer obtained when only one of the carrier tuning ORRs (CT) from the lower branch (WG 2) is tuned to an increased quality factor ("ORR on"). It is possible to identify two regions: one in which the ORR resonance peaks are visible (only in the form of an increased ripple, due to the limited resolution bandwidth of the OSA in use) and one in which the ORR does not sensibly affect the response (central area in figure). This gives an indirect but effective method to identify the frequency range which propagates mostly through the lower branch, being the one in which the difference between the case "ORR off" and "ORR on" is more visible. It appears that the minimum transmission in this case corresponds to the propagation through the upper branch (WG 1), around 1550.5 nm, while the maxima correspond to the lower branch (WG 2), as in the case shown in Fig. 7.39. This measurement was obtained by letting the EM4 DFB laser (DFB-LD 1 in Fig. 7.41) sweep slowly over the frequency band of interest, while employing the max-hold function of the OSA.

7.10.4   Delaying and combining demonstration

After the analysis performed in the previous section, it is now possible to choose two separate optical carrier frequencies and proceed with the demonstration of the basic MWL-OBFN functionalities. The wavelengths shall be chosen in such a way that they can be demultiplexed by AMZI1, propagate in separate paths and be recombined by AMZI2 towards the bar output port (Fig. 7.34). According to the analysis in Fig. 7.42, a possible choice is $\lambda_1 = 1550.42$ nm (≈ 193.36 THz) and $\lambda_2 = 1551.5$ nm (≈ 193.23 THz). The frequency spacing is ≈ 125 GHz.

In order to realize our tests, the setup in Fig. 7.41 has been used. Two DFB lasers
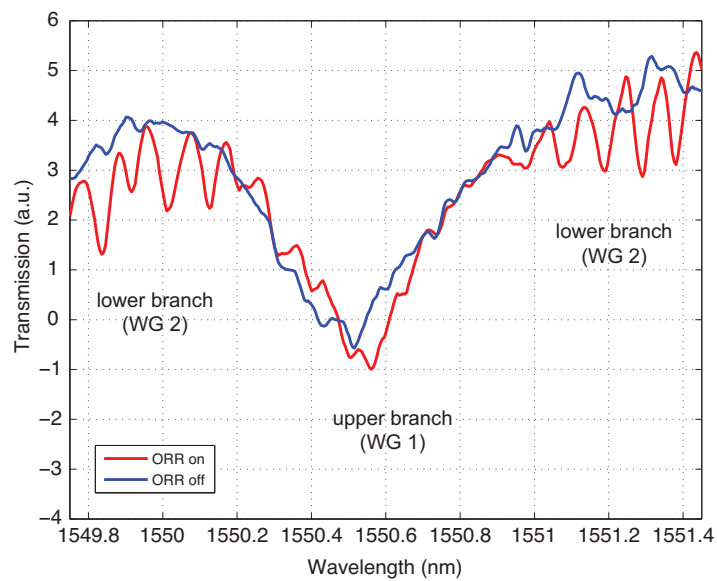
Figure 7.42: Bar transfer of the cascade AMZI1-AMZI2, obtained when all ORRs are tuned to minimum resonance, compared with the same transfer obtained when one of the carrier tuning ORRs (CT) from the lower branch (WG 2) is tuned to an increased quality factor. It is possible to observe that the ripple due to the change in the ORR response appears only at the sides of the figure, allowing to estimate which frequencies propagate in the upper and in the lower branch where the employed ORR is present.

(DFB-LD 1 and DFB-LD 2) generate the optical carriers at frequencies f_1 and f_2. A 3-dB RF splitter is used to divide the RF signal generated by port 1 of the network analyzer (VNA) and feed it to two Mach-Zehnder modulators (MZM) biased in quadrature. The two IM optical signals are combined using a polarization maintaining (PM) combiner. The combined signal is fed to the optical chip using the fiber array unit (FAU) described previously. Note that the use of PM components in the whole signal path preceding the chip is crucial to ensure the desired behaviour for the waveguides, which is dependent on the light polarization. The chip subsection employed for the test is the one shown in Fig. 7.34. At the chip output, a 90:10 optical splitter is used to route part of the signal to an optical spectrum analyzer (OSA), employed to measure the optical carrier frequencies and to compare them with the bar port characteristic in Fig. 7.42, previously stored in memory.

Individual channels

Fig. 7.43 shows the s_{21} parameter, measured over the bandwidth 1-10 GHz, of the bar response of the MWL-OBFN system under test shown in Fig. 7.41, when only one laser at a time is connected to the PM combiner inputs. The RF powers have been equalized while keeping the optical frequencies at the desired values, by tuning both the drive current and the operating temperature of each DFB laser. Note the gain roll-off with frequency, due to the electro-optical response of the MZM and of the PD employed in conjunction with the losses of the RF connectors, as discussed in Chapter 5. The delay characteristics show a delay difference among the paths of approximately 38.1 ps.

Channels combining

When both lasers are connected to the PM combiner, the RF signals which have been separated in the 3-dB RF splitter in Fig. 7.41 are recombined optically on chip. The RF magnitude response shows a corresponding increase of 6 dB with respect to the individual channels (Fig. 7.44). In fact the two electrical signals, which are carried separately in the optical domain by the different wavelengths, are converted back to the electrical domain at the photodetector. At the PD output, the RF signals sum in phase, producing a total electrical signal with double amplitude, thus 4 times the RF instantaneous power (6 dB). This result demonstrates the combining capability of the proposed MWL-OBFN.

It is important to note that, in Fig. 7.44, the power of the combined response decreases faster with frequency than the ones of the individual channels, producing only a 3 dB increase around 7 GHz and no increase around 10 GHz. This can be easily explained by considering that the conclusion of coherent RF combining drawn before is valid only as long as the frequency is sufficiently low to consider two RF signals approximately in phase. In fact, as visible from the phase responses in Fig. 7.43, the two waveforms have a small delay difference of approximately 38 ps. This limited amount of delay produces a phase shift between the two detected RF signals which is negligible below few GHz but, as the frequency increases, the delay starts to play a significant role (i.e. to produce a substantial phase shift between
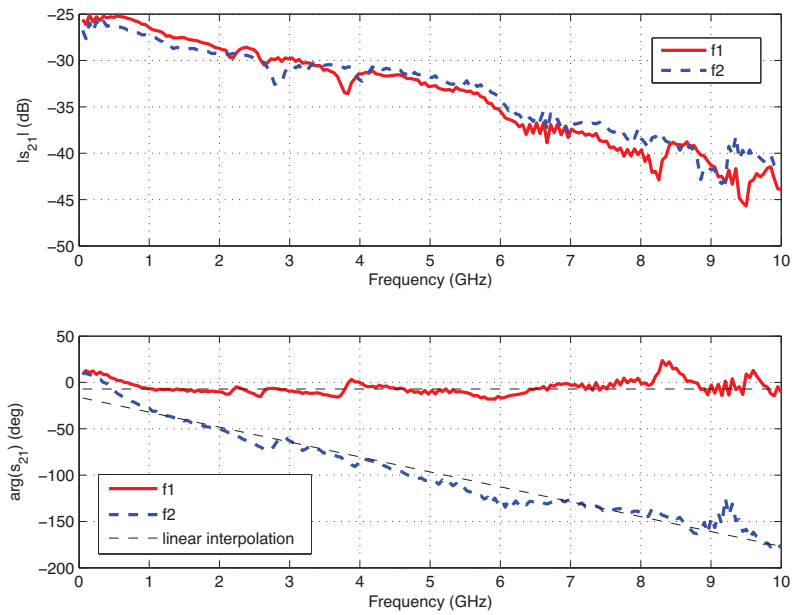
Figure 7.43: RF magnitude and phase response of channel 1 (f_1) and channel 2 (f_2)
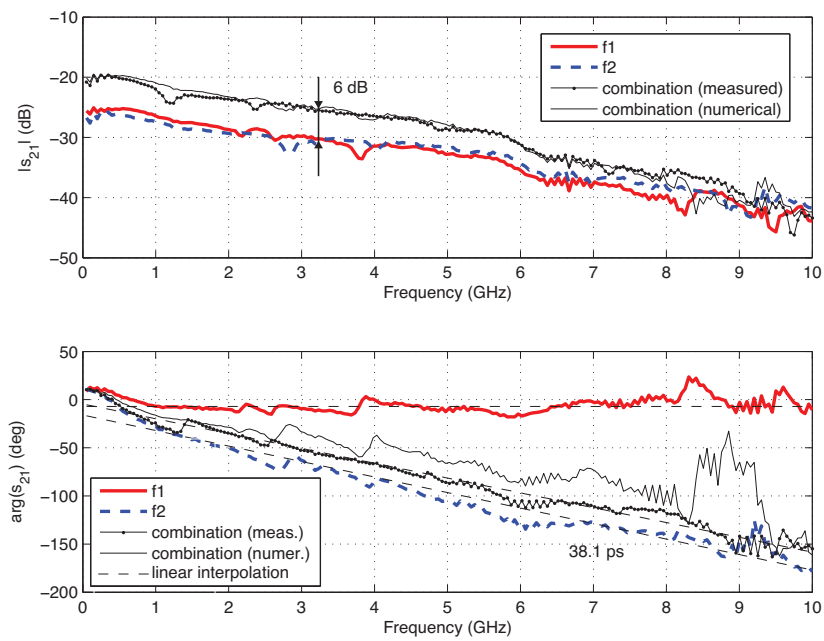
Figure 7.44: RF magnitude and phase response of channel 1 (f_1), channel 2 (f_2), and of the combination (multiplexing) of channels 1 and 2

the RF signals) until, around 13 GHz, the two waves are completely out of phase. If we could extend the RF sweep, we would see that this phenomenon produces an interference pattern as the one seen for the microwave photonic filter described in Chapter 6. In this case, the free spectral range is equal to $1/(38.1\text{ ps}) = 26.247$ GHz.

Another interesting phenomenon worth noticing is the phase response of the combined RF signal. At a first thought, it would be expected that the RF phase response should show a delay which is the average between the delays of the individual RF signals. In practice, the phase response is sensibly closer to the delay of the RF signal carried by the optical frequency f_2, and tends to oscillate in frequency compared to the linear interpolant. This can be easily explained by considering that the RF magnitude transfer is not exactly the same for the two channels (i.e., the RF powers are not perfectly balanced), with a stronger RF power for channel f_2 especially in the frequency range between 3 and 8.5 GHz, thus producing a phase response curve closer to the one of the channel with the strongest power.

For comparison, Fig. 7.44 includes the amplitude and phase responses obtained by numerically combining the two measured responses for f_1 and f_2. The amplitude response matches closely with the measured amplitude response obtained combining the two channels. The phase response, instead, shows a sensible deviation compared to the measured one. This can be explained by considering that the responses of the individual channels and the response of the combined channels were obtained at three different times, and not simultaneously. In the measurement setup, in fact, the individual phase responses are obtained by un-mating one of the two fibers at a time from the setup in Fig. 7.28. During the experiments, a sensible instability was observed in the power of the individual channels, limiting the repeatibility of the experiment. It must be kept in mind that the phase is very sensitive to any amplitude unbalance. For this reason, it is likely that the powers of the individual channels might have changed during the mating-unmating procedure, thus creating an amplitude unbalance which affected the phase response, explaining the deviation from the expected response.

Selective delay

After the demonstration of the combining capability of the MWL-OBFN, we show the capability to generate selective delay to only one of the IM optical signals. For this scope, the ORRs of WG 2 in Fig. 7.34 labeled as "6a" and "6b" have been employed to provide broadband delay to the IM signal at frequency f_2. Fig. 7.45 shows the RF phase response obtained when only DFB-LD 2 is connected to the chip. The phase response obtained when DFB-LD 1 is connected stays substantially unchanged. This demonstrates the capability of the chip to provide broadband delay, selectively to the RF signal modulated on the optical carrier at frequency f_2. The delay is continuously tunable from 0 ps up to approximately 139.7 ps over an instantaneous bandwidth of 10 GHz. Note the attenuation on the RF amplitude response due to the application of the delay, which can be compensated by properly adjusting the optical power of the corresponding laser.
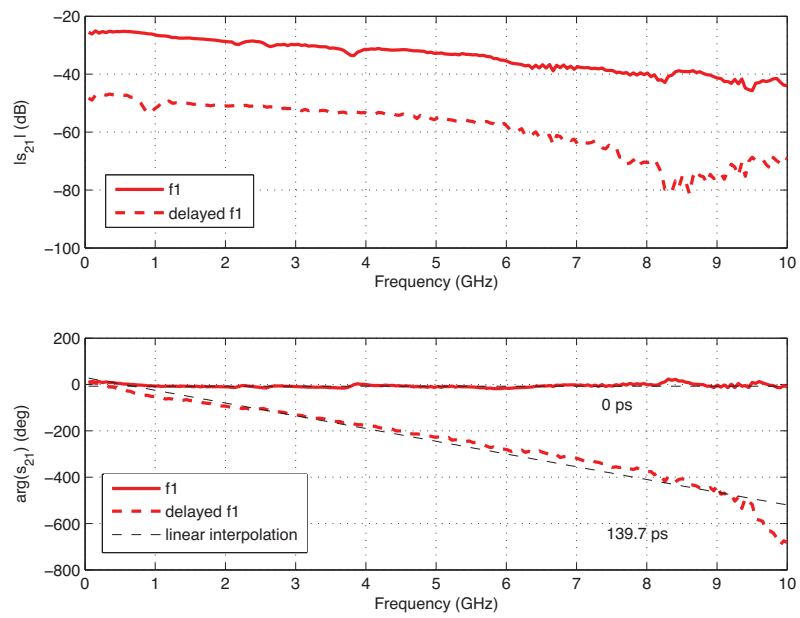
Figure 7.45: RF magnitude and phase response of channel 1 (f_1), compared to the response of channel 1 delayed

7.11 Hybrid integration with MWL laser + MZM array

In a different Memphis workpackage, a multi-wavelength transmitter has been realized and is currently being tested. It is based on indium phosphide (InP) technology and features an array of four integrated DFB lasers and four Mach-Zehnder modulators integrated on a single photonic chip [202, 207]. The signal generated by each laser is modulated by an individual MZM and then multiplexed to a single output. A schematic of this photonic integrated circuit (PIC) is shown in Fig. 7.46. This PIC consists of a four-channel filtered-feedback multi-wavelength laser with four Mach-Zehnder modulators The four lasers operate at different wavelengths, 100 GHz-spaced according to the International Telecommunication Union (ITU) grid [208]. The modulator outputs are multiplexed by an arrayed waveguide grating (AWG) to an single output.
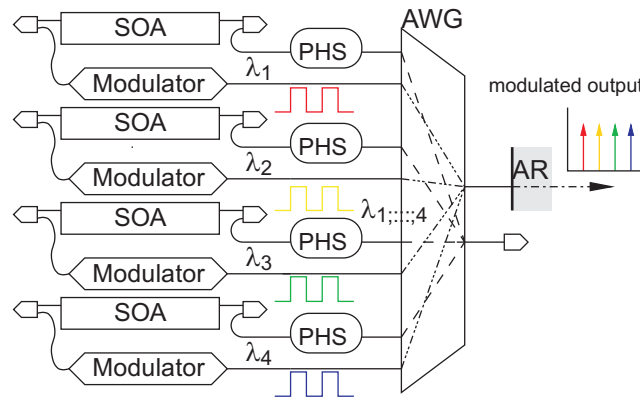
Figure 7.46: Schematic of the MWL transmitter realized in TU/e. SOA: semiconductor optical amplifier; PHS: phase shifter; AR: anti-reflection coating (courtesy of Jing Zhao).
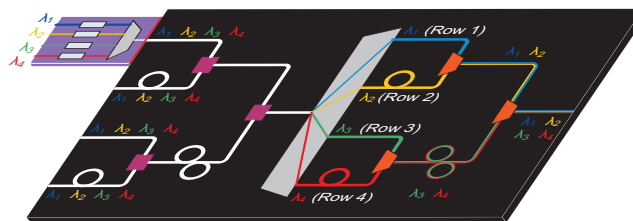
Figure 7.47: Artistic view of the butt coupling between the MWL transmitter and the MWL OBFN

This device can be used to operate as one of the four columns in the functional

schematic shown in Fig. 7.5. In fact, it contains four lasers, four modulators placed in the corresponding optical paths, and a wavelength multiplexer.

The MWL laser chip and the MWL-OBFN chip are going to be integrated via butt-coupling to build the core of the Memphis A2 demonstrator 1. This demonstrator will be used to practically prove the MWL OBFN concept described in this chapter. An artistic view of the butt-coupling between the MWL transmitter and the MWL OBFN is shown in Fig. 7.47.

7.12 OBFN positioning in the system

The schematic in Fig. 7.48 represents a simplified view of the integration of the different components that constitute the signal processing part for the phased array antenna of the Memphis A2 Demonstrator 1 (multiple wavelength OBFN for connected array antenna for radio-astronomy).
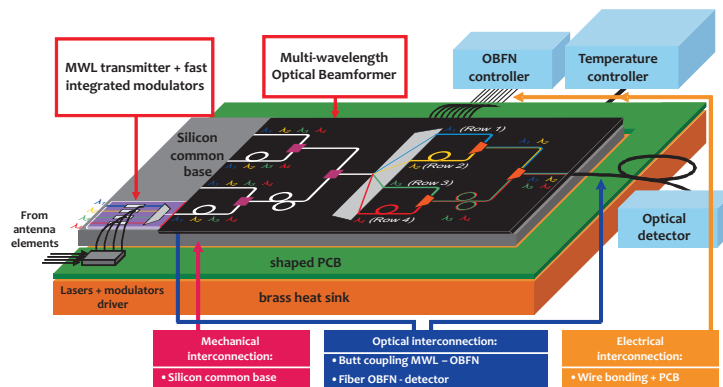
Figure 7.48: Integration schematic for WP A2 demonstrator 1, and OBFN positioning in the system

7.13 Conclusions

A novel idea towards the simplification of an existing OBFN has been proposed. Exploiting the frequency-periodic behaviour of the ORR-based delay units and filters, it is possible to realize a WDM-based multi-signal-path OBFN, thus dramatically reducing system complexity and cost and making possible an integrated realization of a single-chip OBFN for large arrays or multiple-beam applications.

8

Conclusions and directions for further research

8.1 Conclusions

In this thesis we have described the design, implementation, system integration and functional demonstration of integrated optical beamformers for phased array antennas. Our approach pertains to the field of microwave photonics, where photonics technology is employed to assist or replace purely electronic solutions for the realization of a number of signal processing functionalities. In particular, we made use of the integration of photonics and electronics to achieve unprecedented performance for the signal processors that can hardly be provided by electronic solutions alone. In our case, integrated optical waveguides and filters are used to realize a few basic functions, namely signal transport, splitting and combining, multiplexing and demultiplexing, phase shift and time delay. Those basic functions have been combined to realized a complex signal processor to optically control the antenna array, or beamformer, on a single chip.

The result was the demonstration of two novel optical beamformers which demonstrated an instantaneous RF bandwidth up to 8 GHz, with a continuously tunable delay up to approximately 2 ns over 1 GHz bandwidth, a compact layout (16-channels with a total of 40 fully tunable optical ring resonators with an area of 0.7 × 2.2 cm^2), realized on a very low loss substrate (employing TriPleX waveguide technology, which allowed losses of only 0.1 dB/cm with a bending radius as low as 75 μm) and the potential to be produced on large scale with low cost (realized using CMOS compatible fabrication equipment).

We reported the first system integration of an integrated beamformer chip based

on optical ring resonators in a functional demonstrator for radio astronomy applications (Chapter 5), which showed squint-free and seamless beamsteering of 30 degrees over the band from 1 GHz to 1.5 GHz, limited only by the employed antenna characterization setup.

In addition to broadband radio astronomy aperture arrays, another desired application of optical beamsteering is antennas for satellite communications. We recently demonstrated (Chapter 5) that the optical beamformer can be reconfigured to provide squint-free beamsteering over the complete DVB-S band (10.7 GHz to 12.75 GHz) employing a 4-inputs photonic integrated beamformer based on ring resonators.

We showed (Chapter 6) the first demonstration of the delay technique called separate carrier tuning where the optical sideband filter, the delay line and the separate carrier phase tuning unit are integrated on a single chip. We demonstrated a full 360 degree phase shift and a continuous delay tunability up to approximately 400 ps over the band 1 GHz to 2 GHz. The simultaneous functionality of this processor as independently tunable phase shifter and delay line has been demonstrated by implementing a fully reconfigurable, complex-coefficient two tap microwave photonic filter.

Finally, we proposed and experimentally demonstrated a novel, hardware compressive architecture based on on-chip wavelength division multiplexing (WDM), which exploits the frequency-periodic response of optical ring resonators to dramatically reduce the network complexity and, in turn, its area occupation on the wafer (Chapter 7). This allowed a complexity reduction factor of almost 10 for a 16×16 array, and which improves with antenna dimension. This allows to overcome the main limitation of current integrated beamformers, that is, the limited capability to feed very large arrays when using a single chip, and promises the possibility to integrate an unprecedented number of delay channels on a single chip, without need of the complex interconnection of multiple beamformers as shown in Chapter 4. We experimentally demonstrated this concept using a novel device that showed continuously tunable delay generation over the 2-10 GHz bandwidth. This result represents at the same time the record bandwidth (8 GHz) for a complete optical beamformer based on optical ring resonators, and the first integrated beamformer where signals from different antenna elements are processed simultaneously by individual delay lines exploiting the periodic response of ORRs filters. This processor has been implemented in a single chip with the size of 36×8 mm.

8.2   Directions for further research

A number of ideas started to be investigated during the development of this thesis work but could not be brought to the stage of experimental demonstration due to time constraints. Those include:

- *Multibeam applications*. The availability of a set of basic building blocks with proven and repeatable characteristics, realized with low-loss TriPleX waveguide technology from LioniX B.V., allowed us to design complex beamformer

layouts with high performance. A straightforward extension of the capabilities of the processors designed in this thesis is the realization of networks with multiple independent beam ports for simultaneous multi-beam operation, where individual beams can be independently reconfigured. This type of solutions are particularly appealing for spaceborne applications [11,209] where compact, lightweight, broadband and reconfigurable multibeam beamformers operating at high RF frequency bands (K_u-band and K_a-band) are desired for modern communication satellite payloads which pose stringent requirements in terms of performance, size and weight.

- *Monolithic or hybrid integration of active and passive functionalities on a single chip.* Both monolithic and heterogeneous integration have been largely investigated especially in the field of high-speed data communications and optical interconnects, and are starting to be employed in the field of microwave photonics and promise to have a bright future. In fact, thanks to the possibility to integrate the electrical-to-optical and the optical-to-electrical conversion on the same platform together with the passive signal processors will allow, at the same time, to boost the system performance, a huge reduction in the costs of the complete system (which mainly comes from the fact that current MWP systems are realized by integration of discrete off-the-shelf optical components) and improve the system stability and robustness through elimination of the optical fiber interconnections. In addition to that, current multi-project wafer (MPW) runs from all the major foundries that allow to share the fabrication costs are quickly broadening the accessibility of state-of-the-art integrated photonic functionalities for many research customers, also at university level. This is expected to lead to a large increase of the microwave photonic players that will make use of active and passive integrated functionalities on chip to boost the system performance, finally allowing microwave photonic solutions to reach and spread in commercial market applications.

- *Phase modulated beamformers.* Several authors have identified the main limitation of optical beamformers, and more in general of microwave photonics signal processors, in their limited system performance, especially in terms of dynamic range (Chapter 5). Recent works have demonstrated how phase modulation techniques can sensibly improve the dynamic range of analog photonic links [22]. Several authors have proposed either coherent receivers [12] or frequency discriminators [22] based on linear optical filters on a single chip, demonstrating analog optical links with improved dynamic range. In [139], a frequency discriminator and a balanced photodetector have even been integrated in a single chip. Experts in the field have shown how the performance improvement attainable with optimized phase modulated links jointly with hybrid integration of active and passive functionalities can be the answer to the need of microwave photonic processors that equal or surpass the system performance of traditional microwave solutions.

- *Electro-optical tuning.* An important issue in the beamformers presented in

this work is the total power consumption due to thermo-optical tuning, and the speed at which this grows when increasing the beamformer complexity. Besides the total peak power consumption, which can easily reach tens of watts when operating a 40-ORRs beamformer, another important issue is the heat dissipation and the consequent thermal crosstalk. Now that the waveguide technology allows to keep bending losses negligible down to approx. 75 μm of bending radius, the main limiting factor towards footprint reduction becomes the thermal crosstalk between different heaters. In fact, the practical difficulty to remove heat from the chip quickly and effectively in order to maintain a stable average temperature tends to become the main limiting factor in the dimension reduction. At the current state, it is not possible to place heaters closer than a few hundred microns without creating important thermal crosstalk issues. Having an effective electro-optical tuning technology would allow, at the same time, to reduce the power consumption of a factor of ~80k, thus requiring much less power in the temperature stabilization unit, and to realize tuning elements much closer to each other while keeping negligible crosstalk.

- *Use of nonlinear optical phenomena for microwave photonic signal processing.* A particularly recent and expanding interest has been shown by experts in the field towards the use of well-established nonlinear optics effects for RF signal processing. Effects as cross-phase modulation or four-wave mixing [40] are starting to be employed to demonstrate microwave photonic signal processing functionalities in an integrated optical form, like microwave photonic filtering and microwave photonic links, exploiting the high third-order optical nonlinearities shown by silicon-based substrates. We expect that those phenomena will be applied to optical beamforming and MWP links too.

Bibliography

[1] R. Buderi, *The invention that changed the world.* Simon & Schuster, 1996.

[2] R. J. Mailloux, *Phased array antenna handbook.* Artech House, Boston, MA, 2005.

[3] J. D. Kraus, *Antennas.* McGraw-Hill Education, 1988.

[4] R. E. Collin, *Antennas and radiowave propagation.* McGraw-Hill, New York, 1985.

[5] D. Parker and D. C. Zimmermann, "Phased arrays-part 1: theory and architectures," *IEEE Transactions on Microwave Theory and Techniques,* vol. 50, no. 3, pp. 678–687, 2002.

[6] D. Parker and D. C. Zimmermann, "Phased arrays-part 2: implementations, applications, and future trends," *IEEE Transactions on Microwave Theory and Techniques,* vol. 50, no. 3, pp. 688–698, 2002.

[7] S. K. Garakoui, E. A. Klumperink, B. Nauta, and F. van Vliet, "A 1-to-2.5 GHz phased-array ic based on gm-rc all-pass time-delay cells," in *2012 IEEE International Solid-State Circuits Conference Digest of Technical Papers (ISSCC),* pp. 80–82, 2012.

[8] H. Hashemi, T.-S. Chu, and J. Roderick, "Integrated true-time-delay-based ultra-wideband array processing," *IEEE Communications Magazine,* vol. 46, no. 9, pp. 162–172, 2008.

[9] P. Angeletti, G. Gallinaro, M. Lisi, and A. Vernucci, "On-ground digital beamforming techniques for satellite smart antennas," *Proc. 19th AIAA, Toulouse, France,* pp. 1–8, 2001.

[10] P. Angeletti, N. Alagha, and S. D'Addio, "Space/ground beamforming techniques for satellite communications," in *2010 IEEE Antennas and Propagation Society International Symposium (APSURSI),* pp. 1–4, 2010.

[11] M. Sotom, B. Benazet, A. L. Kernec, and M. Maignan, "Microwave photonic technologies for flexible satellite telecom payloads," *35th European Conference on Optical Communications (ECOC'09),* 2009.

[12] T. Berceli and P. Herczfeld, "Microwave photonics—a historical perspective," *IEEE Transactions on Microwave Theory and Techniques*, vol. 58, no. 11, pp. 2992–3000, 2010.

[13] W. Ng, A. A. Walston, G. L. Tangonan, J. J. Lee, I. L. Newberg, and N. Bernstein, "The first demonstration of an optically steered microwave phased array antenna using true-time-delay," *Journal of Lightwave Technology*, vol. 9, no. 9, pp. 1124–1131, 1991.

[14] Satrax B.V. [Online]. Available: `http://www.satrax.nl/`

[15] R. Won, "Microwave photonics shines," *Nature Photonics*, vol. 5, p. 736, 2011.

[16] J. Capmany, J. Mora, I. Gasulla, J. Sancho, J. Lloret, and S. Sales, "Microwave photonic signal processing," *Journal of Lightwave Technology*, vol. 31, no. 4, pp. 571–586, 2013.

[17] D. Marpaung, C. Roeloffzen, R. Heideman, A. Leinse, S. Sales, and J. Capmany, "Integrated microwave photonics," *Laser & Photonics Reviews*, 2013.

[18] The SKA website. [Online]. Available: `http://www.skatelescope.org/`

[19] International workshop on phased array antenna systems for radio astronomy, May 3-5, 2010, Provo, Utah, USA. [Online]. Available: `http://ce.byu.edu/cw/radio/`

[20] S. Ayotte, A. Babin, P. Poulin, M. Poulin, A. Jeanneau, M.-J. Picard, D. Poulin, C.-A. Davidson, M. Aube, I. Alexandre, *et al.*, "Laser synthesizer of the alma telescope: Design and performance," in *2010 IEEE Topical Meeting on Microwave Photonics (MWP 2010)*, pp. 249–252, 2010.

[21] S. Montebugnoli, M. Boschi, F. Perini, P. Faccin, G. Brunori, and E. Pirazzini, "Large antenna array remoting using radio-over-fiber techniques for radio astronomical application," *Microwave and Optical Technology Letters*, vol. 46, no. 1, pp. 48–54, 2005.

[22] D. Marpaung, *High Dynamic Range Analog Photonic Links - Design & Implementation*. PhD thesis, University of Twente, Enschede, 2009.

[23] M. J. Wale, "Technology platforms for photonic integrated circuits," in *Integrated Photonics Research, Silicon and Nanophotonics*, Optical Society of America, 2012.

[24] L. Zhuang, D. Marpaung, M. Burla, W. Beeker, A. Leinse, and C. Roeloffzen, "Low-loss, high-index-contrast Si_3N_4/SiO_2 optical waveguides for optical delay lines in microwave photonics signal processing," *Optics Express*, vol. 19, no. 23, pp. 23162–23170, 2011.

[25] F. F. T. Ulaby, E. Michielssen, and U. Ravaioli, *Fundamentals of Applied Electromagnetics*. Pearson, vii ed. ed., 2010.

[26] C. A. Balanis, *Antenna theory: analysis and design*. Wiley-Interscience, 2012.

[27] H. T. Friis, "A note on a simple transmission formula," *proc. IRE*, vol. 34, no. 5, pp. 254–256, 1946.

[28] A. V. Oppenheim, R. W. Schafer, J. R. Buck, *et al.*, *Discrete-time signal processing*, vol. 5. Prentice Hall Upper Saddle River, 1999.

[29] B. E. Saleh and M. C. Teich, *Fundamentals of photonics*, vol. 32. Wiley-Interscience Hoboken, NJ, 2007.

[30] R. E. Collin, *Foundations for microwave engineering*. John Wiley & Sons, 2007.

[31] J. Capmany and D. Novak, "Microwave photonics combines two worlds," *Nature Photonics*, vol. 1, no. 6, pp. 319–330, 2007.

[32] 32nd ESA Antenna Workshop, Noordwijk, The Netherlands. [Online]. Available: `http://www.congrex.nl/10C09/`

[33] A. Meijerink, C. G. Roeloffzen, R. Meijerink, L. Zhuang, D. A. Marpaung, M. J. Bentum, M. Burla, J. Verpoorte, P. Jorna, A. Hulzinga, and W. van Etten, "Novel ring resonator-based integrated photonic beamformer for broadband phased array receive antennas—part I: Design and performance analysis," *Journal of Lightwave Technology*, vol. 28, no. 1, pp. 3–18, 2010.

[34] C. Alexander and M. Sadiku, *Fundamentals of Electric Circuits*. McGraw-Hill New York, 5th ed. ed., 2012.

[35] J. Brittain, "Thevenin's theorem," *IEEE Spectrum*, vol. 27, no. 3, p. 42, 1990.

[36] W. C. van Etten, *Introduction to random signals and noise*. Wiley, 2006.

[37] C. H. Cox III, *Analog optical links: theory and practice*. Cambridge University Press, 2006.

[38] V. Urick, M. Rogge, F. Bucholtz, and K. Williams, "Wideband (0.045-6.25 GHz) 40 km analogue fibre-optic link with ultra-high (> 40 dB) all-photonic gain," *Electronics Letters*, vol. 42, no. 9, pp. 552–553, 2006.

[39] E. I. Ackerman, G. E. Betts, W. K. Burns, J. C. Campbell, C. Cox, N. Duan, J. L. Prince, M. D. Regan, and H. V. Roussell, "Signal-to-noise performance of two analog photonic links using different noise reduction techniques," in *IEEE/MTT-S International Microwave Symposium*, pp. 51–54, 2007.

[40] G. P. Agrawal, *Fiber-optic communication systems*. Wiley, 2010.

[41] E. Ackerman, G. Betts, W. Burns, J. Campbell, C. Cox, N. Duan, J. Prince, M. Regan, and H. Roussell, "Signal-to-noise performance of two analog photonic links using different noise reduction techniques," in *Proc. IEEE MTT-S Int. Microwave Symp.*, pp. 51–54, 2007.

[42] A. Karim and J. Devenport, "Noise figure reduction in externally modulated analog fiber-optic links," *IEEE Photonics Technology Letters*, vol. 19, no. 5, pp. 312–314, 2007.

[43] V. J. Urick, J. D. McKinney, J. F. Diehl, and K. J. Williams, "Fiber-optic links with all-photonic RF gain and low RF noise figure," in *2011 IEEE MTT-S International Microwave Symposium Digest (MTT)*, pp. 1–4, 2011.

[44] M. Sauer, A. Kobyakov, and J. George, "Radio over fiber for picocellular network architectures," *Journal of Lightwave Technology*, vol. 25, no. 11, pp. 3301–3320, 2007.

[45] A. R. Islam, M. Bakaul, A. Nirmalathas, G. E. Town, *et al.*, "Simplification of millimeter-wave radio-over-fiber system employing heterodyning of uncorrelated optical carriers and self-homodyning of RF signal at the receiver," *Optics Express*, vol. 20, no. 5, pp. 5707–5724, 2012.

[46] R. Palacio, F. Deborgies, and P. Piironen, "Optical distribution of microwave signals for earth observation satellites," in *2010 IEEE Topical Meeting on Microwave Photonics (MWP 2010)*, pp. 74–77, 2010.

[47] D. Yap, O. Efimov, K. Geary, and J. Schaffner, "Compact electro-optic modulator for direct integration into an x-band antenna array front-end," in *2010 IEEE Topical Meeting on Microwave Photonics (MWP 2010)*, pp. 35–38, IEEE, 2010.

[48] The ALMA website. [Online]. Available: `http://www.almaobservatory.org/`

[49] The LOFAR website. [Online]. Available: `http://www.lofar.org/`

[50] J. Yao, "Photonic generation of microwave arbitrary waveforms," *Optics Communications*, vol. 284, no. 15, pp. 3723–3736, 2011.

[51] C. Curcio, *Photonic wideband phased array: an optical time steered antenna based on a new true time delay unit*. PhD thesis, Università degli Studi di Napoli Federico II, Napoli, June 2006.

[52] X. Yi, T. X. Huang, and R. A. Minasian, "Photonic beamforming based on programmable phase shifters with amplitude and phase control," *IEEE Photonics Technology Letters*, vol. 23, no. 18, pp. 1286–1288, 2011.

[53] N. A. Riza, *Selected papers on photonic control systems for phased array antennas*, vol. MS136. SPIE Optical Engineering Press, 1997.

[54] T. Akiyama, A. Satoh, K. Nishizawa, S. Yamamoto, S. Itakura, and Y. Hirano, "Fourier transform optically controlled phased array antenna in receiving operation," in *2009 IEEE Topical Meeting on Microwave Photonics (MWP 2009)*, pp. 1–4, 2009.

[55] T. Akiyama, H. Matsuzawa, K. Sakai, S. Itakura, and Y. Hirano, "Multiple-beam optically controlled beamformer using spatial-and-wavelength division multiplexing," in *2009 IEEE Topical Meeting on Microwave Photonics (MWP 2009)*, pp. 1–4, 2009.

[56] H. Matsuzawa, T. Akiyama, H. Sumiyoshi, T. Iguchi, M. Nagase, Y. Shoji, Y. Fujino, A. Akaishi, and R. Suzuki, "Variable spot scanning antenna using optically controlled beam forming network," in *2010 IEEE Topical Meeting on Microwave Photonics (MWP 2010)*, pp. 397–400, 2010.

[57] L. Goldberg, R. Esman, and K. Williams, "Generation and control of microwave signals by optical techniques," in *IEE Proceedings J (Optoelectronics)*, vol. 139, pp. 288–295, IET, 1992.

[58] R. Soref, "Voltage-controlled optical/RF phase shifter," *Journal of Lightwave Technology*, vol. 3, no. 5, pp. 992–998, 1985.

[59] K. Horikawa, Y. Nakasuga, and H. Ogawa, "Self-heterodyning optical waveguide beam forming and steering network integrated on lithium niobate substrate," *IEEE Transactions on Microwave Theory and Techniques*, vol. 43, no. 9, pp. 2395–2401, 1995.

[60] J. Han, B.-J. Seo, S. Kim, H. Zhang, and H. R. Fetterman, "Single-chip integrated electro-optic polymer photonic RF phase shifter array," *Journal of Lightwave Technology*, vol. 21, no. 12, p. 3257, 2003.

[61] V. M. Hietala, G. A. Vawter, W. Meyer, and S. H. Kravitz, "Phased-array antenna control by a monolithic photonic integrated circuit," in *Orlando'91, Orlando, FL*, pp. 170–175, International Society for Optics and Photonics, 1991.

[62] K. Horikawa, Y. Nakasuga, and H. Ogawa, "Self-heterodyning optical waveguide beam forming and steering network integrated on lithium niobate substrate," *IEEE Transactions on Microwave Theory and Techniques*, vol. 43, no. 9, pp. 2395–2401, 1995.

[63] H. Fetterman, J. Han, H. Zhang, H. Erlig, D. Chang, M.-C. Oh, and W. Steier, "Multiple output photonic RF phase shifters for optically controlled radar systems," in *2002 IEEE MTT-S International Microwave Symposium Digest*, vol. 3, pp. 1937–1940, 2002.

[64] J. Stulemeijer, R. van Dijk, F. van Vliet, D. Maat, and M. Smit, "Photonic chip for steering a four element phased array antenna," in *2000 IEEE Topical Meeting on Microwave Photonics (MWP 2000)*, pp. 20–22, 2000.

[65] G. Grosskopf, B. Kuhlow, G. Przyrembel, R. Eggemann, J. Knuppel, and D. Rohde, "Silica based beamformer for 60 GHz smart antennas," in *27th European Conference on Optical Communications, 2001 (ECOC'01)*, vol. 1, pp. 12–13, IEEE, 2001.

[66] N. A. Riza and D. Psaltis, "Acousto-optic signal processors for transmission and reception of phased-array antenna signals," *Applied Optics*, vol. 30, no. 23, pp. 3294–3303, 1991.

[67] A. Daryoush, P. Herczfeld, V. Contarino, A. Rosen, and Z. Turski, "Optical beam control of mm-wave phased array antennas for communications," *Microwave Journal*, vol. 30, p. 97, 1987.

[68] R. Benjamin and A. Seeds, "Optical beam forming techniques for phased array antennas," in *IEE Proceedings H (Microwaves, Antennas and Propagation)*, vol. 139, pp. 526–534, IET, 1992.

[69] M. Völker, "Coherent all-fibre optical beam-steering technique for phased-array antennas," in *IEE Proceedings J (Optoelectronics)*, vol. 139, no. 4, pp. 305–308, 1992.

[70] C. Belisle, C. Delisle, and J. Oldham, "Photonic differential delay beam forming network for phased-array antennas," in *2000 IEEE Topical Meeting on Microwave Photonics (MWP 2000)*, pp. 81–84, 2000.

[71] J. Coward, C. Chalfant, and P. Chang, "A photonic integrated-optic RF phase shifter for phased array antenna beam-forming applications," *Journal of Lightwave Technology*, vol. 11, no. 12, pp. 2201–2205, 1993.

[72] S. Winnall, A. Lindsay, and G. Knight, "A wide-band microwave photonic phase and frequency shifter," *IEEE Transactions on Microwave Theory and Techniques*, vol. 45, no. 6, pp. 1003–1006, 1997.

[73] S. Henion and P. Schulz, "Electrooptic phased array transmitter," *IEEE Photonics Technology Letters*, vol. 10, no. 3, pp. 424–426, 1998.

[74] N. A. Riza, "Analog vector modulation-based widely tunable frequency photonic beamformer for phased-array antennas," *IEEE Transactions on Microwave Theory and Techniques*, vol. 45, no. 8, pp. 1508–1512, 1997.

[75] I. Blanchflower and A. Seeds, "Optical control of frequency and phase of gaas mesfet oscillator," *Electronics Letters*, vol. 25, no. 5, pp. 359–360, 1989.

[76] R. D. Esman, L. Goldberg, and J. Weller, "Optical phase control of an optically injection-locked fet microwave oscillator," *IEEE Transactions on Microwave Theory and Techniques*, vol. 37, no. 10, pp. 1512–1518, 1989.

[77] X. Zhang and A. Daryoush, "Full 360 degrees phase shifting of injection-locked oscillators," *IEEE Microwave and Guided Wave Letters*, vol. 3, no. 1, pp. 14–16, 1993.

[78] H. Zmuda and E. N. Toughlian, *Photonic aspects of modern radar*. Artech House, Inc., 1994.

[79] E. N. Toughlian and H. Zmuda, "A photonic variable RF delay line for phased array antennas," *Journal of Lightwave Technology*, vol. 8, no. 12, pp. 1824–1828, 1990.

[80] D. Dolfi, J. Huignard, and M. Baril, "Optically controlled true time delays for phased array antenna," in *1989 Orlando Symposium*, pp. 152–161, International Society for Optics and Photonics, 1989.

[81] D. Dolfi, F. Michel-Gabriel, S. Bann, and J.-P. Huignard, "Two-dimensional optical architecture for time-delay beam forming in a phased-array antenna," *Optics Letters*, vol. 16, no. 4, pp. 255–257, 1991.

[82] N. Riza, "Transmit/receive time-delay beam-forming optical architecture for phased-array antennas," *Applied Optics*, vol. 30, no. 32, pp. 4594–4595, 1991.

[83] D. Dolfi, P. Joffre, J. Antoine, J.-P. Huignard, D. Philippet, and P. Granger, "Experimental demonstration of a phased-array antenna optically controlled with phase and time delays," *Applied Optics*, vol. 35, no. 26, pp. 5293–5300, 1996.

[84] N. A. Riza, "Acousto-optic liquid-crystal analog beam former for phased-array antennas," *Applied Optics*, vol. 33, no. 17, pp. 3712–3724, 1994.

[85] N. A. Riza and N. Madamopoulos, "Characterization of a ferroelectric liquid crystal-based time delay unit for phased array antenna applications," *Journal of Lightwave Technology*, vol. 15, no. 7, pp. 1088–1094, 1997.

[86] X. S. Yao and L. Maleki, "A novel 2-d programmable photonic time-delay device for millimeter-wave signal processing applications," *IEEE Photonics Technology Letters*, vol. 6, no. 12, pp. 1463–1465, 1994.

[87] W. Jemison and P. Herczfeld, "Acoustooptically controlled true time delays," *IEEE Microwave and Guided Wave Letters*, vol. 3, no. 3, pp. 72–74, 1993.

[88] P. Herczfeld, A. Daryoush, M. Kieli, S. SiegeI, and R. Soref, "Wide-band true time delay phase shifter devices," in *1987 IEEE MTT-S International Microwave Symposium Digest*, vol. 2, pp. 603–606, 1975.

[89] R. A. Soref, "Programmable time-delay devices," *Applied Optics*, vol. 23, no. 21, pp. 3736–3737, 1984.

[90] A. P. Goutzoulls, D. Davies, and J. Zomp, "Prototype binary fiber optic delay line," *Optical Engineering*, vol. 28, no. 11, pp. 1193–1202, 1989.

[91] E. Ackerman, S. Wanuga, D. Kasemset, W. Minford, N. Thorsten, and J. Watson, "Integrated 6-bit photonic true-time-delay unit for lightweight 3-6 GHz radar beamformer," in *1992 IEEE MTT-S International Microwave Symposium Digest*, pp. 681–684, 1992.

[92] A. Goutzoulis, K. Davies, J. Zomp, P. Hrycak, and A. Johnson, "Development and field demonstration of a hardware-compressive fiber-optic true-time-delay steering system for phased-array antennas," *Applied Optics*, vol. 33, no. 35, pp. 8173–8185, 1994.

[93] Y. Chen, K. Wu, F. Zhao, and R. T. Chen, "Loss compensated photonic true-time delay for phased-array antenna," in *IEEE Antennas and Propagation Society International Symposium*, vol. 4, pp. 4324–4327, 2004.

[94] X. Wang, B. Howley, M. Y. Chen, P. Basile, and R. T. Chen, "Fully-integrated 4-bit true time delay module using polymer optical switches and waveguide delay lines," in *Integrated Photonics Research and Applications*, Optical Society of America, 2006.

[95] Y. Chen, K. Wu, F. Zhao, G. Kim, and R. T. Chen, "Reconfigurable true-time delay for wideband phased-array antennas," in *Proceedings of SPIE*, vol. 5363, pp. 125–130, 2004.

[96] K. Horikawa, I. Ogawa, H. Ogawa, and T. Kitoh, "Photonic switched true time delay beam forming network integrated on silica waveguide circuits," in *1995 IEEE MTT-S International Microwave Symposium Digest*, pp. 65–68, IEEE, 1995.

[97] K. Horikawa, I. Ogawa, T. Kitoh, and H. Ogawa, "Silica-based integrated planar lightwave true-time-delay network for microwave antenna applications," in *Optical Fiber Communications, 1996. OFC'96*, pp. 100–101, 1996.

[98] J. LeGrange, A. Kasper, C. Madsen, M. Cappuzzo, E. Chen, A. Griffin, E. Laskowski, and M. Rasras, "Demonstration of an integrated, tunable high resolution true time delay line," in *The 17th Annual Meeting of the IEEE Lasers and Electro-Optics Society, (LEOS 2004)*, vol. 2, pp. 790–791, IEEE, 2004.

[99] M. S. Rasras, C. K. Madsen, M. A. Cappuzzo, E. Chen, L. T. Gomez, E. J. Laskowski, A. Griffin, A. Wong-Foy, A. Gasparyan, A. Kasper, J. LeGrange, and S. S. Pastel, "Integrated resonance-enhanced variable optical delay lines," *IEEE Photonics Technology Letters*, vol. 17, no. 4, pp. 834–836, 2005.

[100] J. Stulemeijer, F. van Vliet, K. Benoist, D. Maat, and M. Smit, "Compact photonic integrated phase and amplitude controller for phased-array antennas," *IEEE Photonics Technology Letters*, vol. 11, no. 1, pp. 122–124, 1999.

[101] G. Flamand, K. De Mesel, I. Moerman, B. Dhoedt, W. Hunziker, A. Kalmar, R. Baets, P. Van Daele, and W. Leeb, "Inp-based pic for an optical phased-array antenna at 1.06 μm," *IEEE Photonics Technology Letters*, vol. 12, no. 7, pp. 876–878, 2000.

[102] C. T. Sullivan, S. D. Mukherjee, M. K. Hibbs-Brenner, A. Gopinath, E. Kalweit, T. Marta, W. Goldberg, and B. Walterson, "Switched time-delay elements based on AlGaAs/GaAs optical waveguide technology at 1.32 μm for optically

controlled phased-array antennas," in *Aerospace Sensing*, pp. 264–271, International Society for Optics and Photonics, 1992.

[103] D. Yap, W. W. Ng, and R. R. Hayes, "Monolithic integrated optical time delay network for antenna beam steering," June 22, 1993. US Patent 5,222,162.

[104] S. Paquet, F. Chenard, Z. Jakubczyk, M. Belanger, M. Tetu, C. Belisle, G. Lampropoulos, J. Chrostowski, and R. Measures, "Optical delay lines in high-silica (SiO$_2$/Si) waveguides," *SPIE Milestone Series*, vol. 136, pp. 382–385, 1997.

[105] W. Wang, Y. Shi, W. Lin, and J. H. Bechtel, "Waveguide binary photonic true-time-delay lines using polymer integrated switches and waveguide delays," in *SPIE's 1996 International Symposium on Optical Science, Engineering, and Instrumentation*, pp. 200–211, International Society for Optics and Photonics, 1996.

[106] Y. Chen and R. T. Chen, "A fully packaged true time delay module for a k-band phased array antenna system demonstration," *IEEE Photonics Technology Letters*, vol. 14, no. 8, pp. 1175–1177, 2002.

[107] N. A. Riza and D. L. Polla, "Micromechanical fiber optic switches for optical networks," in *Fibers' 92*, pp. 108–126, International Society for Optics and Photonics, 1993.

[108] G. A. Magel, T.-H. Lin, L. Y. Pang, and W. Wy, "Integrated optic switches for phased-array applications based on electrostatic actuation of metallic membranes," *Optoelectronic Signal Processing for Phased Array Antennas IV*, vol. 2155, pp. 107–113, 1994.

[109] Z. Shi, Y. Jiang, B. Howley, Y. Chen, F. Zhao, and R. T. Chen, "Continuously delay-time tunable-waveguide hologram module for x-band phased-array antenna," *IEEE Photonics Technology Letters*, vol. 15, no. 7, pp. 972–974, 2003.

[110] F. Soares, *Photonic Integrated True-Time-Delay Beamformers in InP Technology*. PhD thesis, Eindhoven University of Technology, Eindhoven, September 2006.

[111] R. Soref, "Optical dispersion technique for time-delay beam steering," *Applied Optics*, vol. 31, no. 35, pp. 7395–7397, 1992.

[112] R. Esman, M. Monsma, J. Dexter, and D. Cooper, "Microwave true time-delay modulator using fibre-optic dispersion," *Electronics Letters*, vol. 28, no. 20, pp. 1905–1908, 1992.

[113] R. D. Esman, M. Y. Frankel, J. Dexter, L. Goldberg, M. Parent, D. Stilwell, and D. Cooper, "Fiber-optic prism true time-delay antenna feed," *IEEE Photonics Technology Letters*, vol. 5, no. 11, pp. 1347–1349, 1993.

[114] M. Y. Frankel, P. J. Matthews, and R. D. Esman, "Fiber-optic true time steering of an ultrawide-band receive array," *IEEE Transactions on Microwave Theory and Techniques*, vol. 45, no. 8, pp. 1522–1526, 1997.

[115] P. J. Matthews, M. Y. Frankel, and R. D. Esman, "A wide-band fiber-optic true-time-steered array receiver capable of multiple independent simultaneous beams," *IEEE Photonics Technology Letters*, vol. 10, no. 5, pp. 722–724, 1998.

[116] M. Y. Frankel and R. D. Esman, "True time-delay fiber-optic control of an ultrawideband array transmitter/receiver with multibeam capability," *IEEE Transactions on Microwave Theory and Techniques*, vol. 43, no. 9, pp. 2387–2394, 1995.

[117] M. Y. Frankel, R. Esman, and M. Parent, "Array transmitter/receiver controlled by a true time-delay fiber-optic beamformer," *IEEE Photonics Technology Letters*, vol. 7, no. 10, pp. 1216–1218, 1995.

[118] M. Y. Frankel, P. J. Matthews, and R. D. Esman, "Two-dimensional fiber-optic control of a true time-steered array transmitter," *IEEE Transactions on Microwave Theory and Techniques*, vol. 44, no. 12, pp. 2696–2702, 1996.

[119] D. Tulchinsky and P. Matthews, "Ultrawide-band fiber-optic control of a millimeter-wave transmit beamformer," *IEEE Transactions on Microwave Theory and Techniques*, vol. 49, no. 7, pp. 1248–1253, 2001.

[120] D. T. Tong and M. C. Wu, "A novel multiwavelength optically controlled phased array antenna with a programmable dispersion matrix," *IEEE Photonics Technology Letters*, vol. 8, no. 6, pp. 812–814, 1996.

[121] D. T. K. Tong and M. C. Wu, "Multiwavelength optically controlled phased-array antennas," *IEEE Transactions on Microwave Theory and Techniques*, vol. 46, no. 1, pp. 108–115, 1998.

[122] G. A. Ball, W. Glenn, and W. Morey, "Programmable fiber optic delay line," *IEEE Photonics Technology Letters*, vol. 6, no. 6, pp. 741–743, 1994.

[123] J. Roman, M. Frankel, P. Matthews, and R. Esman, "Time-steered array with a chirped grating beamformer," *Electronics Letters*, vol. 33, no. 8, pp. 652–653, 1997.

[124] J. Medberry, P. Biernacki, and P. Matthews, "Range demonstration of an ultrawideband, continuous, time steered array using a fiber-optic, cascaded grating prism," in *2000 IEEE MTT-S International Microwave Symposium Digest*, vol. 1, pp. 597–600, 2000.

[125] K. O. Hill and G. Meltz, "Fiber bragg grating technology fundamentals and overview," *Journal of Lightwave Technology*, vol. 15, no. 8, pp. 1263–1276, 1997.

[126] A. Molony, C. Edge, and I. Bennion, "Fibre grating time delay element for phased array antennas," *Electronics Letters*, vol. 31, no. 17, pp. 1485–1486, 1995.

[127] J. Corral, J. Marti, S. Regidor, J. Foster, R. Laming, and M. Cole, "Continuously variable true time-delay optical feeder for phased-array antenna employing chirped fiber grating," *IEEE Transactions on Microwave Theory and Techniques*, vol. 45, no. 8, pp. 1531–1536, 1997.

[128] A. N. Bratchikov, "Optical beamfoming technology for active phased array," in *Millennium Conference on Antennas & Propagation Antennas, AP*, pp. 133–138, 2000.

[129] Y. Liu, J. Yao, and J. Yang, "Wideband true-time-delay unit for phased array beamforming using discrete-chirped fiber grating prism," *Optics communications*, vol. 207, no. 1, pp. 177–187, 2002.

[130] V. Italia, M. Pisco, S. Campopiano, A. Cusano, and A. Cutolo, "Chirped fiber bragg gratings for electrically tunable time delay lines," *IEEE Journal of Selected Topics in Quantum Electronics*, vol. 11, no. 2, pp. 408–416, 2005.

[131] M. K. Smit, "New focusing and dispersive planar component based on an optical phased array," *Electronics Letters*, vol. 24, no. 7, pp. 385–386, 1988.

[132] S. Yegnanarayanan, P. Trinh, and B. Jalali, "Recirculating photonic filter: a wavelength-selective time delay for phased-array antennas and wavelength code-division multiple access," *Optics Letters*, vol. 21, no. 10, pp. 740–742, 1996.

[133] B. Jalali and S. Yegnanarayanan, "Optically controlled phased-array antenna using wavelength-selective true time delay," in *Proceedings of 2000 IEEE International Conference on Phased Array Systems and Technology*, pp. 367–370, 2000.

[134] B. Vidal, D. Madrid, J. Coffal, and J. Marti, "Novel photonic true-time-delay beamformer based on the free-spectral-range periodicity of arrayed waveguide gratings and fiber dispersion," *IEEE Photonics Technology Letters*, vol. 14, no. 11, pp. 1614–1616, 2002.

[135] B. Vidal, J. Corral, and J. Marti, "Optical delay line using arrayed waveguide grating in fold-back configuration for phased-array antennas," in *2002 IEEE Topical Meeting on Microwave Photonics (MWP 2002)*, pp. 269–272, 2002.

[136] X. Yi, L. Li, T. X. Huang, and R. A. Minasian, "Programmable multiple true-time-delay elements based on a fourier-domain optical processor," *Optics Letters*, vol. 37, no. 4, pp. 608–610, 2012.

[137] J. Sancho, J. Bourderionnet, J. Lloret, S. Combrié, I. Gasulla, S. Xavier, S. Sales, P. Colman, G. Lehoucq, D. Dolfi, *et al.*, "Integrable microwave filter based on a photonic crystal delay line," *Nature Communications*, vol. 3, p. 1075, 2012.

[138] P. Herczfeld and Y. Li, "Optically fed phased array antenna - revisited," in *Proc. Int. Top. Meeting on Microwave Photonics (invited)*, (Singapore), 2011.

[139] J. Fandiño, J. Doménech, P. Muñoz, and J. Capmany, "Integrated inp frequency discriminator for phase-modulated microwave photonic links," *Optics Express*, vol. 21, no. 3, pp. 3726–3736, 2013.

[140] R. Rotman, O. Raz, and M. Tur, "Analysis of a true time delay photonic beamformer for transmission of a linear frequency-modulated waveform," *Journal of Lightwave Technology*, vol. 23, no. 12, p. 4026, 2005.

[141] X. Xue, X. Zheng, H. Zhang, and B. Zhou, "Optical beamforming networks employing phase modulation and direct detection," *Optics Communications*, vol. 284, no. 12, pp. 2695–2699, 2011.

[142] J. Capmany, S. Sales, I. Gasulla, J. Mora, J. Lloret, and J. Sancho, "Innovative concepts in microwave photonics," *Waves*, 2012.

[143] L. Zhuang, *Ring Resonator-Based Broadband Photonic Beam Former for Phased Array Antennas*. PhD thesis, University of Twente, Enschede, 2010.

[144] L. Zhuang, C. Roeloffzen, R. Heideman, A. Borreman, A. Meijerink, and W. van Etten, "Single-chip ring resonator-based 1× 8 optical beam forming network in cmos-compatible waveguide technology," *IEEE Photonics Technology Letters*, vol. 19, no. 15, pp. 1130–1132, 2007.

[145] G. Lenz, B. Eggleton, C. K. Madsen, and R. Slusher, "Optical delay lines based on optical filters," *IEEE Journal of Quantum Electronics*, vol. 37, no. 4, pp. 525–532, 2001.

[146] C. K. Madsen and J. H. Zhao, *Optical filter design and analysis: a signal processing approach*. Wiley, 2001.

[147] L. Zhuang, C. G. Roeloffzen, A. Meijerink, M. Burla, D. A. Marpaung, A. Leinse, M. Hoekman, R. G. Heideman, and W. van Etten, "Novel ring resonator-based integrated photonic beamformer for broadband phased array receive antennas—part ii: Experimental prototype," *Journal of Lightwave Technology*, vol. 28, no. 1, pp. 19–31, 2010.

[148] R. C. Hansen, *Phased Array Antennas*. John Wiley & Sons, 1998.

[149] G. Abbas, V. Chan, and T. Yee, "A dual-detector optical heterodyne receiver for local oscillator noise suppression," *Journal of Lightwave Technology*, vol. 3, no. 5, pp. 1110–1122, 1985.

[150] S. Shimotsu, S. Oikawa, T. Saitou, N. Mitsugi, K. Kubodera, T. Kawanishi, and M. Izutsu, "Single side-band modulation performance of a linbo< sub> 3</sub> integrated modulator consisting of four-phase modulator waveguides," *IEEE Photonics Technology Letters*, vol. 13, no. 4, pp. 364–366, 2001.

[151] K. Oda, N. Takato, H. Toba, and K. Nosu, "A wide-band guided-wave periodic multi/demultiplexer with a ring resonator for optical fdm transmission systems," *Journal of Lightwave Technology*, vol. 6, no. 6, pp. 1016–1023, 1988.

[152] M. Burla, A. Garcia Garcia, L. Zhuang, A. Meijerink, C. Roeloffzen, D. Marpaung, M. Khan, and W. van Etten, "Optical phase synchronization in coherent optical beamformers for phased array receive antennas," in *LEOS Annual Meeting Conference Proceedings, 2009. LEOS'09. IEEE*, pp. 693–694, 2009.

[153] D. Marpaung, C. Roeloffzen, W. Beeker, B. Noharet, J. Verpoorte, and R. Baggen, *Development of a broadband and squint-free Ku-band phased array antenna system for airborne satellite communications.* Intech, 2011.

[154] H. T. Friis, "Noise figures of radio receivers," *Proceedings of the IRE*, vol. 32, no. 7, pp. 419–422, 1944.

[155] The MEMPHIS website. [Online]. Available: `http://www.smartmix-memphis.nl/`

[156] European Telecommunications Standards Institute (ETSI) website. [Online]. Available: `http://www.etsi.org/technologiesclusters/technologies/satellite/dvb-s/`

[157] Lyngsat. [Online]. Available: `http://www.lyngsat.com/`

[158] M. Burla, C. Roeloffzen, D. Marpaung, M. Khan, and W. van Etten, "A novel design procedure for minimum RF phase error in optical ring resonator-based integrated optical beamformers for phased array antennas," in *IEEE/LEOS Benelux Symposium*, Technical University of Delft, 2010.

[159] D. Marpaung, L. Zhuang, M. Burla, C. Roeloffzen, J. Verpoorte, H. Schippers, A. Hulzinga, P. Jorna, W. Beeker, A. Leinse, *et al.*, "Towards a broadband and squint-free ku-band phased array antenna system for airborne satellite communications," in *Proceedings of the 5th European Conference on Antennas and Propagation (EUCAP)*, pp. 2623–2627, 2011.

[160] M. Burla, C. G. Roeloffzen, L. Zhuang, D. Marpaung, M. R. Khan, P. Maat, K. Dijkstra, A. Leinse, M. Hoekman, and R. Heideman, "System integration and radiation pattern measurements of a phased array antenna employing an integrated photonic beamformer for radio astronomy applications," *Applied Optics*, vol. 51, no. 7, pp. 789–802, 2012.

[161] Lionix B.V. [Online]. Available: `http://www.lionixbv.nl/`

[162] Discovery Semiconductors, Inc. [Online]. Available: `http://www.discoverysemi.com/`

[163] Oclaro, Inc. [Online]. Available: `http://www.avanex.com/`

[164] W. van Etten and J. van der Plaats, *Fundamentals of optical fiber communications*. Prentice Hall, 1991.

[165] K. Daikoku and A. Sugimura, "Direct measurement of wavelength dispersion in optical fibres-difference method," *Electronics Letters*, vol. 14, pp. 149–151, 1978.

[166] D. Marcuse, *Principles of optical fiber measurements*. Academic Press, 1981.

[167] L. Zhuang, M. Burla, C. Roeloffzen, A. Meijerink, D. Marpaung, M. Khan, W. van Etten, A. Leinse, M. Hoekman, and R. Heideman, "RF-to-RF characterization of a phased array receive antenna steering system using a novel ring resonator-based integrated photonic beamformer," in *2009 IEEE Topical Meeting on Microwave Photonics (MWP 2009)*, pp. 1–4, 2009.

[168] T. Mengual, B. Martínez, B. Vidal, and J. Marti, "Wide-band nulling system for antenna array based on a photonic microwave filter and optical delay lines," *Optics Communications*, vol. 282, no. 19, pp. 3878–3882, 2009.

[169] M. Burla, E. Lavabre, C. Roeloffzen, D. Marpaung, L. Zhuang, M. Khan, and W. van Etten, "Automatic transmission parameters measurement and radiation pattern simulation for an RF photonic integrated beamformer," in *IEEE/LEOS Benelux Symposium*, IEEE Photonics Society, 2011.

[170] R. Sorrentino and G. Bianchi, *Microwave and RF engineering*, vol. 1. Wiley, 2010.

[171] Touchstone® file format specification (IBIS open forum April 24, 2009). [Online]. Available: `http://www.eda.org/%ibis/touchstone\_ver2.0/touchstone\_ver2\_0.pdf/`

[172] R. S. Elliott, *Antenna theory and design*. John Wiley & Sons, 2003.

[173] R. Baggen, S. Vaccaro, D. L. del Rio, R. T. Sanchez, and G. Langgartner, "First prototyping of a compact mobile ku-band satellite terminal," in *2010 Proceedings of the Fourth European Conference on Antennas and Propagation (EuCAP)*, pp. 1–4, 2010.

[174] D. Cavallo, A. Neto, and G. Gerini, "Analytical description and design of printed dipole arrays for wideband wide-scan applications," *IEEE Transactions on Antennas and Propagation*, 2012.

[175] M. Burrows, "Closer spacing of geostationary satellites through adaptive nulling at the ground terminal," *IEEE Transactions on Antennas and Propagation*, vol. 35, no. 7, pp. 870–873, 1987.

[176] G. W. Kant, P. D. Patel, S. J. Wijnholds, M. Ruiter, and E. van der Wal, "Embrace: A multi-beam 20,000-element radio astronomical phased array antenna demonstrator," *IEEE Transactions on Antennas and Propagation*, vol. 59, no. 6, pp. 1990–2003, 2011.

[177] P. D. Patel, D. W. Kant, E. Wal, and A. van Ardene, "Phased array antennas demonstrator as a radio telescope-embrace," in *IEEE Antennas and Propagation Society International Symposium, AP-S 2008*, pp. 1–4, 2008.

[178] R. Heideman, D. Geuzebroek, A. Leinse, A. Melloni, F. Morichetti, C. Roeloffzen, A. Meijerink, L. Zhuang, W. van Etten, E. Klein, *et al.*, "Low loss, high contrast optical waveguides based on cmos compatible lpcvd processing," in *Proc. 11th Eur. Conf. on Integrated Optics and Technical Exhibition*, Technical University of Denmark, 2007.

[179] N. Froberg, E. Ackerman, and C. Cox, "Analysis of signal to noise ratio in photonic beamformers," in *Aerospace Conference, 2006 IEEE*, pp. 12–pp, IEEE, 2006.

[180] H. Subbaraman, M. Y. Chen, and R. T. Chen, "Photonic crystal fiber-based true-time-delay beamformer for multiple RF beam transmission and reception of an x-band phased-array antenna," *Journal of Lightwave Technology*, vol. 26, no. 15, pp. 2803–2809, 2008.

[181] B. Ortega, J. L. Cruz, J. Capmany, M. V. Andrés, and D. Pastor, "Variable delay line for phased-array antenna based on a chirped fiber grating," *IEEE Transactions on Microwave Theory and Techniques*, vol. 48, no. 8, pp. 1352–1360, 2000.

[182] M. Burla, D. Marpaung, L. Zhuang, C. Roeloffzen, M. R. Khan, A. Leinse, M. Hoekman, and R. Heideman, "On-chip cmos compatible reconfigurable optical delay line with separate carrier tuning for microwave photonic signal processing," *Optics Express*, vol. 19, no. 22, pp. 21475–21484, 2011.

[183] Y. Huo, S. Sandhu, J. Pan, N. Stuhrmann, M. L. Povinelli, J. M. Kahn, J. S. Harris, M. M. Fejer, and S. Fan, "Experimental demonstration of two methods for controlling the group delay in a system with photonic-crystal resonators coupled to a waveguide," *Optics Letters*, vol. 36, no. 8, pp. 1482–1484, 2011.

[184] W. Xue, S. Sales, J. Capmany, and J. Mørk, "Wideband 360 microwave photonic phase shifter based on slow light in semiconductor optical amplifiers," *Opt. Express*, vol. 18, no. 6, pp. 6156–6163, 2010.

[185] Y. Chen, W. Xue, F. Öhman, and J. Mørk, "Theory of optical-filtering enhanced slow and fast light effects in semiconductor optical waveguides," *Journal of Lightwave Technology*, vol. 26, no. 23, pp. 3734–3743, 2008.

[186] S. Sales, W. Xue, J. Mork, and I. Gasulla, "Slow and fast light effects and their applications to microwave photonics using semiconductor optical amplifiers," *IEEE Transactions on Microwave Theory and Techniques*, vol. 58, no. 11, pp. 3022–3038, 2010.

[187] L. Thévenaz, "Slow and fast light in optical fibres," *Nature Photonics*, vol. 2, no. 8, pp. 474–481, 2008.

[188] S. Chin, L. Thévenaz, J. Sancho, S. Sales, J. Capmany, P. Berger, J. Bourderionnet, and D. Dolfi, "Broadband true time delay for microwave signal processing, using slow light based on stimulated brillouin scattering in optical fibers," *Optics Express*, vol. 18, no. 21, pp. 22599–22613, 2010.

[189] J. Sancho, S. Chin, M. Sagues, A. Loayssa, J. Lloret, I. Gasulla, S. Sales, L. Thévenaz, and J. Capmany, "Dynamic microwave photonic filter using separate carrier tuning based on stimulated brillouin scattering in fibers," *IEEE Photonics Technology Letters*, vol. 22, no. 23, pp. 1753–1755, 2010.

[190] F. Morichetti, A. Melloni, A. Breda, A. Canciamilla, C. Ferrari, M. Martinelli, *et al.*, "A reconfigurable architecture for continuously variable optical slow-wave delay lines," *Opt. Express*, vol. 15, no. 25, pp. 17273–17282, 2007.

[191] J. Cardenas, M. A. Foster, N. Sherwood-Droz, C. B. Poitras, H. L. Lira, B. Zhang, A. L. Gaeta, J. B. Khurgin, P. Morton, M. Lipson, *et al.*, "Wide-bandwidth continuously tunable optical delay line using silicon microring resonators," *Opt. Express*, vol. 18, no. 25, pp. 26525–26534, 2010.

[192] J. Yao, "Microwave photonics," *Journal of Lightwave Technology*, vol. 27, no. 3, pp. 314–335, 2009.

[193] A. J. Seeds, "Microwave photonics," *IEEE Transactions on Microwave Theory and Techniques*, vol. 50, no. 3, pp. 877–887, 2002.

[194] J. Capmany, B. Ortega, D. Pastor, and S. Sales, "Discrete-time optical processing of microwave signals," *Journal of Lightwave Technology*, vol. 23, no. 2, pp. 702–723, 2005.

[195] M. H. Khan, H. Shen, Y. Xuan, L. Zhao, S. Xiao, D. E. Leaird, A. M. Weiner, and M. Qi, "Ultrabroad-bandwidth arbitrary radiofrequency waveform generation with a silicon photonic chip-based spectral shaper," *Nature Photonics*, vol. 4, no. 2, pp. 117–122, 2010.

[196] P. A. Morton and J. B. Khurgin, "Microwave photonic delay line with separate tuning of the optical carrier," *IEEE Photonics Technology Letters*, vol. 21, no. 22, pp. 1686–1688, 2009.

[197] M. Pu, L. Liu, W. Xue, Y. Ding, L. H. Frandsen, H. Ou, K. Yvind, and J. M. Hvam, "Tunable microwave phase shifter based on silicon-on-insulator microring resonator," *IEEE Photonics Technology Letters*, vol. 22, no. 12, pp. 869–871, 2010.

[198] F. Morichetti, A. Melloni, M. Martinelli, R. G. Heideman, A. Leinse, D. H. Geuzebroek, and A. Borreman, "Box-shaped dielectric waveguides: A new concept in integrated optics?," *Journal of Lightwave Technology*, vol. 25, no. 9, pp. 2579–2589, 2007.

[199] A. Loayssa and F. J. Lahoz, "Broad-band RF photonic phase shifter based on stimulated brillouin scattering and single-sideband modulation," *IEEE Photonics Technology Letters*, vol. 18, no. 1, pp. 208–210, 2006.

[200] M. Burla, M. Khan, L. Zhuang, and C. Roeloffzen, "Multiwavelength optical beam forming network with ring resonator-based binary-tree architecture for broadband phased array antenna systems," in *IEEE/LEOS Benelux Symposium*, University of Twente, 2008.

[201] T. H. Cormen, C. E. Leiserson, R. L. Rivest, and C. Stein, *Introduction to algorithms.* MIT press, 2001.

[202] J. Zhao, P. J. Williams, M. K. Smit, and X. Leijtens, "Monolithic integrated filtered-feedback multi-wavelength laser," in *Optical Fiber Communication Conference*, Optical Society of America, 2012.

[203] C. G. H. Roeloffzen, *Passband flattened binary-tree structured add-drop multiplexers using SiON waveguide technology.* PhD thesis, University of Twente, Enschede, 2002.

[204] B. Verbeek, C. Henry, N. Olsson, K. Orlowsky, R. Kazarinov, and B. Johnson, "Integrated four-channel mach-zehnder multi/demultiplexer fabricated with phosphorous doped sio_2 waveguides on si," *Journal of Lightwave Technology*, vol. 6, no. 6, pp. 1011–1015, 1988.

[205] Labview, Inc. [Online]. Available: `http://www.ni.com/labview/`

[206] National Aerospace Laboratory. [Online]. Available: `http://www.nlr.nl/`

[207] J. Zhao, K. Dijkstra, M. J. Wale, P. Maat, M. K. Smit, and X. J. Leijtens, "Monolithically integrated filtered-feedback multi-wavelength laser with mach-zehnder modulators," in *Proc. 16th Eur. Conf. on Integrated Optics and Technical Exhibition*, vol. 1, 2012.

[208] International Telecommunication Union, recommendation *G.694.1 (Spectral grids for WDM applications: DWDM frequency grid)*. [Online]. Available: `http://www.itu.int/rec/TREC-G.694.1-201202-I/en/`

[209] ESA ARTES program. [Online]. Available: `http://telecom.esa.int/telecom/`

[210] M. Burla, M. Khan, D. Marpaung, C. Roeloffzen, P. Maat, K. Dijkstra, A. Leinse, M. Hoekman, and R. Heideman, "Squint-free beamsteering demonstration using a photonic integrated beamformer based on optical ring resonators," in *2010 IEEE Topical Meeting on Microwave Photonics (MWP 2010)*, pp. 401–404, 2010.

A

Spherical Coordinate System

A.1 Spherical Coordinate System

A spherical coordinate system is a coordinate system used in a three-dimensional space. The position of a point is specified by three numbers:

- the radial distance of that point from a fixed origin,

- the polar angle measured from a fixed zenith direction,

- the azimuth angle of its orthogonal projection on a reference plane that passes through the origin and is orthogonal to the zenith, measured from a fixed reference direction on that plane.

An example showing the representation of the position of point P is given in Fig. A.1.

A.2 Conversion between spherical and cartesian coordinates

For our applications, it is of interest to be able to convert between a spherical and a cartesian system of coordinates in three dimensions. Below are the formulas used for the conversions.
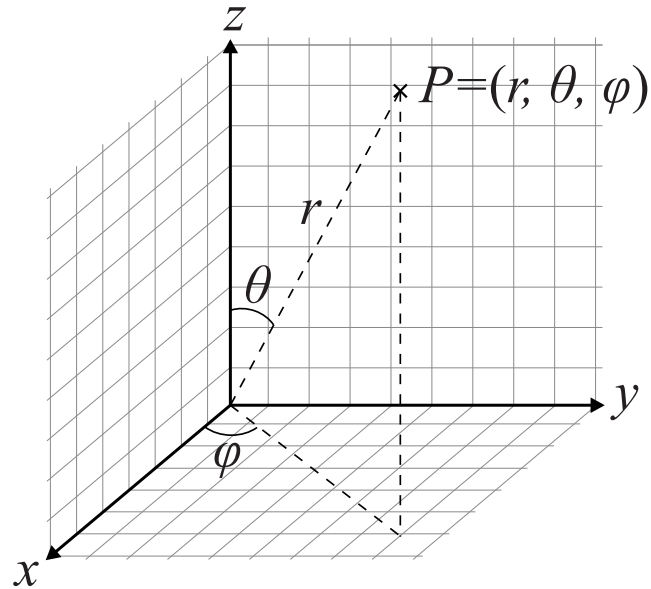
Figure A.1: Representation the point *P* in a spherical coordinate system

- Cartesian to Spherical

$$r = \sqrt{x^2 + y^2 + z^2} \tag{A.1}$$

$$\varphi = \arctan\left(\frac{y}{x}\right) \tag{A.2}$$

$$\vartheta = \arctan\left(\frac{z}{r}\right) \tag{A.3}$$

- Spherical to Cartesian

$$x = r\sin\vartheta\cos\varphi \tag{A.4}$$

$$y = r\sin\vartheta\sin\varphi \tag{A.5}$$

$$z = r\cos\vartheta \tag{A.6}$$

B

Design of tunable delay units based on optical ring resonators

B.1   Introduction

In this Appendix we present the design procedure used to determine the architecture of the delay units used in optical ring resonator (ORR) based integrated optical beam forming networks (OBFN) for microwave phased array antenna applications described in this thesis. Given the system specifications of minimum RF signal bandwidth (2.05 GHz), propagation loss in the optical waveguide (0.2 dB/cm) and maximum phase error allowed in band ($\pi/16$), the method is used to determine the number of ORRs required in each delay unit for minimum complexity and, in turn, minimum footprint in the realized chip. The effects of the RF phase errors obtained with the described procedure are also analyzed. The result shows negligible degradation in the array radiation pattern when imposing a maximum phase error of $\pi/16$ or lower.

We describe a novel design procedure for optical beamformers based on optical ring resonators. Taking into account the bandwidth, beamsteering angle and maximum phase error requirements, the method determines the OBFN layout with minimum complexity and footprint.

B.2   Design of the Symmetric Binary Tree OBFN structure

In our study we assume the most common case of linear or planar arrays, with identical, equally spaced antenna elements (AEs). Let us assume the array on the xy plane of a Cartesian coordinate system. An antenna element placed in the origin is chosen as reference AE with zero delay. It can be shown that, for a desired pointing direction (ϑ_0, φ_0), the required delay at the p-th element located at (x_p, y_p) equals

$$\Delta\tau_p = \frac{\sin(\vartheta_0)\cos(\varphi_0)x_p + \sin(\vartheta_0)\sin(\varphi_0)y_p}{c_0} \tag{B.1}$$

indicating that the required delay tuning range increases with the space coordinate of the AE. This motivates the choice of *binary tree* architecture as the structure of lowest complexity for the OBFN, since different delay paths can share the same delay units to achieve the desired linear delay profile, as shown in Fig. B.1. The symmetry of the structure comes from the general need to steer the beam in both directions, without need of additional delay offset compensation.
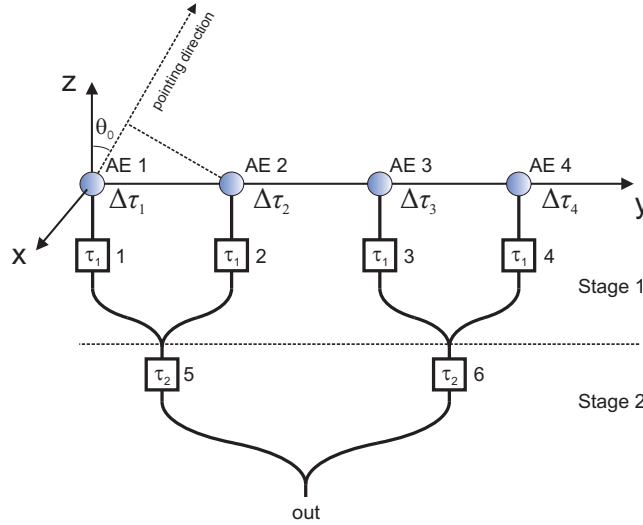
Figure B.1: Architecture of a symmetric binary tree 4×1 OBFN feeding a 4 elements linear array. Note how delay units 5 and 6 are shared among multiple paths.

In this architecture, the maximum delay tuning ranges τ_1, τ_2 for the delay units in stages 1 and 2 are given by

$$\tau_1 = \frac{1}{2}\tau_2 = (\Delta\tau_{n+1} - \Delta\tau_n)_{\max} = \frac{d\sin(\vartheta_{0,\max})}{c_0} \ , \ n = 1,...,3 \tag{B.2}$$

In our example, we consider an antenna tile for K_u-band satellite communications, where $d = 23.6$ mm and $\vartheta_{0,\max} = 60$ degrees, obtaining $\tau_1 = 68.13$ ps and $\tau_2 = 136.26$ ps.

B.3 Design of the delay units

The required delays are implemented by ORR based delay units. Those components are optical filters with a frequency periodic response, the period being called free spectral range (FSR) (see Chapter 4). Within its optical band, the ORR can be tuned to approximate the desired linear phase dispersion characteristic of an ideal delay line, where the slope is proportional to the amount of delay. The bandwidth of the delay element is defined as the range of frequencies where the phase error $\epsilon < \epsilon_{\max}$, which is the maximum allowed by the design specifications, obtained by the maximum acceptable beam pointing fluctuation. Simulations show that at K_u-band this effect is negligible if $\epsilon < \pi/16$. For a single ORR, the bandwidth decreases when the required delay increases, in a quasi inversely proportional manner [210], and it can be increased by cascading additional ORRs [33, 147]. The design consists in determining the number of ORRs in each delay unit, based on three system level requirements:

- optical bandwidth;

- maximum delay tuning range required, obtained from Eq. (B.2) based on the AE spacing and the maximum scanning angle;

- maximum phase deviation from ideal;

and on two technological parameters: maximum FSR of the ORRs and waveguide losses. The design procedure makes use of an ORR simulator based on LabView software [205], which accounts for the effects of the technological parameters. The design steps are as follows.

1. The simplest structure is considered as a starting point, that is, each delay element is composed by one ORR only.

2. The phase response of each of the resulting optical paths (from the n-th antenna element, AE_n, to the output, see Fig. B.1) is simulated, and tuned to approximate the desired maximum delay for that path, which is obtained from Eq. (B.2). The tuning is performed in such a way to maximize the band in which the phase error (that is, the difference between the desired phase characteristic and the phase of the ORR delay unit) is within the maximum allowed by the design specifications (Fig. B.2).

3. The bandwidth of each path is evaluated.

4. If any of those bands is below the required RF band, the complexity of the beamformer must be increased by adding extra ORRs in the delay elements (starting from the highest stage) and the design steps 2, 3 and 4 are repeated.
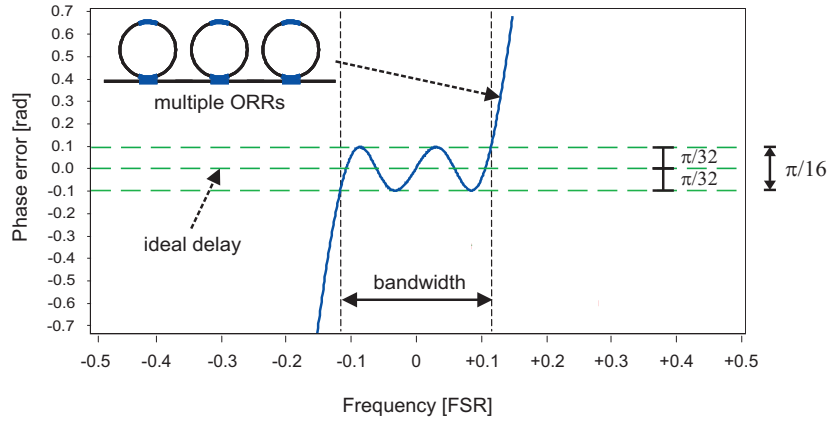
Figure B.2: ORR based delay elements: phase error response

This procedure can be easily extended to the case of a planar array, as is the example of a 4×4 OBFN for a K_u-band antenna. The system specifications are shown in Table B.1 (FSR of the ORRs = 20 GHz, waveguide loss = 0.2 dB/cm), together with the bandwidth of each OBFN path. The obtained layout is displayed in Fig. B.3.

Table B.1: Specifications of a 4×4 OBFN for a K_u-band antenna

Specification	Value
Frequency range	1.05 – 3.10 GHz (IF band DVB-S)
Scan angle (elevation, azimuth)	-60 to +60 degrees
OBFN input subarray spacing (x and y dir.)	23.6 mm
Max phase error (between adjacent inputs)	$\pi/16$
Antenna configuration	Planar, separable illumination
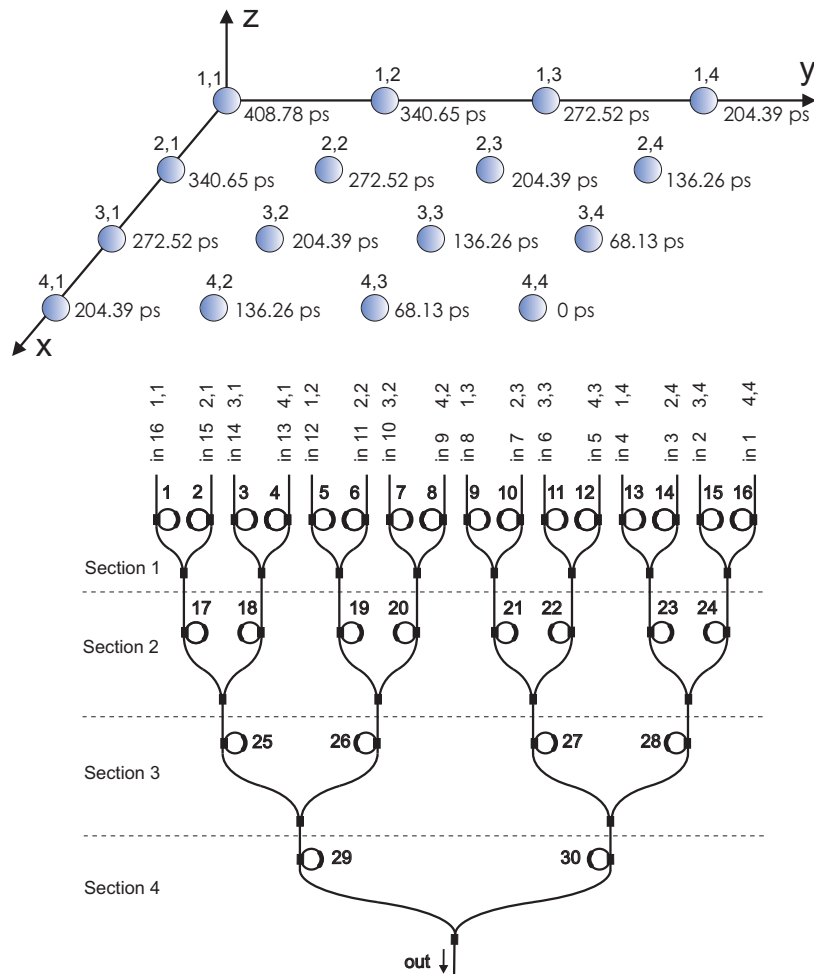
Figure B.3: Example of OBFN for a 4×4 K_u-band planar antenna

Table B.2: Delays and bandwidths in the 4×4 OBFN for a K_u-band antenna

Optical input	Required delay	Bandwidth
4, 4	0 ps	$\gg FSR$
4, 3	68.13 ps	$0.238 \, FSR = 4.7660$ GHz
4, 2	136.26 ps	$0.146 \, FSR = 2.9297$ GHz
4, 1	204.39 ps	$0.135 \, FSR = 2.6953$ GHz
3, 4	68.13 ps	$0.238 \, FSR = 4.7660$ GHz
3, 3	136.26 ps	$0.189 \, FSR = 3.7890$ GHz
3, 2	204.39 ps	$0.141 \, FSR = 2.8125$ GHz
3, 1	272.52 ps	$0.133 \, FSR = 2.6535$ GHz
2, 4	136.26 ps	$0.146 \, FSR = 2.9297$ GHz
2, 3	204.39 ps	$0.135 \, FSR = 2.6953$ GHz
2, 2	272.52 ps	$0.115 \, FSR = 2.3047$ GHz
2, 1	340.65 ps	$0.111 \, FSR = 2.2266$ GHz
1, 4	204.39 ps	$0.135 \, FSR = 2.6953$ GHz
1, 3	272.52 ps	$0.127 \, FSR = 2.5391$ GHz
1, 2	340.65 ps	$0.111 \, FSR = 2.2266$ GHz
1, 1	408.78 ps	$0.107 \, FSR = 2.1484$ GHz

B.4   Case study: design of delay units for MWL-OBFN

In Chapter 7 a novel concept for a hardware-compressive multi-wavelength OBFN (MWL-OBFN) was introduced. The procedure for determining the number of ORRs to be used in each stage was introduced in Sec. 7.6.2 and the detailed calculation is reported in this example.

The band of the OBFN is given by the input-output path which has the smallest bandwidth. For the considered architecture, since all paths have the same number of ORRs, the one with the smallest bandwidth is the one requiring the highest delay, that is, the one corresponding to the antenna element (1, 1), passing by the rings 12-10-6-4 (from now on, we will refer to the paths by the sequence of ring resonators present in that path, as done here). The simulation of the ring tuning for the evaluation of the delay bandwidth is performed below. Due to the way the beamformer is designed and connected to the elements of the array, there is a specific order for the simulation of the optical delay paths. To evaluate the band of the path with the highest delay (12-10-6-4) it is necessary to first simulate other paths. In detail, the ring tuning shall be performed in the following order:

1. Tuning of **ring 4** in order to provide the required 125 ps delay to antenna element (2, 4), path 8-7-5-4;

2. Keeping the same tuning for ring 4, tuning of **ring 6** in order to provide the required 187.5 ps delay to antenna element (1, 4), path 8-7-6-4;
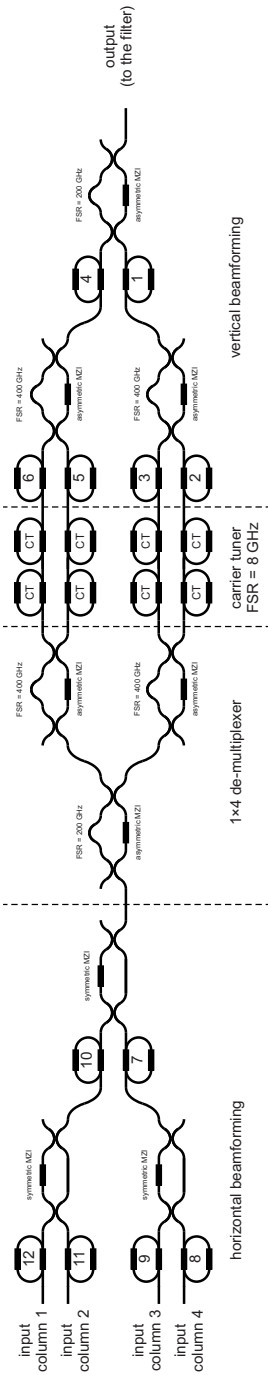
Figure B.4: Proposed OBFN architecture with 1 ORR per stage, in all delay sections. Resulting bandwidth: 2.39 GHz

Table B.3: MWL-OBFN characteristics

Characteristic	Value
Horizontal Beamformer	
Stage 1 (τ_1)	1 ORR
Stage 2 (τ_2)	1 ORR
Vertical Beamformer	
Stage 1 (τ_1)	1 ORR
Stage 2 (τ_2)	1 ORR
FSR of the ORRs	25 GHz
RTT of the ORRs (T)	40 ps
Required delay bandwidth	$\geq 2\,\text{GHz}(= 5\,\text{GHz} - 3\,\text{GHz})$
Max delay ripple[a] in band $\pi/16 = \pm\pi/32$	
Optical waveguide loss	0.2 dB/cm

---

[a]Maximum deviation from the ideal phase response.

3. Keeping the same tuning for rings 4 and 6, tuning of **ring 10** in order to provide the required 312.5 ps delay to antenna element (1, 2), path 11-10-6-4;

4. Keeping the same tuning for rings 4, 6 and 10, tuning of **ring 12** in order to provide the required 375 ps delay to antenna element (1, 1), path 12-10-6-4.

Path 8-7-5-4

- Required delay (additional with respect to the reference path): 125 ps

- Normalized required delay: $3.125T$

- Total required delay for the I/O path (considering also the minimum delay T introduced by the ORRs): $\tau_{8-7-5-4} = 4T + 3.125T = 7.125T$

- Active ORRs: ring 4

- Delay bandwidth: 0.131 FSR = 3.27 GHz

Path 8-7-6-4

- Required delay (additional with respect to the reference path): 187.5 ps

- Normalized required delay: $4.6875T$

- Total required delay for the I/O path (considering also the minimum delay T introduced by the ORRs): $\tau_{8-7-6-4} = 4T + 4.6875T = 8.6875T$

- Active ORRs: ring 4, ring 6

- Delay bandwidth: 0.121 FSR = 3.027 GHz

Path 11-10-6-4

- Required delay (additional with respect to the reference path): 312.5 ps

- Normalized required delay: $7.8125T$

- Total required delay for the I/O path (considering also the minimum delay T introduced by the ORRs): $\tau_{11-10-6-4} = 4T + 7.8125T = 11.8125T$

- Active ORRs: ring 4, ring 6, ring 10

- Delay bandwidth: 0.0996 FSR = 2.49 GHz

Path 12-10-6-4

- Required delay (additional with respect to the reference path): 375 ps

- Normalized required delay: $9.375T$

- Total required delay for the I/O path (considering also the minimum delay T introduced by the ORRs): $\tau_{12-10-6-4} = 4T + 9.375T = 13.375T$

- Active ORRs: ring 4, ring 6, ring 10, ring 12

- Delay bandwidth: 0.0957FSR = 2.39GHz > 2GHz

The analysis described in this paragraph showed that, in the situation of Fig. B.4, one ORR per each stage is sufficient to implement a beamformer with a phase ripple in the passband below $\pi/16$ over a bandwidth of 2.39 GHz, as from specification (min. required bandwidth: 2 GHz).

B.5   Conclusions

In this Appendix we have shown a novel design procedure for symmetric binary tree optical beamformers, using as example a design for a K_u-band phased array antenna for satellite reception. The method allows to design the beamformer with minimum complexity based on the given system specifications and technological constraints.

Acknowledgments

D'Oh! I tried hard and failed miserably. The lesson is, never try!

I kind of liked reading this sentence in the template that I worked out together with Arjan to fix all the bumps and errors, before being able to start writing this little book here. I have a feeling that a number of "miserable failures" have occurred in those years to me as well, but I also feel that this wasn't that bad, at the end of the day. Like Homer Simpson, in the sentence above, remembering that life is a place to enjoy, I also think that if everything goes smooth things are too easy, right? I must admit I have more delight, in these days, by remembering how the bad things have been overcome and lead to this book, then to the things which went just smooth. Someone said "we chose to do these and other things, not because they are easy, but because they are hard!" That guy wasn't that lucky after all, but for the hard challenges he accepted he surely stayed in history. And when I write this, I think about all the people who have been or are right now through hard times in doing their job.

I want to warmly thank my assistant-promotor and daily supervisor, Dr. Chris Roeloffzen, for many things indeed... but mostly for his trust and support in the moments of discouragement. For never losing hope and, helping me to see the bright side. With a honest smile, you gave me the strength to go on in the moments of difficulty. For his support to my ideas and always being available to discuss, even at 5 pm on Friday :) Your trust has been the engine that pushed me through this sometimes very hard journey towards the degree. I can never thank you enough for spending so much of your precious time reading, reviewing, giving very important feedback on this thesis, for the only sake of making sure I had a good work, at times which were already busy enough for you. But most, you taught me with your example to be honest in my work. This is such a precious and rare quality you have. I will not forget.

I want to thank very much my promotor, Prof. Wim van Etten. Thank you so much for all the time you spent and the efforts in reviewing my thesis, despite the hard deadlines and the fact that I was so far away. Thanks for your feedback which allowed to transform this from a draft to a real book.

I also want to express my gratitude to all the members of the Committee: thank you for accepting to review my thesis and to share your time and expertise in this very special occasion for me. Thank you!

David, I hope we'll get the chance to work together again, sometimes, somewhere... (hopefully there will be no over-qualified monkey applying to the same position and taking our place!). I find it hard to say in words how grateful I am for

ways supportive with the people within it, friendly to all, from the big professors to the newly-arrived students. Prof. Capmany, thank you very much for having accepted to take part in my defense, coming all the way from Spain. I am honored to have you in my committee. Thanks to everybody in your group, Juan, Joan, Mario, Ivana, Salvador and all our friends-colleagues from Valencia: it has been great to get to know you in Valencia in 2009 and then meeting you again at conferences. I hope we can keep in touch for future endeavors together! Prof. Herczfeld, thank you for being so kind to sharing your slides and your encouragement about this work. I am truly honored to have had the chance to talk to an expert like you. Iiiiivan... great that we started together, end up far away a number of times, but somehow always getting back close at a couple of euros distance (Enschede-Gronau... You still travel for free across Germany, right?) :) It was great going to conference together. Salutami Neo se lo rivedi (scritto bene stavolta, visto???) Rocco, thanks for sharing so many "momenti demenziali" all together. :) Ramiro y Mariana, I had a great time when you were in Twente. I wish you all the best for a bright career! You shall teach me how to prepare *mate* at some point, so we drink it all together with Rosario, ok? Laura, thanks for the Tori Amos concert... let's go again! Beautifuldiscovery: you're so great. Keep singing! Andreea, thanks for your great help and beautiful friendship. Thanks so much for all your Singapore tips, your souvenirs from around the world, and most of all for your invaluable help during the "decision times". I don't forget! Jean Pascal, Finally you not only joined me in Canada... you actually overshot a bit too far to the other side!! Let's try to meet up at some point, for another beer + Daft Punk dance night! Anupoma, Shawraw, Asif, Dhrubo, and all the Bangla-Enschede community!!! When are we going to have another almost-legal van-trip? :) Sig. Minuto, thanks for sharing the effort to make sure the food at casa Carloni would never be wasted, ever; and for making sure that parties would be over just at the right time. :) Martin and all the people at the Voedselbank: thanks for your sincere friendship! Ik ben zo blij dat ik jullie heb ontmoet. Bedankt voor uw vriendschap, voor het zijn zulke goede mensen en... de Nederlands lessen! Bionda, Inske and Amke: thanks for your hospitality and your friendship! Frate'... eeeh! Nummeparecoreetto che mo te sei trasferitooo a Hirversumm... maaa... ti convieneee?? L'*Osteria der Burla D'Oro* t'aspetta in Canada! Elia, Luisa e Orlando, ma sete propio gajardi! Thanks for all your hospitality and giving me a large plate of properly cooked "fischiotti" all the times I was hungry and alone :) Hopefully see you in Pisa! Nur, Angela e Asietta: grazie per la vostra preziosa amicizia! Speriamo di venire presto a vedere la nuova casa... e la nuova donna di casa! Simona, Fausto, Edward e Carmen, grazie per la macchina, i dolci stupendi, i consigli preziosi! Buona fortuna ad Eindhoven. Giulia, Pietro e Giovanni, che spettacolo avervi conosciuti! Quanto di più autentico uno può sperare di trovare in terra straniera! Grazie per l'amicizia, e per ricordarmi cosa significa cucina italiana, cuore italiano, vicinanza italiana... e più! Stefano e Marieke. I am so glad we met. As you said, not that often but... those times, you were there! And that made the difference. Francesco Santini, grazie per la tua amicizia e bontà sincera! Keep going eastwards!! Sander Huisman, thanks for our 1-hour lunch-photography discussions, enjoyed that! Yunyun, you've been soooo nice! Thanks! Hardboard people: thanks for welcoming me and introducing

me to the world of wakeboarding... amazing fun (and muscle pain indeed)! Thanks for noticing my curiosity and inviting me to join! Thanks to Foton people, I had great fun taking pics together and serving as "beginner bartender" once in my life :) Marianne and Hans Dom, Tobias and Lieke: thanks for the *duende* you brought to my Enschede-life!!! I miss you a lot since I left Enschede, especially our lovely afternoon discussions about flamenco and many more things, accompanied by your passionate guitar playing, your unique kindness and your delicious coffee :) I am grateful to you for how close I felt you were especially during the final times with my thesis, you were always ready to give a smile and a warm word of encouragement. I hope we can always keep in contact and have much more time to spend together!!! Please visit me in Canada and let's meet up in a trip to Andalucia! Eduard, thanks for the pleasant discussions... Now, it's time: *have a seat, enjoy the view!* :) Albert van Duin and team of the Starparty: thanks for sharing your sincere enthusiasm for stargazing (and, in your case, much more than that!) and going out in freezing nights to taste that great feeling of capturing weak and beautiful objects on your telescopes. Ina, complimenti ancora per il tuo italiano e grazie della tua amicizia sincera!!! Spero di rivederti molto presto! Klaas, I would like to thank you warmly for being so nice and helpful while sharing the long days at the anechoic chamber measurements of the demonstrator in Astron. It has been hard work but for I learned really a lot from you. Now I know how to be persistent despite unexpected results; it takes some time to finally reach the right path. And anyway, *hardlopers zijn doodlopers*, right? All the best and thanks. Adriaan, same applies to you: during the Smart project demonstration I was amazed by your skills. It has been a great opportunity for me to spend time at NLR and work with Leimeng and Chris under your expert guidance. I am grateful I had the chance to learn from your experience. Keep cycling high! Pieter Jorna, I want to thank you for all the time you spent with me, trying to understand the obscure secrets behind antenna feeding networks :) You are really talented, I wish you all the best and a bright academic future. Jaco Verpoorte, thanks a lot for all the very nice discussions, it was great working together! I hope we will have that chance again. Jing, I really enjoyed having you in the same project. You've always been so nice and helpful, not only in work-related stuff, but also when talking with you about everything! You're really nice. I wish you a lot of *succes* with your future! Looking forward to the next kart race! Elango & Shanthi, I had a great time with you. I enjoyed your super-spicy food, your hospitality, and the rides back from Drenthe munching chips :) It was great to meet again before leaving, thanks for finding the time and for the book! Elango=Pirla! Alex Budianu... uaa, can imi dai banii?! (Btw, are you Jimmy Ray? for sure you're a Soup-a-Star!!) :) Bernhard, I wish you all the very best! When you come to Canada I'll make sure we have a projector for our promised surf movie :) Arjan, thanks for the very good discussions, your LaTeX tips, and your countless efforts to make me come on time to the group presentations! :) Yakup bhei... *yoksun diye geldi esti bahar... yoksun diye yandıaşkına can...* I will miss you, aşkın! (Don't tell Ansfrida plz)... Anne and Rajeev, thanks for all your help, the evenings at your place and all the trips to choose the best car (black!) :) All the best for your life. Merhaba Ben! The girls of Twente love you! I am so jealous! Fatou 1 & 2, it was great to have you

in the group, I hope I can get to meet both of you again soon... maybe in Canada?! Olghina, wow - that was quick! All the best congrats for your 2 big news, wedding and baby! I miss our chats and the fun we had together. Oya, Sinem, Muharram, Ramazan, Bilge, Janettina, Cem, Elif, Can, Berk, Pinar... and the whole Turkish community in Enschede. I especially enjoyed your companies and your parties are the best! (btw I can still do the warrior dance) :) Valeria, grazie per la tua forte amicizia ai tempi di Enschede! É stato bellissimo poter condividere le ricette oltreoceano - vi aspettiamo a te e Coso in Canadà! Ibsen Cardenas, thanks for the honest discussions, I hope you have all the best in your life. Rodhaan Al Galidi, thanks for your hospitality, for letting me use your *oud* and for being so kind to me. I am honored to have met you and having been able to share thoughts with you. Jan-Pieter van der Giessen, you are a great musician, thanks for your dedication, you are a model for me. Jet Rootlieb, thanks for your way of making us love the Dutch language! You're an amazing teacher. Rosary group: to Aryo and all my friends from Ariens, thanks for bringing a big invisible, silent but unstoppable stream of hope in our happy or less-happy days. Andrea, you are a beautiful person. Thanks for inviting me to your wedding! All the best to you and Jaap for the most beautiful Colombian-Dutch family ever :) Fr Smits, thanks for your help since the first days I spent in Holland, for your suggestions and support. Thanks for the care you put in what you do! I look forward to see you again. Fr Andre Monninkhof, thanks for your care about the Ariens community, your committment and your good heart. Olaf Bruggeling, it was great to meet you. I never forget your words and all your encouragement, for really understanding what was going on in my mind and helping me with your experience. I wish you the very best and all the blessings for your life! Alfons Groenland, thanks for asking me to be your photographer! I spent a great day and I was so happy to be there to catch every moment of your wedding. All the best and congrats for your beautiful family. Chaitanya and Audrey, it was great to share the time in Enschede and I wait for you in Montreal! Thanks Chaitanya for bringing peace and a breath of fresh air (in all sense!) in my busy Canadian life! Amir Ghaffari, thanks for the nice chats at the coffee machine, sharing ideas about microwave engineering, and the shared feelings about the hard times of the end of PhD! I wish you all the best for your future career. I want to especially thank all the students who worked directly or indirectly with me: Jack, Martin, Diederik, Steven, Yen, Laura, Fabien, Cedric, Marc and Laila, Ludovic and Emma. I am grateful to each and everyone of you for your assistance and your contributions at different stages of this work. Alejandro, thanks for your friendship, I wish you to realize what you want most and will make you happy! A special thanks to Robert, Roelof, Christiaan, Martijn. Of course we started the very best B2 project of all time, and that was thanks to the passion you put into it! I'm sure our friend Frank Kooiman is proud of you too. Mircea, we still have to go drink that beer! Let's do it tonight ;) Thanks to the "alma latina en Enschede", L.A. Voz! Amazing how you managed to warm up the life of many in Enschede with your latin spirit! Lorenzo and Vicky, you are the responsible for saving us from the grey Dutch days with your food and dance nights at your place. Lorenzo & Vicky for presidents! Chilangos Habaneros: you really saved me! You filled up my time in Enschede with world music, emotions, new tempos (*caballo!*) and... ron!

Biography

Maurizio Burla was born in Orvieto (Terni), Italy, on the 13th August 1982. In February 2005 he received his B.Sc. degree (summa cum laude) from the University of Perugia, Italy, with a thesis on a low-cost X-K_u band microwave radiometer for forest fire detection, under the supervision of Dr. F. Alimenti. Then he spent seven months at the University of Bristol, UK, as an Erasmus student for the development of his M.Sc. thesis, regarding the design and realization of planar multiband antennas based on fractal architecture, for Wireless-over-Fiber transceiver applications. From December 2006 to April 2007 he was intern at Delta-Utec Space Research & Consultancy, Leiden, the Netherlands, working among the YES2 (Young Engineers' Satellite 2) project, on System Integration and Testing of the RF section of YES2 satellite. After his M.Sc. graduation (summa cum laude) in Electronic Engineering in November 2007, under the joint supervision of Prof. R. Sorrentino (University of Perugia, Italy) and Prof. M. Cryan (University of Bristol, UK), he joined the System Engineering group at AleniaSIA S.p.A., Torino, Italy, working on the Avionic System of the Alenia C-27J Spartan aircraft. Since July 2008 he has worked at the Telecommunication Engineering Group of the University of Twente as a PhD student. His work is on advanced optical beamformers based on integrated optical ring resonators, and is part of the Memphis project. During those years, he has worked in conjunction with several Dutch companies and research institutes, as Astron, NLR, TNO, LioniX BV, Satrax BV. While at the University of Twente, he has co-supervised a total of 21 international students. In September 2011 he gave an invited talk on the topic of Microwave Photonics at IRA-CNR, Medicina, Italy. Maurizio Burla received the Runner-up Student Award at the 2011 IEEE International Topical Meeting on Microwave Photonics (MWP2011), 18-21 Oct 2011, Singapore. His work has been selected to appear in the Research Highlights of the December 2011 Technology Focus of Nature Photonics. He was also a co-recipient of the second Best Student Team Award at the International Astronautical Congress 2008, Glasgow, Scotland, for his work in the YES2 project, and of the Best Poster Award at the MEMPHIS General Assembly 2008, Amersfoort, The Netherlands. Since October 2012 he is a postdoctoral research fellow at INRS-EMT, Montréal, Canada, in the group of Prof. José Azaña, working on integrated-waveguide technologies for ultrafast all-optical signal processing and microwave photonics.

List of publications

Journal publications

1. <u>M. Burla</u>, D. Marpaung, L. Zhuang, A. Leinse, M. Hoekman, R. Heideman, C. Roeloffzen, "Integrated Photonic K_u-Band Beamformer Chip with Continuous Amplitude and Delay Control," *IEEE Photonics Technology Letters*, vol. 25, no. 12, pp. 1145-1148, April 2013.

2. M. R. H. Khan, E. H. Bernhardi, D. A. I. Marpaung, <u>M. Burla</u>, R. M. de Ridder, K. Wörhoff, M. Pollnau, C.G.H. Roeloffzen, "Dual frequency Distributed Feedback Laser with an Optical Frequency Locked Loop for Microwave Signal Generation", *IEEE Photonics Technology Letters*, vol. 24, no. 16, pp. 1431-1433, Aug. 2012.

3. <u>M. Burla</u>, M. R. H. Khan, L. Zhuang, D. A. I. Marpaung, C. G. H. Roeloffzen, P. Maat, K. Dijkstra, A. Leinse, M. Hoekman, R.G. Heideman, "System Integration and Radiation Pattern Measurements of a Phased Array Antenna employing an Integrated Photonic Beamformer for Radio Astronomy Applications," *Applied Optics*, vol. 51, no. 7, pp. 789–802, 2012.

4. D. A. I. Marpaung, L. Chevalier, <u>M. Burla</u>, C. G. H. Roeloffzen, "Impulse radio ultrawideband pulse shaper based on a programmable photonic chip frequency discriminator," *Optics Express*, vol. 19, no. 25, pp. 24838–24848, 2011.

(cited in the *Technology Focus* of *Nature Photonics*, Dec. 2011)

5. L. Zhuang, D. A. I. Marpaung, <u>M. Burla</u>, W. C. Beeker, A. Leinse, C. G. H. Roeloffzen, "Low-loss, high-index-contrast Si3N4/SiO2 optical waveguides for optical delay lines in microwave photonics signal processing. *Optics Express*, vol. 19, no. 23, pp. 23162–23170, 2011.

6. <u>M. Burla</u>, D. A. I. Marpaung, L. Zhuang, C. G. H. Roeloffzen, M. R. H. Khan, A. Leinse, M. Hoekman, R. Heideman, "On-chip CMOS compatible reconfigurable optical delay line with separate carrier tuning for microwave photonic signal processing", *Optics Express*, vol. 19, no. 22, pp. 21475–21484, Dec. 2011.

(selected for the *Research Highlights Technology Focus* in *Nature Photonics*, Dec. 2011)

7. A. Meijerink, C. G. H. Roeloffzen, R. Meijerink, L. Zhuang, D. A. I. Marpaung, M.J. Bentum, <u>M. Burla</u>, J. Verpoorte, P. Jorna, A. Hulzinga, W. van Etten, "Novel ring resonator-based integrated photonic beamformer for broadband phased array receive antennas – Part I: Design and performance analysis," *IEEE Journal of Lightwave Technology*, vol. 28, no. 1, pp. 3–18, Jan. 2010.

   (Highlighted in *Photonics Journal* "Breakthrough in Photonics 2010")

8. L. Zhuang, C. G. H. Roeloffzen, A. Meijerink, <u>M. Burla</u>, D. A. I. Marpaung, A. Leinse, M. Hoekman, R.G. Heideman, W. van Etten, "Novel ring resonator-based integrated photonic beamformer for broadband phased array receive antennas – Part II: Experimental prototype," *IEEE Journal of Lightwave Technology*, vol. 28, no. 1, pp. 19–31, Jan. 2010.

   (Highlighted in *Photonics Journal* "Breakthrough in Photonics 2010")

Conference contributions

1. <u>M. Burla</u>, L. Zhuang, D. Marpaung, M. R. Khan, A. Leinse, W. Beeker, M. Hoekman, R. Heideman, and C. Roeloffzen, "On-Chip, CMOS-compatible, Hardware-Compressive Integrated Photonic Beamformer based on WDM", *Proc. of the 2013 IEEE International Topical Meeting on Microwave Photonics (MWP 2013)*, Alexandria, VA, USA, October 28-31, 2013.

2. A. Leinse, R. G. Heideman, M. Hoekman, F. Schreuder, F. Falke, C. G. H. Roeloffzen, L. Zhuang, <u>M. Burla</u>, D. Marpaung, D. H. Geuzebroek, R. Dekker, E. J. Klein, P. W. L. van Dijk, R. M. Oldenbeuving, "TriPleX waveguide platform: low-loss technology over a wide wavelength range," *Proc. SPIE 8767, Integrated Photonics: Materials, Devices, and Applications II*, Grenoble, France, 24 April 2013, paper 87670E, doi:10.1117/12.2020574.

3. M. R. H. Khan, E.H. Bernhardi, D. A. I. Marpaung, <u>M. Burla</u>, R.M. de Ridder, K. Worhoff, M. Pollnau, C. G. H. Roeloffzen, "Highly stable microwave carrier generation using a dual-frequency distributed feedback laser," *Proc. of the 2012 IEEE International Topical Meeting on Microwave Photonics (MWP 2012)*, Noordwijk, The Netherlands, Oct. 2012, pp. 1–4.

4. <u>M. Burla</u>, D. Marpaung, L. Zhuang, M. R. H. Khan, C. Roeloffzen, A. Leinse, M. Hoekman, R. Heideman, "CMOS-compatible integrated optical delay line for broadband K_u-band satellite communications," *Proc. of the 2011 IEEE International Topical Meeting on Microwave Photonics (MWP 2012)*, Noordwijk, The Netherlands, Oct. 2011, pp. 120–123.

5. L. Zhuang, D. Marpaung, <u>M. Burla</u>, M. Khan, C. Roeloffzen, W.P. Beeker, A. Leinse, R. Heideman, "On-chip microwave signal processors in low-loss, high-index-contrast Si_3N_4/SiO_2 waveguides", *European Conference on Integrated Optics (ECIO 2012)*, Barcelona, 18-20 April 2012.

6. A. Leinse, R. Heideman, W.P. Beeker, C. Brunnink, C. Roeloffzen, L. Zhuang, D. Marpaung, M. Burla, "TriPleX™photonic platform technology", *European Conference on Integrated Optics (ECIO 2012)*, Barcelona, 18-20 April 2012.

7. L. Zhuang, D. A. I. Marpaung, M. Burla, C. G. H. Roeloffzen, W.P. Beeker, A. Leinse, P. van Dijk, "Low-loss and programmable integrated photonic beamformer for electronically-steered broadband phased array antennas", *Proc. of the IEEE Photonics Conference (IPC 2011)*, Arlington, Virginia, USA, 9-13 Oct 2011, pp. 137–138.

8. M. Burla, M. R. H. Khan, D. A. I. Marpaung, L. Zhuang, C. G. H. Roeloffzen, A. Leinse, M. Hoekman, R. Heideman, "Separate carrier tuning scheme for integrated optical delay lines in photonic beamformers," *Proc. of the 2011 IEEE International Topical Meeting on Microwave Photonics jointly held with 2011 Asia Pacific Microwave Photonics (MWP 2011)*, Singapore, Oct. 2011, pp. 1-4.

(Runner-up Best Student Paper Award at MWP 2011)

9. D. A. I. Marpaung, L. Zhuang, M. Burla, C. G. H. Roeloffzen, B. Noharet, Q. Wang, W.P. Beeker, A. Leinse, R. Heideman, "Photonic integration and components development for a Ku-band phased array antenna system," *Proc. of the 2011 IEEE International Topical Meeting on Microwave Photonics jointly held with 2011 Asia pacific Microwave Photonics (MWP 2011)*, Singapore, 18-21 Oct 2011, pp. 1–4.

10. M. R. H. Khan, D. A. I. Marpaung, M. Burla, C. G. H. Roeloffzen, "A novel measurement technique to estimate the RF beat-linewidth of free-running heterodyning system using a photonic discriminator", *Proc. of the 2011 IEEE International Topical Meeting on Microwave Photonics jointly held with 2011 Asia Pacific Microwave Photonics (MWP 2011)*, Singapore, 18-21 Oct 2011, pp. 1–4.

11. L. Zhuang, D. A. I. Marpaung, M. Burla, R. Boot, A. Hulzinga, W.P. Beeker, P. van Dijk, C. G. H. Roeloffzen, "Development of an integrated photonic beamformer for electronically-steered Ku-band phased array antenna," *Proc. of the Avionics, Fiber-Optics and Photonics Technology Conference 2011*, San Diego, California, USA, 4-6 Oct 2011, pp. 41–42.

12. M. R. H. Khan, D. A. I. Marpaung, M. Burla, C. G. H. Roeloffzen, E.H. Bernhardi, R.M. de Ridder, "Investigation on the performance of an optically generated RF local oscillator signal in Ku-band DVB-S systems, *Proc. of the 30th URSI General Assembly and Scientific Symposium*, Istanbul, Turkey, 13-20 Aug 2011, pp. 1–4.

13. D. A. I. Marpaung, L. Zhuang, M. Burla, C. G. H. Roeloffzen, J. Verpoorte, H. Schippers, A. Hulzinga, P. Jorna, W.P. Beeker, A. Leinse, R. Heideman, B. Noharet, Q. Wang, B. Sanadgol, "Towards a broadband and squint-free ku-band

phased array antenna system for airborne satellite communications," *Proc. of the 5th European Conference on Antennas and Propagation (EUCAP 2011)*, Rome, Italy, 11-15 Apr 2011, pp. 2774–2778.

14. M. Burla, C. G. H. Roeloffzen, D. A. I. Marpaung, M. R. H. Khan and W. van Etten, "A Novel Design Procedure for Minimum RF Phase Error in Optical Ring Resonator Based Integrated Optical Beamformers for Phased Array Antennas," *Proc. of the IEEE/LEOS Benelux 2010*, Delft, The Netherlands, Nov. 2010, pp. 245–248.

15. M. Burla, M. R. H. Khan, D. A. I. Marpaung, C. G. H. Roeloffzen, P. Maat, K. Dijkstra, A. Leinse, M. Hoekman, R.G. Heideman, "Squint-Free Beamsteering Demonstration using a Photonic Integrated Beamformer Based on Optical Ring Resonators," *Proc. of the IEEE International Topical Meeting on Microwave Photonics*, Montréal, Canada, Oct. 2010, pp. 401–404.

16. M. Burla, M. R. H. Khan, D. A. I. Marpaung, C. G. H. Roeloffzen, P. Maat, K. Dijkstra, A. Leinse, M. Hoekman, R.G. Heideman, "Photonic integrated beamformers for broadband radio astronomy," *International Workshop on Phased Array Antenna Systems for Radio Astronomy*, Brigham Young University, Provo, Utah, USA, May 2010.

17. M. R. H. Khan, M. Burla, C. G. H. Roeloffzen, D. A. I. Marpaung, and W. van Etten, "Phase noise analysis of an RF local oscillator signal generated by optical heterodyning of two lasers ," *Proc. of the 14th Annual Symposium of the IEEE Photonics Benelux Chapter*, Brussels, Belgium, November 2009.

18. L. Zhuang, M. Burla, C. G. H. Roeloffzen, A. Meijerink, D. A. I. Marpaung, M. R. H. Khan, W. C. van Etten, A. Leinse, M. Hoekman, R.G. Heideman, "RF-to-RF Characterization of a Phased Array Receive Antenna Steering System Using a Novel Ring Resonator-Based Integrated Photonic Beamformer," *Proc. of the IEEE International Topical Meeting on Microwave Photonics*, Valencia, Spain, Oct. 2009.

19. M. Burla, A. García García, L. Zhuang, A. Meijerink, C. G. H. Roeloffzen, D. A. I. Marpaung, M. R. H. Khan and W. C. van Etten, "Optical Phase Synchronization in Coherent Optical Beamformers for Phased Array Receive Antennas," *Proc. of the 22nd Annual Meeting of the IEEE Photonics Society*, Belek-Antalya, Turkey, October 2009.

20. M. R. H. Khan, M. Burla, C. G. H. Roeloffzen, D. A. I. Marpaung, W. C. van Etten, "Analysis of phase noise and cnr degradation of externally generated lo signal in LNB for Ku-band DVB-S systems by heterodyning two lasers," *Proc. of the URSI Benelux (International Union of Radio Science) Forum 2009*, Delft, The Netherlands, Jun. 2009.

21. M. Burla, M. R. H. Khan, L. Zhuang, C. G. H. Roeloffzen, "Multiwavelength optical beam forming network with ring resonator-based binary-tree archi-

tecture for broadband phased array antenna systems," *Proc. of the IEEE/LEOS Benelux Symposium*, Enschede, The Netherlands, Nov. 2008, pp. 99–102.

22. G.C. Cucarella, A. Cichocki, <u>M. Burla</u>, "Development, test and flight results of the RF systems for the YES2 tether experiment", *Proc. of the 59th International Astronautical Congress 2008*, Glasgow, Scotland, Oct. 2008.

(Runner-up Best Student Team Award at IAC 2008)